Advancing Musculoskeletal Robot Design for Dynamic and Energy-Efficient Bipedal Locomotion

TECHNISCHE
UNIVERSITÄT
DARMSTADT

Vom Fachbereich Informatik der
Technischen Universität Darmstadt
zur Erlangung des akademischen Grades einer
Doktor-Ingenieurin (Dr.-Ing.)
genehmigte

Dissertation

von

Dipl.-Inform. Katayon Radkhah
(geboren in Frankfurt/Main, Deutschland)

Referent:	Prof. Dr. Oskar von Stryk
Koreferent:	Prof. Koh Hosoda, PhD (Osaka University, Japan)
Tag der Einreichung:	23.04.2013
Tag der mündlichen Prüfung:	18.06.2013

D17
Darmstadt 2014

Contents

Abstract

Achieving bipedal robot locomotion performance that approaches human performance is a challenging research topic in the field of humanoid robotics, requiring interdisciplinary expertise from various disciplines, including neuroscience and biomechanics. Despite the remarkable results demonstrated by current humanoid robots—they can walk, stand, turn, climb stairs, carry a load, push a cart—the versatility, stability, and energy efficiency of humans have not yet been achieved. However, with robots entering our lives, whether in the workplace, in clinics, or in normal household environments, such improvements are increasingly important.

The current state of research in bipedal robot locomotion reveals that several groups have continuously demonstrated enhanced locomotion performance of the developed robots. But each of these groups has taken a unilateral approach and placed the focus on only one aspect, in order to achieve enhanced movement abilities;—for instance, the motion control and postural stability or the mechanical design. The neural and mechanical systems in human and animal locomotion, however, are strongly coupled and should therefore not be treated separately. Human-inspired musculoskeletal design of bipedal robots offers great potential for enhanced dynamic and energy-efficient locomotion but also imposes major challenges for motion planning and control.

In this thesis, we first present a detailed review of the problems related to achieving enhanced dynamic and energy-efficient bipedal locomotion, from various important perspectives, and examine the essential properties of the human locomotory apparatus. Subsequently, existing insights and approaches from biomechanics, to understand the neuromechanical motion apparatus, and from robotics, to develop more human-like robots that can move in our environment, are discussed in detail. These thorough investigations of the interrelated essential design decisions are used to develop a novel design for a musculoskeletal bipedal robot, BioBiped1, such that, in the long term, it is capable of realizing dynamic hopping, running, and walking motions. The BioBiped1 robot features a highly compliant tendon-driven actuation system that mimics key functionalities of the human lower limb system. In experiments, BioBiped1's locomotor function for the envisioned gaits is validated globally. It is shown that the robot is able to rebound passively, store and release energy, and actively push off from the ground. The proof of concept of BioBiped1's locomotor function, however, marks only the starting point for our investigations, since this novel design concept opens up a number of questions regarding the required design complexity for the envisioned motions and the appropriate motion generation and control concept.

For this purpose, a simulator specifically designed for the requirements of musculoskeletally actuated robotic systems, including sufficiently realistic ground reaction forces, is developed. It relies on object-oriented design and is based on a numerical solver, without model switching, to enable the analysis of impact peak forces and the simulation of flight phases. The developed library also contains the models of the actuated and passive mono- and biarticular elastic tendons and a penalty-based compliant contact model with nonlinear damping, to incorporate the collision, friction, and stiction forces occurring during ground contact. Using these components, the full multibody system (MBS) dynamics model is developed. To ensure a sufficiently similar behavior of the simulated and the real musculoskeletal robot, various measurements and parameter identifications for sub-models are performed. Finally, it is shown that the simulation model behaves similarly to the real robot platform.

The intelligent combination of actuated and passive mono- and biarticular tendons, imitating important human muscle groups, offers tremendous potential for improved locomotion performance but also requires a sophisticated concept for motion control of the robot. Therefore, a further contribution of this thesis is the development of a centralized, nonlinear model-based method for motion generation and control that utilizes the derived detailed dynamics models of the implemented actuators. The concept is used to realize both computer-generated hopping and human jogging motions. Additionally, the problem of appropriate motor-gear unit selection prior to the robot's construction is tackled, using this method.

The thesis concludes with a number of simulation studies in which several leg actuation designs are examined for their optimality with regard to systematically selected performance criteria. Furthermore, earlier paradoxical biomechanical findings about biarticular muscles in running are presented and, for the first time, investigated by detailed simulation of the motion dynamics. Exploring the Lombard paradox, a novel reduced and energy-efficient locomotion model without knee extensor has been simulated successfully.

The models and methods developed within this thesis, as well as the insights gained, are already being employed to develop future prototypes. In particular, the optimal dimensioning and setting of the actuators, including all mono- and biarticular muscle-tendon units, are based on the derived design guidelines and are extensively validated by means of the simulation models and the motion control method. These developments are expected to significantly enhance progress in the field of bipedal robot design and, in the long term, to drive improvements in rehabilitation for humans through an understanding of the neuromechanics underlying human walking and the application of this knowledge to the design of prosthetics.

Keywords: Musculoskeletal robot design, compliant tendon-driven actuation, mono- and biarticular muscle-tendon units, multibody system dynamics simulation, bipedal robot locomotion, motion control, locomotion performance, energy consumption

Zusammenfassung

Die Realisierung zweibeiniger Roboterfortbewegung mit der Leistungsfähigkeit, die der des Menschen nahekommt, stellt noch immer eine große Herausforderung im Forschungsgebiet der humanoiden Robotik dar und erfordert umfassende Fachkenntnisse in verschiedenen Disziplinen, einschließlich der Neurowissenschaften und Biomechanik. Obwohl gegenwärtige Laufroboter unter anderem gehen, stehen, sich drehen, Treppen aufsteigen und eine Last tragen können, ist die Vielseitigkeit, Stabilität und Energieeffizienz des Menschen noch unerreicht. Diese Kriterien sind aber umso wichtiger, je stärker Roboter Einzug in unser alltägliches Leben halten werden – sowohl am Arbeitsplatz als auch in Krankenhäusern oder normalen häuslichen Umgebungen.

Der heutige Stand der Forschung in zweibeiniger Roboterfortbewegung bringt einige schon länger bestehende Gruppen zum Vorschein, die zwar eine kontinuierlich verbesserte Fortbewegungsperformanz der entwickelten Roboter vorzeigen können, aber sich durch eine einseitige Vorgehensweise auszeichnen. Jede Gruppe hat bisher das Augenmerk auf nur einen für performantes Laufen bedeutenden Teilaspekt gelegt – auf die Regelung und Stabilisierung der vorgesehenen Bewegung oder das mechanische Design. Das neuronale und mechanische System in Mensch und Tier sind jedoch bei der Fortbewegung stark aneinander gekoppelt und sollten daher nicht getrennt betrachtet werden. Ein vom Menschen inspiriertes Muskelskelettdesign eröffnet hierbei die Möglichkeit, größere Fortschritte bei der Umsetzung dynamischer und energieeffizienter Fortbewegung zu erzielen, stellt aber auch besondere Herausforderungen an die Bewegungsplanung und -regelung.

In der vorliegenden Arbeit wird zunächst aus den Blickwinkeln der relevanten Teildisziplinen die Herausforderung, zweibeinige Fortbewegung zu realisieren, analysiert. Zum einen werden die aus biomechanischer Sicht wesentlichen Eigenschaften des menschlichen Bewegungsapparates näher beleuchtet. Zum anderen werden die bisherigen Forschungsergebnisse und unterschiedlichen Herangehensweisen aus der Biomechanik, um den neuromechanischen Bewegungsapparat zu verstehen, und aus der Robotik, um menschenähnlichere Roboter zu entwickeln, die sich in unserem Umfeld bewegen, detailliert beschrieben. Die aus dieser Untersuchung erzielten Erkenntnisse werden genutzt, um ein neuartiges Design für den zweibeinigen Muskelskelettroboter BioBiped1 zu entwerfen, der in der Lage ist, langfristig dynamische und energieeffiziente Bewegungen auszuführen. Das Design zeichnet sich durch einen hochkomplexen elastischen Aktuierungsapparat aus, der auf wichtigen Eigenschaften des menschlichen Bewegungsapparates basiert. In Experimenten werden zunächst die zentralen Funktionalitäten des motorischen Bewegungsapparates des Roboters für die angestrebten Gangarten untersucht. Es kann gezeigt werden, dass der Roboter in der Lage ist vom Boden passiv abzuprallen, Energie zu speichern und freizusetzen und sich aktiv vom Boden abzustoßen. Dieser Konzeptnachweis für die motorische Bewegungsfunktion von BioBiped1 markiert jedoch nur den Startpunkt für die weiteren Untersuchungen, denn dieses neuartige Designkonzept wirft zahlreiche fundamentale Fragen bezüglich der nötigen Designkomplexität für die geplanten Bewegungen und des entsprechenden Verfahrens zur Bewegungsplanung und -ausführung auf.

Daher wird ein Simulator speziell für die Anforderungen elastisch aktuierter Roboter mit realistischen Bodenkontaktkräften entwickelt. Er basiert auf objektorientiertem Design und einem numerischem Integrationsverfahren mit einheitlichem Modell, um Aufprallkräfte analysieren und Flugphasen simulieren zu können. Die enthaltene Bibliothek umfasst unter anderem sowohl die

Modelle der aktuierten und der passiven, mono- und biartikulären elastischen Seilzüge als auch ein elastisches Kontaktmodell mit nichtlinearer Dämpfung, um die während eines Kontaktes auftretenden Kollisions-, Reibungs- und Haftungskräfte berücksichtigen zu können. Mithilfe dieser Bausteine wird das vollständige Dynamikmodell des BioBiped1-Mehrkörpersystems erstellt. Damit ein ausreichend übereinstimmendes Verhalten der simulierten und realen Roboterplattform gewährleistet ist, werden zusätzlich unterschiedliche Messungen und Parameteridentifikationen für Teilmodelle durchgeführt. Das Verhalten des Kontakt- und des vollständigen Robotermodells werden abschließend anhand von Experimenten an der Roboterplattform validiert.

Die intelligente Integration von menschenähnlichen Muskelsehnenfunktionalitäten verspricht von bedeutendem Vorteil für die optimale Koordinierung und Aktuierung der Beingelenke zu sein, stellt jedoch auch eine große Herausforderung für die Bewegungserzeugung und -regelung dar. Daher besteht ein weiterer wichtiger Beitrag der Arbeit in der Entwicklung eines zentralen nichtlinearen modellbasierten Ansatzes, der die zuvor hergeleiteten detaillierten Dynamikmodelle der implementierten Aktuatoren verwendet, um Steuerung und Regelung in einem geeigneten Maße zu kombinieren. Mithilfe dieses Konzepts gelingt es, sowohl computergenerierte eindimensionale Hüpf- als auch menschliche zweidimensionale Joggingbewegungen auszuführen. Das Verfahren wird auch eingesetzt, um das Problem der geeigneten Motorgetriebewahl im Vorfeld der Roboterkonstruktion in den Griff zu bekommen.

Die Arbeit schließt mit einer Anzahl von Simulationsstudien ab, in denen unterschiedliche Auslegungen der Beinaktuierung auf ihre Optimalität bezüglich zuvor sorgfältig ausgewählter Performanzkriterien geprüft werden. Ferner werden frühere paradoxe biomechanische Erkenntnisse zu biartikulären Muskeln beim Rennen wiederentdeckt und erstmals mithilfe detaillierter Simulation der Bewegungsdynamik untersucht. Damit kann durch die Anwendung des Lombard-Paradoxons ein neuartiges reduziertes und energieeffizientes Bewegungsmodell ohne aktiven Kniestrecker entwickelt werden.

Die in dieser Arbeit entwickelten Modelle, Methoden und gewonnenen Erkenntnisse werden bereits zur Entwicklung zukünftiger Prototypen eingesetzt. Insbesondere die optimierte Auslegung und Einstellung der Aktuatorik, einschließlich aller mono- und biartikulärer Seilzüge, basieren auf den abgeleiteten Entwurfsrichtlinien und sind anhand der Simulationsmodelle und des Bewegungserzeugungsverfahrens eingehend geprüft worden. Es wird erwartet, dass diese Entwicklungen den Fortschritt im Forschungsbereich des zweibeinigen Roboterdesigns maßgeblich beschleunigen werden und auf lange Sicht auch zum Vorteil des Menschen in der Rehabilitation eingesetzt werden können, um einerseits die verschiedenen Kontrollprozesse für unsere Laufbewegungen zu verstehen und andererseits die Weiterentwicklung von Prothesen voranzutreiben.

Stichworte: Muskelskelettroboterdesign, nachgiebige Seilzugaktuierung, mono- und biartikuläre Muskelsehneneinheiten, Mehrkörpersystemdynamiksimulation, zweibeinige Roboterfortbewegung, Bewegungsregelung, Fortbewegungsperformanz, Energieverbrauch

List of Figures

List of Tables

Symbols

Robot and Actuator Kinematics

N	[-]		degrees of freedom
q_i, $\dot{q}_i$, $\ddot{q}_i$	[rad]		angular position, velocity, and acceleration of joint i
θ_i, $\dot{\theta}_i$, $\ddot{\theta}_i$	[rad]		angular position, velocity, and acceleration of motor rotor i
$\boldsymbol{q}$	[rad]	$N \times 1$	joint position state vector
$\boldsymbol{\theta}$	[rad]	$N \times 1$	motor position state vector
θ, α	[rad]		Denavit-Hartenberg parameters
d, a	[m]		Denavit-Hartenberg parameters
${}^0\boldsymbol{r}_i$	[m]	3×1	position of coordinate frame i with respect to base frame
${}^0\boldsymbol{R}_i$	[rad]	3×3	orientation of coordinate frame i with respect to base frame
$P_{\mathrm{H}**}$	[m]	3×1	tendon fixation points for hip actuator
$P_{\mathrm{K}**}$	[m]	3×1	tendon fixation points for knee actuator
$P_{\mathrm{A}**}$	[m]	3×1	tendon fixation points for ankle actuator
$P_{*\mathrm{A}*}$	[m]	3×1	tendon fixation points for active actuator
$P_{*\mathrm{AJ}}$	[m]	3×1	tendon fixation points for active actuator on joint side
$P_{*\mathrm{AM}}$	[m]	3×1	tendon fixation points for active actuator on motor side
$P_{*\mathrm{P}*}$	[m]	3×1	tendon fixation points for passive actuator
$P_{*\mathrm{PJ}}$	[m]	3×1	tendon fixation points for passive actuator at the joint
$P_{*\mathrm{PF}}$	[m]	3×1	fixed tendon fixation points for passive actuator

Elastic Tendon Actuators

k_e	$[\mathrm{N/m}]$	constant stiffness of extension spring in a tendon actuator
I_r	$[\mathrm{kg\,m^2}]$	rotor inertia
I_g	$[\mathrm{kg\,m^2}]$	gearbox inertia
$\boldsymbol{I}_\mathrm{m}$	$[\mathrm{kg\,m^2}]$	diagonal rotor and gearbox inertia matrix
$\boldsymbol{D}_\mathrm{vg}$	$[\mathrm{Nms/rad}]$	diagonal rotor and gearbox damping matrix
R_a	$[\Omega]$	DC motor armature resistance
L_a	[H]	DC motor armature inductance
k_t	$[\mathrm{Nm/A}]$	DC motor torque constant
k_v	$[\mathrm{Vs/rad}]$	DC motor speed constant
τ_m	[Nm]	generated motor torque
u	[V]	DC motor voltage
i	[A]	DC motor current
$\boldsymbol{\tau}_\mathrm{e,J}$	[Nm]	torque transmitted to the joint through an elastic spring
$\boldsymbol{\tau}_\mathrm{e,M}$	[Nm]	torque transmitted to the motor through an elastic spring
$\boldsymbol{\tau}_\mathrm{ext}$	[Nm]	external torques
$\boldsymbol{\tau}_\mathrm{f}$	[Nm]	friction torques

Robot Dynamics

$\boldsymbol{H}(\boldsymbol{q})$	$N \times N$	inertia matrix
$\boldsymbol{C}(\boldsymbol{q}, \dot{\boldsymbol{q}})$	$N \times N$	vector of centrifugal, gyroscopic, and Coriolis effects
$\boldsymbol{g}(\boldsymbol{q})$	$N \times N$	gravity force vector

Contact Dynamics

k_c	$[\mathrm{N/m}]$	collision stiffness
p_N	[m]	collision penetration
$\dot{p}_\mathrm{N}$	$[\mathrm{m/s}]$	collision penetration velocity

Abbreviations

b-SEA	bidirectional SEA
u-SEA	unidirectional SEA
BF	Biceps Femoris (muscle)
CAD	Computer-aided design
CoM	Center of mass
CoT	Cost of transport
DC	Direct-current
DoF	Degree of freedom
EMG	Electromyography
RF	Rectus femoris (muscle)
GAS	Gastrocnemius (muscle)
GL	Gluteus Maximus (muscle)
GRF	Ground reaction forces
ILIO	Iliopsoas (muscle)
IMU	Inertial measurement unit
MBS	Multibody system
METArob	Simulator
PAM	Pneumatic artificial muscle
PD	Proportional-derivative
PL	Popliteus (muscle)
SEA	Series elastic actuator
SLIP	Spring-loaded inverted pendulum
SOL	Soleus (muscle)
TA	Tibilias anterior (muscle)
TD	Touch-down
TDc	Touch-down contralateral (leg)
TO	Take-off

TOc	Take-off contralateral (leg)
VAS	Vastus lateralis (muscle)
ZMP	Zero-moment point

1 Introduction

1.1 Background and Motivation

With the growing need for safe operation of robots in human environments, agile robots with human-like embodiment and locomotion will become indispensable. Such robots are beneficial in diverse scenarios, if abilities are provided for them to move on smooth and rough terrain, to climb stairs, to avoid or step over obstacles, and to move at various speeds. Energy-efficient bipeds with such capabilities are objects of interest in many areas, but are still not available today. Service robotics, which comprises domestic and public servicing, aims at helping humans at home, in hospitals, shops, and many more environments. Such robots would also offer important benefits, compared to wheeled robots, in space robotics, which imposes high requirements regarding mobility and autonomy, and in rescue robotics for dangerous missions, where human life would be at risk. However, developing robots with these capabilities still involves several, yet unsolved, challenging research tasks.

Since 1970, the problem of bipedal locomotion has attracted substantial interest within robotics, with a particular focus on achieving postural stability [172, 157, 59, 49, 76]. Some of the first and best-developed approaches to generating human-like walking patterns are centered around classical postural stability criteria, such as the zero-moment point (ZMP) [171] or the foot-rotation indicator [53]. WL-10RD, developed by Takanishi and Kato, is the first ZMP-based robot that successfully realized dynamic walking [157, 73]. Today, ASIMO is one of the best-known bipedal robots capable of dynamically stable walking, based on the ZMP scheme [59, 158, 161, 159, 160, 2]. A current version of the robot is shown in Fig. 1.1.

Figure 1.1.: ASIMO: the best-known example of a ZMP-based bipedal robot.

All robots based on the ZMP method and related schemes have fully actuated and feedback controlled joints in common. The legs usually have at least six mechanical degrees of freedom (DoFs) and the feet are equipped with force sensors that are used to measure the ZMP [73]. In order to keep the center of mass (CoM) on a level path and to avoid the kinematic singularity of full knee extension, the knees of both legs need to be flexed during one step. In conjunction with the completely stiff actuation by large or heavily-geared motors, this leads to high energy

consumption [85]. As a result of the stiff actuation and high-gain position control of the joints, natural dynamics and self-stability cannot be exploited to significantly reduce the energy needs for bipedal robot locomotion. Running movements of such robots are estimated to require a very large amount of steady state power, which cannot yet be supplied for several hours by current battery technology [166]. Therefore, the remarkably stable and versatile walking ability demonstrated by ZMP-controlled robots comes at the expense of poor energy efficiency, which is not the case for human locomotion.

Dynamically stable running was studied by, e. g., Raibert [139]. He developed a controller for legged hopping robots, based on three elements: controlling the forward velocity, body pitch, and hopping height. Using telescopic legs, he demonstrated dynamically stable hopping, as well as somersaults, with one-legged hopping machines. This basic approach was also successfully applied to 3-D one-legged, bipedal and quadrupedal robots. These well-recognized legged machines, however, cannot stand still, because feet are missing.

The so-called passive dynamic walker, pioneered by McGeer [96], defined a different paradigm, i. e., the concept of natural cyclic behavior on an inclined plane, and initiated the beginning of a new era, in which the special focus was on the mechanical design. A passive dynamic walker is a purely passive (i. e., not actuated) mechanical system with which reasonably stable walking can be produced by the appropriate balance between energy injection, due to the slope and loss at impacts (cf. Fig. 1.2). The principles were soon adopted for powered bipedal walkers, so that they could also walk on level planes with low energy needs [23]. Dynamic walking robots can produce economical gaits, but lack diversity in locomotion [85]. Due to underactuated and underpowered joints and curved feet, they cannot walk up stairs, stand still, or vary their walking speed. They are also characterized by very narrow stability regions and restricted robustness against perturbations of the specific periodic walking motion [132].

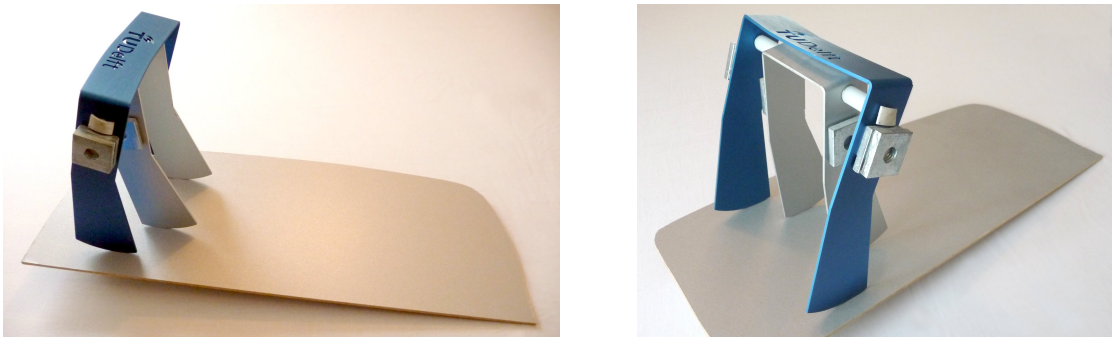

(a) **(b)**

Figure 1.2.: A passive dynamic walking toy of about 15 cm height, developed at a workshop during the Dynamic Walking 2008 conference. It can be easily built and fine-tuned by applying the original principles discovered by McGeer [96].

Today, human-like bipedal locomotion is still a major research field. The broad interest in this field is also due to its enormous potential for improvements. Despite the remarkable results demonstrated by current humanoid robots—they can walk, stand, turn, climb stairs, carry a load, or push a cart—the performance, versatility, stability, and energy efficiency displayed by humans have not yet been achieved. Neither form of legged locomotion, ZMP-based or dynamic walking robots, currently provides both versatile and energy-efficient, stable gaits [85]. Obviously, in all of these deliberations, we must never lose sight of one important fact: our superior locomotor

system is the result of a long evolution. Nevertheless, with all the enormous efforts by so many researchers around the globe, one might wonder why better robot locomotion performance has not yet been achieved, despite considerable progress in the field. First of all, one must clearly state that the ZMP-based robots and the passive dynamic walkers come from very different, quite opposite research directions, the former addressing the essential aspect of joint actuation and control and the latter the importance of mechanical design and the resulting passive dynamic abilities. These aspects, however, are strongly coupled in human and animal locomotion and should therefore not be treated separately. Raibert combined both directions in his dynamically moving robots, but did not consider implementing further important features incorporated in the human musculoskeletal system design. His approach was based on a deliberate reduction of unnecessary DoFs to realize a pragmatically designed, relatively simple mechanical system design. Also, at that time, the prevailing opinion among biomechanics and robotics researchers was that running and walking are represented by different biomechanical and biodynamical paradigms [9, 15]. To achieve further significant progress, it is essential

- to further understand the fundamental principles underlying human locomotion,
- to broaden awareness of the mutually important roles of biomechanics and robotics, and
- to achieve successful transfer of the insights gained to the design and development of robots.

Bridging the gap between artificial and natural bipedal systems requires not only improvements in sensorimotor and learning capabilities, but also an appropriate motion apparatus with adaptable elasticity, because even the best software cannot overcome the limitations of mechanical design [98]. An appropriate motion apparatus may be achieved by using human-like muscle-tendon complexes that enable compliant and variable actuation and joint coupling. If such a system is properly designed, the overall control can be simplified by benefitting from the intrinsic dynamics of the mechanical system. The combination of proper actuation modules and intelligent control methods is regarded as an important key approach towards versatile and energy-efficient walking robots. As stated by Koditschek *et al.*, "[...] neural and mechanical systems are dynamically coupled to one another, and both play essential roles in control. [...] The major challenge is to discover the secrets of how they [the brain, muscles and skeleton] function collectively as an integrated whole" ([83], p. 251).

In keeping with these overall goals and considerations, this thesis investigates several important aspects and principles, from developing musculoskeletal bipedal robots that incorporate important features of the human lower limb system to the corresponding simulation models that capture the system dynamics in sufficient detail, in order to develop motion controllers and analyze various leg actuation designs for dynamic and energy-efficient locomotion behavior.

1.2 Context

This PhD thesis has evolved in the context of the BioBiped project[1]. The project was launched in mid-2009 as a collaborative project of the TU Darmstadt's Simulation, Optimization and Robotics Group and the Locomotion Laboratory at TU Darmstadt (formerly at the University of Jena). Its long-term goal is to develop a biologically inspired musculoskeletal humanoid robot that is

[1] The link to the project website: `http://www.biobiped.de`

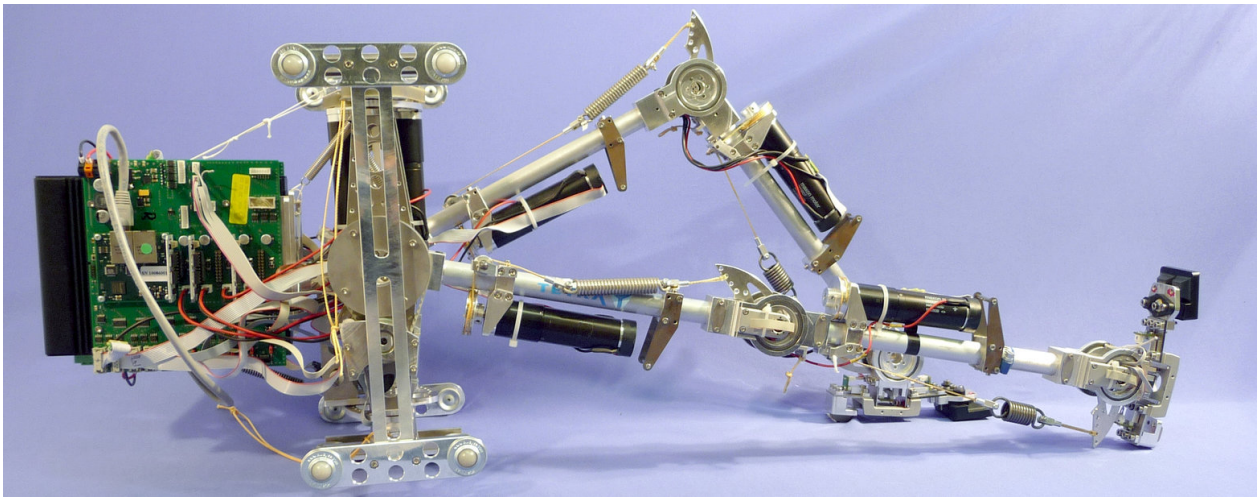

Figure 1.3.: BioBiped1 robot: the first prototype of a planned series of robots with gradually increased bipedal locomotion capabilities.

capable of three-dimensional (3-D) hopping, running, and walking (in this order), including performing transitions between these gaits, and standing, within a single kinematic leg design. The underlying strategy is to investigate and evaluate hypotheses and results from biomechanics by transferring them to the design of a series of prototypes with successively enhanced designs and capabilities. An iterative development and experimental evaluation of new concepts for bio-inspired humanoid robots will be carried out in close interaction with the development and application of both conceptual and physically detailed simulation models related to their motion dynamics [132].

This highly ambitious project goal inevitably demands a technical implementation of the key characteristics of the human musculoskeletal leg system: (1) segmentation and (2) elastic leg behavior. Whether a more human-like leg functionality can be achieved by harnessing the intrinsic dynamics of a properly designed mechanical musculoskeletal motion system is explored [131]. With regard to the actuation, the goal is not to develop new actuators, but rather to investigate the achievable locomotion performance by utilizing existing, well-established technologies in a bio-inspired setup to mimic muscle-tendon complexes and their functionality: tendon-driven series elastic actuation based on geared electric motors, extension springs, and tendons.

To achieve the long-term goal of human-like running and walking abilities, a number of platforms with gradually increased capabilities are planned. For the first prototype, the BioBiped1 robot (depicted in Fig. 1.3), the investigations are focused on an adequate fundamental locomotor function that is suited for multi-modal locomotion abilities. This includes the ability to (1) generate sufficient repulsive leg forces during stance phase to achieve clear flight phases, referred to as leg compression/extension during stance, and (2) perform fast and accurate swing motions with sufficient ground clearance and propulsion during the swing phase, referred to as forward- and backward-swinging of the leg [132]. The purpose of BioBiped1 is to prove, by experiment, that dynamic jogging can be achieved using an elastic, musculoskeletal, three-segmented leg design.

The aim of a revised version of the robot, which takes into account experimental results for improvements of the mechanics and electronics, is to demonstrate the capability of cyclic

stability during jogging. The following robot version aims at the capability of jogging, walking, and standing in the sagittal plane by studying variations in the foot design that enable heel-toe walking and fore-foot jogging motions. Additional actuation and mass in the trunk will also be analyzed for stabilization purposes by effectively making use of the upper body's movements. With the final robot version, it is planned to demonstrate the capability of all gaits without any external aids for postural stabilization. To this end, the effects of adding an additional degree of freedom (DoF) in the ankle joint, to enable foot roll motions, and adding arms in the trunk, for contralateral arm motions, will be investigated [132].

Several hypotheses guide the research towards the aforementioned goal. The most important hypothesis is:

- *The central humanoid locomotion capability should be jogging and not walking.*

For a robot that should be capable of hopping, running, and walking motions, it is necessary to ensure that the requirements for the mechanically most demanding gaits are met. We consider the hopping and running gaits as almost equally challenging, in terms of their mechanical requirements. Because walking is considered to be the more complex biomechanical model, it is expected that walking motions can be achieved by solving the algorithmic motion control problem, rather than addressing any hardware issues. This also provides the explanation for the concentration on this atypical order of gaits (hopping, running, and walking) [132].

Further, it is assumed that properly designed legs with compliant joint behavior reduce the need for active postural stability control. In contrast to the conventional approaches for generating robotic walking and running gaits, in the BioBiped project, we pursue the idea that motion and postural stability control should be encoded to a certain extent by the mechanical features of the musculoskeletal system, with emphasis on self-stability. Passive dynamic walkers and studies on various biomechanical models have shown that an appropriate mechanical system can react to perturbations in a variety of stable and robust ways. Postural stability is not considered as an outcome of the control system alone, but as the desired outcome of a well-studied system design of compliant actuation and motion dynamics. Therefore, at the current stage of the investigations, the trunks of the BioBiped platforms and of the simulation models are constrained to vertical (1-D) or in-plane motions (2-D). Postural stability will be dealt with at a later stage, following the realization of elastic leg operation [132].

In addition to these hypotheses, it is important to note that motion generation and control are closely linked to the mechanics of the robot. If properly designed, the intrinsic dynamics of the mechanical locomotor system will support the development of more efficient and less complex control strategies. The same holistic view is necessary when establishing objective criteria for human-like locomotion. Meaningful criteria that rate the degree of human resemblance of a motion can be formulated only with detailed consideration of the manner of motion generation.

In conclusion, this project is noteworthy because of its biologically and human-inspired approach to developing a system that comes close to the functionalities of the human locomotor system and that is capable of multi-modal locomotion. In particular, the unusual strategy for the leg functionality providing first the capability of hopping and running and subsequently walking motions is unique to this project. Moreover, the project endeavors to answer many challenging research questions ranging from the development of an appropriate motion apparatus to an intelligent controller by utilizing the findings of biomechanical and robotics research in a holistic way. This thesis contributes to the ambitious project goals in a number of ways, as described next.

1.3 Outline of the Thesis

In order to achieve the goal of dynamic, energy-efficient locomotion performance based, in particular, on a compliant mechanical robot design that is inspired by the human musculoskeletal system, advances in various areas are necessary.

Chapter 2: Musculoskeletal Bipedal Robots

In order to develop robots with more human-like locomotory behavior, it is essential to first decide upon the necessary fundamental features of the robot's mechanical design; this requires consideration of insights about the human musculoskeletal lower limb system as well as of the main features of the gaits to be realized with the robot, i. e., at this stage, investigations of hopping and running motions. A key question about the robot design involves the role of the various mono- and biarticular muscle groups during dynamic locomotion. This question must be answered, in order to design appropriate technical actuation and control concepts based on tendon-driven series elastic actuators (SEAs). It also must be clarified, by which musculoskeletal configurations and properties, hopping and running gaits are characterized. In this context, the use of the very widespread and popular term "human-like" in the literature is discussed and a more elaborate definition for this term and its use in this thesis is proposed. Further, we review some of the most relevant results obtained by the biomechanics and robotics community with respect to their transfer to novel musculoskeletal bipedal robot designs. These topics are treated in Chapter 2. Finally, the design considerations and details of the technical realization of the first prototype built within the BioBiped project, BioBiped1, are presented. Experiments that validate the concept of locomotor function are presented. In this regard, we also concisely outline the questions addressed by this thesis.

Chapter 3: Detailed Physical Modeling, Simulation, and Identification of the BioBiped Prototypes for Dynamic Locomotion and Impact Analysis

The objective of developing a dynamically locomoting robot must lead to a real robotic hardware platform. To successfully achieve this ambitious goal, it is highly recommended, for several reasons, to make use of a sufficiently realistic modeling and simulation methodology, in addition to the robot hardware.

It is important to distinguish between investigations that need to be completed prior to and after the robot's construction. Prior to the robot's construction, the design question, including, in particular, the dimensioning of the actuators, is of paramount importance. Omitting a thorough investigation related to the required actuation units would otherwise possibly lead to the development and selection of actuators with which the intended robot locomotion performance cannot be met. After the robot's construction, the simulation methodology and the created models of the robot kinematics and dynamics offer an ideal framework for various fundamental investigations and analyses. They allow the efficient and cost-effective testing of different design ideas and control strategies, without the dangers normally associated with direct experimentation with a novel prototype of a real physical system.

Moreover, it should be noted that using only experimental data to understand the motion dynamics of complex musculoskeletal robots like BioBiped has fundamental drawbacks, since

many important variables are not measurable in experiments. For example, systematically identifying the role of the deployed tendons during the designed motion trajectories and the impact of their dynamics on the joint, leg, and overall robot behavior is difficult, due to the complexity and redundancy of the musculoskeletal actuation.

The simulator must therefore be capable of serving as an analysis and design tool for the development of the musculoskeletal robot BioBiped1. Its design should allow investigators to easily study various actuator combinations and arrangements and to evaluate the ground reaction forces (GRF) of running robots with flight phases. Because existing simulation environments and software packages available at the time of this thesis project did not meet these important requirements, appropriate simulation and modeling libraries are developed within this thesis. Currently, this topic is more interesting than ever, because of the increasing interest in musculoskeletal robots and the many fundamental research questions related to them. However, modeling the actuation concepts integrated into BioBiped1's legs is a challenging task. Despite the use of classical electrical drives, BioBiped1's actuation dynamics is highly nonlinear, due to the nonlinearly coupled elastic tendons and the many passive elastic tendons connecting one or even two joints to a limb. Another main component that needs to be provided by the libraries is the ground contact model. Because ground contact has a massive influence on the interplay of all actuated and passive tendons and the overall robot dynamics, a detailed, sufficiently reasonable modeling of the ground, which represents a similar major challenge, is very essential. Otherwise, the development of control strategies that can be directly transferred to the real robot system cannot be adequately supported. These two parts of the dynamics model are a prerequisite for retrieving reliable results and are presented in detail in Chapter 3.

Finally, it is important to demonstrate a sufficiently similar behavior of the simulated and the real musculoskeletal robot. This behavior does not necessarily have to be measured quantitatively; qualitative measurements can lead to reliable predictions of the real robot's behavior and its dynamics properties. Therefore, concluding this chapter, the focus is placed on experimental validation of the most relevant model components, namely, the actuator models and the ground contact model. Extensive measurements and parameter identifications for these sub-models were performed on the real robot to achieve a good agreement between the real robot and the simulation model. It is shown that the simulation model captures all important properties of the real robot platform, including the occurring ground contact, sufficiently well, for meaningful studies of robot motion and control in simulations.

Chapter 4: Motion Generation and Control for Musculoskeletal Bipedal Robots

BioBiped1's complex actuation dynamics raises the question about suitable controllers that consider the specific mechanical structure and resulting motion dynamics of the robot. Musculoskeletal systems are only as beneficial as the control system allows. A motion generation and control method that does not fully account for the actuation and motion dynamics cannot take the best possible advantage of its intrinsic dynamics; instead, it is likely to interfere with it and, thus, worsen the dynamic motion performance of the system. This will not only lead to enforced motions, but also to higher energy consumption.

Therefore, the task is to develop a model-based approach for motion generation and control that utilizes the complex, musculoskeletal tendon actuators of BioBiped1 such that the amount of energy supplied by the motors can be reduced. As mentioned previously, the postural stability

issue is not dealt with in this thesis. The upper body motions of the robot and simulation model are therefore restricted to 1-D or 2-D.

In Chapter 4, we will review common approaches to realize dynamic bipedal locomotion and discuss the applicability of sinusoidal trajectories to utilize the intrinsic dynamics of musculoskeletal robots. Subsequently, we will concentrate mainly on a centralized, nonlinear model-based method combining feedforward and feedback control that is specifically developed for compliantly actuated systems like BioBiped1. The advantage of the method is that it creates a common basis for comparisons among musculoskeletally varied leg actuation designs characterized by different types and numbers of actuators integrated, as well as actuation parameters. Because we consider joint angle data to be eligible reference data, comparisons with different compliant actuation or even stiff actuation also become practicable. This approach makes it possible to determine each tendon's contribution to the overall joint dynamics and, in this way, to tune the requirements demanded of the motors. Extensive simulation results for computer-generated hopping and human running motions, together with a detailed discussion of fine-tuning and further extension possibilities offered by the method, are presented.

It is also shown that the method can be applied to successfully tackle the problem of appropriate motor-gear unit selection prior to the robot's construction. For this purpose, a representative set of hopping and running motions with high step frequencies is chosen beforehand and then subsequently analyzed with respect to the actuation requirements.

Chapter 5: Investigating Leg Actuation Design versus Locomotion Performance for Dynamic and Energy-Efficient Locomotion

Only after validation of the essential components of the musculoskeletal robot motion dynamics model, the realistic physical actuator, and ground contact models, is it possible to carry out a number of crucial simulation studies and to really understand the fundamental advantages that BioBiped1's mechanical system has to offer. The focus of the investigations is a better understanding of the functions and roles of the actuated and passive tendons during the proposed hopping and running motions.

The studies are divided into three parts. In the first part, we consider the impact-reducing effects of mechanical elasticities on the motor-gearboxes. Various leg actuation designs from stiff actuation to highly compliant actuation involving BioBiped1's complex musculoskeletal system are compared in a specific simulation setup. The simulation models with PD-controlled leg joint trajectories are set to a specific configuration and dropped from different heights. The maximum torques arriving at the gearboxes, together with further selected dynamic performance criteria, such as the passive rebound height and the flight phase initiated by the first bounce, are analyzed and compared between the different leg actuation designs. With this study, we confirm not only the well-perceived advantage of mechanical compliance, in terms of impact absorption, but also clarify the advantage of tendon elasticity over joint elasticity. The study concludes with a summary of insights that we gained from the different test cases.

The subsequent studies seek to determine the role and contributions of the mono- and biarticular tendons during in-place hopping motions, through step-by-step synthesis of the available muscle-tendon units. Starting with the minimal set of all active muscle-tendon units, the musculoskeletal system is iteratively enhanced by adding a passive mono- or biarticular tendon, to include, finally, seven tendon units. We ask the question: "What would happen if?" to investigate the functionalities of the individual muscle-tendon units in a forward manner (forward

causality). For this purpose, the motors are excited by open-loop sinusoidal trajectories such that alternating flexion and extension of the joints are initiated to achieve two-legged hopping motions. The motor trajectories and control are not altered; thus, the causes of any observed effects and changes can be clearly identified. In detailed multibody system (MBS) dynamics simulations that incorporate the previously derived mathematical models of all actuator types, the effects of the different variations or layouts of the actuation system are examined. The investigated performance criteria applied to rate different designs of the musculoskeletal locomotor system include the duty factor, ground clearance, patterns of the GRF, and the energy consumption. In order to derive further design guidelines for future prototypes, the interplay and interdependencies of motion performance and mechanical design are analyzed for a slightly modified actuation system. We demonstrate that, by changing the attachment location of a tendon on the joint side, the sign of the resultant joint torques can be varied, which may lead to different demands on the parameter layout of all tendons contributing to the joint actuation and reduced or increased energy requirements for the motor-gearbox. Knowledge about these regulating "screws" of the mechanical design provides the system designer with powerful tools to tune the dynamic properties of the mechanical locomotor system as desired.

The third category of simulation studies has the goal of determining energy-reducing leg actuation designs for given joint trajectories for hopping motions while preserving a minimum amount of dynamic locomotion performance. Whereas energy consumption also plays a role in the studies mentioned above, here, it is also additionally ensured that a common reference basis is created, despite varying musculoskeletal leg actuation. Using the model-based motion control, presented in Chapter 4, it is ensured that, even with different musculoskeletal leg actuation, the same 1-D hopping motion with identical joint angle trajectories is achieved. This approach provides further important insights into the proper leg actuation design and parameter settings required to obtain the desired dynamic and energy-efficient hopping motions.

Chapter 6: Conclusion and Outlook

In Chapter 6, the thesis concludes with a summary and discussion of all contributions and aspects addressed by this PhD research project. It also provides a list of relevant future investigations that could be based on the foundations laid by this thesis.

2 Musculoskeletal Bipedal Robots

2.1 Introduction

Towards the goal of human-like locomoting bipedal robots, efforts from both the biomechanics and robotics community are required to better understand the principles underlying human locomotion and to mathematically formulate these insights such that the gained knowledge can be used, processed and applied to the design and development of robots interacting successfully in human environments. In this chapter we will review various important insights from both communities. In this context we will first elaborate on the important characteristics of the human lower limb system and of human hopping, running and walking gaits. Finally we will present the novel musculoskeletal design of the first BioBiped1 prototype along with the goals and ideas behind. The chapter concludes with the experimental proof of concept of BioBiped1's locomotor function and the questions dealt within this thesis.

2.2 Human Lower Limb System

A healthy human lower limb system has several important properties that allow a variety of different motions. First of all the leg consists of three segments (and not only two or one). Second it behaves compliantly thanks to the vast number of muscle-tendon systems acting within the limb system. Then of course, there are also other elements, e. g. the foot segment with specific properties like the toes, that play a crucial role in enabling the different motions. Here, we focus on the leg segmentation and compliant leg behavior.

2.2.1 Segmentation

The human leg is divided into three segments: thigh, shank and foot. This arrangement has several advantages. As stated in [16], it enables gearing, i. e., different transmission of muscle velocity into velocities at the leg tip, which may be used while changing gaits. The three-segmented leg is beneficial with respect to behavior variability and structural stability.

2.2.2 Elastic Leg Behavior

The human lower limb system is supported by a very large number of muscle-tendon groups featuring specific properties that have not been yet mimicked successfully by any robot actuator technology, as we will also see in Section 2.6. In this section we will elaborate on the function of muscles, rather than their biological properties. In a nutshell, the biological low-inertia muscle is capable of generating high power and force, of varying its tension depending on the muscle fiber velocity and length, and of varying its stiffness. The tendon, connecting the muscle to the bone and capable of efficient mechanical energy storage due to its elasticity, helps to transmit the forces to the rigid bone by pulling on them and causing movement.

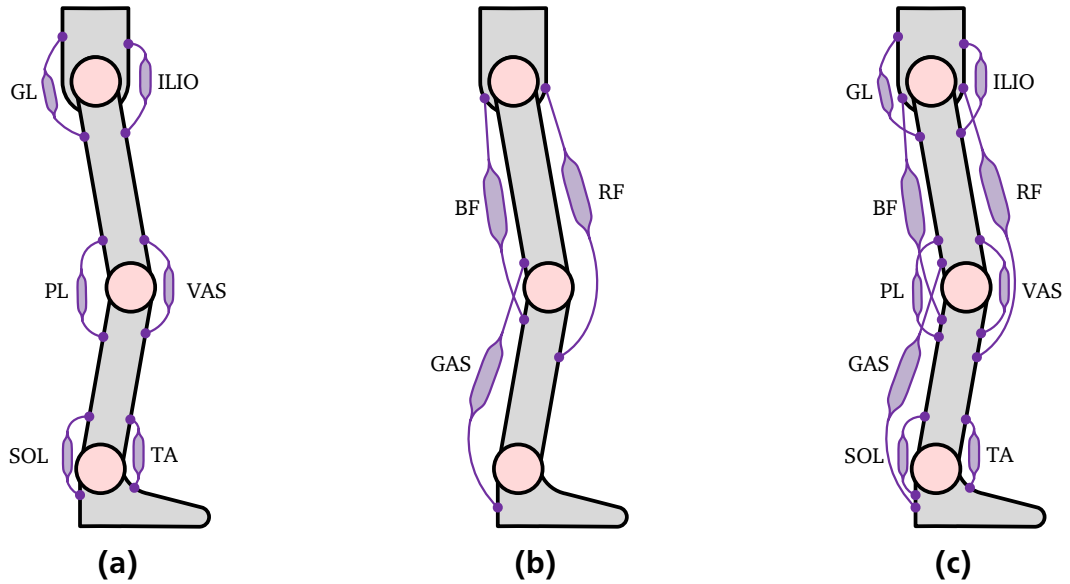

Figure 2.1.: Human musculoskeletal leg system: (a) antagonist-agonist configuration of flexors and extensors in each human planar leg joint; (b) two-joint muscles; (c) overview of nine important muscles during human legged locomotion.

For the purpose of a versatilely moving bipedal robot [133], we select the nine most relevant muscle groups known to share the necessary work in sagittal plane during legged locomotion (cf. Fig. 2.1c). These essential human actuation complexes are divided into monoarticular and biarticular ones, spanning either one joint or two joints. All these muscles perform different tasks; redundant functionalities can be identified, but take place due to individual activation patterns not necessarily simultaneously.

Let us start with the monoarticular muscles, depicted in Fig. 2.1a. Each planar joint of the human leg has a pair of monoarticular antagonist-agonist muscles for driving the connected limb. The hip pair consists of the muscles *Iliopsoas* (ILIO), flexing the hip, and *Gluteus Maximus* (GL), extending it. In the knee, *Popliteus* (PL) takes on the role of flexion and *Vastus lateralis* (VAS) the role of extension. Finally, *Tibilias anterior* (TA) is responsible for flexing, also known as dorsiflexion, and *Soleus* (SOL) for extending the ankle joint, also known as plantarflexion.

In addition, the human leg has a number of biarticular muscles, of which the three most important ones are shown in Fig. 2.1b. The muscles *Rectus Femoris* (RF) and *Biceps Femoris* (BF) cross both the hip and knee joint. While RF acts as combined knee extensor and hip flexor, BF behaves exactly the other way. Note, that BF is one of three muscles acting within the hamstrings muscle group. *Gastrocnemius* (GAS), which is attached to the knee and ankle joint, extends the ankle and flexes the knee joint.

These nine muscles contribute to the dynamic locomotion behavior of humans by sharing the necessary work in a highly “intelligent” and very well organized way causing a chain of energy transfer depending on the specific gait. The monoarticular muscles are known to strongly contribute to the task of power generation, e. g., during jogging [55]. The biarticular muscles are reported to mainly transfer energy from proximal to distal joints. They coordinate the synchronization of the coupled joints and, thus, also the distribution of joint stiffness and energy within the segmented leg [72]. By suitable activation and coordination of these muscles explosive leg extension movements are enabled that are otherwise impossible due to the limitation of the

power delivered by monoarticular muscles alone [170]. When neither muscle is active, the joint can swing freely [82].

This is a quite general and also common description of the above named muscles' actions often found in literature and popular biomechanics books such as [31]; it does not reveal the actually very complex, gait-dependent functionalities of the one- and two-joint muscles within the segmented leg. We therefore picked out some of the most interesting - by no means exhaustive - observations made by biomechanics researchers in various studies involving human subjects.

- Analyzing two-legged jumps of experienced jumpers [167], it was found that the muscle GAS plays an important role during plantarflexion, one of the most important processes during dynamic gaits. It reinforces the process by supporting the extension of the ankle joint and, thus, the lift-off from ground. In [167] it is explained that the activation of GAS is initiated with a delay of about 30-50 ms and resembles a catapult action of the Achilles tendon. Thus, GAS is particularly helpful at the end of the push-off phase. It opposes knee extension, consequently avoiding an over-extension of the knee, and reinforces plantarflexion. Thanks to the activation, the contraction of the knee extensors can continue without any energy losses and further power can be delivered. This chain of actions leads finally to a transformation of rotations in joints to translation of the body [167]. In summary of this study, it can be said that RF, VAS, GL, and GAS contribute to the high mean power output of 2000-3000 W per ankle found in plantarflexion during jumping. GL and VAS deliver power until the end of push-off, then the opposing effects of RF and GAS result in net flexing torques which decelerate the angular velocities of the hip and knee extension [167].

- In a later study it was argued that "biarticular leg muscles significantly contribute to the work done at joints due to transfer of power during explosive leg extensions" [72]. Accordingly, power is transferred mainly from hip to knee joint during jumping and sprinting. A minor power transfer can also be detected in the opposite direction, namely from knee to hip joint by the hamstrings; but the power transfer from hip to knee joint by RF is much higher. The contribution of these muscles to the total joint power amount to around the same percentage during jumping and sprinting. These observations could be also made regarding the GAS muscle. The results confirm previous hypotheses that biarticular muscles in general contribute to a proximodistal energy transport, i. e., from proximal to distal joints and in this way help to convert body segment rotations into desired translations of the body center of gravity.

- In [176] it was stated that 80 % of the mechanical power during the gait cycle is generated by the plantarflexors, illustrating their importance.

- During hopping and running, knee extension and plantarflexion occur almost simultaneously [177].

- A highly interesting insight was gained by the reading of [175], as it opposes the prevailing assumption regarding the role of the hamstrings as knee extensor. Accordingly, this was labeled by Lombard in 1903 the "paradoxical" function of biarticular muscles. Later, the details of this functionality were explained further by [44, 107, 12] and complemented by [175] as follows: Provided that the free end of the leg is guided, the hamstrings not only extend the hip, but also the knee joint. During the support phase of the sprint the

synchronous extension of hip and knee joint takes place for knee angles above -35 ° (see Fig. 2.2). Paradoxical muscle actions were also observed to be true for the GAS muscle during the last part of the ground phase during sprinting; there, GAS acted as synergist extending the knee joint at knee angles above -40 ° [154].

- In the context of biarticular muscle functionalities, the length of the moment arms also play an important role. According to [31], GAS has a 5 cm moment arm at the ankle and 3.5 cm moment arm at the knee depending on the knee angle. This means, during plantarflexion it contributes to the knee moment 50 % less than to the ankle moment. The hamstrings have moment arms of 6-7 cm at the hip and 3.5 cm at the knee. During stance phase, "their contribution to hip extension is about twice their contribution to knee flexion" [31]. Only RF has approximately equally long moment arms, namely 5 cm at the hip and 4 cm at the knee joint.

This list of various observations made by biomechanics researchers shows that there are many different insights into the dynamics of the human lower limb system depending on the perspective and the conducted experiments. It also shows that muscles in general take on manifold roles that still may not have been completely identified. This poses the challenge to robotics researchers which reported properties of the muscles to imitate and to further analyze in robot systems and whether the results obtained by a robot system need to be consistent with biomechanical findings.

2.3 Key Characteristics of Human Motion Trajectories

It can be agreed upon that human motions vary in complexity and degree of dynamics. For the remainder of this thesis, it is important to review some of the most important features of the dynamic motions under investigation, which comprise mainly hopping and running motions. For completeness and better comparability of the different gaits, some of the main characteristics of walking motions will be reviewed as well.

A common level of detail of description of human movement is accomplished by the use of the kinematic terms position, velocity and acceleration. This purely kinematic description of motion ignores the causes of motion [142]. However, the kinetic causes of motion, either due to body mass, interactions with the surroundings or mechanical interactions within the musculoskeletal system, must not be neglected. For brevity, we focus here, in particular, on the characteristics of the joint angle curves within a step for the hip, knee and ankle joints about the pitch axis, and on the specific patterns of the resultant GRF, i. e., the reaction forces provided by the support surface on which the movement is performed [142].

When we walk or run, there is always a period of support and nonsupport for each leg, known as stance and swing phase, respectively. The stance phase begins when the foot contacts the ground, referred to as footstrike, and ends when the foot leaves the ground, referred to as toe-off. Subsequently, the swing phase follows from toe-off to footstrike [142]. A stride or gait cycle contains four occurrences of footstrike and toe-off, two events for each limb. Starting with a limb and referring to the other limb as the contralateral, we can name the following events: right footstrike (TD), right toe-off (TO), left footstrike (TDc), left toe-off (TOc). Each stride contains two steps where a step can be defined as the part of the cycle from the toe-off (or footstrike) of one foot to the toe-off (or footstrike) of the other foot. The duty factor stands for the fraction of time a foot spends on the ground relative to the stride period [83].

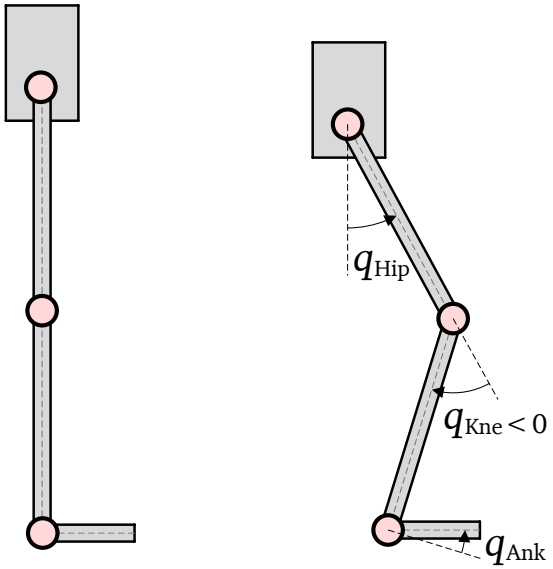

Figure 2.2.: The picture illustrates the sign conventions for the measured sagittal joint angles of a human subject and the simulated/real robot platform. In the leg configuration shown on the right side, the knee angle is negative whereas both hip and ankle angle are positive. The zero configuration of the leg is illustrated on the left side.

For the following human movement analyses, we employ human motion data obtained from human gait experiments at the Locomotion Laboratory of previously Jena University, now TU Darmstadt [89]. Using an instrumented treadmill with force sensors and a camera system, consisting of eight high speed infrared cameras, kinematic data of 21 healthy subjects walking and running at speeds ranging from 0.5 to 2.5 m/s were collected. The reference motions consist of mean joint angles in the sagittal plane recorded at discrete time points during a gait cycle.

The joint angles are measured as relative joint angles between two adjacent segments. In the zero configuration the leg is straight with the foot completely touching the ground, which corresponds to a 90° angle. The positive measurement directions are indicated in Fig. 2.2. While the ankle and hip angle increase with joint flexion, the knee angle increases with joint extension. A completely bent knee has the inner joint angle of −90°. These sign conventions are used also in all studies of the following chapters.

2.3.1 Running and Hopping

Fig. 2.3 shows the running gait patterns of 21 healthy human subjects, marked in light grey color. The running speeds vary from 1.8 to 2.4 m/s [89]. The diagrams depict the trajectories of the GRF and sagittal joint angles. The green colored trajectories represent the gait data of a selected subject characterized by cycle time 0.8022 s, step frequency 2.4944 Hz and step length 0.9626 m. The corresponding normalized GRF of both legs and the events TO, TD, TOc, TDc are illustrated as well indicating the stance and swing phases. Scaling the normalized GRF by a body weight of 75 kg, maximum forces of around 2000 N can occur. Note the large deviations of the joint angle trajectories among all subjects and from the mean values. The deviations indicate the variability of human motion in general. Nevertheless, we will pick out some general observations using the experimental human gait data from [89].

As indicated by the GRF in Fig. 2.3, the selected running pattern includes only single support phases, i. e., each foot has individual ground contact phases. The shaded areas represent the gait phases in which both legs leave the ground. A single cycle contains alternating sequences of support and nonsupport. The cycle starts directly with the stance phase of one leg followed by a much longer swing phase. The computed duty factor of a leg for this running gait amounts to 33 % which corresponds well to the generally known stance phase durations of 30 % for the running gait [142]. For sprinting, the duty factor is known to further decrease to 20 %.

The GRF are very close to the typical vertical single-humped patterns known from the running and hopping gait. Note however the smaller bumps at the beginning of the patterns which differ for each of the 21 gaits.

The friction forces in locomotion direction indicate very well the breaking torques occurring particularly in the knee and ankle joints during the first half of the stance phase. In the second half of the stance phase the horizontal forces are positive indicating the required acceleration for take-off. The same observations can be made for the contralateral leg. The change of sign in the friction forces coincides with the highest vertical compression force at mid-stance at which the CoM attains its lowest position. Conversely, the CoM is at its peak at mid-swing.

Let us also consider the joint functions during stance and swing phase. The joint angle trajectories are characterized by several peaks within a gait cycle. During stance, all leg joints perform a slight flexion initiating leg compression. Shortly before take-off, the joints prepare for leg extension. The heel-off at the end of stance phase initiates leg swing with ground clearance [71]. Fast leg rotation during swing is provided by hip flexion, knee flexion and late ankle extension [151].

Further popular gait analyses are based on the leg force-length curves. Their computation requires underlying kinematics and dynamics models which usually contain certain model assumptions, for example regarding the segment kinematics which is subject to errors due to skin movement. Determining the joint torque or joint power include further modeling and measurement errors, caused by neglected wobbling mass dynamics in the model, mismatch of segment masses, CoM positions and moments of inertia, or mismatch of joint constraints [89]. Additional errors can be traced back to slightly different sampling frequencies returned by the sampling clocks of the different measurement devices [89].

Despite these inevitably error-prone calculations, analyses of the joint torque-angle courses or the leg force-length curves are often applied by biomechanists to obtain a more detailed notion of the inherent so-called global leg dynamics. A constant slope or almost constant slope in the leg force-length relation, which is also referred to as the leg's work loop, is regarded as linear stiffness. In running almost linear leg force-length relations can be detected at all speeds, i. e., energy losses and supplies indicated by enclosed negative or positive areas are almost in balance. Further, the linear leg stiffness increases with the running speed [89]. However, a linear leg force-length relation does not entail a linear joint stiffness [143]. Fig. 2.4 gives an idea of the hip, knee and ankle joint stiffness during running. In the diagrams, the normalized torques of the subject, highlighted in Fig. 2.3, occurring during the complete gait cycle are plotted against the joint angles. It can be recognized that the joint stiffness can only hardly be approximated by linear stiffness for selected phases. Linear stiffness values can be partially assigned to the first and second half of stance or swing phase. Additionally, due to the inevitable errors and simplified model assumptions mentioned above these curves and any resultant conclusions drawn from such analyses should be treated with caution.

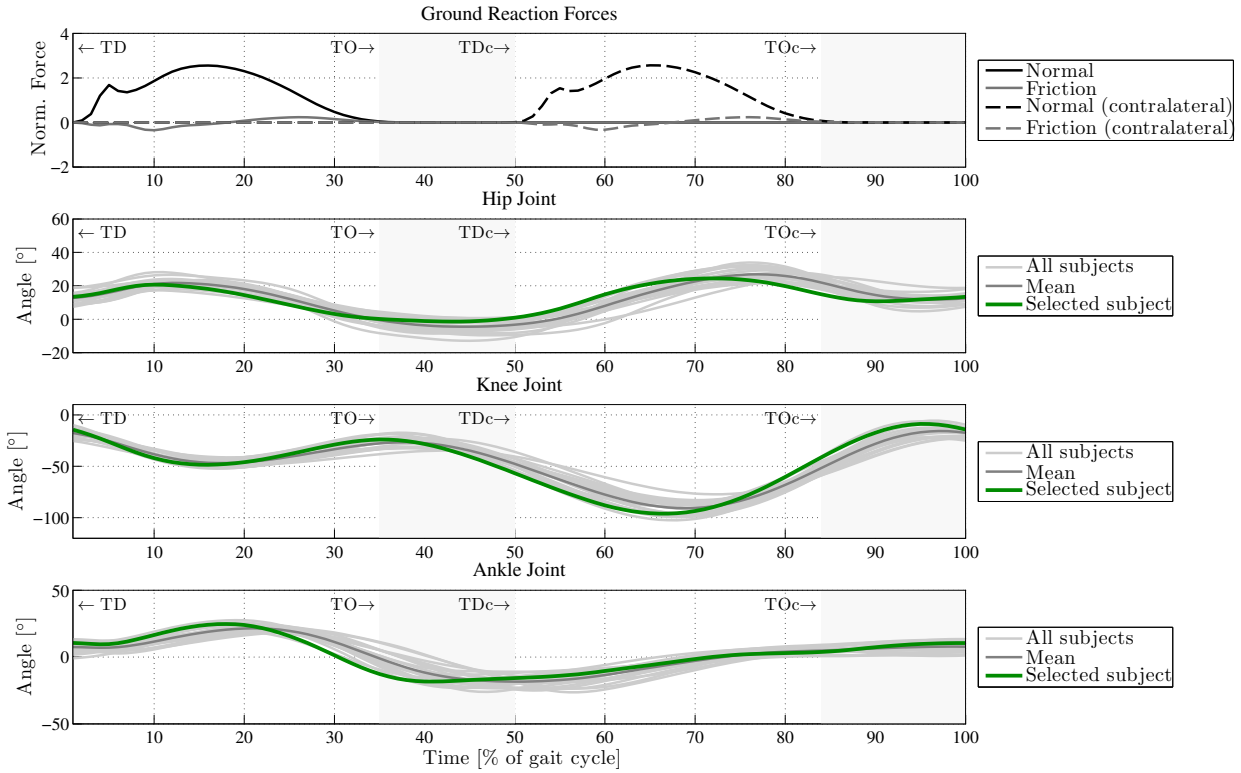

Figure 2.3.: Overview of the sagittal joint angles of the hip, knee, and ankle joint during a running gait cycle of 21 human subjects (human gait data obtained from [89]): In the topmost diagram the normalized GRF of a selected subject, whose joint angles are marked in green in the following diagrams, are depicted. The shaded areas represent flight phases in which both legs are in the air.

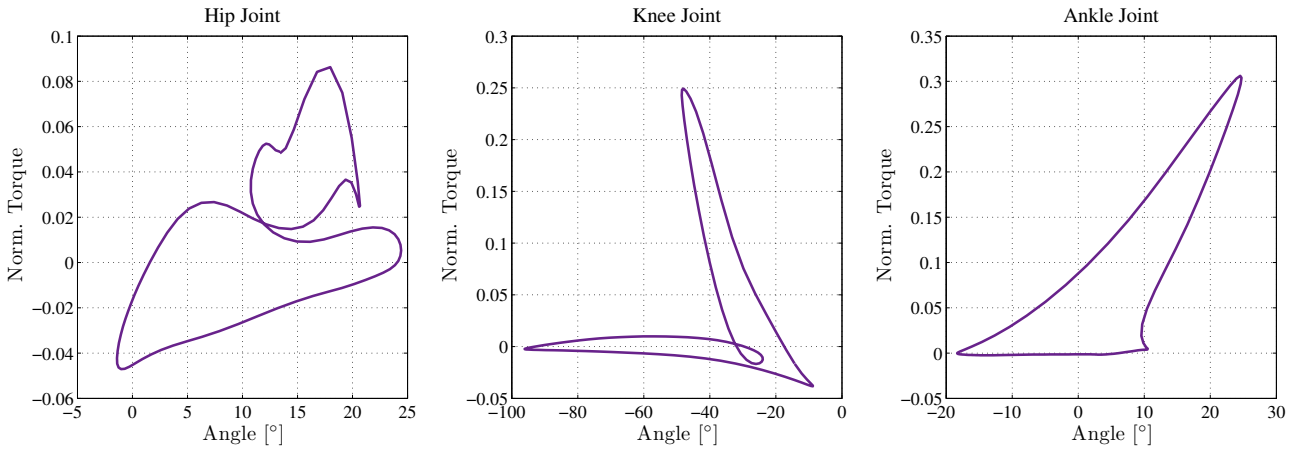

Figure 2.4.: Torque-angle courses during a complete human running gait cycle for the hip, knee, and ankle joint of the selected subject highlighted in Fig. 2.3 (human gait data obtained from [89]).

As for hopping, both legs move symmetrically, i. e., the GRF of both feet overlap. Therefore only one ground contact interaction per leg occurs within one cycle, the following ground contact

falls into the next cycle. The joint motions are similar to running: flexion and extension in all joints occur almost synchronously according to the current phase.

2.3.2 Walking

During walking there is always at least one foot on the ground and for a brief period of each cycle both feet are on the ground, known as double support [142]. Thus, walking can be described as an alternating sequence of single and double support phases. Stance phases during walking are reported to last almost 60 % of the stride. For race-walking, the stance phase decreases to 50 % [142].

Fig. 2.5 illustrates the joint angle trajectories of 21 human subjects walking at speeds ranging from 0.9 to 1.2 m/s. The topmost diagram depicts the normalized GRF of the selected subject marked in green in the below joint angle diagrams. The selected gait is characterized by cycle time 1.0903 s, step frequency 1.8372 Hz and step length 0.5724 m.

Clearly different from the running gait are the 'M-shaped' vertical GRF during walking. This typical camel-back pattern of the vertical GRF and the double support, which are represented by the shaded areas, both characterize walking [48]. The duty factor for the selected gait amounts to 63.87 %. The impact forces after touch-down are rather small compared to running.

To complete the analyses of the walking motion characteristics, the torque-angle courses of the selected gait are illustrated in Fig. 2.6. In contrast to running, here linear spring properties are even less often existent.

2.3.3 General Remarks

These characteristics analyses should not hide the fact that the identifiable patterns and properties of the above investigated motions are only limited indicators for a specific gait. Researchers have found out that the running and walking gait are not clearly distinguishable by the popular criteria, locomotion speed or aerial phases. Humans can walk and run at the same speed and aerial phases have been detected during professional race-walking at fast speeds of 3.6 m/s [18]. On the other hand, double support phases have been found during slow running, i. e., with duty factor $d > 0.5$ [100]. The occurrence of aerial phases is thus not unique for running and their absence does not refer necessarily to a walking gait [89].

A helpful criterion for distinguishing running from walking is the phase relation between kinetic and potential energy. Walking is considered as an out-of-phase gait as potential and kinetic energies change largely out of phase. Thus, the total energy changes only a little throughout a walking step [99, 19]. Conversely, running is regarded as an in-phase gait. Here, changes in the kinetic energy of the CoM due to forward speed and the potential energy of the CoM due to vertical velocity are substantially in phase [99], leading to large changes of the total energy in a cycle.

A deeper and more profound understanding of the differences, similarities and main properties of human gaits may be acquired through extensive analyses of experimental databases. Such databases, however, are still not fully available [89]. Additionally it should be noted that fundamental progress in this research area also requires understanding the neural system and mechanisms behind these motions.

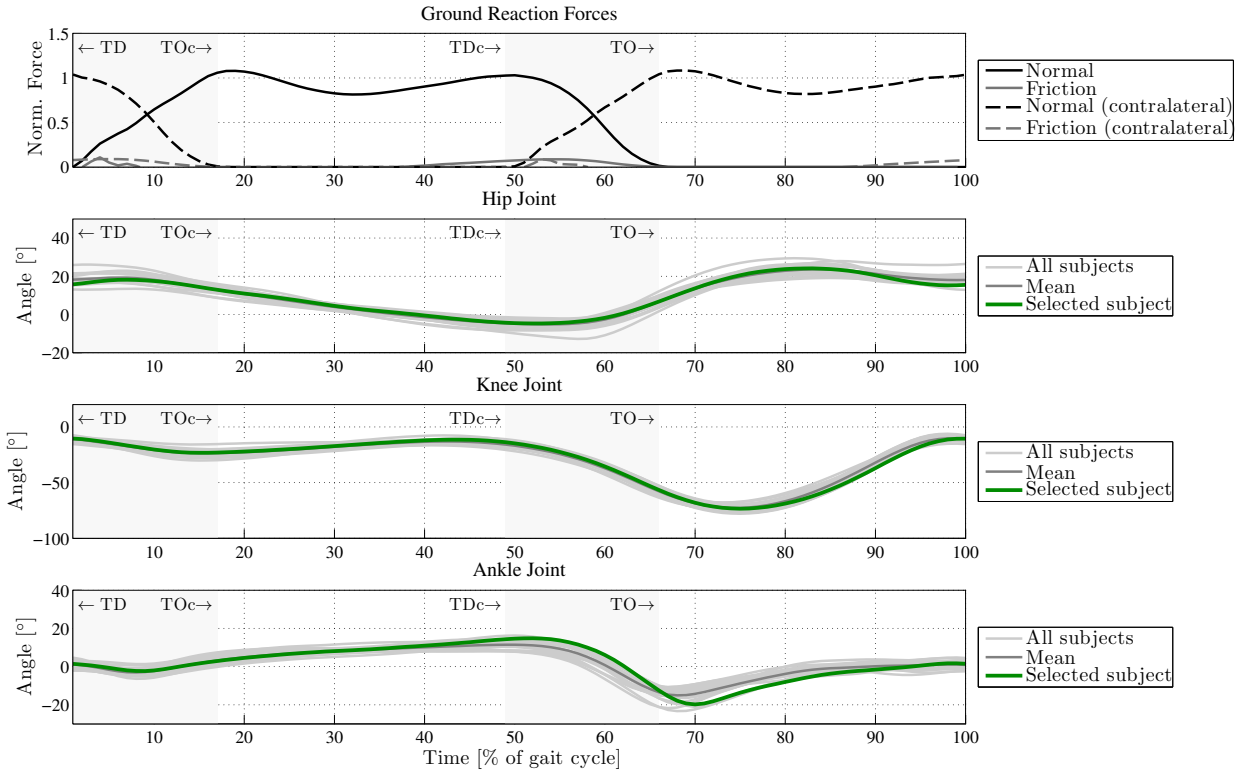

Figure 2.5.: Overview of the sagittal joint angles of the hip, knee, and ankle joint during a walking gait cycle of 21 human subjects (human gait data obtained from [89]): In the topmost diagram the normalized GRF of a selected subject, whose joint angles are marked in green in the following diagrams, are depicted. The shaded areas represent double support phases in which both legs are in contact with the ground.

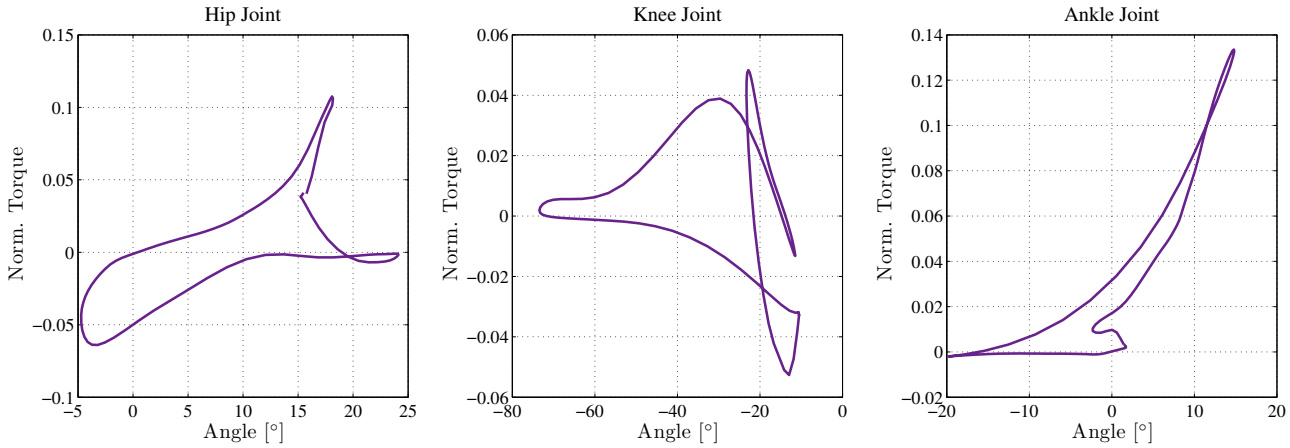

Figure 2.6.: Torque-angle courses during a complete human walking gait cycle for the hip, knee, and ankle joint of the selected subject highlighted in Fig. 2.5 (human gait data obtained from [89]).

2.4 What is "Human-like" Bipedal Locomotion?

In the literature widespread use of the term "human-like" with respect to locomotion or gait can be found. It is often used to assess a presented, specific locomotion performance implying that human motion is perceived as optimal or, at least, worthy of imitation without providing any evidence for such a statement, as for instance in [108]. Human movements in general, however, are not by default optimal, as diverse counter-examples in biology prove [124].

Let us try to shed more light on the exemplary uses of this term [137], noting before that unfortunately the overwhelming majority of authors take a general but not rigorously specified understanding of "human-like locomotion" for granted and do not attempt to explain the use of this term in their work (e.g. [163, 147]). However, the different works may have very individual interpretations and definitions of this term. Others implicitly provide hints for their individual conception of the term. McGeer presents some snapshots of the robot motion sequence in [97] and formulates: "The gait of figure 2 is obviously anthropomorphic" (p. 1644). Additionally, he compares his and the robot model's step frequency to support his assessment. Visual comparison of snapshots is a popular tool also in Schultz and Mombaur [148]. The obtained numerical results are compared with snapshots of a professional athlete's running gait. "The periodic running motion looks very natural, (compare the corresponding animation at our website)" ([148], p. 789). Further it is argued based on the visual comparison, that "[...], the qualitative match is very good" ([148], p. 790). Joint angle histories are not compared; instead biomechanical gait characteristics such as duty factor, step length, contact/friction forces and the vertical center of gravity motion patterns are computed and compared to those known from a human. In [71], Iida *et al.* compare the sagittal joint angle histories obtained from the simulation and real robot model to human joint kinematics. Partial similarities in only two of the three sagittal leg joints, good agreement with the vertical CoM patterns and low similarities of the GRF are considered as sufficient to term the obtained bipedal locomotion "human-like". Besides, it is pointed out that self-stabilization of a gait is seen as a further important property of human locomotion. According to Ogura *et al.* walking with a constant waist height and bent knees is not very "human-like": "The ability to walk with stretched knees is an important quality that a humanoid robot should possess in order for it to mimic human motion" ([119], p. 3976). The heel-contact and toe-off are considered as other important characteristics of human walking. "Thus, if the robot realizes not only walking with stretched knees but also heel-contact and toe-off motions, it can be said that its walking style, in comparison to those of other humanoid robots, is more similar to that of humans" ([119], p. 3976). As proof of concept it is shown that the GRF of the robot agree very well in pattern and peaks with those collected from a human subject. Collins and Ruina [24] consider energy consumption, computed by the well known cost of transport (CoT) (cf. Section 4.5), as a measure to rate the degree of "human-likeness". A robot walking at low CoT, like the Cornell biped, is regarded as quite "human-like". For others, as in [114], a characteristic of "natural human-like motion" in general is the exploitation of the passive body dynamics.

This widely varying use of the term "human-like" suggests that a general understanding and common definition for the term "human-like locomotion" is missing. This results in different views regarding locomotion performance evaluation, without a generally accepted understanding of the neuromechanics and core functionality underlying human locomotion. The problem of the lack of a taxonomy leads also to the issue of the lack of benchmarks. For the purpose of

benchmarks and valid comparability of results among the different research groups, it should be therefore aimed at developing a comprehensive common definition for the term "human-like locomotion" that will provide valuable guidelines, significantly enhance the progress in the field of humanoid robot locomotion and also enable applications to human health. Solving this problem requires combined efforts of biomechanists and roboticists and probably at least one single PhD thesis dedicated only to this topic. Therefore, in order to increase the understanding of the studies performed within the scope of this thesis and of the related use of this term, we will briefly discuss closely interrelated questions, namely:

- Which are the main features of human motion performance that are desirable to be realized by robots [134]?
- Further, how are these features embodied and related to each other [134]?

Human motion capture data offers a wealth of data ranging from GRF to Electromyography (EMG) and kinematic data. But the essential question is which of all these reference data actually capture the necessary information about the human motion dynamics. So far, all these data seem to contain redundant information. For instance, the GRF not only provide information about the patterns and forces. Using the GRF we can compute also the duty factor of the motion and in this way get an idea of the gait type. Additionally, the GRF let us derive the course of the CoM and consequently reveal the altitude difference of the CoM. EMG data, on the other hand, capture the electrical activity of skeletal muscles. There is controversy in the biomechanics community whether it is also possible to estimate from EMG data the forces produced by the muscles. Recently, Sartori *et al.* reported on the feasibility of such estimation [145]. They demonstrated that by considering all the DoFs of the joints spanned by a muscle it is possible to estimate the muscle forces. Previous research, that had stated the opposite, used models about a single DoF. Despite this interesting research result, so far EMG data are not considered as reliable source of information to be used for realizing similar motions on robots. Another very popular opportunity, often applied in robotics and graphics research, is the use of kinematic data.

The question remains which of these above sources may play a role to support the development of a motion controller that produces the qualitatively best possible motions on a robot. For example, the relation of CoM or ground contact dynamics to joint angle trajectories is not unique, i. e., the same joint angle configurations can lead to different CoM locations or GRF. But there must be some dependency that is worth being analyzed. Further, it is not clear how joint angle courses affect the energy consumption.

While for the moment it does not appear to be possible to formulate a generally accepted answer to the above posed questions, it seems that we still have a clear idea of what we would consider as comparable to human motion. This can be strongly observed during new demonstrations of ASIMO's locomotion capabilities [2], which generate a vivid debate about their "human-likeness". Apparently, both kinematic constraints and high dynamic mobility, expressed by clear ground clearances and long flight phases, are important features for our judgment on the degree of resemblance to human jogging motion. Low energy consumption is a further criterion for considering motions performed by robots as comparable to human capabilities. Due to the open issues already discussed and the missing knowledge of the truly underlying mechanisms of human locomotion it can be agreed upon that we are far away from claiming a motion being human-like. Instead, the goal should be to demonstrate improved locomotion performance and to present novel insights by studies in different related areas. In this thesis the

term “human-like” with respect to locomotion performance is avoided as much as possible and, if used, shall indicate any prevalent similarities to the human sagittal leg joint angle courses and ground contact dynamics provided a low energy-consumption. The simulated and real robot dynamics will be studied in detail with respect to the aforementioned important characteristics known from human gait analyses (cf. Chapter 4 and 5).

2.5 Templates and Further Important Findings from Biomechanics

The broad interest in understanding the principles underlying human locomotion explains the wealth of research found in biomechanics to establish representative models of human locomotion behavior that are accepted as common basis for further research. In this context, many simple and more complex models, labeled as templates and anchors [45], up to highly complex models can be distinguished. A template, also referred to as conceptual model, is defined as the simplest model with the least number of variables and parameters that exhibits a targeted behavior. It can be used to investigate various hypotheses that are subsequently cross-validated by means of experimental data. But it cannot deliver any information on the contribution of the neuromusculoskeletal system as it does not incorporate any detailed mechanism. Such questions can only be answered by more elaborate realistic models, such as anchors or even more complex models incorporating the human musculoskeletal system. An anchor must have embedded within it the behavior of its templates [45].

Templates have been employed to understand the global leg function and properties of human locomotion [10, 11, 15, 19, 37, 96, 79]. In contrast to this is the internal leg function, which addresses issues of design and control of a segmented leg itself [151]. Two of the probably most famous templates are the inverted pendulum [9], depicted in Fig. 2.7a as a stiff rod, and the spring-loaded inverted pendulum (SLIP) [15], illustrated in Fig. 2.7b as a massless spring attached to a point mass. Both have been used to generate a number of insights:

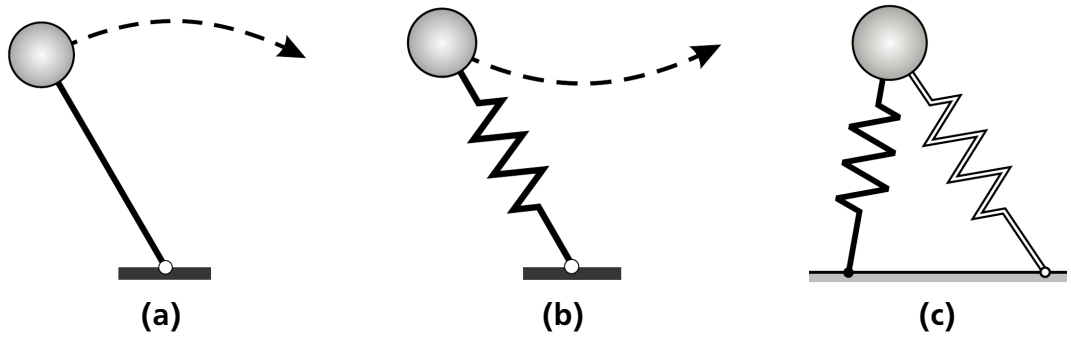

Figure 2.7.: Famous conceptual models: (a) inverted pendulum; (b) spring-mass model, also known as SLIP; (c) bipedal spring-mass model (figures adapted from [48]).

- Cavagna *et al.* recognized that the energetic fluctuations of the CoM of walkers and runners, which are out-of phase during walking and in-phase for running, can be described remarkably well by the inverted pendulum and the SLIP model, respectively [19].
- Blickhan found that the spring-mass model can describe sufficiently well the general features of the hopping and running gait, i. e., during stance phase the ratio between leg

compression and leg force is approximately constant [15]. By studying the model, he also determined the hopping frequency at which high hops can be produced economically: namely at the preferred hopping frequency. In a subsequent study [37], it was clarified that at frequencies lower than the preferred the body did not behave in a spring-like manner. At higher frequencies the spring-like behavior could be still observed, but the motions required more energy. Due to the shortened ground contact time, the time available to apply force to the ground was shortened as well, which means that a higher muscular force had to be generated.

- Applying the Froude number, which originates from fluid dynamics describing there the ratio between kinetic and potential energies, Alexander explains that the transition from walking to running occurs at $v \geq \sqrt{g\,l}$ and therefore depends on the gravitational acceleration g , the leg length l from the CoM to the ground and the walking speed v [11]. Aside from changes in gravitation, gait transitions, in general, can be evoked by either changing the system energy or adjusting the overall compliance and angle of attack of the leg [16].

- The importance of self-stability, the ability of a system to stabilize in the presence of disturbances without the need for sensing the disturbances or its direct effects, was found numerically for the spring-mass model during running [150]. Within a narrow range of angles of attack, depending on the speed, the SLIP model could self-stabilize itself in the presence of disturbances, i. e., the CoM returned to the limit-cycle trajectory without any feedback control.

- With the use of the inverted pendulum and SLIP model for walking and running, respectively, the hypothesis of different mechanical and dynamical paradigms for these gaits was established. Full and Koditschek recognized, however, that the inverted pendulum fails to describe the 'M-shaped' vertical GRF occurring during human walking [45]. More complex models of walking were more successful in representing the well known patterns occurring during walking [116, 122, 183]. However, the desire to establish a simple model that comes close to the properties of human walking led to the model development of Geyer *et al.* [48]. It was shown that just by adding a second leg the bipedal spring-mass model could well incorporate the double support of the walking motion and, in this way, also capture the typical pattern of the GRF (cf. Fig. 2.7c).

  This insight is of great significance, since it signalized for the first time that the fundamental gaits of walking and running are much less different than generally assumed and that compliant legs are crucial for both bipedal running and walking [48]. Using a more elaborate model in [71], consisting of three-segmented legs with two servomotors and four passive joints constrained by eight tension springs, it was demonstrated that a simple oscillation of the hip motors can lead to two stable gaits, namely walking and running. Therefore, the model can be regarded as an anchor with the behavior of the bipedal spring-mass template model embedded. From that research inspired, the JenaWalker II platform was constructed [152] (cf. Section 2.6).

- In recent studies such as [79] it was analyzed how leg stiffness and damping ratio changed with increasing speed using a slightly modified bipedal spring-mass model based on subject data of walking on a treadmill. The model was tuned to match human GRF at different gait speeds.

Further important insights refer to the share between feedforward and feedback control during human or animal locomotion. Full and Koditschek have argued that it is difficult to locate the origin of control, as neural and mechanical system are both essential and dynamically coupled. It is hypothesized that the control of slow, variable-frequency locomotion is dominated by the nervous system, whereas during rapid rhythmic locomotion the control seems to reside more within the mechanical system [45]. This hypothesis is supported by observations of instantaneous stiffness adaptation mechanisms in both human hopping and running experiments [38, 42]. Muscle stiffness may increase and compensate for a softer ground without any delay, according to the concept of "preflex" [90]. In this context, a further hypothesis is that there is no switch in the central control while changing speed and gait.

Aside from the template models, researchers have also been very keen on developing more complex models to study the internal leg function [116, 122, 183] and to establish more biologically plausible models of bipedal locomotion than the standard spring-mass model [71]. For instance, Hoy *et al.* [64] developed a musculoskeletal model of the human lower extremity for computer simulation studies of muscle-tendon function and muscle coordination during movement. It was found that due to different parameters, such as tendon slack length or moment arm, each actuator develops peak moment at a different joint angle. Further it was concluded that neglecting tendon in analyses of muscle-tendon force or moment about joints can lead to erroneous predictions of human muscle-tendon function.

Summarizing this section, human and animal locomotion are not only highly complex, but also not fully understood, which makes it very difficult to be studied directly by accordingly complex models. Templates turned out to be very useful to study the global function and have been used to develop robots with impressive locomotion behavior such as the Raibert hoppers [139]. But it is equally important to investigate the internal leg function. With templates only basic principles can be revealed that do not depend on the actual actuation details of body structure [45]. They cannot deliver sufficient information on how mechanisms work or provide causal explanations of detailed neural and musculoskeletal mechanisms and give guidelines for robot designs. Additionally, templates fail in capturing "all" characteristics of a specific motion, which brings us to the question how to decide which features are essential to be captured and which are not. For instance, the SLIP model does not adequately predict the effect of impacts and energy losses in the leg during running. More elaborate models that include the properties of the human lower limb system are essential. Particularly the topic of self-stability shows that the necessity for fully feedback controlled locomotion can be reduced by the stabilizing properties of muscle-tendon complexes and reflexes which need to be introduced into the mechanical structure of the robot. Rapid adaptation to small unpredictable bumps in the ground can be taken over by mechanical response of the muscle-tendon system and the slack in the joints which is technically possible by employing electrical motors coupled to spring-damper systems [125]. Therefore, the validity of simple models should not be overstressed [15].

2.6 Robotic Developments towards Improved Locomotion Performance

The previous brief excursion into the state of the art in the closely related disciplines of robotic bipedal locomotion let us highlight important features of the human musculoskeletal lower limb system and of the gaits under investigation. The short review of open issues, template and complex models illustrates the difficulty of achieving improved robot locomotion that approaches

human motion performance. Certainly, there are diverse research pathways that may bring us closer to this goal.

Recently we could observe significant progress in the ZMP-based robots. The recent videos of ASIMO's locomotion performance are impressive and exhibit enormously improved dynamics, agility and speed of the ASIMO robot [2]. Based on past available publications it can be assumed that the recent developments have been achieved in the same manner as for the previous: by complex motion control using highly sophisticated and significantly improved sensors and actuators [158, 161, 159, 160]. In recent literature, attempts to leverage biological insights into the sophisticated engineering approaches of the ZMP-based robot could be recognized. For instance, in [123] it was suggested to design a more human-like desired ZMP trajectory by means of a motion capture technique and direct ZMP measurement of human walking. In another walking pattern generation method using the ZMP criterion human walking characteristics, such as lateral and vertical hip displacement or foot swing height that were obtained by capturing human walking data, were successfully integrated on a robot to realize more natural, but also stable motions [65].

Based on the early successes with his hopping machines, Raibert continued to build together with his team at Boston Dynamics, financed by DARPA, the four-legged robot BigDog and the succeeding anthropomorphic bipeds, Petman and Atlas. Similarly to BigDog, the bipeds are actuated by hydraulic cylinders. According to the oral communications, the legs are not or just minimally equipped with mechanical compliance in the ankle and knee joints. The motion generation is based on sophisticated control strategies. Petman was reported to walk at about $5\ \frac{km}{h}$.

While all of the main groups, emerging either from the ZMP-based robots or from Raibert hoppers and passive dynamic walkers, make their own efforts so far and continuously demonstrate better results, one main aspect has attracted increasing attention in the recent years: compliant actuation. It has been identified as an important key towards natural motion performance.

2.6.1 Compliant Actuation

In fact, the use of compliant actuators is increasing in finger systems [121], exoskeletons [168], prostheses [61], humanoid robots [60] and musculoskeletal upper torsos [95]. Raibert demonstrated in the 80s that springy legs can substantially contribute to more energy-efficient locomotion and simplified control [139]. The concept of storing and releasing energy during contact with the ground, observed in animals and humans, has been realized on many robots so far. The idea of using springs, particularly serial springs, was promoted very early also by Alexander. He suggested mainly three uses [10]:

1. the pogo stick principle to bounce along on springs helps to save energy and to reduce unwanted heat production,
2. return springs to halt the legs at the end of each forward/backward swing and start them swinging the other way help to save further energy,
3. compliant foot pads that can reduce forces at impact of feet with the ground and support better road holding by preventing vibrations.

Today the reasons for the use of compliant actuators are manifold and vary depending on the application from safe human-robot interaction to dynamic smooth and energy-efficient legged

locomotion. Aiming at increased performance and safety of robots, various types of compliant actuators can be differentiated. In the following we give an overview of the various research directions that have emerged since Raibert's hopping machines.

Pneumatic Artifical Muscles

Pneumatic artificial muscles (PAMs) are muscle-like actuators aiming at mimicking the properties of human muscles: high power-to-weight ratio, relatively efficient operation, scalable force, elastic energy storage, and power output [92].

The McKibben muscle is the probably most well-known pneumatic artificial muscle [21]. Due to the high compressibility of air, such PAM behaves very compliant like a spring. It can only exert pulling forces, i. e., usually two PAMs in a antagonist-agonist configuration are necessary to drive a joint in both directions. Therefore, it falls into the category of antagonistically controlled stiffness actuator according to [56]. The advantages of a PAM typically include backdrivability and high force production at low speeds and low mass. The disadvantages are the nonlinear characteristics—like muscles have, too—, hysteresis which makes control very difficult, high threshold of pressure to generate force, and the need for pressurized air which makes it energetically inefficient and loud.

Another PAM recently developed is the pleated pneumatic artificial muscle, which according to the authors reduces the hysteresis and overcomes the threshold of pressure [56]. It has been installed in the biped Lucy to realize slow walking in the sagittal plane [169]. The robot has in total six DoFs, three in each leg for the pitch motions in each joint, and is prevented from falling sidewards by a guiding mechanism.

Series Elastic Actuators

A further famous compliant actuator is the series elastic actuator (SEA), developed by Pratt and Williamson [126], who laid the foundations for a paradigm shift in design and philosophy for the next generation of actuators. In the original SEA an electrical geared motor is connected by a rotational spring with fixed stiffness to the joint. The physical compliance of the actuator is limited by the spring constant and cannot be changed during operation. Force respectively impedance control is enabled by measuring the spring elongation and returning it in a feedback loop. Since the actuator controls the equilibrium position of the spring, it belongs to the group of equilibrium-controlled stiffness actuator.

This actuation principle enables lower reflected inertia by the decoupling of the joint from the motor, shock tolerance, energy storage and release, and less damage to the environment. The SEA is characterized in general by low impedance, high force-fidelity, low friction and good bandwidth. As a result, SEAs are well suited for use in legged robots. The 2-D biped Spring Flamingo is one of the first robots in which these actuators had been deployed for improved walking performances [20].

Tendon- and cable-based versions of SEAs followed and were implemented not only in manipulators, but also in bipedal robots. The Delft bipedal robots Flame and TUlip use several Bowden cable-driven SEAs for the actuation of the hip, knee, and ankle pitch joints which are required to perform highly fast dynamic motions [60]. However, the maximum walking speeds reported amount to only 0.45 m/s. Furthermore, due to the high reduction actuation, these robots are, in general, not tailor-made for fast gaits that require high energy input during ground contact, such as running or hopping. Hutter *et al.* argued that high spring compliance in combination with low damping enables storing and releasing a substantial amount of energy during ground

contact phases [70]. The authors have built an articulated, two-segmented leg, ScarlETH, to analyze its performance and suitability for deployment in a quadrupedal running robot. The legs are actuated by SEAs based on a chain/cable pulley design.

Also for other applications, such as wearable assistive devices or exoskeletons, novel actuators based on the series elastic actuation principle provide clear advantages. The Robotic tendon, for instance, reduces substantially the energy consumption of a wearable assistive device [61]. An impedance-controlled gait rehabilitation robot was shown to yield good performance results, provided a well chosen spring stiffness [168].

While the original intention of the SEA's pioneers was solely a more accurate and stable force/torque control, the additional advantages that came along the SEA inspired many new developments of compliant actuators, in order to come close to the functionalities of our natural archetypes. Adjustable physical compliance has emerged as most desirable property of an actuator, in order to control the natural frequency of the system for safer human robot-interaction and improved legged locomotion behavior.

Variable Impedance Actuators

The AMASC (Actuator with Mechanically Adjustable Series Compliance) is an antagonistically controlled stiffness actuator where two motors independently control the no-load position and physical compliance of the joint [67]. It was specifically designed for running robots to apply variable stiffness as an additional control parameter in order to adjust the overall leg property. The MACCEPA (Mechanically Adjustable Compliance and Equilibrium Position Actuator) [57] is a further actuator with adaptable compliance targeted at enabling the biped Veronica to walk at different speeds. Results of this testing and any gained benefits by using these variable compliant actuators, however, are not known to the author.

Recently we experience an even huger wealth of research on variable impedance actuators. Within the EU project VIACTORS, a number of novel actuators with variable stiffness and damping have been developed [6]. The constructed actuators often comprise several custom-made motors, Harmonic drive gears, nonlinear spring mechanisms and tendons where additional motors are employed to adjust the lever arm or spring stiffness. Such actuation units present modular, integrable solutions that can be well adaptable to the desired task. By this modular solution, dynamic coupling effects that may be undesirable from a controller point of view are eliminated.

While such actuation units represent impressive sophisticated engineering approaches, it still remains to be shown that they provide additional advantages in fast dynamic legged robotics. To date, research studies have mostly focused on manipulation tasks as application for these actuators. One main disadvantage of actuators with adaptable compliance is the increased model complexity which poses a challenge for the development of the motion controller. Further, due to the additional motor for tuning the joint behavior it is very difficult to keep the reflected mass and inertia low.

In fact, the ideas behind the AMASC eventually were integrated in the development of the electric cable differential (ECD) leg eliminating the mechanically adjustable stiffness intentionally because of the additional mechanical complexity and the reduced energy storage capacity of the springs [68]. The bipedal robot MABEL was assembled of two such ECD legs to overcome the problems the predecessor BiMASC had with the AMASC actuator. So far, it has demonstrated successfully walking over small obstacles.

These incremental advances show how difficult it really is to realize a bipedal walking and running machine moving in a more "human-like" fashion than existing robots. So, the question is whether the desired leg properties can be also achieved by less complex actuators. According to the ideas expressed in [85], it may be sufficient to enhance conventional actuators by addition of design features: for instance add a powered latch, a mechanical stop to avoid knee hyperextension or a clutch to engage or disengange the motor as desired.

Active Compliance

An active compliant actuator is a completely stiff actuator that mimics the behavior of a spring by software control. The controller calculates the deviation from the desired torque/force based on measurement of the current torque/force and commands it to the actuator. Obvious disadvantages are that such actuator cannot store any energy and that shocks cannot be absorbed. The advantage is online adaptable compliance. However the bandwidth of actively controlled compliance depends on the bandwidth of the sensors, actuators, and controller frequency. Despite these constraints, several research groups have successfully utilized active compliance for high-speed locomotion [149, 1].

2.6.2 Musculoskeletal Bipedal Robot Designs

Designing and developing new actuators with more of the properties of the human muscle-tendon complex is only one of the many tasks that have to be fulfilled in order to come close to the powerful human musculoskeletal system enabling the human to such versatile dynamic movements that no robot has been capable of replicating yet. In Section 2.2 it was shown that the leg segmentation and the arrangement of mono- and biarticular muscles also play an enormous role.

To the knowledge of the author, Hosoda, Lewis, Niiyama and their co-authors are among the first to discuss in robotic literature biologically inspired musculoskeletal leg design as a requirement for dynamically locomoting legged robots [63, 82, 118]. They all have built different versions of human-like musculoskeletal leg prototypes with the intention to replicate motion capabilities of the human muscular system and its functionalities and to use it beneficially for dynamic locomotion.

In retrospect one could argue that also Lucy has a musculoskeletal design, as each sagittal leg joint is equipped with two pneumatic muscles in antagonist-agonist configuration for a bidirectional actuation [169]. However, it was not intended to target at a human-like musculoskeletal arrangement nor to investigate the roles of the muscle-like actuators in a systematic manner. It also did not have any artificial biarticular muscles implemented.

Hosoda *et al.* developed a number of anthropomorphic musculoskeletal robots to study several issues such as adaptive and multi-modal locomotion, contributions and limitations of artificial pneumatic muscles, and the roles and functions of the essential muscle groups shown in Fig. 2.1c [63, 162, 62]. In [162] Takuma *et al.* presented a 3-D bipedal robot that could walk from standing and jump only because the robot's leg compliance could be tuned from finite to infinite. It is shown that adaptable leg compliance is a prerequisite for multi-modal locomotion. The leg joints were driven by antagonistic McKibben pneumatic muscles, similar to the configuration displayed in Fig. 2.1a. Previously first efforts to realize walking, running and jumping were made on a 2-D bipedal robot with four legs, i. e., two inner and two outer legs, to avoid sideway falling down [63]. The authors emphasize that a robot capable of different gaits needs

to have fast response against impacts and tunable compliance mechanisms, since for walking, for instance, stiffer joints are required than for running. Here the suitability of antagonistic pneumatic muscles is particularly highlighted, as the stiffness of a muscle can be simply regulated by changing the amount of air inside. Basic feedforward controllers for the operation of the valves were employed based on ground contact sensing to realize walking, running, and jumping. Specifically the attention should be drawn to a pneumatically driven monopod which incorporated the main nine muscle groups involved in human locomotion (cf. Fig. 2.1c) to investigate biomechanical findings during jumping [62]. In various jumping experiments the role and functions of the nine muscles were studied in different configurations by feedforward control and many insights stated previously by biomechanics researchers could be confirmed. For instance, the synchronization of joints is indeed coordinated by biarticular muscles, which the controller would otherwise need to explicitly take care of in a conventionally built robot without such actuator. Thus it is argued that "complicated body structure simplifies the control scheme" [62]. It is hypothesized that the stability of jumping motions can be further improved by applying also feedback control.

Niiyama *et al.* studied the role of the body in explosive movements [118]. For achieving enormous jumping heights and producing large instantaneous forces, a bio-inspired biped, Mowgli, with monoarticular and biarticular muscles was developed. As for the actuation, three McKibben muscles are used in each leg for the hip, knee, and ankle joint. Motivated by the human musculoskeletal system, one of the muscles in each leg span two sagittal joints. Additionally, passive springs are implemented as counteracting torques to those generated by the main active artificial muscles. The robot was capable of achieving jumping heights of more than 50 % of its height and subsequently landing softly. Such results have not yet been achieved by conventionally built robots with the commonly used stiff electrical joint actuators and it is doubtful that the near- and mid-term future brings considerably improved rotary joint actuators. In a further research work, Niiyama developed the human-inspired, pneumatically driven musculoskeletal Athlete robot [117]. The anatomical structure including the configuration of muscles, range of motion, maximum forces of muscles, and moment arms are reported to be similar to the human. From the muscles shown in Fig. 2.1c, the following are implemented: GL, ILIO, BF, RF, VAS, GAS, TA. Additionally, the hip adductors and abductors are integrated. With this quite complex musculoskeletal system, Niiyama explored passive direction control of bouncing by preset stiffness values, soft landing and postural control of standing.

The previously described studies have in common the use of pneumatic artificial McKibben muscles in the built robots. With respect to the long-term goal of energy-efficient and mobile bipedal robots, however, the use of pneumatics is not recommended. Pneumatic actuators require a dedicated compressed-air source and careful construction in order to avoid low efficiency. However, in the meantime the integration of muscle-tendon complexes seems to become increasingly a widely supported idea. In the context of wearable robotic systems, such as assistive exotendons, the beneficial energy-saving power transfer of elastic tendon devices spanning even more than two joints, also known as polyarticular devices, was recognized in 2003 [166]. Based on the results of a numerical simulation study, van den Bogert suggested utilizing passive elastic polyarticular devices in assistive exotendons to reduce the total energy consumption and, in this way, to increase battery life.

The Kotaro humanoid robot [106] is one of the first electrically actuated full-body robots with a complete torso including shoulders, elbows and hands and even a head with eyes and ears featuring a quite complex musculoskeletal system driven by 90 - 120 motors. The "muscles"

consist of chemical fibers, direct-current (DC) motors and pulleys. However, in contrast to the previous robots, the concept and development of Kotaro did not aim at better bipedal locomotion behavior. Rather the goal was the construction of a novel flexible-spine humanoid comparable to the human musculoskeletal system. Kotaro demonstrated pedaling a cycle by self-repeated training in the real world and also realized standing. In 2007 a successor version with improved mechanics, sensors and actuators, called Kojiro, was presented [105]. The actuators were enhanced with the newest available electrical Maxon brushless motors. Any new motion performances were not shown. The series of robots with increasing resemblance to humans with respect to joints' stiffness, redundancy and powerful performance was continued by the robot Kenzoh [115]. Here the authors state for the first time the goal of performing dynamic tasks such as catching a ball to demonstrate the benefits of the highly complex musculoskeletal structure. In a current research work Asano *et al.* focus on the lower thigh design of their humanoid robot Kenshiro [13]. It represents the presently most complex musculoskeletal lower leg design with body configuration, joint structure, actuation structure arrangement and joint torque all based on the human lower thigh. The built humanoid robot shall be used as a human body simulator to improve understanding the human biomechanics. Electrical actuation with high reduction gearboxes in combination with wires and locking mechanisms are implemented to represent the main mono- and biarticular muscles described in Section 2.2. Additional elastically actuated tendons are integrated to support the foot roll motion, summing up to in total 13 actuated tendons for each leg. However, after this series of highly sophisticated engineering approaches to design human-like robots, the challenging task of motion control concepts is yet to be solved.

The construction of an electrically actuated lower limb with full musculoskeletal leg design, similar to the developments of Hosoda *et al.* [62] and Niiyama [117], was discussed in [82]. The built monopod includes all muscles illustrated in Fig. 2.1c, except for PL and BF. The muscles are represented by servomotors connected by stiff Kevlar straps to the joints, thus all being active. Klein *et al.* emphasized the important role of biarticular muscles during running and jumping motions and reproduced the proximo-distal energy transfer of the GAS muscle in experiments with the constructed leg. It was shown that the transfer of peak power depends on the exact timing between biarticular and affected monoarticular muscles, i. e., GAS and SOL muscle. In [81] the authors presented a further completed leg design by the addition of PL and BF.

It is striking that the previously mentioned electrically actuated robots are not yet capable of basic human gaits such as slow jogging or hopping. Thus, the question arises which degree of design complexity and control concepts are needed for musculoskeletal robots to successfully perform motions that humans are capable of. In this context, research on the underactuated JenaWalker I and II platforms showed that embedding the functions of only a few mono- and biarticular leg muscles and tuning the corresponding parameters appropriately are sufficient to enable the robot to walking and slow jogging motions [71, 152]. Both models have a similar morphology: the legs are three-segmented and the hips are coupled to the feet by four passive tension springs representing the GAS, BF, RF and TA muscle. With a height of 45 cm versus 20 cm, JenaWalker II can be considered as the large-scale version of its predecessor, JenaWalker I. In order to adjust the rest length of the springs, additional servo motors were deployed at the hip joints. The motions were generated by basic sinusoidal oscillations fed to DC motors located at the hip joints. Despite these amazing results, the missing of an upper body and the supporting boom of the robot at the hip joints can be considered as a strong limitation of the construction and approach [152].

Recently another ambitious project has been launched with the goal to develop a fast, but also efficient and robust bipedal robot, the FastRunner, inspired by the musculoskeletal system of the ostrich [27]. The project addresses the difficulty of achieving a good balance between speed, energy efficiency and stability in current robots. It is envisioned to realize energy efficiency by electrical actuation in the hip joints in combination with an entire network of elastic elements, of which some are engaged or disengaged according to the current gait phase. So far, analyzes are only performed in simulation. A first prototype version of the planned robot has to be completed yet.

2.7 BioBiped: A Novel Musculoskeletal Bipedal Robot Design

The BioBiped project aims at the long-term realization of human-like hopping, running and walking. It is assumed that this goal is greatly supported by a well thought-out musculoskeletal three-segmented lower limb system that implements the previously highlighted, some of the main characteristics of the human musculoskeletal leg system, namely segmentation and elastic leg behavior. Special attention is placed on compliant actuation using active and passive human-like muscle-tendon elasticities. The above literature review and experiences gained by other robotics researchers underpin this hypothesis. In a series of robot developments and even exoskeletons it could be shown that the integration of human-like muscle-tendon functionalities can be of great advantage with respect to dynamic and energy-efficient locomotion. Further it has been recognized that electrical actuation can particularly contribute to autonomous and energy-efficient locomotion. As another important point, it should be mentioned, that even though fast dynamic gaits such as running or hopping require different leg stiffness than walking, the use of variable impedance actuators is not recommended as first step. Handling of such complex actuators which are still under development has not yet been successfully realized in fast dynamic robot locomotion. Instead, first the interplay of the important muscle groups highlighted in Fig. 2.1c should be fully exploited. Subsequently it is still possible to vary leg stiffness by a clutch engaging or disenganging a motor as suggested in [85]. Finally, the JenaWalker II robot serves as a further inspiring example. Dynamic walking and jogging motions could be realized on a rather basic underactuated mechanical system that was efficiently actuated by electrical motors in connection with passive elastic tendons.

In principle, electrical actuators offer a number of benefits besides high continuous power per unit mass (up to 300 W/kg) and high efficiency ($> 90\,\%$) [92]. Further advantages are the compact size, ease of utilization, and high-bandwidth control. From a robotics standpoint, gearing results in the undesirable characteristics of friction, backlash, and compliance, which make accurate control difficult. However, achieving higher torques without using gears is only possible with increased motor size which would in turn result in heavier overall weight of the leg. Therefore, we chose to add gearing and elastic transmission in order to enable higher torques without increasing the motor size.

Of course, both gearing and elastic transmission also introduce some drawbacks. While the gearing reduces the resulting joint velocities, the elastic transmission makes tracking of a given joint trajectory more difficult and the envisaged motion control clearly affects the exploitation degree of the natural robot dynamics. Consequently, there is a trade-off between the desired velocities, torques and efficiency of the intended motion control. This will be subject of further discussion in Section 4.7. In general, however, we believe that the advantages of this constellation outweigh any disadvantage and that electrically driven muscle-tendon like actuators offer

tremendous potential for legged locomotion that needs to be fully investigated by developing suitable simulation models and hardware platforms.

In cooperation with TETRA GmbH, Ilmenau, the first two prototypes, BioBiped1 (cf. Fig. 2.8) and BioBiped2, have been built. Both prototypes have three-segmented compliant legs with identical actuator types, to be presented in the following section, and a simple trunk for stabilization purposes. Taking into account experimental results for improvements of the mechanics and electronics, BioBiped2 can be considered as a revised version of BioBiped1. As the research and analyses carried out within this thesis are centered around the BioBiped1 robot, we will next shed more light on the technical realization of BioBiped1.

2.7.1 Technical Realization of BioBiped1 and its Actuation Concept

The BioBiped1 robot, depicted in Fig. 2.8, is about 1.1 m tall in extended position and weighs around 10 kg. The segment lengths are based on scaled-down anthropometric data. The mass distribution with the upper body weighing around 57 % of the robot's total weight corresponds almost to that of humans where the upper body's weight amounts to 60 %. Segment masses and lengths as well as foot dimensions are indicated in Fig. 2.8. Masses and lengths of the segments were extracted from the CAD files. The segment lengths were additionally also measured. Further dynamics data, such as inertia and CoM of segments are presented along with the dynamics model used for the simulations in Chapter 3.

As for the robot's motion degrees, both legs have a rotational DoF each in hip, knee and ankle joint along the pitch axis, and an additional DoF in the hip along the roll axis for lateral stabilization in the frontal plane. Additionally, the upper body has a DoF along the pitch axis for stabilization purposes. Each of these DoFs is supported by an electric motor. Details of the actuation follow below. Note that at this stage, as previously stated, stabilization issues are ignored in order to entirely focus first on a proper leg design for the intended gaits. Therefore, the rotational DoF in the trunk is fixed to zero and the upper body's movements are restricted to 1-D vertical motions by an external constraining mechanism. It is attached to the pelvis of the robot and equipped with four sets of rollers, shown in Fig. 2.9, sliding with low friction in vertical guides. In this regard, also the legs are restricted to move only in the sagittal plane, i. e., the hip roll DoF is ignored.

For the purpose of monitoring, evaluating and analyzing the robot's motions a number of sensors have been included. A concise overview of the sensing and control system is provided in Fig. 2.9. In order to calculate and stabilize the robot's posture a six DoF inertial sensor measuring angular speed and linear acceleration in all three axes (Analog Devices inertial measurement unit ADIS16364) is mounted on the hip of the robot. Two position sensors are implemented at each joint: one 12-Bit Hall encoder directly at each joint measuring the absolute joint angular position and one incremental encoder at each of the electrical actuators. Further each foot is equipped with three force sensors, one in the middle of the foot measuring the horizontal force and one each at heel and forefoot measuring the normal force, as illustrated in Fig. 2.11c.

The robot carries an on-board computer in its trunk featuring an Intel Atom processor. In combination with batteries the robot will be able to operate autonomously. At the current stage of developments, external power supply is used and software development as well as testing is carried out on an external laptop. For later autonomous operation, however, the on-board computer will be used instead to run the control software on top of a real-time Linux system. The robot's software is based on the Orocos Real-Time Toolkit [3] as an abstraction layer for the real-

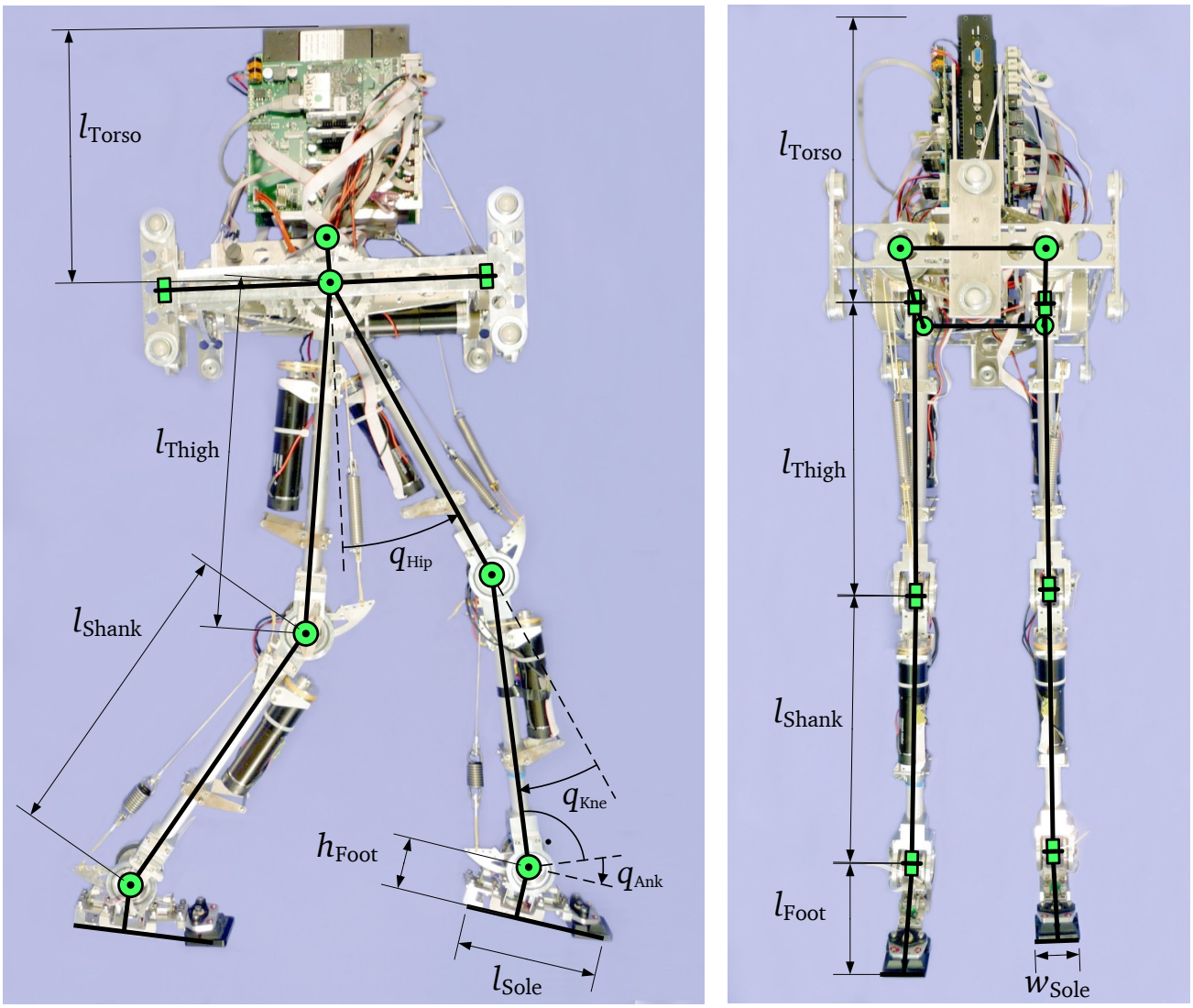

Dimensions and masses	
Segment lengths	$l_{Torso} = 269\,\text{mm}$; $l_{Thigh} = 330\,\text{mm}$; $l_{Shank} = 330\,\text{mm}$; $l_{Foot} = 122\,\text{mm}$
Foot dimensions	$h_{Foot} = 67\,\text{mm}$; $l_{Sole} = 165\,\text{mm}$; $w_{Sole} = 40\,\text{mm}$
Leg length	0.727 m (from hip to sole with extended leg)
Segment masses	$m_{Torso} = 5.332\,\text{kg}$; $m_{Thigh} = 0.843\,\text{kg}$; $m_{Shank} = 0.804\,\text{kg}$; $m_{Foot} = 0.342\,\text{kg}$
Total mass	$\sim 9.2\,\text{kg}$ (the CoM is located at $\sim 0.14\,\text{m}$ above the hip joint)

Figure 2.8.: Main kinematics and dynamics data of the BioBiped1 robot.

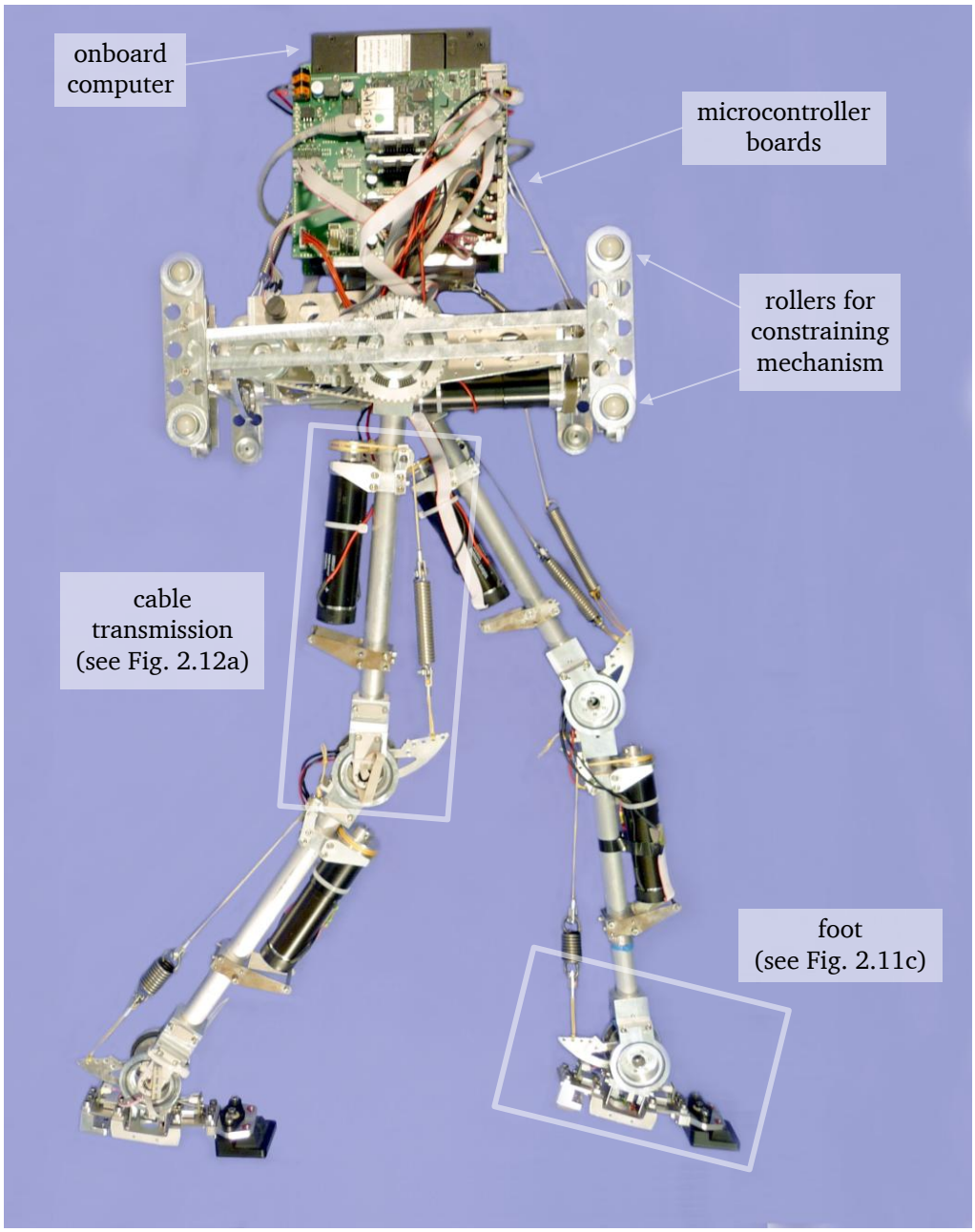

Sensors [132]	
IMU	ADIS 16364 with 6 axes (angular speed: 3 axes; linear acceleration: 3 axes)
Encoders	incremental for motor position, absolute for joint position
Force sensors	custom-made, 3 axes per foot (parallel to the sole for the entire foot and normal to the sole for the forefoot and the heel pads)
Control system [132]	
Hardware	2 custom-made microcontroller boards and an on-board control computer communicating via EtherCAT bus
Software	Orocos Real-Time Toolkit[3] and Robot Operating System (ROS)[4]

Figure 2.9.: Sensing and control system of the BioBiped1 robot: Details of the foot force sensing and cable transmission system for the knee and ankle extension are provided in Fig. 2.11c and 2.12a, respectively.

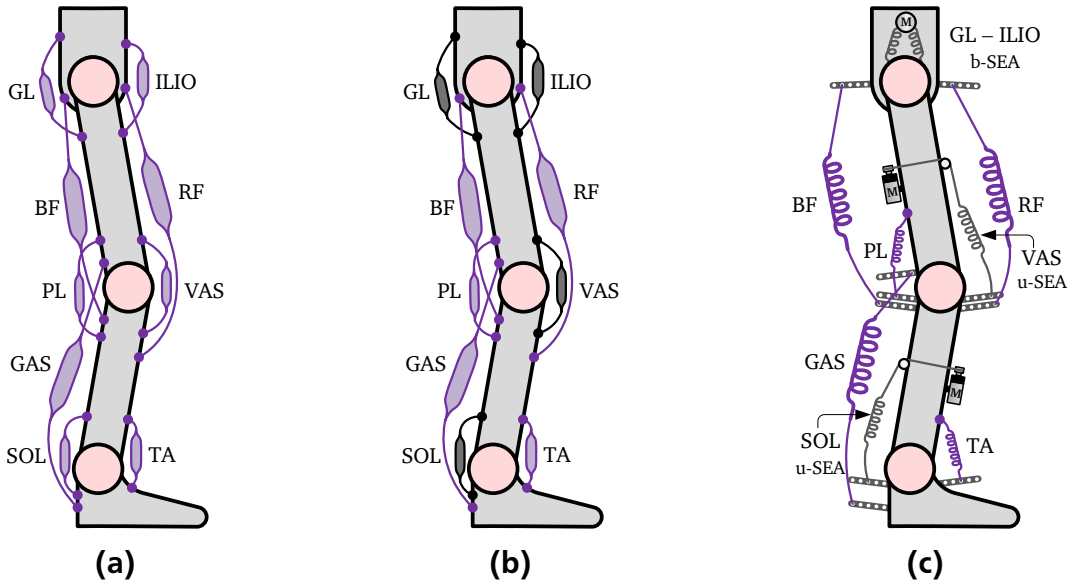

Figure 2.10.: Chronological evolution of the conceptualization of BioBiped1's actuation from left to right: (a) essential human muscle groups during locomotion; (b) muscle-tendon units that are actuated by a motor are indicated by dark grey color, while nonactuated muscle-tendon units, referred to as passive tendons, are marked in purple; (c) constructed version of BioBiped1's actuation.

time functionality. Network communication with the graphical user interface is facilitated by the Robot Operating System (ROS) [4]. Two custom-made microcontroller boards are interfacing the analog and digital sensors as well as the motors. Communication with the on-board computer takes place via an EtherCAT bus system at high speed and low latency.

The actuation decisions for BioBiped1 are based on the previously described biomechanical insights (cf. Section 2.2). As shown in Fig. 2.10a and discussed in Section 2.2, human dynamic locomotion is enabled and supported mainly by nine muscle groups. Further, in accordance with the main hypothesis of the BioBiped project, that the central locomotion capability should be jogging and not walking, the focus of present investigations lies on fast dynamic motions that are mechanically demanding. Therefore, an appropriate mechanical leg realization is considered as an essential task and requirement for paving the way for a more human-like locomoting robot [132]. The incorporation of all nine muscle groups is hence a logical implication of the aforementioned thoughts. These muscle groups are realized in BioBiped1 by active and passive tendons, indicated by grey and purple color, respectively, as depicted in Fig. 2.10b. Accordingly, the majority of the tendons, five out of nine, are integrated without motors; they act completely passively based on joint configurations and external forces. All other tendons actuated by a motor represent human-like muscle-tendon complexes. For simplicity we will use the term tendon for both the active and passive type. The technical realization of the tendons is illustrated in Fig. 2.10c and explained further below.

With respect to the planned fast dynamic motions, active energy supply is potentially needed for each leg joint. For the hip joints, connecting the trunk and the legs, a bidirectional actuation was proposed, i. e., both extension and flexion of the joint are actively supported (cf. Section 3.4). For the knee and ankle joints, however, it was decided to support only the direction of extension actively based also on the fact that flexor muscles are generally much smaller than extensor

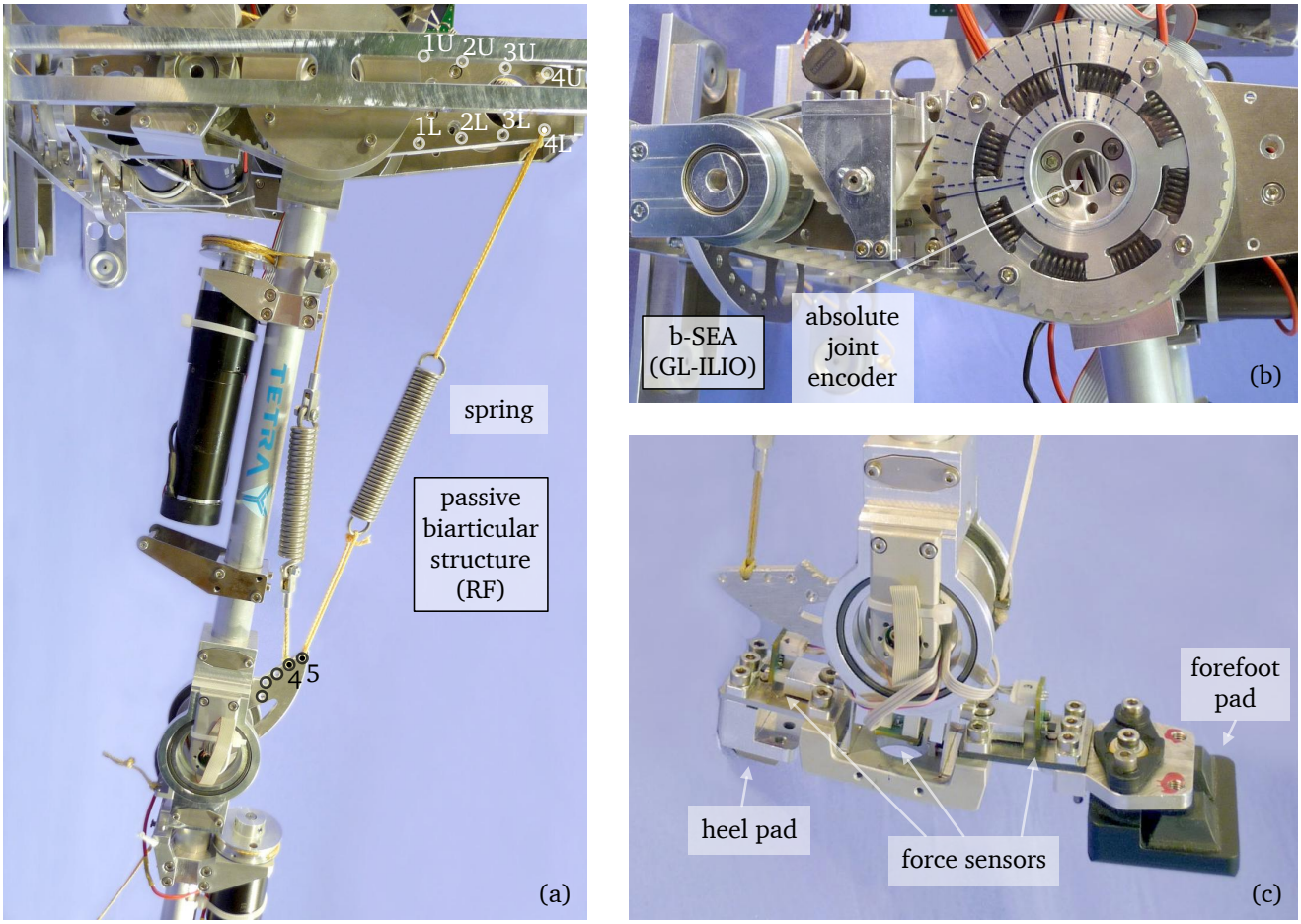

Figure 2.11.: Technical realization of important elements of the BioBiped1 platform: (a) passive biarticular tendon RF with several force application points at both ends; (b) b-SEA hip actuation representing GL-ILIO; (c) foot force sensing system measuring forces parallel and perpendicular to the foot.

muscles. This specific motor implementation enables a fast extension of the joints for a powerful lift-off from the ground during hopping and propelling the leg forward during jogging [133]. The flexing occurs then passively. This actuation configuration will be analyzed in greater depth in Section 3.4 along with the developed actuator models.

The actuators used are geared rotary electric DC motors (RE30 Maxon motors, 60 W, 24 V, with planetary reduction gearbox GP 32C with gear ratio of 66:1) [131]. Each leg joint is actuated by one such unit: one for the bidirectional hip actuation and one each in knee and ankle joint for the active extension. In total, six motors are used for both legs. These actuators had been selected prior to the robot's construction using a model-based method that determines the motor signals required for given human joint trajectories [133]. The method represents one of the contributions of this thesis and is described in Section 4.3. In the following, a closer look is taken at the technical implementation of the tendons illustrated in Fig. 2.10c.

Hip actuation: As depicted in Fig. 2.11b, the hip motor is connected via a timing belt to the joint. The transmission from motor to joint is not rigid due to small compression springs aligned in an inner ring around the joint. As soon as the timing belt is moved by the motor, the springs start compressing. This elastic transmission principle corresponds in its functionalities to

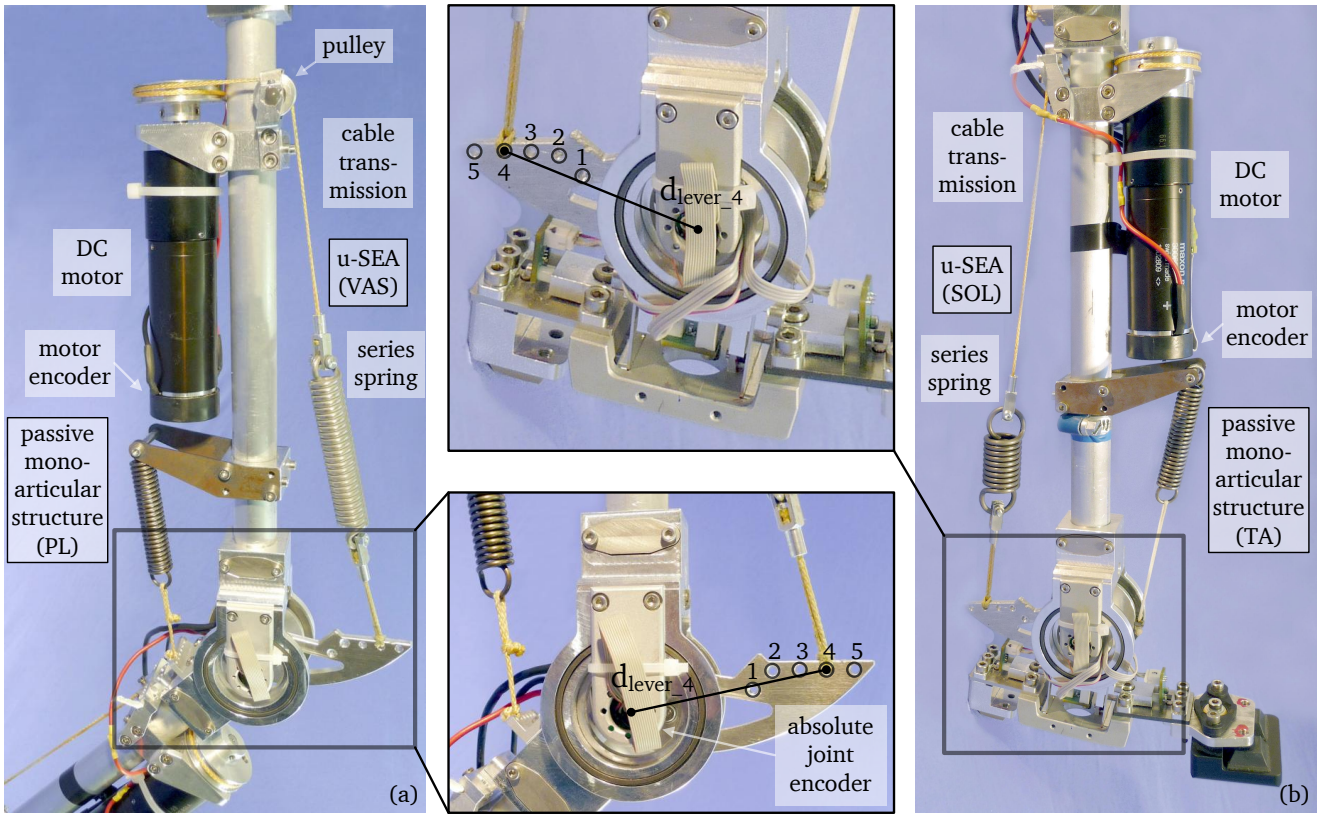

Figure 2.12.: Actuation system of the knee and ankle joint: (a) cable transmission for the knee extension mimicking the human VAS muscle with a close-up of the attachment system; (b) cable transmission for the ankle extension representing the human SOL muscle with a close-up of the attachment system.

that of the original SEA [126] introducing elasticity directly in the joint. As the motor actuates both flexion and extension of the hip through this transmission principle, representing this way the muscle pair ILIO-GL, we introduce the notion of *bidirectional SEA* (b-SEA) for this type of actuator.

Knee and ankle actuation: The knee and ankle joints are each actuated by a combination of a *unidirectional SEA* (u-SEA) and its passive counterpart. Each joint is actively extended by an elastic tendon, consisting of the motor connected to the joint via a Dyneema tendon with built-in extension spring. As illustrated in Fig. 2.12, the motor adjusts the equilibrium length of the elastic tendon by winding the tendon around the pulley attached to the motor axle. On the joint side five different force application points can be chosen to attach the tendon to the joint at distances of $36.4, 43.0, 50.8, 58.7, 66.5$ mm from the joint center (cf. Fig. 2.12). This actuation concept introduces varying lever arms and transmission ratios aside from highly nonlinear output torque and stiffness functions. Both, the VAS and SOL muscle, are represented by a u-SEA. The flexing muscles in knee and ankle joint, PL and TA, are implemented as passive tendons by a Dyneema tendon with built-in extension spring, referred to as *monoarticular, passive tendon*. For attaching the tendon at the joint again several different attachment points are available. This actuation system comprised of monoarticular, active and passive u-SEA generates two opposing torques.

The biarticular muscles, RF, BF, and GAS, are realized in the same way as the passive tendons PL and TA, with the difference that they connect two segments. Here again, the construction allows to choose different fixation points and springs as well. These tendons represent the group of *biarticular, passive tendons*. The realization of the tendon RF is exemplary shown in Fig. 2.11a.

Note that only the b-SEA, ILIO-GL, and the active tendons, VAS and SOL, are always integrated in BioBiped1. Depending on the motions, a passive tendon, mono- as well as biarticular, can be detached and attached as desired. This allows a better synthesis and diverse investigations as we will see in Chapter 5.

2.7.2 Experimental Evaluation of BioBiped1's Locomotor Function

The beneficial effects of BioBiped1's intrinsically compliant actuation system could be observed already in early experiments that had the purpose of globally validating the overall robot design [132]. The focus of the experiments was placed on investigations regarding the repulsive axial leg function (leg compression/extension during stance), which is directed mainly towards the capability to generate sufficient repulsive leg forces during stance phase to achieve clear flight phases. Further, the ability of the robot to generate (actively) enough thrust to induce continuous hopping motions was investigated. Finally, these two capabilities were combined to demonstrate synchronous two-legged hopping motions.

Passive Rebound

We first analyzed the ability of the robot to rebound passively, i. e., support high forces and impacts during the landing and subsequent support phase and recover part of the energy stored in the springs during the support phase. The robot was dropped in a slightly flexed leg configuration from a height of 15 cm. In the slightly flexed leg configuration the knee and ankle joint had the angular position $q_{\mathrm{Kne}} = -25^\circ$ and $q_{\mathrm{Ank}} = -14^\circ$, respectively. For recalling the zero position of the joints see Fig. 2.2. Table 2.1 contains all parameter settings of the elastic transmissions. The motors of the knee and ankle joint extension tendons were P-controlled to constantly keep their initial position. Snapshots of the motion are illustrated in Fig. 2.13. As shown, the motions of the robot were not rigidly constrained. Therefore, in order to prevent the robot from falling backward or forward after collision with the ground, the robot had to be stabilized by ropes. The forces were measured by a padded Kistler measurement force plate and normalized to BioBiped1's body weight. Several important observations could be made:

- The robot was able to rebound and lift off its weight by about 5 cm.
- It was capable of rebounding at least twice (cf. Fig. 2.14).
- The initiated flight phase between the first and second bounce lasted for about 150 ms (cf. Fig. 2.14).
- The robot was capable of storing and releasing energy passively.
- The mechanical elasticities prevented the transmission of the peaks to the gearboxes.

It could be also recognized that the peaks arriving at the joints and, thus, at the motors decrease distally being smallest at the hip level. Note that a slight additional damping of the impact forces was due to the padding of the Kistler measurement force plate. These results were achieved by

Table 2.1.: Settings of the leg actuation for the experimental proof of concept of BioBiped1's elastic leg operation.

Experiment	Joint	Tendon	Stiffness [N/mm]	Attachment [number]	Rest angle [deg]
Passive rebound	Knee	VAS	7.9	5	-25
		PL	Rope	1	-25
		GAS	4.1	1	-25
	Ankle	SOL	6.7	3	-14
		TA	Rope	1	-14
		GAS	4.1	5	-14
Active push-off	Knee	VAS	15.5	3	-55
		PL	Rope	1	-55
		GAS	4.1	1	-55
	Ankle	SOL	7.9	3	-5
		TA	Rope	1	-5
		GAS	4.1	1	-5
Synchronous hopping	Knee	VAS	15.5	5	-65
		PL	4.1	1	-65
	Ankle	SOL	12.9	5	23
		TA	4.1	1	23

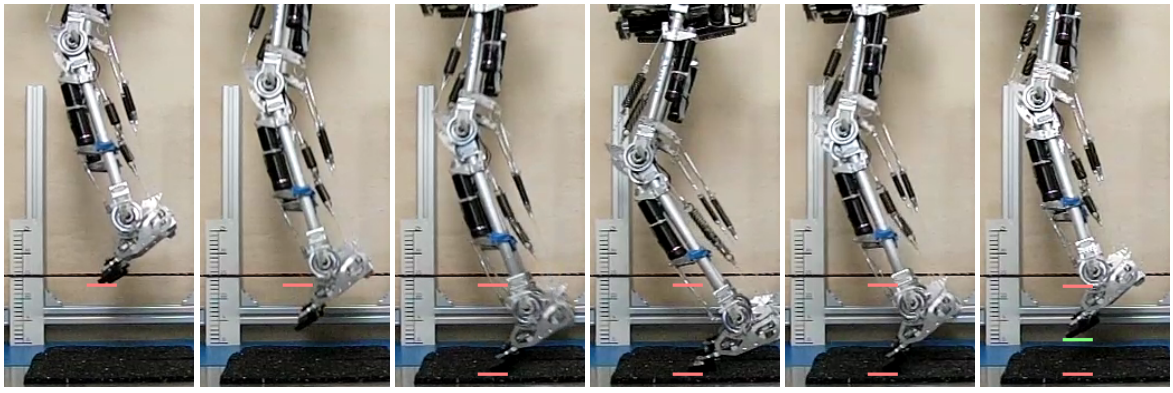

apex (-0.1s) | falling (-0.03s) | touch-down (0.013s) | compression (0.073s) | lift-off (0.163s) | apex (0.263s)

Figure 2.13.: Passive rebound and soft landing of BioBiped1 after 15 cm drop (timestamps correspond to Fig. 2.14).

trial and error adjustment of the properties of the ankle and knee extensors, SOL and VAS, and the passive biarticular muscle GAS. The passive antagonists, PL and TA, were integrated solely as ropes.

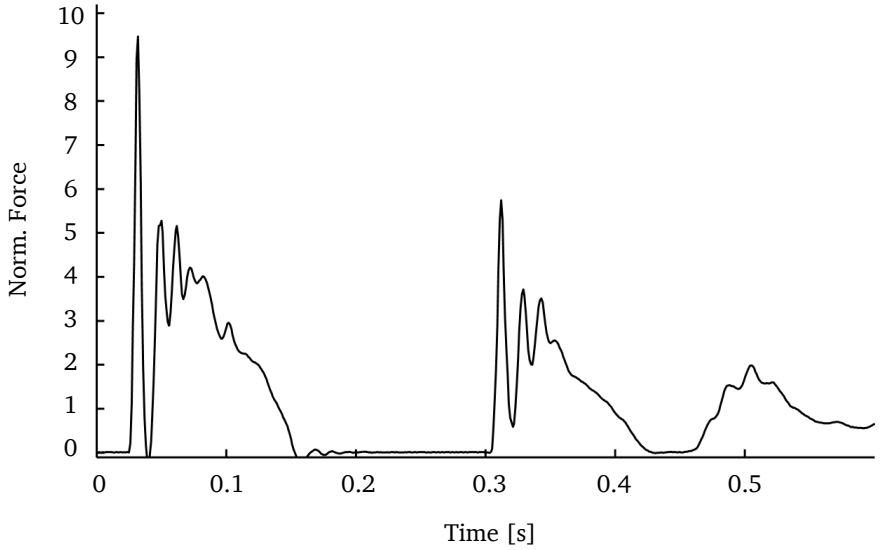

Figure 2.14.: Vertical GRF of both legs in total during the passive rebound shown in Fig. 2.13. The forces were measured by a padded Kistler measurement force plate and normalized to BioBiped1's body weight.

Active Push-off

In the second experiment the robot's capability to push off actively from the ground is evaluated. Starting from a bent position, the robot straightened its legs using knee and ankle actuators. Snapshots are illustrated in Fig. 2.15. The GRF are depicted in Fig. 2.16. In its bent starting position, the robot supported its own weight only on the forefoot and was stabilized by ropes. Due to this external stabilization, the vertical force is slightly below the robot's own weight, as can be seen in Fig. 2.16. Subsequently, the ankle and knee actuators were powered at the nominal voltage (24 V) to move the legs into a straight position hereby pushing the robot off the ground. A clear flight phase of about 80 ms can be seen in the vertical GRF obtained by the force-plate starting just before 0.4 s (Fig. 2.16). The motion did not yet comprise a return into starting position after lift-off, which would have led to a longer flight phase. Instead, as it touched down with its legs still fully extended on its toe tips, causing high impact forces, the robot had to be supported horizontally.

These results show that the robot is able to push off actively from the ground. Although the flight phase was quite short, the performance can be improved through better synchronization of knee and ankle, by, for instance, adding the biarticular GAS tendon to the leg actuation.

Synchronous Two-Legged Hopping

Combining these two capabilities, we could show that BioBiped1 is capable of dynamic synchronous two-legged hopping with clear ground clearances and flight phases. The motion of the robot was constrained to vertical movements. The motors were P-controlled to switch periodically the reference positions between two sets of values. These corresponded to configurations with retracted (knee and ankle bent) and extended (knee and ankle straightened) legs. The angle change was approximately 30 ° for the knee joint and 26 ° for the ankle joint. The durations of the extension and the retraction phase were set to 200 ms and 160 ms, respectively. The joint

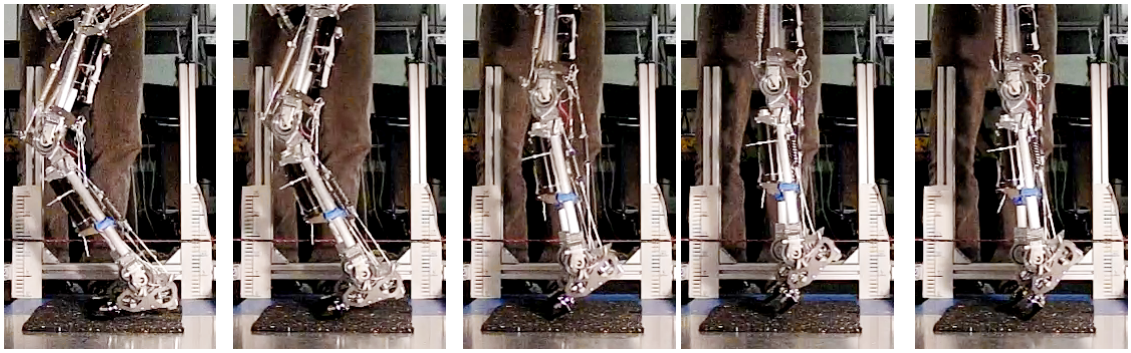

base (0.118s) pushing up (0.308s) lift-off (0.385s) in flight (0.445s) touch-down (0.465s)

Figure 2.15.: Push-off from the ground with active knee and ankle (timestamps correspond to Fig. 2.16).

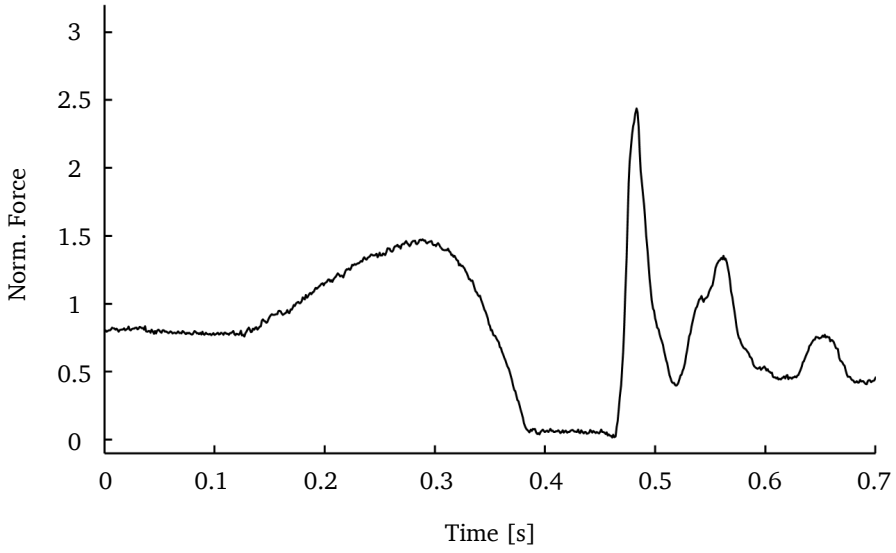

Figure 2.16.: Vertical GRF of both legs in total during the active push-off shown in Fig. 2.15. The forces were normalized to BioBiped1's body weight.

angle position sensors were not used for feedback control. Thus the joint motions were only feedforward controlled in this experiment.

In these first experiments, using this setup, continuous hopping could be generated with at least 30 hopping phases in a row. Flight phase durations as long as 200 ms and ground clearances of several centimeters could be achieved. A video of the recorded motions is provided at `http://www.youtube.com/user/biobiped`.

These preliminary results validate the robot design, as they demonstrate its ability to support high forces and impacts during the landing and to produce the required power to initiate and sustain continuous hopping motion, a requisite for the realization of running gaits. Yet, this proof of concept of BioBiped1's locomotor function marks only the starting point for our investigations.

2.7.3 Questions and Hypotheses

The questions treated in this thesis are tightly related to and based on the specific actuation design of this novel robot. BioBiped1's actuation features a new concept and raises many questions and challenges. In this chapter, we have addressed important questions to set a coherent basis for the studies performed in this thesis:

1. Which properties of the human lower limb system are the most important and thus have to be considered in the design of a robot aimed for dynamic and energy-efficient locomotion? (see Section 2.2)

2. What are the important characteristics of human locomotion? (see Section 2.3)

3. What are the main features of human motion performance that should be realized in robots? (see Section 2.4)

4. What is our definition of human-like locomotion? (see Section 2.4)

Obviously, the main questions that arise with regard to the goal of achieving dynamic and energy-efficient motions that are comparable to human locomotion performance are related to (1) the necessary degree of design complexity and (2) the required concept for motion generation and control. These questions contain several sub-questions that will be addressed in the following chapters:

1. What are the requirements for the models and the simulation environment? (see Chapter 3)

2. Which level of detail is necessary for the modeling? (see Chapter 3)

3. How can we realize dynamic motions such as running or hopping in musculoskeletal robots? (see Chapter 4)

4. How can the maximum amount of actuation requirements demanded from the motors for the target motions be determined prior to the robot's construction? (see Chapter 4)

5. What can be gained by the high number of passive tendons? (see Chapter 5)

6. Are all nine active and passive tendons required for the envisioned gaits? (see Chapter 5)

7. Which design guidelines can be derived for future prototypes? (see Chapter 5)

We hypothesize that the nonlinear musculoskeletal actuation, as realized and modeled here, has clear advantages over linear elastic joint actuation and certainly over conventional stiff joint actuation. Furthermore, dynamic coupling effects within the leg actuation that simultaneously affect more than one joint are strongly desired, in contrast to the philosophy of those research groups that focus on variable stiffness actuators. The task is to gain benefit from these passive coupling effects. Energy-efficient actuation for dynamically locomoting bipedal robots is considered as a positive side effect of a well-elaborated musculoskeletal system.

Certainly there is a wealth of further research questions from closely related areas that, however, are beyond the scope of this thesis. These questions will be suggested for future work in Chapter 6.

2.8 Reference to Own Publications

A preliminary version of Section 2.2 was published in: Proceedings of the IEEE/RSJ International Conference on Intelligent Robots and Systems 2011 [133]. A condensed version of Section 2.4 was published in: Proceedings of the Workshop on "Benchmarking of Human-like Robotic Locomotion" at the IEEE International Conference on Humanoid Robots 2013 [137].

The measurements, sensing, and control system of BioBiped1, presented in Section 2.7.1, as well as a condensed version of Section 2.7.2, were published in an adapted form in: International Journal of Humanoid Robotics [132]. The development of the robot platforms BioBiped1 and BioBiped2 is a joint effort of the BioBiped project members[1]. The work presented in Section 2.7.2 was carried out in collaboration with Christophe Maufroy, Moritz Maus, Dorian Scholz, and André Seyfarth and published in [132].

The actuation concept of BioBiped1, described in Section 2.7.1, was published in: Proceedings of the IEEE/RSJ International Conference on Intelligent Robots and Systems 2012 [131].

[1] http://www.biobiped.de/team/

3 Detailed Physical Modeling, Simulation, and Identification of the BioBiped Prototypes for Dynamic Locomotion and Impact Analysis

3.1 Motivation and Requirements

Engineering progress in the development of robots is based on suitable models and simulation environments. An ideal simulation environment allows different design ideas and control strategies to be tested efficiently without the dangers normally associated with direct development on a real physical system. In the case of the highly complex, bio-inspired musculoskeletal system of BioBiped1, introduced in the previous chapter, another motivation for using models and simulations outweighs the reason given above. Even with the same number of DoFs, the BioBiped models are characterized by a much higher parameter dimensionality than other robots, due to the novel highly elastic mechanical design that comprises several series elastic tendons spanning one or two joints. Capturing all the model properties and details directly on the hardware platform is relatively challenging and tedious. A more feasible approach is to analyze the overwhelming number of properties and reciprocal effects in simulation. With a simulation-based approach, we can define important requirements and necessary levels of details that the models and simulation environment should comply with. In turn, the tailored and customized models and the simulation environment offer several advantages:

- detailed analyses of the active and passive elastic tendons,
- design and testing of various controllers,
- investigating biomechanical hypotheses,
- application of learning algorithms,
- hardware-in-the-loop optimization of the physical robot prototype, and
- testing in general prior to a direct implementation on the robot.

In addition to these emerging opportunities, the simulated models make it possible to derive design guidelines for future prototypes, with respect to the actuation and mechanics. However, both tasks, modeling the robot system and developing the appropriate simulation environment, become even more challenging with increasing demands.

For the mentioned goals, both sufficiently detailed MBS dynamics models of the robot prototypes and an appropriate simulation environment are required. Existing tools and software are only of limited use for our needs and goals. In general, musculoskeletal systems are represented as rigid body systems and, in this way, enable the use of standard methods for efficient calculations of inverse and forward dynamics, as proposed in [28, 40, 75, 51, 120, 173, 181]. Most robotics simulators and libraries concentrate on conventionally built robotic systems with rigid links and actuators coupled directly to the joints. Some simulators also cover gearbox or drivetrain elasticity [25]. In [102], a simulator for a bipedal robot with SEAs was presented. The simulator is based on symbolic solutions of the multibody dynamics equations and switches between dynamics models for the single and double support phases. OpenSim [33] is a freely

available, extensible software system that allows users to develop models of musculoskeletal structures and create dynamic simulations of movement, also carrying out forward dynamics simulations. AnyBody [29], although it is a quite advanced modeling tool, does not allow any facilities for forward dynamic analysis. However, the design and development goals mentioned require, in particular, forward dynamics computations.

The requirements posed on the models and on the simulation environment can be derived as follows. For deriving novel design guidelines or comparing different actuators, detailed mathematical models of the actuators to be investigated are required. A complete analysis includes the detailed MBS dynamics model. For such studies, an object-oriented design would be desired, to ease the analyses and data management.

For designing and testing various controllers, the environment needs to facilitate inverse/forward dynamics and kinematics computations. Additionally, a well-developed animation functionality would also support the development and debugging processes. It should be possible, for instance, to restart the animation, highlight parts of the model, vary the animation speed, and study each single frame.

Additionally, for investigating biomechanical hypotheses, a good model of the forces interacting with the environment is required, i. e., in the case of a bipedal robot, the ground contact and sliding effects. This is very important, since efficient control strategies for manipulators and legged robots are based on sufficiently accurate and realistic contact modeling. In this regard many simulation software packages share the same deficiency. Either no, or a too simplifying, or a computationally expensive contact model is considered.

Finally, when carrying out hardware experiments, it is important to ensure that the simulation model matches the behavior of the real robot. Furthermore, the simulator should enable the study of optimization problems, such as hardware-in the loop optimizations.

The METArob[1] simulator was developed as an analysis and design tool for the development of biologically inspired compliant robot arms and bipedal systems [87]. Within this self-developed simulation environment we implemented the models of the BioBiped prototypes, which are described on two different levels: (1) rigid whole-body structure (cf. Section 3.3) and (2) actuation level (cf. Section 3.4). These two levels are consistently connected by the corresponding transmitted torques. The actuation of such robots is extremely challenging. The detailed models of the employed actuation concepts need to provide for analyses of the characteristic curves and for the identification of their roles during a motion. Finally, model-based motion control relies heavily on the quality of these models.

For the simulation of impacts and ground contact phases, it is essential to model and simulate realistic GRF with high time-resolution within a reasonable computational time. Therefore, instead of impulse-based collision handling, elastic deformation of the contact area with nonlinear material damping is used, with a finite state machine, to simulate dynamic and static friction [87]. The detailed mathematical models for the ground contact dynamics are presented in Section 3.5, respectively in Appendix A.

In addition to developing a suitable simulation environment and detailed models, it is necessary to ensure that the real hardware platforms and the simulation models behave in a similar manner. Therefore, as a final component, a parameter identification is required. The validation and calibration of the sub-models and the complete robot model are described in Section 3.7.

[1] META stands for “musculoskeletally arranged elastic tendon actuators”.

In the following, we will first give an overview of the characteristics and features of the developed simulator in which the models are embedded. Subsequently, we present the key elements of the modeling. Finally, we demonstrate that the simulation model behaves similarly to the real robot platform.

3.2 Software Structure of the METArob Simulator

Answering the questions posed in Section 2.7.3 requires a simulator that allows to convert an actuator of a robot model into another type of actuator while preserving the output properties common to both actuators. Furthermore, the simulator should enable the study of impact forces and ground contact dynamics with static and dynamic friction and of bipedal dynamic locomotion with flight phases. The METArob simulator is based on a numerical solver without model switching to enable the analysis of impact peak forces and the simulation of flight phases. This approach can result in slower simulation speed but allows to also model dynamic and static friction, which is implemented in the simulator as a finite state machine.

The main design goal of the simulator is a modular modeling of robot arms and bipedal robots with rigid links driven by various types of stiff and compliant actuators. The simulator allows to define a robot consisting of rigid serial link chains connected to a robot base. Each joint can be actuated by one or multiple actuators. The simulator natively supports actuators based on DC motors, combinations of active and passive, mono- and biarticular elastic tendons, and bidirectional SEAs, as displayed in Figure 3.1.

The simulator was implemented using the object-oriented technical computing language MATLAB. Object-oriented design is chosen in order to prevent difficult and error-prone design and management of data passed to functions. Data and operations are encapsulated in the objects. Where possible, existing toolboxes are used for standard algorithms, such as the Robotics Toolbox, which provides essential robotics algorithms for dynamics, kinematics, and path planning [26]. Basic simulations are performed using only the MATLAB language. For more complex simulations, such as ground contact with static and dynamic friction states, Simulink und SimMechanics models are used. These models are automatically generated from the robot objects and can then be further enhanced by the user.

Figure 3.2 describes a typical simulation workflow. The focus of the simulator design was placed on creating reproducible results that can be easily analyzed, post-processed, and compared with experimentally measured data. In the first simulator stage we create the model, define the kinematic and dynamic parameters, use predefined robot types based on the number of DoFs, and define the actuator types for each joint. Subsequently the trajectories are defined. The blue boxes mark optional functionalities, such as automatically generating a Simulink model based on the given definitions. It is also possible to load measurement data from experiments to use them either as input trajectories or, for instance, for the purpose of comparisons. Finally, the simulation can be started with desired settings and the results can be analyzed, post-processed, or animated. The process of comparing the data of several simulation runs with different sets of parameters is substantially supported by the object-oriented simulator design.

The object-oriented design of the actuators allows to easily interchange the actuators of an existing robot model. Given actuators can be also transformed into other types of actuators with comparable reflected parameters, allowing to easily compare various actuator designs with similar torque and velocity characteristics. For example, the hip joints of the BioBiped1 model are actuated by a b-SEA. In contrast to a common DC motor, the total transmission ratio of a

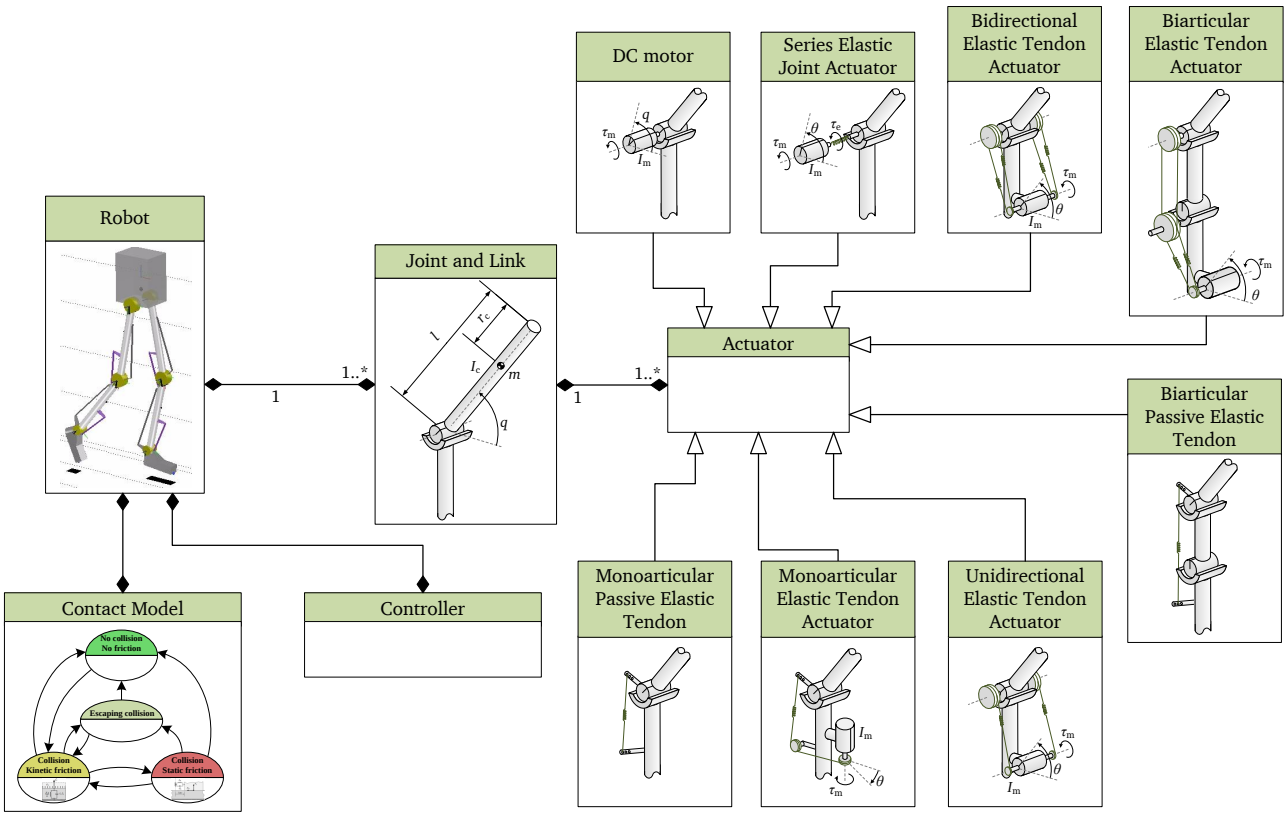

Figure 3.1.: Example for the object structure of a bipedal robot model. The model is defined by a serial chain of rigid links. For each joint, multiple actuators of different types can be defined.

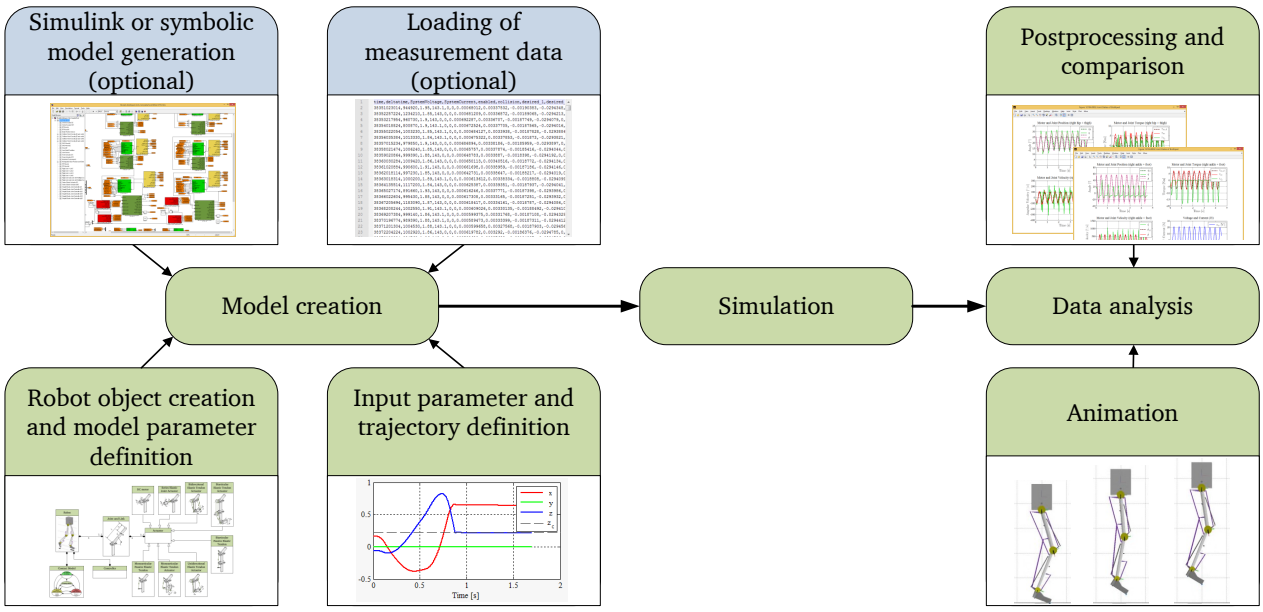

Figure 3.2.: Typical workflow of a simulation process: model creation, simulation, and analysis.

b-SEA is comprised of the gearbox ratio and of the additional transmission ratio of the pulleys. When converting a b-SEA into a normal DC motor, the total transmission ratio is preserved in order to obtain actuators with comparable reflected parameters. In the following code example, `a1` is a b-SEA extracted from the hip joint of the BioBiped1 model and converted into a common DC motor `a2`:

```
robot = RobotModels.BioBiped1();
a1 = robot.Link(1).Actuator;
a2 = Actuators.DcMotor(a1);
a1.compareWith(a2)
```

The comparison of the actuators yields the following output on the command line:

```
[Object Classes]
- a1: 'Actuators.bSEA'
- a2: 'Actuators.DcMotor'
- NOTE: class types differ!

[Common Properties of a1 and a2]
- Values of property 'ng' differ:
  + a1.ng = 23
  + a2.ng = 80

[Exclusive Properties of a1]
- a1.de = 0
- a1.ke = 60
- a1.np = 3.4783
```

which shows that the resulting DC motor has a gearbox transmission ratio `a2.ng = 80` that equals the product of the b-SEA gearbox transmission ratio `a1.ng = 23` and the b-SEA pulley transmission ratio `a1.np = 3.4783`. The b-SEA elasticity `a1.ke` and damping `a1.de` are not modeled in a DC motor and are therefore omitted.

The simulator is used for the analysis of hopping and running motions of the bipedal robot BioBiped1 and for impact and clamping safety analysis of the BioRob robot arm with elastic tendon actuators [86] (cf. Fig. 3.3). The simulator is also used for the dimensioning of the actuation parameters, such as the type of DC motors, the gearbox ratios, and the spring stiffnesses (cf. Chapter 4).

As the simulator allows to transform a given robotic system into another system with different actuators but comparable reflected parameters, it is very well suited for the systematic comparison of different actuation systems for a given robot design to study the contribution of each single actuator of a robot system with musculoskeletally arranged actuators. These studies will be presented in Chapter 5.

3.3 Modeling the Rigid Joint-Link Structure

The concept of a multibody system can be understood as an abstract collection of bodies whose relative motions are constrained by means of joints and other more complicated constraints, such as springs or pulley systems [87]. In general, it is possible to clearly identify combinations of different components that will appear more than once in a multibody system. Therefore, it is recommended to build ready combinations and, in this way, to make a complex model more manageable and understandable.

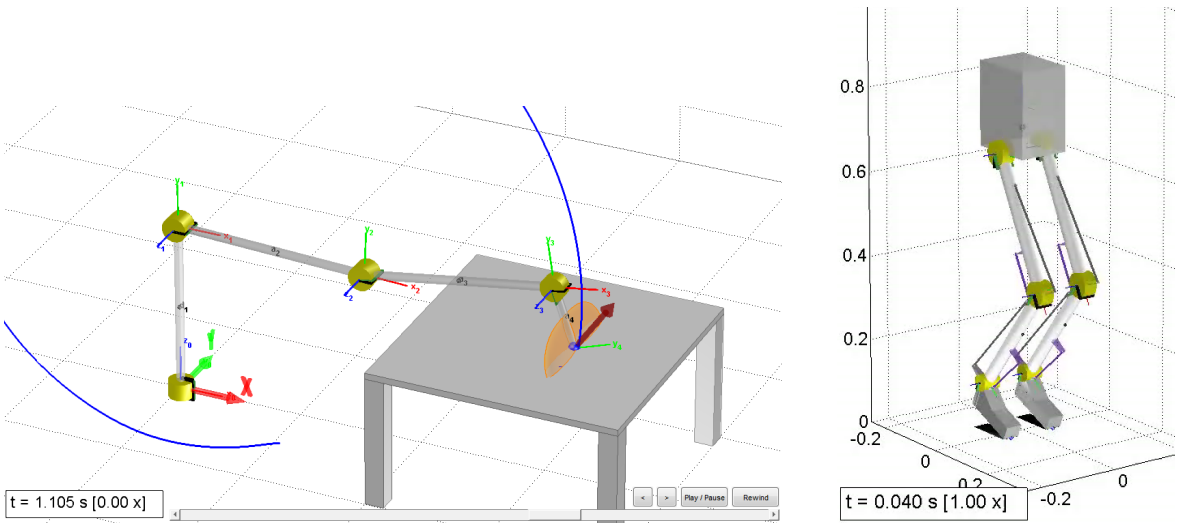

Figure 3.3.: Analysis of the impact forces of a manipulator with four DoFs driven by elastic tendon actuators [86] (left) and simulation of flight phases of a hopping bipedal robot with musculoskeletally arranged actuators (right).

Among the ready combinations are blocks for rigid joint-link structures that take either torques as input and compute the commonly required outputs (positions, velocities, accelerations) or take positions, velocities, and accelerations as inputs and compute the inverse dynamics. Such blocks can also incorporate upper and lower joint boundaries. Furthermore, the dynamics model of a robot often needs blocks for representing the base or solely a rigid link. The rigid body dynamics of BioBiped1 consists of a torso and two three-joint-link serial chains representing the legs that are attached to the torso (cf. Fig. 3.4).

For the assignment of the position and orientation of a coordinate frame within the rigid joint-link structure we apply the conventions of Denavit-Hartenberg [34] (cf. Fig. 3.4). The formalism is also used to compute the initial length of the robot to be able to initialize it correctly for a direct start from the ground. The kinematics is also used for the visualization.

The classical formulation for the equations of motion, expressed in the Lagrangian form, are as follows:

$$\boldsymbol{\tau}_{\mathrm{e,J}} + \boldsymbol{\tau}_{\mathrm{ext}} = \boldsymbol{H}(\boldsymbol{q})\,\ddot{\boldsymbol{q}} + \boldsymbol{C}(\boldsymbol{q},\dot{\boldsymbol{q}}) + \boldsymbol{g}(\boldsymbol{q}) \tag{3.1}$$

where $\boldsymbol{q} = (q_{\mathrm{Hip\_r}}, q_{\mathrm{Hip\_l}}, q_{\mathrm{Kne\_r}}, q_{\mathrm{Kne\_l}}, q_{\mathrm{Ank\_r}}, q_{\mathrm{Ank\_l}})^T \in \mathbb{R}^6$. $\boldsymbol{\tau}_{\mathrm{e,J}}$ is the generalized efforts vector, including the joint actuation torques, and $\boldsymbol{\tau}_{\mathrm{ext}}$ stands for the torques generated by the ground contact. $\boldsymbol{H}(\boldsymbol{q})$ represents the symmetric, positive-definite joint-space inertia matrix, $\boldsymbol{C}(\boldsymbol{q},\dot{\boldsymbol{q}})$ is the vector of centrifugal, gyroscopic, and Coriolis effects, and $\boldsymbol{g}(\boldsymbol{q})$ is the generalized gravity force vector. The generated SimMechanics model uses an ordinary differential equation (ODE) solver of Simulink to solve these equations of motion.

3.4 Modeling the Actuation

One of the core contributions of this chapter is modeling the challenging second level of the robot description: the actuation dynamics [131]. As elaborated in Chapter 2, we do not target at the development of novel actuators but at the most beneficial setup of geared electrical DC

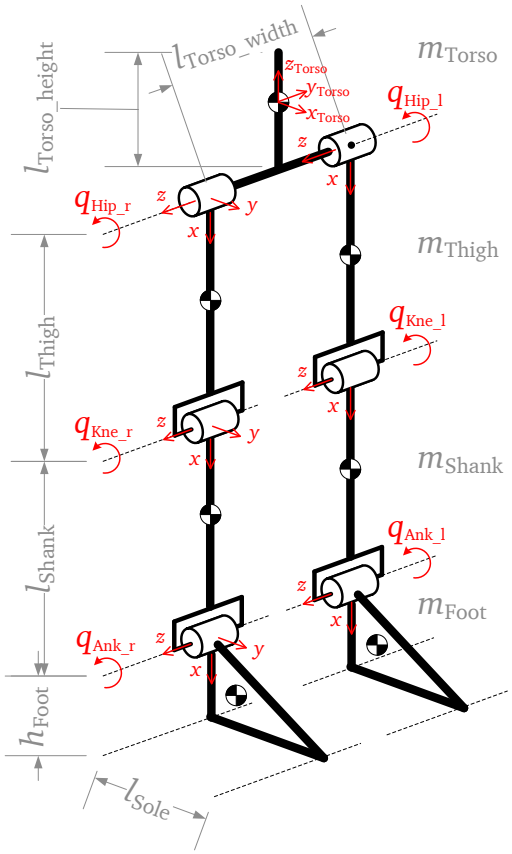

Link Lengths	
$l_{\text{Torso\_height}}$	269 mm
$l_{\text{Torso\_width}}$	120 mm
l_{Thigh}	330 mm
l_{Shank}	330 mm
l_{Foot}	122 mm
h_{Foot}	67 mm
l_{Sole}	165 mm

Link Masses	
m_{Torso}	5.332 kg
m_{Thigh}	0.843 kg
m_{Shank}	0.804 kg
m_{Foot}	0.342 kg

Figure 3.4.: Main kinematics and dynamics data of BioBiped1's rigid skeleton.

motors, tendons, and extension springs resulting in the nine active and passive, human-like muscle-tendon complexes that are integrated in BioBiped1's legs. The actuation concepts can be divided into bidirectional and unidirectional actuation. Further, we differentiate between mono- and biarticular tendons. In total, the legs are actuated by four different actuator types: (1) monoarticular, b-SEA, (2) monoarticular, u-SEA, (3) monoarticular, passive tendon, and (4) biarticular, passive tendon.

Before we proceed with modeling these different elastic transmissions, we first elaborate on the model of a permanent-magnet DC motor with planetary gearbox, which is a common component of the monoarticular b-SEA and u-SEA.

3.4.1 Preliminaries

Electrical and mechanical motor dynamics

To enable the examination of motor currents and voltages, the electrical motor dynamics is modeled as

$$u = u_{\text{R}} + u_{\text{L}} + u_{\text{ind}}$$

$$\text{where} \quad u_{\text{R}} = R_{\text{a}}\, i = \frac{R_{\text{a}}}{k_{\text{t}}}\, \tau_{\text{m}}\,, \quad u_{\text{L}} = L_{\text{a}}\, \frac{di}{dt} = \frac{L_{\text{a}}}{k_{\text{t}}}\, \frac{d\tau_{\text{m}}}{dt}\,, \quad u_{\text{ind}} = k_{\text{v}}\, \dot{\theta}\,.$$

with input voltage u, armature resistance R_a, armature inductance L_a, torque constant k_t, speed constant/back-emf k_v, and generated motor torque τ_m, which drives the rotor. $\dot{\theta}$ denotes the current motor angular velocity. Neglecting the effect of armature inductance, we can simplify the equation for the inverse electrical motor dynamics to

$$u = \frac{R_a}{k_t}\,\tau_m + k_v\,\dot{\theta} \tag{3.2}$$

This equation permits the required voltages u for given motor torques τ_m to be computed.

The mechanical motor dynamics for the computation of τ_m is composed of a frictional term τ_f, an inertial term τ_i, and the torque induced by the elastic transmission in the case of an elastic actuator $\tau_{e,M}$:

$$\tau_m = \tau_f + \tau_i + \tau_{e,M} \tag{3.3}$$

The notation $\tau_{e,M}$ with the subscripts $_{e,M}$ has been chosen to indicate an elastic torque induced on the motor. For an elastic torque induced by the transmission on the joint side, we introduce the notation $\tau_{e,J}$. The friction torque τ_f includes only viscous friction. Coulomb friction is not incorporated, as it can be ignored for fast dynamic motions which conform to the envisioned motions with the BioBiped models. Here follows the formula for τ_f:

$$\tau_f = d_{vg}\,\dot{\theta} \qquad \text{with } d_{vg} \cong d_r + d_g\,. \tag{3.4}$$

d_r and d_g stand for the rotor and gearbox damping, respectively. The inertia torque τ_i is determined as follows:

$$\tau_i = (I_r + I_g)\,\ddot{\theta}\,, \tag{3.5}$$

where I_r and I_g stand for the rotor and gearbox inertia, respectively. $\ddot{\theta}$ represents the motor acceleration. Now we can write the complete formula for τ_m:

$$\tau_m = (I_r + I_g)\,\ddot{\theta} + d_{vg}\,\dot{\theta} + \tau_{e,M} \tag{3.6}$$

Substituting (3.6) in (3.2) we obtain:

$$u = \frac{R_a}{k_t}\left((I_r + I_g)\,\ddot{\theta} + d_{vg}\,\dot{\theta} + \tau_{e,M}\right) + k_v\,\dot{\theta} \tag{3.7}$$

The scheme of the complete motor model is depicted in Fig. 3.5.

Reflected variables

So far, we have neglected the transmission ratio between motor and joint side. The total transmission ratio z consists of the motor gear ratio, n_g, and an additional transmission ratio caused by the elastic coupling of gearbox and joint, n_p:

$$z = n_g\,n_p\,. \tag{3.8}$$

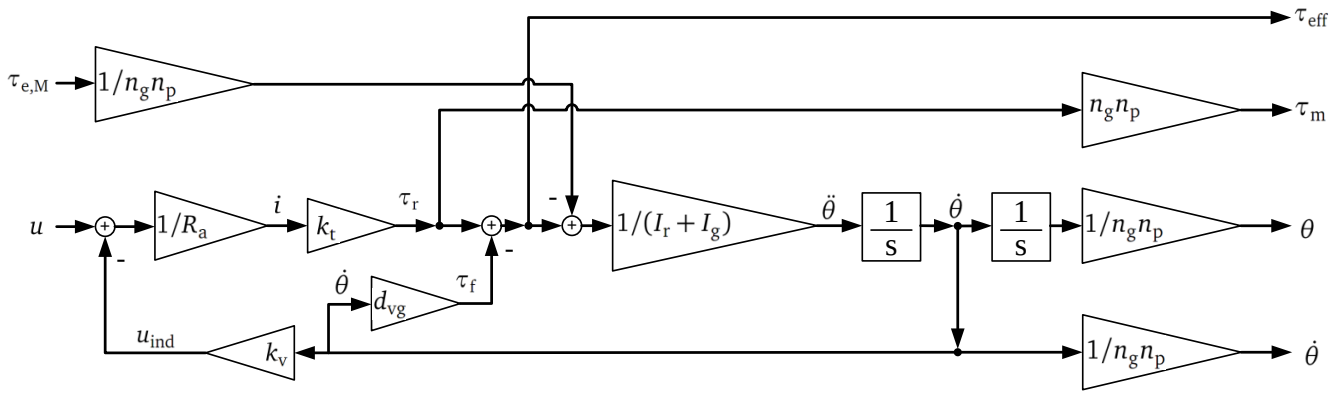

Figure 3.5.: Scheme of the electrical and mechanical motor dynamics of a permanent-magnet DC motor.

In the case that there is no further elastic coupling after the gearbox, the value of n_p is set to 1. Furthermore, it should be noted that the transmission ratio can be either constant or a highly nonlinear function depending on the motor and joint position.

The power conservation holds for an idealized gearbox:

$$\dot{\theta}^* \tau_m^* = \dot{\theta} \tau_m , \tag{3.9}$$

i. e., the product of *reflected* motor velocities and torques, indicated by the asterisk, must be equal to the product of the nonreflected motor velocities and torques. Solving 3.9 for τ_m^* results in the following formulation for the reflected torques:

$$\tau_m^* = \frac{\dot{\theta}}{\dot{\theta}^*} \tau_m \tag{3.10}$$

$$= z \tau_m . \tag{3.11}$$

To account for the losses generated in the gearbox we had previously introduced the gearbox friction in 3.4. The friction torques will be also reflected to the joint side:

$$\tau_f = (d_r + d_g) \dot{\theta} \tag{3.12}$$

$$\frac{\tau_f^*}{z} = d_{vg} z \dot{\theta}^* \tag{3.13}$$

$$\tau_f^* = z^2 d_{vg} \dot{\theta}^* \tag{3.14}$$

These computations are repeated to also reflect the torques of inertia to the joint side:

$$\tau_i = (I_r + I_g) \ddot{\theta} \tag{3.15}$$

$$\frac{\tau_i^*}{z} = (I_r + I_g) z \ddot{\theta}^* \tag{3.16}$$

$$\tau_i^* = z^2 (I_r + I_g) \ddot{\theta}^* \tag{3.17}$$

Thus, both inertia and friction are increased by factor z^2 when reflected to the joint side. To summarize, all motor variables and parameters are rewritten with respect to the joint side, as reflected variables:

$$\dot{\theta}^* = \frac{1}{z}\dot{\theta} \qquad \text{with} \quad z = n_g\, n_p \quad \text{and} \quad |z| > 1 \tag{3.18}$$

$$\tau_m^* = z\,\tau_m \tag{3.19}$$

$$I_r^* = z^2\,(I_r + I_g) \tag{3.20}$$

$$d_{vg}^* = z^2\,(d_r + d_g) \tag{3.21}$$

For the sake of simplicity, in the remainder of this thesis, reflected variables are not asterisked.

With these elementary models we can now proceed with modeling the different actuators deployed in BioBiped1's legs. For the sake of comparability to and evaluation of the elastic actuation, described in Section 3.4.3ff., we will also use stiff actuators. For simplicity, we start off with this most basic model.

3.4.2 Stiff Actuator

In the case of a stiff actuator, the motor-gear unit and the joint are directly coupled. The model equations given above still apply; however, numerical problems might occur, because the reflected motor and joint position, as well as the reflected motor torque and joint torque, are almost equal: $\theta \cong q$ and $\tau_{e,M} \cong \tau_{e,J}$. Note that the notation $\tau_{e,M}$ refers here to stiff joint dynamics. Therefore, we will use a slightly different scheme, shown in Fig. 3.6.

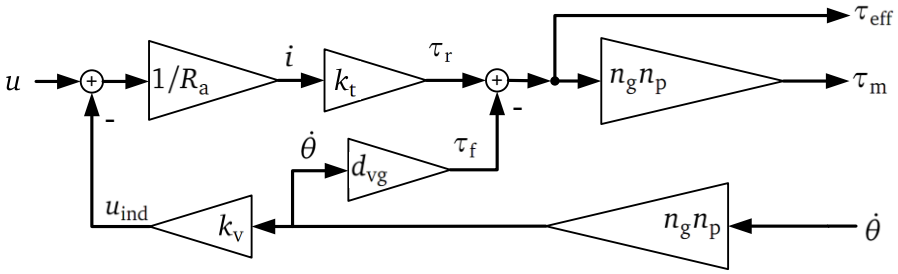

Figure 3.6.: Scheme of the electrical and mechanical motor dynamics of a permanent-magnet DC motor for a stiff actuator.

Instead of the required motor position, as displayed in Fig. 3.5, here the necessary motor torque is computed based on the incoming joint velocity, which is equal to the reflected motor velocity. Therefore, friction torques are directly included. Due to the stiff coupling between motor and joint, the reflected inertias of the motor and gear can be added on top of the link inertias of the rigid joint-link structure, in this way, eliminating the inertial term in (3.3):

$$\tau_m = \tau_f + \tau_{e,J} \tag{3.22}$$

The term $(I_r + I_g)\,\ddot{\theta}$ is now included in the inertia matrix of (3.1). Note also that due to the stiff coupling the value of n_p is set to 1. The resulting equation for u can be written as:

$$u = \frac{R_a}{k_t}\,(d_{vg}\,\dot{\theta} + \tau_{e,J}) + k_v\,\dot{\theta} \tag{3.23}$$

3.4.3 Monoarticular, Bidirectional Series Elastic Actuator

From the utilized compliant actuators, the b-SEA represents the simplest actuation concept, as it describes a linear transmission relation. It is solely used in the hip joint for rotations along the pitch axis. The elastic transmission decouples motor and rigid joint-link structure into two mechanically independent systems. The actuation principle, as implemented in the hip joint (cf. Fig. 3.7a), can be approximated by the actuation concept depicted in the drawing of Fig. 3.7b, where the motor-gearbox is antagonistically coupled to the joint by two identical tendons with built-in extension springs.

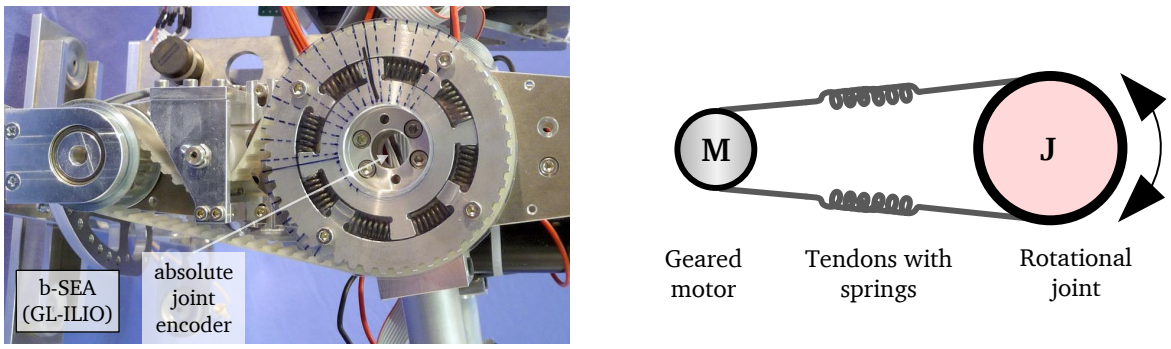

Figure 3.7.: Construction (a) and drawing (b) of the bidirectional series elastic actuator (b-SEA) used for the hip actuation.

For tendon and spring we define a combined stiffness and damping parameter, k_e and d_e. Assuming a small mass of the tendon and spring, their kinetic energy can be neglected, compared to the kinetic energy of the other mechanical robot parts. The torque transmitted to the joint through the elastic spring of constant torsional stiffness k_e and damping d_e is:

$$\tau_{\mathrm{e,J}} = k_\mathrm{e}\,(\theta - q) + d_\mathrm{e}\,(\dot{\theta} - \dot{q}) \tag{3.24}$$

with q and θ denoting the measured joint and motor position. Note that the same torque is also exerted on the motor for this special case of transmission: $\tau_{\mathrm{e,M}} = \tau_{\mathrm{e,J}}$ holds for reflected variables. The scheme of this actuation concept is depicted in Fig. 3.8. Due to the choice of fixed lever arms, both n_p and k_e are treated as parameters with constant values. Note also that the motor controls the equilibrium position of the transmission.

3.4.4 Monoarticular, Unidirectional Series Elastic Actuator

Removing one of the tendons of the b-SEA in Fig. 3.7b results in a solely unidirectional actuation of the coupled joint. Both knee and ankle extension occur by a u-SEA with dynamically varying lever arms, just like the human counterpart. The torsional joint stiffness can be formulated as a nonlinear function depending on the motor and joint angle.

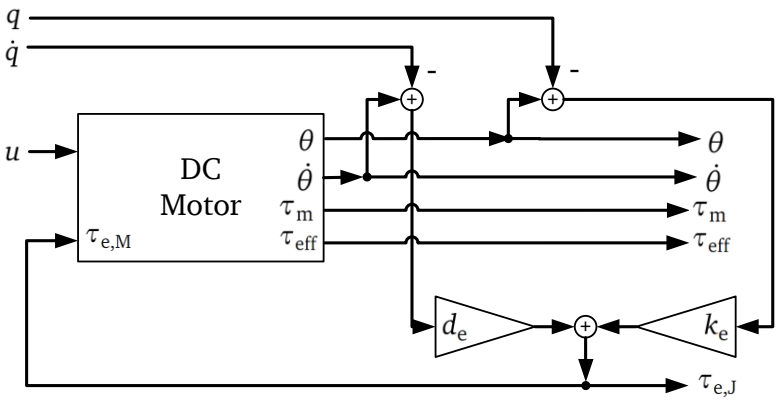

Figure 3.8.: Scheme of the transmission dynamics of a b-SEA including the complete motor dynamics as displayed in Fig. 3.5.

Knee Transmission

A schematic drawing of the unidirectional series elastic actuation concept is shown exemplary in Fig. 3.9c for the knee joint. In contrast to the b-SEA, here we have a strong nonlinear coupling of the joint to the motor. The elastic transmission creates different torques on the joint and motor. Transmission ratio, lever arm, and output stiffness nonlinearly change during joint movement. For the formulation of the equations we locate coordinate reference frames on the thigh segment at the height of the pulley, around which the tendon is wound by the motor, and directly in the knee joint, S_H and S_K. We make the assumption that the origin of the frames, tendon, and attachment points span exactly one plane such that the third dimension of each vector $\in \mathbf{R}^3$ in the following equations can be set to zero.

A number of points were assigned to the actuation mechanism illustrated in Fig. 3.9c. Their definitions are provided as follows. P_{KAJ} defines the chosen moving fixation point at which the tendon is attached on the joint side, whereas P_{KAM} represents the starting point of the tendon directly at the pulley. The selected subscripts $_{\mathrm{KAM}}$ and $_{\mathrm{KAJ}}$ are acronyms for "K(nee) A(ctive) M(otor)" and "K(nee) A(ctive) J(oint)". The distance vectors of these points from the corresponding coordinate frames are denoted as ${}^{H}\boldsymbol{p}_{\mathrm{KAM}}$ and ${}^{K}\boldsymbol{p}_{\mathrm{KAJ}}$. For rotations from S_H into the joint system S_K we use the following elementary rotation matrix around the z-axis about the angle q:

$$ {}^{H}\boldsymbol{R}_K(q) = \mathrm{Rot}_z(q) = \begin{pmatrix} \cos q & -\sin q & 0 \\ \sin q & \cos q & 0 \\ 0 & 0 & 1 \end{pmatrix}. \tag{3.25} $$

For translations from the origin of S_H to the origin of S_K we use the vector:

$$ {}^{H}\boldsymbol{r}_K = \begin{pmatrix} 0 \\ -d_{\mathrm{KM2J}} \\ 0 \end{pmatrix}, \tag{3.26} $$

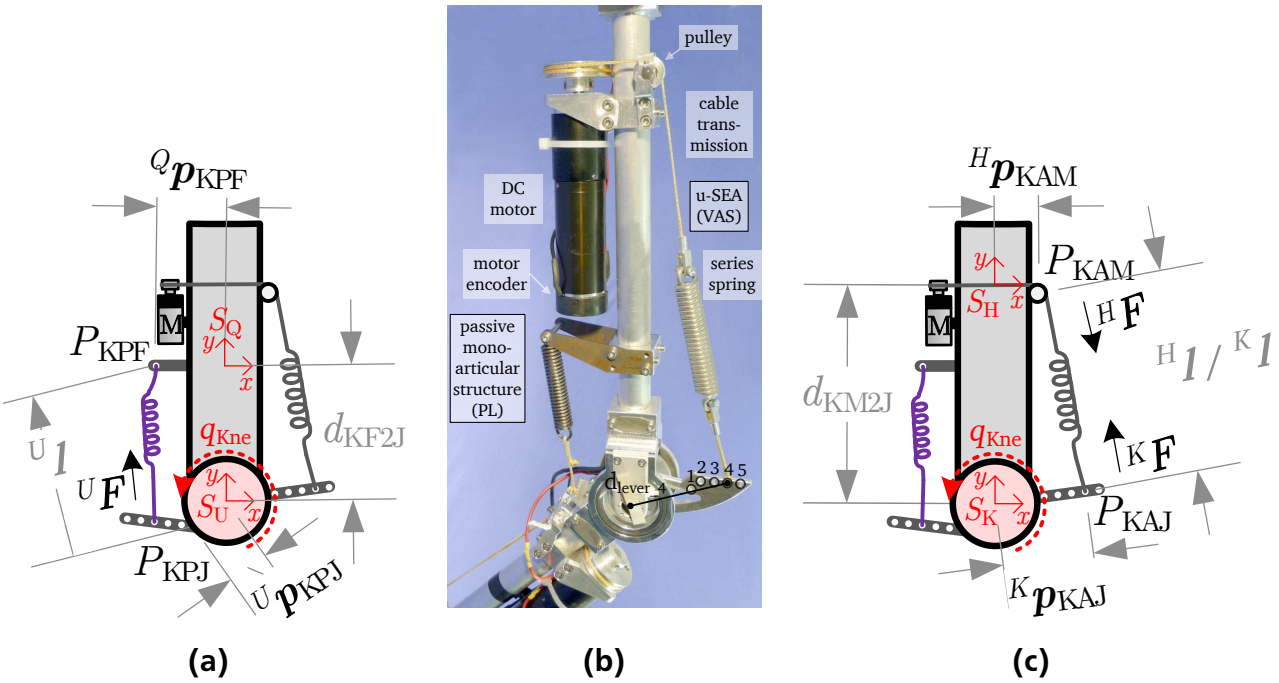

Figure 3.9.: Knee actuation: (b) construction; (a) schematic drawing of the PL tendon for the joint flexion; (c) drawing of the active counterpart VAS for the extension. The distance of the five attachment points from the knee joint vary between 36.4 for the nearest and 66.5 mm for the farthest fixation point (cf. close-up in Fig. 2.12a).

where d_{KM2J} stands for the distance between the origins of the S_H and S_K frame. As ${}^{H}\boldsymbol{R}_{K}$ is an orthogonal matrix, the reverse relations are defined as follows:

$$ {}^{K}\boldsymbol{R}_{H}(q) = ({}^{H}\boldsymbol{R}_{K}(q))^{T} \tag{3.27} $$

$$ {}^{K}\boldsymbol{r}_{H}(q) = -({}^{H}\boldsymbol{R}_{K}(q))^{T}\,{}^{H}\boldsymbol{r}_{K} \tag{3.28} $$

Both rotation and translation can be combined to one transformation matrix. For transformations from S_H to S_K we can write the following matrix:

$$ {}^{H}\boldsymbol{T}_{K}(q) = \begin{pmatrix} {}^{H}\boldsymbol{R}_{K}(q) & {}^{H}\boldsymbol{r}_{K} \\ 0 & 1 \end{pmatrix} \tag{3.29} $$

We apply the method of virtual work and displacement to compute the motor and joint torques. For this purpose, we first calculate the extension of the built-in spring. The elongation depends on the amount of tendon wrapped on the gearbox shaft and on the joint state. At the rest angle q_0 the tendon is at rest. Neglecting the deformation of the tendon, we can formulate any change in the spring as follows:

$$ \Delta l(q,\theta) = \left\| {}^{K}\boldsymbol{l}(q) \right\| - \left\| {}^{K}\boldsymbol{l}(q_0) \right\| + \theta\, r_{\mathrm{M}} \tag{3.30} $$

with r_{M} denoting the radius of the gearhead output shaft. ${}^{K}\boldsymbol{l}$ is the length vector of the tendon in the S_K system:

$$ {}^{K}\boldsymbol{l}(q) = {}^{K}\boldsymbol{p}_{\mathrm{KAM}}(q) - {}^{K}\boldsymbol{p}_{\mathrm{KAJ}} \tag{3.31} $$

For further computations, we also need the length vector of the tendon defined in the S_H system:

$$ {}^{H}\boldsymbol{l}(q) = {}^{H}\boldsymbol{p}_{\mathrm{KAJ}}(q) - {}^{H}\boldsymbol{p}_{\mathrm{KAM}} \tag{3.32} $$

Note that it does not make any difference whether to compute Δl as formulated in (3.30) or as described with vectors expressed in the S_H frame:

$$ \Delta l(q,\theta) = \left\| {}^{H}\boldsymbol{l}(q) \right\| - \left\| {}^{H}\boldsymbol{l}(q_0) \right\| + \theta\, r_{\mathrm{M}}\,, \tag{3.33} $$

The vectors ${}^{K}\boldsymbol{p}_{\mathrm{KAM}}$ and ${}^{H}\boldsymbol{p}_{\mathrm{KAJ}}$ can be computed as follows:

$$ {}^{K}\boldsymbol{p}_{\mathrm{KAM}}(q) = {}^{K}\boldsymbol{r}_{H}(q) + {}^{K}\boldsymbol{R}_{H}(q)\,{}^{H}\boldsymbol{p}_{\mathrm{KAM}} \tag{3.34} $$

$$ \begin{aligned} {}^{H}\boldsymbol{p}_{\mathrm{KAJ}}(q) &= {}^{H}\boldsymbol{T}_{K}(q) \begin{pmatrix} {}^{K}\boldsymbol{p}_{\mathrm{KAJ}} \\ 1 \end{pmatrix} \\ &= {}^{H}\boldsymbol{r}_{K} + {}^{H}\boldsymbol{R}_{K}(q)\,{}^{K}\boldsymbol{p}_{\mathrm{KAJ}} \end{aligned} \tag{3.35} $$

At $q = q_0$ and $\theta = 0$ tendon forces ${}^{K}\boldsymbol{F}$ are equal to zero. Slacking of the tendon is not modeled. If the change in tendon length is zero or less than zero, i. e., $\Delta l(q,\theta) \leq 0$, forces are set to 0. Only spring extensions are considered to determine the occurring forces:

$$ {}^{K}\boldsymbol{F}(q,\theta) = \begin{cases} k_{\mathrm{e}}\, \Delta l(q,\theta) \frac{{}^{K}\boldsymbol{l}(q)}{\left\| {}^{K}\boldsymbol{l}(q) \right\|} & \text{for } \Delta l(q,\theta) > 0 \\ 0 & \text{for } \Delta l(q,\theta) \leq 0 \end{cases} \tag{3.36} $$

k_{e} is the constant stiffness of the extension spring. The torque exerted on the joint by the spring elongation can now be defined as the following cross and dot product:

$$ \begin{aligned} {}^{K}\boldsymbol{\tau}(q,\theta) &= {}^{K}\boldsymbol{p}_{\mathrm{KAJ}} \times {}^{K}\boldsymbol{F}(q,\theta) \\ &= \boldsymbol{p}_{\mathrm{lever}}(q) \times {}^{K}\boldsymbol{F}(q,\theta) \end{aligned} \tag{3.37} $$

$$ \tau_{\mathrm{e,J}}(q,\theta) = {}^{K}\boldsymbol{\tau}(q,\theta) \bullet e_Z \tag{3.38} $$

where $\boldsymbol{p}_{\mathrm{lever}}$ is the vector for the lever arm of the tendon in the S_K frame. For clarity, we refer to $\tau_{\mathrm{e,J}}$ as τ_{VAS}. Depending on the overall implemented tendons in the leg, the torque τ_{VAS} is only one component of the joint torque $\tau_{\mathrm{e,J}}$. The complete output function for each joint will be discussed separately in Section 3.4.7. The direction of the joint rotation depends on the motor and joint state, in addition to gravitational and antagonistic forces: Whether the joint moves in positive or negative direction is influenced by all external forces acting on the knee joint. These can be either gravitational forces or passive forces introduced by the passive, monoarticular and biarticular tendons.

The nonlinearly changing lever arm d_{lever} only depends on q:

$$ d_{\mathrm{lever}}(q) = \left\| \boldsymbol{p}_{\mathrm{lever}}(q) \right\| \tag{3.39} $$

$$ \text{with} \quad \boldsymbol{p}_{\mathrm{lever}}(q) = {}^{K}\boldsymbol{p}_{\mathrm{KAJ}} - \frac{{}^{K}\boldsymbol{p}_{\mathrm{KAJ}} \bullet {}^{K}\boldsymbol{l}(q)}{\left\| {}^{K}\boldsymbol{l}(q) \right\|^2}\, {}^{K}\boldsymbol{l}(q) \tag{3.40} $$

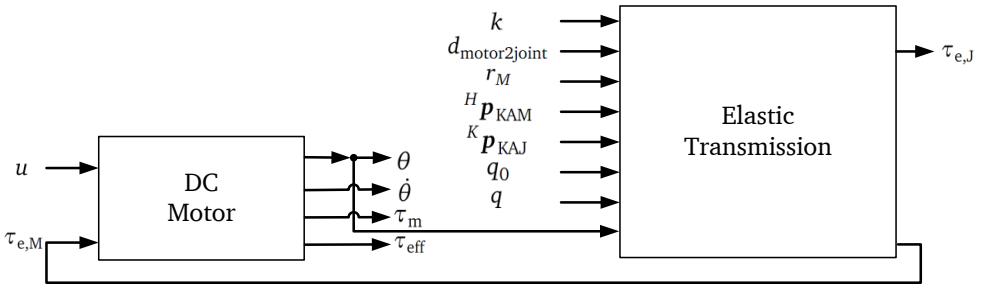

Figure 3.10.: Scheme of the transmission dynamics of the u-SEA VAS for the active knee extension.

The computation of the motor torques caused by the spring elongation follows almost the same procedure as for the joint torques. We first need to determine the tendon forces in the S_H frame, as performed in (3.36):

$$ {}^H\boldsymbol{F}(q,\theta) = \begin{cases} k_{\text{e}}\,\Delta l(q,\theta)\frac{{}^H\boldsymbol{l}(q)}{\|{}^H\boldsymbol{l}(q)\|} & \text{for } \Delta l(q,\theta) > 0 \\ 0 & \text{for } \Delta l(q,\theta) \leq 0 \end{cases} \tag{3.41} $$

substituting Δl by (3.30) and ${}^H\boldsymbol{l}$ by (3.32). An important difference, however, is that, in contrast to the moving attachment point P_{KAJ}, the point P_{KAM} is fixed. Thus, the cross product can be simplified to:

$$ \tau_{\text{e,M}}(q,\theta) = -r_{\text{M}} \left\| {}^H\boldsymbol{F}(q,\theta) \right\| \tag{3.42} $$

Due to the nonlinear transmission from the gearbox to the joint, in contrast to a b-SEA, joint and motor are affected by different torques: $\tau_{\text{e,J}} \neq \tau_{\text{e,M}}$. During spring extension, negative forces occur in the S_H frame. This, in turn, means that negative torques act on the motor. During usual motor operation, when the motor is pulling the tendon, these negative torques oppose the positively directed motor torques. Thus, the motor needs to do extra work to compensate for the negative tendon torques.

Although k_{e} has a fixed constant stiffness, the resulting *total transmission stiffness* changes with n_{p}, which changes nonlinearly depending on the motor and joint angle. The value changes of n_{p} also affect the acting torques and, in this way, the sensed transmission stiffness despite the fixed mechanical stiffness.

A scheme of the inputs and outputs of the u-SEA for the knee joint is shown in Fig. 3.10.

Ankle Transmission

The above procedure and equations given from (3.25) to (3.42) are also applicable to the u-SEA in the ankle joint to compute the lever arms, motor torques, and joint torques τ_{SOL}. Depending on the leg configuration, several tendons can be acting on the same joint and, in this way, contributing to the overall joint dynamics. Therefore, to avoid confusion, we assign different letters and names to the frames and points marked in Fig. 3.11. However, the positive and negative rotation directions are always identical. The definitions of the points assigned to the

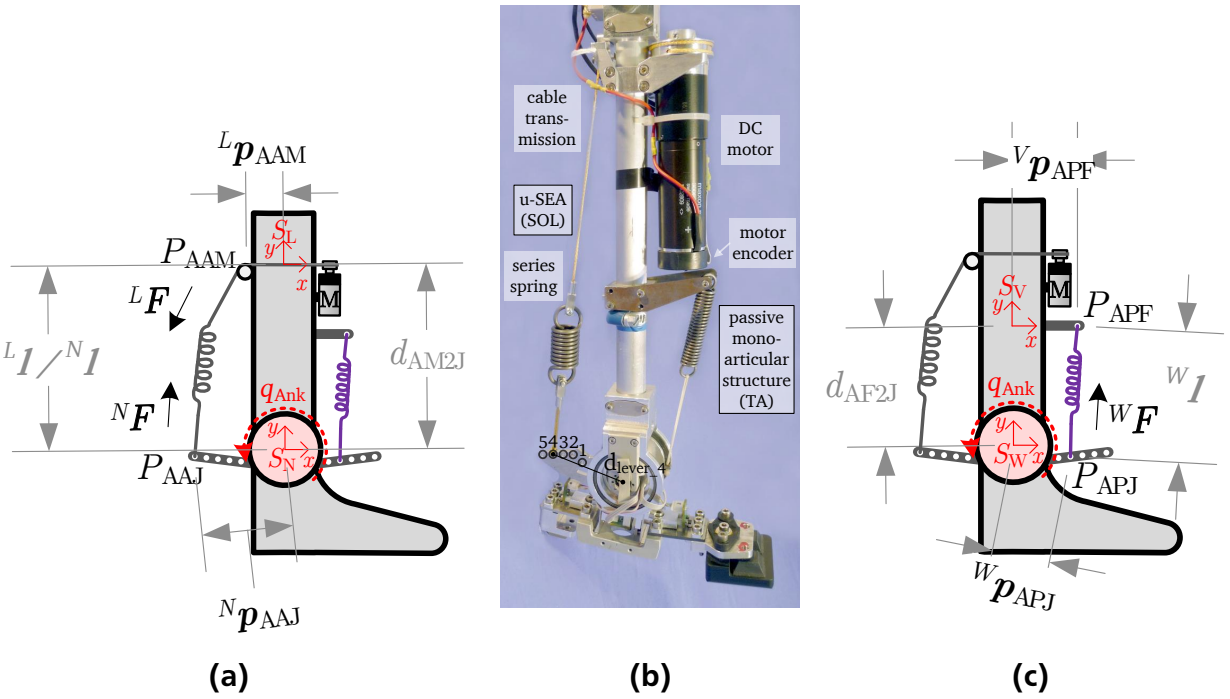

Figure 3.11.: Ankle actuation: (b) construction; (a) schematic drawing of the SOL tendon for the joint extension; (c) drawing of the TA tendon. The attachment points 1–5 on the joint side vary between distances of 36.4 for the nearest and 66.5 mm for the farthest fixation point, cf. close-up in Fig. 2.12b.

actuation mechanism are provided in Table 3.1. The introduced reference frames S_L and S_N are located on the shank segment at the height of the pulley and directly in the ankle joint, respectively. Similar to (3.30), we first compute the changes in the spring:

$$\Delta l(q,\theta) = \left\| {}^N\boldsymbol{l}(q) \right\| - \left\| {}^N\boldsymbol{l}(q_0) \right\| - \theta\, r_\mathrm{M} \tag{3.43}$$

with θ denoting the motor position and r_M the radius of the gearhead output shaft. The exact definition of ${}^N\boldsymbol{l}$ and other necessary equations for its computation are provided in Table 3.1. Subsequently, we can determine the tendon forces caused by the spring extension:

$${}^N\boldsymbol{F}(q,\theta) = \begin{cases} k_\mathrm{e}\, \Delta l(q,\theta)\, \dfrac{{}^N\boldsymbol{l}(q)}{\left\| {}^N\boldsymbol{l}(q) \right\|} & \text{for } \Delta l(q,\theta) > 0 \\ 0 & \text{for } \Delta l(q,\theta) \leq 0 \end{cases} \tag{3.44}$$

and the torques exerted on the ankle joint:

$$\begin{aligned} {}^N\boldsymbol{\tau}(q,\theta) &= {}^N\boldsymbol{p}_\mathrm{AAJ} \times {}^N\boldsymbol{F}(q,\theta) \\ &= \boldsymbol{p}_\mathrm{lever}(q) \times {}^N\boldsymbol{F}(q,\theta) \end{aligned} \tag{3.45}$$

$$\tau_\mathrm{e,J}(q,\theta) = {}^N\boldsymbol{\tau}(q,\theta) \bullet e_Z \tag{3.46}$$

$\boldsymbol{p}_\mathrm{lever}$ is the vector for the lever arm of the tendon in the S_N frame and is computed as follows:

$$\boldsymbol{p}_\mathrm{lever}(q) = {}^N\boldsymbol{p}_\mathrm{AAJ} - \frac{{}^N\boldsymbol{p}_\mathrm{AAJ} \bullet {}^N\boldsymbol{l}(q)}{{}^N\boldsymbol{l}(q) \bullet {}^N\boldsymbol{l}(q)} \cdot {}^N\boldsymbol{l}(q) \tag{3.47}$$

Table 3.1.: Definitions for the dynamics modeling of the u-SEA SOL.

P_{AAM}	Starting point of the tendon at the pulley; $_{\text{AAM}}$ stands for "A(nkle) A(ctive) M(otor)"
P_{AAJ}	Fixation point of the tendon on the joint side; $_{\text{AAJ}}$ stands for "A(nkle) A(ctive) J(oint)"
${}^{L}\boldsymbol{p}_{\text{AAM}}$	Constant distance vector of the fixed point P_{AAM} from the origin of S_L
${}^{N}\boldsymbol{p}_{\text{AAJ}}$	Constant distance vector of the moving fixation point P_{AAJ} from the origin of S_N
${}^{L}\boldsymbol{R}_{N}(q)$	$= \text{Rot}_z(q)$, cf. (3.25)
${}^{L}\boldsymbol{r}_{N}$	$= \begin{pmatrix} 0 & -d_{\text{AM2J}} & 0 \end{pmatrix}^T$, translation vector from the origin of S_L to the origin of S_N
${}^{N}\boldsymbol{R}_{L}(q)$	$= ({}^{L}\boldsymbol{R}_{N}(q))^T$
${}^{N}\boldsymbol{r}_{L}(q)$	$= -({}^{L}\boldsymbol{R}_{N}(q))^T \, {}^{L}\boldsymbol{r}_{N}$
${}^{L}\boldsymbol{p}_{\text{AAJ}}(q)$	$= {}^{L}\boldsymbol{r}_{N} + {}^{L}\boldsymbol{R}_{N}(q) \, {}^{N}\boldsymbol{p}_{\text{AAJ}}$
${}^{N}\boldsymbol{p}_{\text{AAM}}(q)$	$= {}^{N}\boldsymbol{r}_{L}(q) + {}^{N}\boldsymbol{R}_{L}(q) \, {}^{L}\boldsymbol{p}_{\text{AAM}}$
${}^{L}\boldsymbol{l}(q)$	$= {}^{L}\boldsymbol{p}_{\text{AAJ}}(q) - {}^{L}\boldsymbol{p}_{\text{AAM}}$, length vector of the tendon in S_L
${}^{N}\boldsymbol{l}(q)$	$= {}^{N}\boldsymbol{p}_{\text{AAM}}(q) - {}^{N}\boldsymbol{p}_{\text{AAJ}}$, length vector of the tendon in S_N

The Euclidean norm is applied, as in (3.39), to determine the length of the lever arm. In the remainder of this thesis, the ankle joint torque $\tau_{\text{e,J}}$ caused by the SOL tendon is referred to as τ_{SOL}.

The computation of the motor torques caused by the spring elongation follows the same scheme as presented in (3.41)–(3.42). First, the tendon forces in the S_L frame are calculated:

$$ {}^{L}\boldsymbol{F}(q,\theta) = \begin{cases} k_{\text{e}} \, \Delta l(q,\theta) \, \frac{{}^{L}\boldsymbol{l}(q)}{\left\| {}^{L}\boldsymbol{l}(q) \right\|} & \text{for } \Delta l(q,\theta) > 0 \\ 0 & \text{for } \Delta l(q,\theta) \leq 0 \end{cases} \tag{3.48} $$

and then the motor torques:

$$ \tau_{\text{e,M}}(q,\theta) = r_{\text{M}} \left\| {}^{L}\boldsymbol{F}(q,\theta) \right\| \tag{3.49} $$

Based on the defined axes of S_L the SOL torques on the motor are positively directed towards the spring rest length, whereas the SOL torques on the joint, τ_{SOL}, are negatively directed.

The scheme of inputs and outputs, as implemented in Matlab Simulink, is similar to that of the u-SEA VAS in the knee joint which is illustrated in Fig. 3.10.

3.4.5 Monoarticular, Passive Tendon

The equations for a monoarticular, passive tendon can be set up in a similar way. The main difference between a monoarticular, passive and active tendon is that, in the case of a passive

tendon, the spring elongation solely depends on the coupled joint angle. Both in the knee and ankle joint, passive tendons generate torques that are opposed to those caused by the u-SEAs, depending on the defined rest lengths of the tendons and the current joint configurations.

Passive Knee Flexion

For the description of the passive knee flexion, we assign two frames on the thigh, one at the height of the tendon fixation on the link, S_Q, and the other directly in the joint, S_U. For brevity, the important points marked in Fig. 3.9a are listed together with their definitions in Table 3.2. As soon as the VAS tendon is extended, or, more specifically, as soon as the knee joint is moved away from the rest length angle q_0 of the PL tendon in the positive rotation direction, PL starts inducing a negative torque on the knee at a specific time instant. The exact time instant depends on the set rest length angle. As mentioned before, the spring elongation only depends on the coupled joint angle q. Therefore, the motor term in (3.30) and (3.43) can be eliminated:

$$\Delta l(q) = \left\| {}^U\boldsymbol{l}(q) \right\| - \left\| {}^U\boldsymbol{l}(q_0) \right\| \tag{3.50}$$

${}^U\boldsymbol{l}$ denotes the tendon length vector in the S_U frame, as depicted in Fig. 3.9a. Its computation is defined in Table 3.2. Subsequently, the computation of the force vector, ${}^U\boldsymbol{F}$, and torque generated by PL on the knee joint, τ_{PL}, can be carried out according to (3.36)-(3.38) or (3.44)-(3.46):

$$\begin{aligned}
{}^U\boldsymbol{F}(q) &= \begin{cases} k_{\mathrm{e}}\, \Delta l(q)\, \frac{{}^U\boldsymbol{l}(q)}{\left\| {}^U\boldsymbol{l}(q) \right\|} & \text{for } \Delta l(q) > 0 \\ 0 & \text{for } \Delta l(q) \leq 0 \end{cases} && (3.51)\\
{}^U\boldsymbol{\tau}(q) &= {}^U\boldsymbol{p}_{\mathrm{KPJ}} \times {}^U\boldsymbol{F}(q) && (3.52)\\
&= \boldsymbol{p}_{\mathrm{lever}}(q) \times {}^U\boldsymbol{F}(q) && (3.53)\\
\tau_{\mathrm{e,J}}(q) &= {}^U\boldsymbol{\tau}(q) \bullet e_Z && (3.54)
\end{aligned}$$

The knee joint torque $\tau_{\mathrm{e,J}}$ caused by the PL tendon is referred to as τ_{PL} and is negative. The passive tendon induces a change in joint position which contributes as external forces to the equations of motion. In the following control cycle, the motor can react to these changes.

The equation for the computation of the lever arm is already well known. For completeness, we write the equation for the computation of the lever arm vector:

$$\boldsymbol{p}_{\mathrm{lever}}(q) = {}^U\boldsymbol{p}_{\mathrm{KPJ}} - \frac{{}^U\boldsymbol{p}_{\mathrm{KPJ}} \bullet {}^U\boldsymbol{l}(q)}{{}^U\boldsymbol{l}(q) \bullet {}^U\boldsymbol{l}(q)}\, {}^U\boldsymbol{l}(q) \tag{3.55}$$

Passive Ankle Flexion

The same procedure also applies to the passive TA tendon to determine τ_{TA} on the ankle joint. The tendon induces positive torques on the ankle joint. Transformations take place between the S_V and S_W frame. The required equations are listed in Table 3.3.

Table 3.2.: Definitions for the dynamics modeling of the passive tendon PL.

P_{KPF}	Fixation point of the tendon on the link; $_{\text{KPF}}$ stands for "K(nee) P(assive) F(ixed)"
P_{KPJ}	Fixation point of the tendon at the joint; $_{\text{KPJ}}$ stands for "K(nee) P(assive) J(oint)"
${}^{Q}\boldsymbol{R}_{U}(q)$	$= \text{Rot}_z(q)$, cf. (3.25)
${}^{Q}\boldsymbol{r}_{U}$	$= \begin{pmatrix} 0 & -d_{\text{KF2J}} & 0 \end{pmatrix}^T$, translation vector from the origin of S_Q to the origin of S_U
${}^{U}\boldsymbol{R}_{Q}(q)$	$= ({}^{Q}\boldsymbol{R}_{U}(q))^T$
${}^{U}\boldsymbol{r}_{Q}(q)$	$= -({}^{Q}\boldsymbol{R}_{U}(q))^T \, {}^{Q}\boldsymbol{r}_{U}$
${}^{U}\boldsymbol{p}_{\text{KPF}}(q)$	$= {}^{U}\boldsymbol{r}_{Q}(q) + {}^{U}\boldsymbol{R}_{Q}(q) \, {}^{Q}\boldsymbol{p}_{\text{KPF}}$
${}^{U}\boldsymbol{l}(q)$	$= {}^{U}\boldsymbol{p}_{\text{KPF}}(q) - {}^{U}\boldsymbol{p}_{\text{KPJ}}$, length vector of the tendon in S_U

Table 3.3.: Definitions for the dynamics modeling of the passive tendon TA.

P_{APF}	Fixation point of the tendon on the link; $_{\text{APF}}$ stands for "A(nkle) P(assive) F(ixed)"
P_{APJ}	Fixation point of the tendon at the joint; $_{\text{APJ}}$ stands for "A(nkle) P(assive) J(oint)"
${}^{V}\boldsymbol{R}_{W}(q)$	$= \text{Rot}_z(q)$, cf. (3.25)
${}^{V}\boldsymbol{r}_{W}$	$= \begin{pmatrix} 0 & -d_{\text{AF2J}} & 0 \end{pmatrix}^T$, translation vector from the origin of S_Q to the origin of S_U
${}^{W}\boldsymbol{R}_{V}(q)$	$= ({}^{V}\boldsymbol{R}_{W}(q))^T$
${}^{W}\boldsymbol{r}_{V}(q)$	$= -({}^{V}\boldsymbol{R}_{W}(q))^T \, {}^{V}\boldsymbol{r}_{W}$
${}^{W}\boldsymbol{p}_{\text{APF}}(q)$	$= {}^{W}\boldsymbol{r}_{V}(q) + {}^{W}\boldsymbol{R}_{V}(q) \, {}^{V}\boldsymbol{p}_{\text{APF}}$
${}^{W}\boldsymbol{l}(q)$	$= {}^{W}\boldsymbol{p}_{\text{APF}}(q) - {}^{W}\boldsymbol{p}_{\text{APJ}}$, length vector of the tendon in S_W
$\Delta l(q)$	$= \left\| {}^{W}\boldsymbol{l}(q) \right\| - \left\| {}^{W}\boldsymbol{l}(q_0) \right\|$, spring extension
${}^{W}\boldsymbol{F}(q)$	$= \begin{cases} k_{\text{e}} \, \Delta l(q) \, \frac{{}^{W}\boldsymbol{l}(q)}{\left\| {}^{W}\boldsymbol{l}(q) \right\|} & \text{for } \Delta l(q) > 0 \\ 0 & \text{for } \Delta l(q) \leq 0 \end{cases}$, tendon forces
${}^{W}\boldsymbol{\tau}(q)$	$= {}^{W}\boldsymbol{p}_{\text{APJ}} \times {}^{W}\boldsymbol{F}(q) = \boldsymbol{p}_{\text{lever}}(q) \times {}^{W}\boldsymbol{F}(q)$, torques caused by the TA tendon
$\tau_{\text{e,J}}(q)$	$= {}^{W}\boldsymbol{\tau}(q) \bullet e_Z = \tau_{\text{TA}}$
$\boldsymbol{p}_{\text{lever}}(q)$	$= {}^{W}\boldsymbol{p}_{\text{APJ}} - \frac{{}^{W}\boldsymbol{p}_{\text{APJ}} \bullet {}^{W}\boldsymbol{l}(q)}{{}^{W}\boldsymbol{l}(q) \bullet {}^{W}\boldsymbol{l}(q)} \, {}^{W}\boldsymbol{l}(q)$, the lever arm vector

3.4.6 Biarticular, Passive Tendon

A distinctive feature of biarticular tendons is that their dynamics affect simultaneously two joints, i. e., the force exerted on each elastic spring-tendon is dependent on the angles of the two coupled joints. Although in robotic literature in recent years the use of biarticular actuators has been evident, we could not find complete equations. To our knowledge, this is the first attempt to present complete methods. We apply the virtual work and displacement method from above to compute the joint torques induced on the coupled joints. Each leg has three biarticular tendons: RF, BF, and GAS. Only the GAS tendon has often been subject of literature in many recently published approaches and is also known to take on important tasks during fast explosive motions. Therefore, in the following, a sample calculation is performed for the GAS tendon applying the virtual work and displacement method.

Passive Knee Flexion and Ankle Extension

A drawing of the GAS tendon is given in Fig. 3.12. First, it is essential to capture the orientation and position of the used reference frames S_{Kne} and S_{Ank} with respect to each other. Both frames are directly located on the joint axles:

$$
{}^{\mathrm{Kne}}\boldsymbol{T}_{\mathrm{Ank}}(q_{\mathrm{Kne}}, q_{\mathrm{Ank}}) = \begin{pmatrix} \mathrm{Rot}_z(q_{\mathrm{Kne}} + q_{\mathrm{Ank}}) & \mathrm{Rot}_z(q_{\mathrm{Kne}})\,{}^{\mathrm{Kne}}\boldsymbol{r}_{\mathrm{Ank}} \\ 0 & 1 \end{pmatrix} \tag{3.56}
$$

$$
\begin{aligned}
{}^{\mathrm{Ank}}\boldsymbol{T}_{\mathrm{Kne}}(q_{\mathrm{Ank}}, q_{\mathrm{Kne}}) &= {}^{\mathrm{Kne}}\boldsymbol{T}_{\mathrm{Ank}}(q_{\mathrm{Kne}}, q_{\mathrm{Ank}})^{-1} \\
&= \begin{pmatrix} (\mathrm{Rot}_z(q_{\mathrm{Kne}})\mathrm{Rot}_z(q_{\mathrm{Ank}}))^T & -(\mathrm{Rot}_z(q_{\mathrm{Kne}})\mathrm{Rot}_z(q_{\mathrm{Ank}}))^T \mathrm{Rot}_z(q_{\mathrm{Kne}})\,{}^{\mathrm{Kne}}\boldsymbol{r}_{\mathrm{Ank}} \\ 0 & 1 \end{pmatrix} \\
&= \begin{pmatrix} \mathrm{Rot}_z(q_{\mathrm{Ank}})^T \mathrm{Rot}_z(q_{\mathrm{Kne}})^T & -\mathrm{Rot}_z(q_{\mathrm{Ank}})^T\,{}^{\mathrm{Kne}}\boldsymbol{r}_{\mathrm{Ank}} \\ 0 & 1 \end{pmatrix}
\end{aligned} \tag{3.57}
$$

q_{Ank} and q_{Kne} denote the ankle and knee angle. ${}^{\mathrm{Kne}}\boldsymbol{r}_{\mathrm{Ank}}$ represents the translation vector from the origin of the S_{Kne} frame to the origin of S_{Ank}:

$$
{}^{\mathrm{Kne}}\boldsymbol{r}_{\mathrm{Ank}} = \begin{pmatrix} 0 \\ -d_{\mathrm{K2A}} \\ 0 \end{pmatrix} \tag{3.58}
$$

with d_{K2A} referring to the distance between the two origins on the y-axis. Subsequently, we can express the moving tendon fixation points P_{GA} and P_{GK} relative to these frames as follows:

$$
{}^{\mathrm{Kne}}\boldsymbol{p}_{\mathrm{GA}}(q_{\mathrm{Kne}}, q_{\mathrm{Ank}}) = {}^{\mathrm{Kne}}\boldsymbol{T}_{\mathrm{Ank}}(q_{\mathrm{Kne}}, q_{\mathrm{Ank}})\,{}^{\mathrm{Ank}}\boldsymbol{p}_{\mathrm{GA}}\,, \tag{3.59}
$$

$$
{}^{\mathrm{Ank}}\boldsymbol{p}_{\mathrm{GK}}(q_{\mathrm{Ank}}, q_{\mathrm{Kne}}) = {}^{\mathrm{Ank}}\boldsymbol{T}_{\mathrm{Kne}}(q_{\mathrm{Ank}}, q_{\mathrm{Kne}})\,{}^{\mathrm{Kne}}\boldsymbol{p}_{\mathrm{GK}}\,. \tag{3.60}
$$

${}^{\mathrm{Kne}}\boldsymbol{p}_{\mathrm{GK}}$ is the constant distance vector of the moving tendon fixation point P_{GK} relative to the origin of S_{Kne} and ${}^{\mathrm{Ank}}\boldsymbol{p}_{\mathrm{GA}}$ represents the constant distance vector of the moving tendon fixation point P_{GA} relative to the origin of S_{Ank}. An extension of the spring takes place if $\Delta l(q_{\mathrm{Ank}}, q_{\mathrm{Kne}}) > 0$ holds, where:

$$
\Delta l(q_{\mathrm{Kne}}, q_{\mathrm{Ank}}) = \left\| {}^{\mathrm{Kne}}\boldsymbol{l}(q_{\mathrm{Kne}}, q_{\mathrm{Ank}}) \right\| - \left\| {}^{\mathrm{Kne}}\boldsymbol{l}(q_{\mathrm{Kne}\,0}, q_{\mathrm{Ank}\,0}) \right\| \tag{3.61}
$$

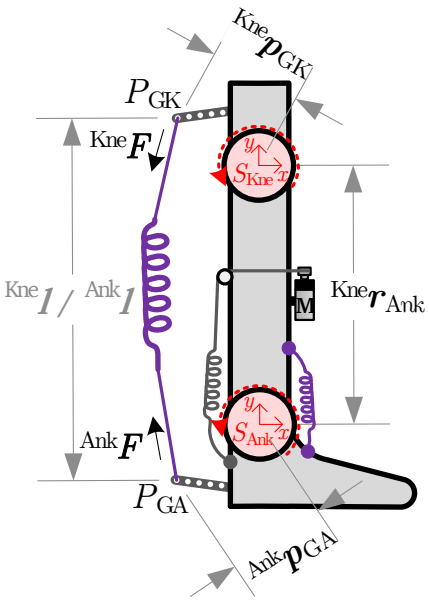

Figure 3.12.: Schematic drawing of the GAS tendon, representing the biarticular muscle for flexing the knee and extending the ankle joint.

and

$$^{\text{Kne}}\boldsymbol{l}(q_{\text{Kne}}, q_{\text{Ank}}) = -^{\text{Kne}}\boldsymbol{p}_{\text{GA}}(q_{\text{Kne}}, q_{\text{Ank}}) + {}^{\text{Kne}}\boldsymbol{p}_{\text{GK}} \tag{3.62}$$

with $q_{\text{Ank}\,0}$ and $q_{\text{Kne}\,0}$ denoting the rest angles in ankle and knee joint. The occurring tendon force is computed similar to (3.36) and (3.41):

$$^{\text{Kne}}\boldsymbol{F}(q_{\text{Kne}}, q_{\text{Ank}}) = k_{\text{e}}\,\Delta l(q_{\text{Kne}}, q_{\text{Ank}})\,\frac{^{\text{Kne}}\boldsymbol{l}(q_{\text{Kne}}, q_{\text{Ank}})}{\|{}^{\text{Kne}}\boldsymbol{l}(q_{\text{Kne}}, q_{\text{Ank}})\|} \tag{3.63}$$

The spring force can be also expressed relative to the S_{Ank} frame:

$$^{\text{Ank}}\boldsymbol{F}(q_{\text{Ank}}, q_{\text{Kne}}) = k_{\text{e}}\,\Delta l(q_{\text{Ank}}, q_{\text{Kne}})\,\frac{^{\text{Ank}}\boldsymbol{l}(q_{\text{Ank}}, q_{\text{Kne}})}{\|{}^{\text{Ank}}\boldsymbol{l}(q_{\text{Ank}}, q_{\text{Kne}})\|} \tag{3.64}$$

$$\text{where} \quad {}^{\text{Ank}}\boldsymbol{l}(q_{\text{Ank}}, q_{\text{Kne}}) = {}^{\text{Ank}}\boldsymbol{p}_{\text{GK}}(q_{\text{Ank}}, q_{\text{Kne}}) - {}^{\text{Ank}}\boldsymbol{p}_{\text{GA}}\,. \tag{3.65}$$

In fact, we can use the same tendon force to compute the torques on both joints. It is only important that the tendon force is expressed in the corresponding coordinate system. That means, we can also write:

$$^{\text{Kne}}\boldsymbol{F}(q_{\text{Ank}}, q_{\text{Kne}}) = \text{Rot}_z(q_{\text{Kne}} + q_{\text{Ank}})\,{}^{\text{Ank}}\boldsymbol{F}(q_{\text{Ank}}, q_{\text{Kne}}) \tag{3.66}$$

The result is identical to $^{\text{Kne}}\boldsymbol{F}$ as computed in (3.63). This relationship also applies to other variables such as $^{\text{Ank}}\boldsymbol{l}$ that can be transformed to the knee system as follows:

$$^{\text{Kne}}\boldsymbol{l}(q_{\text{Ank}}, q_{\text{Kne}}) = \text{Rot}_z(q_{\text{Kne}} + q_{\text{Ank}})\,{}^{\text{Ank}}\boldsymbol{l}(q_{\text{Ank}}, q_{\text{Kne}}) \tag{3.67}$$

To retrieve the torques at knee and ankle joint produced by the GAS tendon we apply the cross product:

$$^{\text{Kne}}\boldsymbol{\tau}(q_{\text{Kne}}, q_{\text{Ank}}) = {}^{\text{Kne}}\boldsymbol{p}_{\text{GK}} \times {}^{\text{Kne}}\boldsymbol{F}(q_{\text{Kne}}, q_{\text{Ank}}) \tag{3.68}$$

$$^{\text{Ank}}\boldsymbol{\tau}(q_{\text{Ank}}, q_{\text{Kne}}) = {}^{\text{Ank}}\boldsymbol{p}_{\text{GA}} \times {}^{\text{Ank}}\boldsymbol{F}(q_{\text{Ank}}, q_{\text{Kne}}) \tag{3.69}$$

As in (3.37), $^{\text{Kne}}\boldsymbol{p}_{\text{GK}}$ and $^{\text{Ank}}\boldsymbol{p}_{\text{GA}}$ are both exchangeable with the corresponding moment arm vectors. Consequently, $^{\text{Kne}}\boldsymbol{\tau}$ and $^{\text{Ank}}\boldsymbol{\tau}$ can be also computed as follows:

$$^{\text{Kne}}\boldsymbol{\tau}(q_{\text{Kne}}, q_{\text{Ank}}) = \boldsymbol{p}_{\text{lever}_{\text{Kne}}}(q_{\text{Kne}}, q_{\text{Ank}}) \times {}^{\text{Kne}}\boldsymbol{F}(q_{\text{Kne}}, q_{\text{Ank}}) \tag{3.70}$$

$$^{\text{Ank}}\boldsymbol{\tau}(q_{\text{Ank}}, q_{\text{Kne}}) = \boldsymbol{p}_{\text{lever}_{\text{Ank}}}(q_{\text{Ank}}, q_{\text{Kne}}) \times {}^{\text{Ank}}\boldsymbol{F}(q_{\text{Ank}}, q_{\text{Kne}}) \tag{3.71}$$

The equations for the moment arm vectors are:

$$\boldsymbol{p}_{\text{lever}_{\text{Kne}}}(q_{\text{Kne}}, q_{\text{Ank}}) = {}^{\text{Kne}}\boldsymbol{p}_{\text{GK}} - \frac{{}^{\text{Kne}}\boldsymbol{p}_{\text{GK}} \bullet {}^{\text{Kne}}\boldsymbol{l}(q_{\text{Kne}}, q_{\text{Ank}})}{{}^{\text{Kne}}\boldsymbol{l}(q_{\text{Kne}}, q_{\text{Ank}}) \bullet {}^{\text{Kne}}\boldsymbol{l}(q_{\text{Kne}}, q_{\text{Ank}})} {}^{\text{Kne}}\boldsymbol{l}(q_{\text{Kne}}, q_{\text{Ank}}) \tag{3.72}$$

$$\boldsymbol{p}_{\text{lever}_{\text{Ank}}}(q_{\text{Ank}}, q_{\text{Kne}}) = {}^{\text{Ank}}\boldsymbol{p}_{\text{GA}} - \frac{{}^{\text{Ank}}\boldsymbol{p}_{\text{GA}} \bullet {}^{\text{Ank}}\boldsymbol{l}(q_{\text{Ank}}, q_{\text{Kne}})}{{}^{\text{Ank}}\boldsymbol{l}(q_{\text{Ank}}, q_{\text{Kne}}) \bullet {}^{\text{Ank}}\boldsymbol{l}(q_{\text{Ank}}, q_{\text{Kne}})} {}^{\text{Ank}}\boldsymbol{l}(q_{\text{Ank}}, q_{\text{Kne}}) \tag{3.73}$$

To summarize, the torque amount induced by the GAS tendon on the knee joint is:

$$\tau_{\text{GAS,Kne}}(q_{\text{Kne}}, q_{\text{Ank}}) = {}^{\text{Kne}}\boldsymbol{\tau}(q_{\text{Kne}}, q_{\text{Ank}}) \bullet e_Z \tag{3.74}$$

respectively on the ankle joint:

$$\tau_{\text{GAS,Ank}}(q_{\text{Ank}}, q_{\text{Kne}}) = {}^{\text{Ank}}\boldsymbol{\tau}(q_{\text{Ank}}, q_{\text{Kne}}) \bullet e_Z \tag{3.75}$$

The same procedure can be applied to compute the torque amount exerted at the hip and knee joint by the passive BF and RF tendon. The technical realization of the RF tendon is shown in Fig. 2.11a. RF is responsible for the hip flexion and knee extension. The torque generated by RF at the hip and knee joint is referred to as $\tau_{\text{RF,Hip}}$ and $\tau_{\text{RF,Kne}}$, respectively. The passive tendon BF extends the hip and flexes the knee joint. The torque induced by BF on the hip and knee joint is denoted as $\tau_{\text{BF,Hip}}$ and $\tau_{\text{BF,Kne}}$, respectively.

Actuation of the GAS tendon

Note that, in case the biarticular tendon GAS shall be actuated, small modifications need to be performed. The above function (3.61) must be extended by the motor term:

$$\Delta l(q_{\text{Kne}}, q_{\text{Ank}}) = \left\| {}^{\text{Kne}}\boldsymbol{l}(q_{\text{Kne}}, q_{\text{Ank}}) \right\| - \left\| {}^{\text{Kne}}\boldsymbol{l}(q_{\text{Kne}\,0}, q_{\text{Ank}\,0}) \right\| - \theta\, r_{\text{M}} \tag{3.76}$$

The torques generated on the motor are positive:

$$\tau_{\text{e,M}}(q_{\text{Kne}}, q_{\text{Ank}}, \theta) = r_{\text{M}} \left\| {}^{\text{Kne}}\boldsymbol{F}(q_{\text{Kne}}, q_{\text{Ank}}, \theta) \right\| \tag{3.77}$$

3.4.7 Output Functions and Characteristic Curves

Now that the torque amounts caused by all actuator types are known, we can formulate the general output torque functions for each joint. Let us introduce the following general notations for joint torques generated by a

- b-SEA: τ_{bsea},
- u-SEA: τ_{usea},
- monoarticular, passive tendon: τ_{mono}, and
- biarticular, passive tendon: τ_{bi} .

While the number of b-SEAs, u-SEAs, and monoarticular, passive tendons are restricted to one per leg joint, the number of biarticular tendons can be up to three. For simplicity, we consider at the moment only one biarticular torque component per joint. Then, the general output torque function for the hip joint is:

$$\tau_{\text{e,J}}(q,\theta,q_2) = \tau_{\text{bsea}}(q,\theta) + \tau_{\text{bi}}(q,q_2) \tag{3.78}$$

where τ_{bsea} is defined in (3.24). As each biarticular tendon affects two coupled joints simultaneously, it is clear that the hip function is additionally influenced by the angle of the second coupled leg joint, denoted as q_2; in this case it is the knee joint angle.

The knee and ankle joint torques are composed of the torques generated by a u-SEA, its passive counterpart, and one or two biarticular tendons:

$$\tau_{\text{e,J}}(q,\theta,q_2) = \tau_{\text{usea}}(q,\theta) + \tau_{\text{mono}}(q) + \tau_{\text{bi}}(q,q_2) \tag{3.79}$$

Here as well, the output functions not only depend on the corresponding joint angle q and motor position θ, but also on the angle q_2 of the joint crossed by a biarticular tendon.

Deriving (3.78) and (3.79) with respect to θ, q, and q_2 yields the following output stiffness functions:

$$\dot{\tau}_{\text{e,J}}(q,\theta,q_2) = \frac{\mathrm{d}\tau_{\text{bsea}}}{\mathrm{d}\theta} + \frac{\mathrm{d}\tau_{\text{bsea}}}{\mathrm{d}q} + \frac{\mathrm{d}\tau_{\text{bi}}}{\mathrm{d}q} + \frac{\mathrm{d}\tau_{\text{bi}}}{\mathrm{d}q_2} \tag{3.80}$$

$$\dot{\tau}_{\text{e,J}}(q,\theta,q_2) = \frac{\mathrm{d}\tau_{\text{usea}}}{\mathrm{d}\theta} + \frac{\mathrm{d}\tau_{\text{usea}}}{\mathrm{d}q} + \frac{\mathrm{d}\tau_{\text{mono}}}{\mathrm{d}q} + \frac{\mathrm{d}\tau_{\text{bi}}}{\mathrm{d}q} + \frac{\mathrm{d}\tau_{\text{bi}}}{\mathrm{d}q_2} \tag{3.81}$$

Applying above general formula, we obtain the following exact output joint torque functions for the leg configuration illustrated in Fig. 2.10c:

$$\tau_{\text{e,Hip}}(q_{\text{Hip}},\theta_{\text{Hip}},q_{\text{Kne}}) = \tau_{\text{GLILIO}}(q_{\text{Hip}},\theta_{\text{Hip}}) + \tau_{\text{RF,Hip}}(q_{\text{Hip}},q_{\text{Kne}}) + \tau_{\text{BF,Hip}}(q_{\text{Hip}},q_{\text{Kne}}) \tag{3.82}$$

$$\begin{aligned}\tau_{\text{e,Kne}}(q_{\text{Kne}},\theta_{\text{Kne}},q_{\text{Ank}}) = {} & \tau_{\text{VAS}}(q_{\text{Kne}},\theta_{\text{Kne}}) + \tau_{\text{PL}}(q_{\text{Kne}}) + \tau_{\text{GAS,Kne}}(q_{\text{Kne}},q_{\text{Ank}}) \\ & + \tau_{\text{RF,Kne}}(q_{\text{Kne}},q_{\text{Hip}}) + \tau_{\text{BF,Kne}}(q_{\text{Kne}},q_{\text{Hip}})\end{aligned} \tag{3.83}$$

$$\tau_{\text{e,Ank}}(q_{\text{Ank}},\theta_{\text{Ank}},q_{\text{Kne}}) = \tau_{\text{SOL}}(q_{\text{Ank}},\theta_{\text{Ank}}) + \tau_{\text{TA}}(q_{\text{Ank}}) + \tau_{\text{GAS,Ank}}(q_{\text{Ank}},q_{\text{Kne}}) \tag{3.84}$$

Obviously, the describing output equations can become quite complex. From all joint equations, the knee output function (3.83) is the most sophisticated one, as the highest number of tendons, i. e., five in the case of the complete leg configuration, contribute to the knee joint dynamics. The joint dynamics of the knee are strongly characterized by high dynamic coupling effects incorporating the ankle and hip joint. The lowest coupling effects take place at the ankle joint, which is spanned by only one tendon that also crosses the knee joint, i. e., GAS. These analyses might be astonishing, judging from the fact that the mechanical realization of these active and passive tendons may appear as rather simple, as their implementation does not require any novel developments at first sight. Apparently, the integration of tendons, consisting of basic single modules such as DC motor gearboxes, springs, and tendons, can introduce a high degree of nonlinearity and complexity enhancing tremendously the design space. The output functions (3.82)-(3.84) are highly nonlinear and depend, in addition to the motor and joint positions, on several parameters, such as chosen attachment point for a tendon, its rest length, and the deployed spring stiffness. The b-SEA in the hip is the only actuator that has fixed settings due to its construction (cf. Section 3.4.3). Analysis of the design space and characteristic curves of a single u-SEA is performed in the following. An extensive analysis of the complete parameter space involving all tendons is beyond the scope of this section. To enhance the range of analyses we will formulate the necessary equations to determine the equilibrium length of a u-SEA.

Computing q at the Equilibrium Length of a u-SEA

In this section, a single u-SEA, as modeled for the knee transmission, is considered. At equilibrium length of the spring tendon, neither forces nor torques occur. This, in turn, means that the spring tendon is at rest and not extended. Thus $\Delta l = 0$ is true, indicating $-\theta\, r_{\mathrm{M}} = \left\|{}^{H}\boldsymbol{l}(q)\right\| - \left\|{}^{H}\boldsymbol{l}(q_0)\right\|$. In general, it is possible to solve this equation for both q and θ. For the motion generation, presented in Chapter 4, both solutions are required. In contrast to the solution for q, the solution for θ is straightforward, as it is included linearly. Therefore, it is omitted here.

Let us now compute the specific angle q, at which the spring is at rest, for a given motor angle θ. We first separate in 3.33 the terms that have a constant value from those depending on q:

$$\Delta l(q,\theta) = \left\|{}^{H}\boldsymbol{l}(q)\right\| - \left\|{}^{H}\boldsymbol{l}(q_0)\right\| + \theta\, r_{\mathrm{M}} \tag{3.85}$$

$$0 \stackrel{!}{=} \left\|{}^{H}\boldsymbol{l}(q)\right\| - \left\|{}^{H}\boldsymbol{l}(q_0)\right\| + \theta\, r_{\mathrm{M}}$$

$$\leftrightarrow \quad \left\|{}^{H}\boldsymbol{l}(q)\right\| = \left\|{}^{H}\boldsymbol{l}(q_0)\right\| - \theta\, r_{\mathrm{M}} \tag{3.86}$$

For a given motor angle θ, we determine the joint angle q at which the spring tension does not change anymore. As soon as the motor has reached its defined position, no further forces or torques will be produced. Until that time instant, however, forces and torques will be generated supporting the joint to reach the equilibrium angle. Let us recall the following equations from Section 3.4.4:

$${}^{H}\boldsymbol{l}(q) = {}^{H}\boldsymbol{p}_{\mathrm{KAJ}}(q) - {}^{H}\boldsymbol{p}_{\mathrm{KAM}} \tag{3.87}$$

$$\begin{aligned} {}^{H}\boldsymbol{l}(q_0) &= {}^{H}\boldsymbol{p}_{\mathrm{KAJ}}(q_0) - {}^{H}\boldsymbol{p}_{\mathrm{KAM}} \\ &= {}^{H}\boldsymbol{r}_{K} + {}^{H}\boldsymbol{R}_{K}(q_0)\,{}^{K}\boldsymbol{p}_{\mathrm{KAJ}} - {}^{H}\boldsymbol{p}_{\mathrm{KAM}} \end{aligned} \tag{3.88}$$

Substituting (3.87) and (3.88) in (3.86) yields:

$$\left\| {}^{H}\boldsymbol{r}_K + {}^{H}\boldsymbol{R}_K(q_0)\,{}^{K}\boldsymbol{p}_{\mathrm{KAJ}} - {}^{H}\boldsymbol{p}_{\mathrm{KAM}} \right\| - \theta\, r_{\mathrm{M}} = \left\| {}^{H}\boldsymbol{p}_{\mathrm{KAJ}}(q) - {}^{H}\boldsymbol{p}_{\mathrm{KAM}} \right\| \tag{3.89}$$

By squaring both sides of (3.89), we can eliminate the Euclidean norm computations:

$$\begin{aligned} &\underbrace{\left({}^{H}\boldsymbol{r}_K + {}^{H}\boldsymbol{R}_K(q_0)\,{}^{K}\boldsymbol{p}_{\mathrm{KAJ}} - {}^{H}\boldsymbol{p}_{\mathrm{KAM}}\right)^2}_{b^2} + \theta^2\, r_{\mathrm{M}}^2 \\ -2\,\theta\, r_{\mathrm{M}} &\sqrt{\left({}^{H}\boldsymbol{r}_K + {}^{H}\boldsymbol{R}_K(q_0)\,{}^{K}\boldsymbol{p}_{\mathrm{KAJ}} - {}^{H}\boldsymbol{p}_{\mathrm{KAM}}\right)^2} = \underbrace{\left({}^{H}\boldsymbol{p}_{\mathrm{KAJ}}(q) - {}^{H}\boldsymbol{p}_{\mathrm{KAM}}\right)^2}_{c^2} \\ &\boldsymbol{b}^2 + \theta^2\, r_{\mathrm{M}}^2 - 2\,\theta\, r_{\mathrm{M}}\,\sqrt{\boldsymbol{b}^2} \;=\; \boldsymbol{c}^2 \end{aligned} \tag{3.90}$$

While b is a vector with constant values, c is a vector with variables depending on q. Let us break down the term c

$$\boldsymbol{c} = {}^{H}\boldsymbol{p}_{\mathrm{KAJ}}(q) - {}^{H}\boldsymbol{p}_{\mathrm{KAM}} = {}^{H}\boldsymbol{r}_K + {}^{H}\boldsymbol{R}_K(q)\,{}^{K}\boldsymbol{p}_{\mathrm{KAJ}} - {}^{H}\boldsymbol{p}_{\mathrm{KAM}} = \mathrm{var.} \tag{3.91}$$

into its single elements. For this purpose, we introduce two new variable names:

$$\boldsymbol{d} \equiv {}^{K}\boldsymbol{p}_{\mathrm{KAJ}} = \mathrm{const.} \tag{3.92}$$

$$\text{and } \boldsymbol{e} \equiv {}^{H}\boldsymbol{r}_K - {}^{H}\boldsymbol{p}_{\mathrm{KAM}} = \mathrm{const.} \tag{3.93}$$

Now we are settled to break down the term c into single numbers and variables:

$$\begin{aligned} c_1^2 + c_2^2 + c_3^2 &= \left(\boldsymbol{e} + {}^{H}\boldsymbol{R}_K\, d\right)^2 \\ &= \left(\boldsymbol{e} + \begin{pmatrix} d_1\cos q - d_2\sin q \\ d_1\sin q + d_2\cos q \\ d_3 \end{pmatrix} \right)^2 \end{aligned} \tag{3.94}$$

We recall that the third dimension of these vectors can be set to zero: $d_3 = 0$ und $e_3 = 0$. This leads to further simplifications:

$$\begin{aligned} c_1^2 + c_2^2 &= \left(\begin{pmatrix} e_1 \\ e_2 \end{pmatrix} + \begin{pmatrix} d_1\cos q - d_2\sin q \\ d_1\sin q + d_2\cos q \end{pmatrix} \right)^2 \\ &= \begin{pmatrix} e_1 \\ e_2 \end{pmatrix}^2 + 2 \begin{pmatrix} e_1 \\ e_2 \end{pmatrix}^T \begin{pmatrix} d_1\cos q - d_2\sin q \\ d_1\sin q + d_2\cos q \end{pmatrix} + \begin{pmatrix} d_1\cos q - d_2\sin q \\ d_1\sin q + d_2\cos q \end{pmatrix}^2 \\ &= e_1^2 + e_2^2 + 2e_1(d_1\cos q - d_2\sin q) + 2e_2(d_1\sin q + d_2\cos q) \\ &+ (d_1\cos q - d_2\sin q)^2 + (d_1\sin q + d_2\cos q)^2 \qquad (3.95) \\ &= e_1^2 + e_2^2 + d_1^2 + d_2^2 + \cos q(2e_1d_1 + 2e_2d_2) + \sin q(-2e_1d_2 + 2e_2d_1) \qquad (3.96) \end{aligned}$$

Subsequently, the formulation (3.96) can be substituted in (3.90):

$$\boldsymbol{b}^2 + \theta^2\, r_{\mathrm{M}}^2 - 2\,\theta\, r_{\mathrm{M}}\,\sqrt{\boldsymbol{b}^2} = e_1^2 + e_2^2 + d_1^2 + d_2^2 + \cos q(2e_1d_1 + 2e_2d_2) + \sin q(-2e_1d_2 + 2e_2d_1)$$

$$\leftrightarrow \quad A = \sin q\, C - \cos q\, B \tag{3.97}$$

$$\text{where} \quad A \equiv \boldsymbol{b}^2 + \theta^2\, r_{\mathrm{M}}^2 - 2\,\theta\, r_{\mathrm{M}}\, \sqrt{\boldsymbol{b}^2} - e_1^2 - e_2^2 - d_1^2 - d_2^2 \tag{3.98}$$

$$B \equiv (-2e_1 d_1 - 2e_2 d_2) \tag{3.99}$$

$$C \equiv (2e_2 d_1 - 2e_1 d_2)\,. \tag{3.100}$$

Equation (3.97) represents an algebraic equation with A, C, and B representing constant numbers and trigonometric terms containing q. Here is an iterative procedure for solving (3.97) for q. Let us first recall that a real number can be expressed in the form $a + bi$ with an imaginary part of zero. The expression can be given in polar coordinates (ρ, q):

$$z = \rho(\cos q + i \sin q) = \rho e^{iq}\,. \tag{3.101}$$

Then the following formulations are valid:

$$\mathrm{Re}(-e^{iq}) = \mathrm{Re}(-\cos q - i \sin q) = -\cos q \tag{3.102}$$

$$\mathrm{Re}(-ie^{iq}) = \mathrm{Re}(-i \cos q + \sin q) = \sin q \tag{3.103}$$

$$\mathrm{Im}(e^{iq}) = \sin q \tag{3.104}$$

$$\mathrm{Im}(-ie^{iq}) = -\cos q \tag{3.105}$$

The first approach is to denote (3.97) as complex number with real parts:

$$A = -\cos q\, B + \sin q\, C \tag{3.106}$$

$$= \mathrm{Re}(-e^{iq})B + \mathrm{Re}(-ie^{iq})C \tag{3.107}$$

$$= \mathrm{Re}(-e^{iq}B - ie^{iq}C) \tag{3.108}$$

$$= \mathrm{Re}(e^{iq} \underbrace{(-B - iC)}_{e^{i\gamma}D}) \tag{3.109}$$

$$= \mathrm{Re}(e^{iq} e^{i\gamma} D) \tag{3.110}$$

$$= \mathrm{Re}(e^{i(q+\gamma)} D) \tag{3.111}$$

$$= \cos(q + \gamma) D \tag{3.112}$$

Before solving (3.112) for q, we need to determine the value of γ and D as follows:

$$e^{i\gamma} D = -B - iC \tag{3.113}$$

$$\leftrightarrow \quad D(\cos\gamma + i \sin\gamma) = -B - iC \tag{3.114}$$

$$\rightarrow \quad D \cos\gamma = -B \tag{3.115}$$

$$\text{and} \quad \rightarrow \quad D \sin\gamma = -C \tag{3.116}$$

By division of (3.115) and (3.116) we obtain:

$$\tan\gamma = \frac{C}{B} \quad \leftrightarrow \quad \mathrm{atan2}(C, B) = \gamma \tag{3.117}$$

Subsequently, we can substitute the value of γ in (3.115) or (3.116) and solve for D:

$$D\cos\gamma = -B \quad \leftrightarrow \quad D = \frac{-B}{\cos\gamma} \tag{3.118}$$

$$\text{or} \quad D\sin\gamma = -C \quad \leftrightarrow \quad D = \frac{-C}{\sin\gamma} \tag{3.119}$$

Now that the value of D and γ is known, we can determine the value of q in (3.112):

$$A = \cos(q+\gamma)D \tag{3.120}$$

$$\leftrightarrow \quad \frac{A}{D} = \cos(q+\gamma) \tag{3.121}$$

$$\leftrightarrow \quad \text{acos}(\frac{A}{D}) = q+\gamma \tag{3.122}$$

$$\leftrightarrow \quad q = \text{acos}(\frac{A}{D}) - \gamma \tag{3.123}$$

Due to $\cos q = \cos(-q)$, a second solution is: $q = -\text{acos}(\frac{A}{D}) - \gamma$.

Another approach would be to denote (3.97) as complex number with imaginary parts:

$$A = -\cos q\, B + \sin q\, C \tag{3.124}$$

$$= \text{Im}(-ie^{iq})B + \text{Im}(e^{iq})C \tag{3.125}$$

$$= \text{Im}(e^{iq}\underbrace{(-iB+C)}_{e^{i\gamma}D}) \tag{3.126}$$

$$= \text{Im}(e^{iq}e^{i\gamma}D) \tag{3.127}$$

$$= \text{Im}(e^{i(q+\gamma)}D) \tag{3.128}$$

$$= \sin(q+\gamma)D \tag{3.129}$$

Again we first need to determine the value of γ and D:

$$e^{i\gamma}D = C - iB \tag{3.130}$$

$$\leftrightarrow \quad D(\cos\gamma + i\sin\gamma) = C - iB \tag{3.131}$$

$$\rightarrow \quad D\cos\gamma = C \tag{3.132}$$

$$\text{and} \quad \rightarrow \quad D\sin\gamma = -B \tag{3.133}$$

By division of (3.132) and (3.133) we obtain:

$$\tan\gamma = \frac{-B}{C} \quad \leftrightarrow \quad \text{atan2}(-B, C) = \gamma \tag{3.134}$$

The value of γ is substituted in (3.132) or (3.133) to compute D:

$$D\cos\gamma = C \quad \leftrightarrow \quad D = \frac{C}{\cos\gamma} \tag{3.135}$$

$$\text{or} \quad D\sin\gamma = -B \quad \leftrightarrow \quad D = \frac{-B}{\sin\gamma} \tag{3.136}$$

Replacing γ and D by their computed values in (3.129) we obtain the solution for q:

$$A = \sin(q+\gamma)D \tag{3.137}$$

$$\frac{A}{D} = \sin(q+\gamma) \tag{3.138}$$

$$\operatorname{asin}(\frac{A}{D}) = q+\gamma \tag{3.139}$$

$$q = \operatorname{asin}(\frac{A}{D}) - \gamma \tag{3.140}$$

Due to $\sin q = \sin(\pi - q)$, another valid solution is $q = -\operatorname{asin}(\frac{A}{D}) - \gamma + \pi$. Note that shifting both solutions by any multiple of 2π in either positive or negative direction yields further valid solutions, as the sine and cosine function are periodic functions with period 2π.

Computing Gravity Compensating Initial States

For gravity compensation, it needs to be ensured that the torques generated in the joints match the torques caused by the gravitational forces:

$$\tau_{\mathrm{e,J}} \stackrel{!}{=} \tau_{\mathrm{G}} \,. \tag{3.141}$$

By means of the previously derived actuator models, it is possible to solve this equation for the motor position θ.

Characteristic Curves

We investigate the dynamics caused by the VAS tendon with stiffness $15\mathrm{k}\,^{\mathrm{N}}/_{\mathrm{m}}$, neglecting all passive torque amounts in (3.83); thus, simplifying (3.83) to:

$$\tau_{\mathrm{e,Kne}} = \tau_{\mathrm{VAS}}(q_{\mathrm{Kne}}, \theta_{\mathrm{Kne}}) \tag{3.142}$$

The diagrams in Fig. 3.13 display the motor and joint torques induced by the u-SEA in the workspace $\theta = [0, 90°]$ and $q = [-90°, 0]$ at rest angle $q_0 = -90°$, corresponding to a bent knee, for the attachment point number 5 (cf. Fig. 3.14). At the end position of the q-interval, $q = 0°$, the knee is completely extended. The curves illustrate very well the nonlinear dependency of the joint and motor torques on the joint movement. The motor and joint torques, however, are linearly dependent on the motor movement, when the joint angle is fixed.

The curves are different for varied attachment points, as shown in Fig. 3.14. Even with an incomplete joint torque function for the knee joint incorporating only one tendon, the dimension of the design space with its many key parameters appears as quite large. Due to this complexity, behavior predictions for a joint, when all tendons are included, are difficult. Only, with regard to the antagonistic muscles, it is clear that, for instance, the co-contraction of PL which introduces opposing torques on the motor makes the knee stiffer. The same holds true for the muscle pair in the ankle.

The behavior change affected by a biarticular tendon, however, is not predictable as, regardless of the generally known role of the tendon, the timing of its action, in addition to the assigned

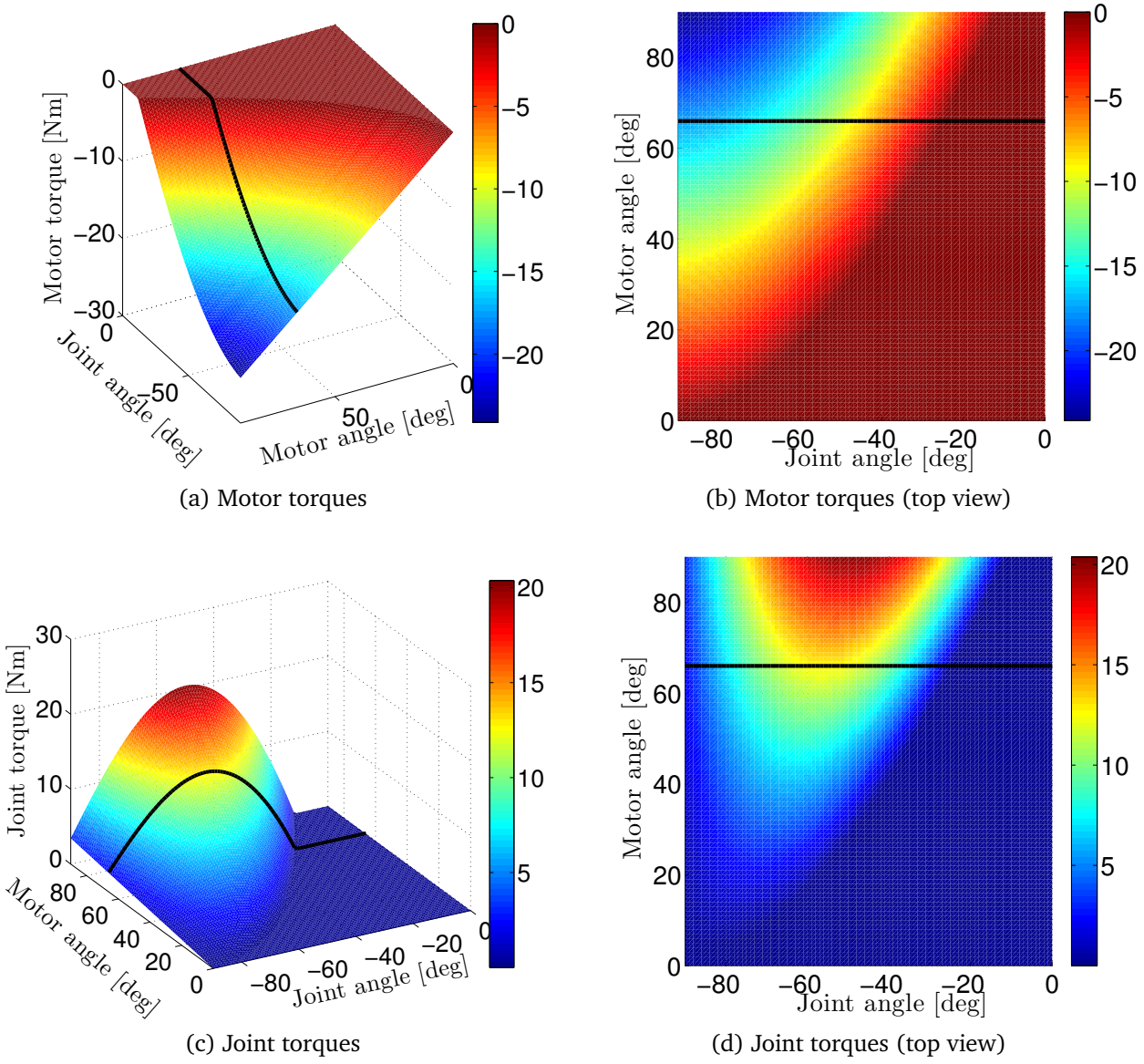

(a) Motor torques

(b) Motor torques (top view)

(c) Joint torques

(d) Joint torques (top view)

Figure 3.13.: Characteristic curves of the monoarticular u-SEA VAS: motor torques in the view from the front (a) and from the top (b) for $q_0 = -90°$, $\theta = [0, 90°]$, $q = [-90°, 0]$, and attachment point number 5 (AP 5); joint torques in the front view (c) and top view (d). The black line represents the curves at motor angle $\theta = 66°$ (cf. Fig. 3.14). In flat areas slacking of the tendon occurs.

stiffness and attachment point, plays an important role. The specific time instant is determined by the chosen rest length. For instance, as for the torque amounts induced by RF and GAS on the knee joint, the change in total joint torque over the complete time interval might be compensated by each other as they produce opposing torques. But, regarding the same time instant, this statement is not valid, as, in the optimal case, RF and GAS take on their designated tasks in different phases. For general statements beyond these rough statements, a sophisticated framework is required that allows to analyze the effects of variations in spring stiffnesses, attachment points, and rest lengths on the overall joint behavior with respect to well-chosen gait-specific performance criteria.

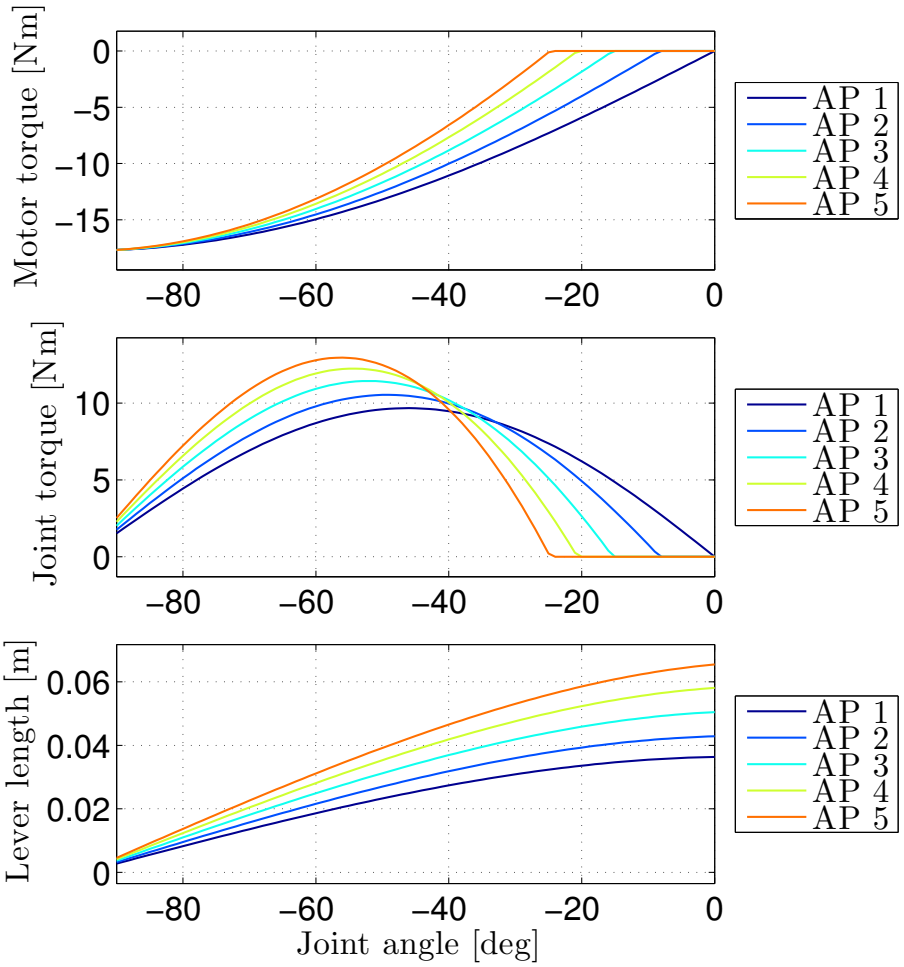

Figure 3.14.: Motor torques, joint torques, and lever lengths for the same parameters settings as in Fig. 3.13 for all attachment points, abbreviated as AP in the legends above, when the motor is fixed at $\theta = 66°$. The black line in all diagrams from Fig. 3.13 is equal to the curve "AP 5" in the corresponding diagrams of the joint and motor torques.

Discussion

A number of current research projects also focus on the development of variable stiffness and damping joints [6]. The constructed actuators often comprise several custom-made motors, Harmonic drive gears, nonlinear spring mechanisms, and tendons where additional motors are employed to adjust lever arms or spring stiffnesses. Such actuation units present modular, integrable solutions that can be well adapted to the desired task. By this modular solution, dynamic coupling effects are eliminated. While such actuation units represent impressive sophisticated engineering approaches, it remains unclear whether such modules are necessary for the intended tasks.

By the interplay of the tendons, as arranged in BioBiped1's leg configuration, the stiffness and general behavior of a joint as well as those of the entire leg and overall robot can be changed. Therefore, exploring first the role of each tendon individually during the intended motions has a higher priority than providing the possibility for on-the-fly stiffness changes of the mechanically deployed springs. It should be also noted that due to the specific technical realization of the

actuator types the sensed transmission stiffness can be indirectly adapted by the rest length, attachment point, and actual joint and motor angle configuration.

3.5 Modeling the Ground Contact

Modeling a dynamic contact is a still quite challenging problem [87]. According to [77] (p. 647) a contact model needs to "characterize both the forces that can be transmitted through the contact as well as the allowed relative motions of the contacting bodies". These model components can be computed by "the geometry of the contacting surfaces and the material properties of the parts which dictate friction and possible contact deformation" [77] (p. 647). Since we are interested in predicting realistic contact forces including kinetic and static friction and the deformations caused by a collision, we choose a compliant point contact for modeling the foot-ground contact interface. Furthermore, in case it is necessary, a point contact can be easily extended to a plane contact [41].

Contact dynamics can be modeled by either penalty-based or analytical methods. While analytical methods are capable of producing relatively stable results even with large sampling time, they are often quite time-consuming. Furthermore, realistic impact and friction forces are difficult to predict. It is possible that no solution or multiple solutions are found, and energy conservation principles may be violated in frictional impacts [174]. Penalty-based methods [66, 94] generate forces at the point contacts based on the elastic and viscous properties of the material. They incorporate deformations and losses of energy and can easily be enhanced by friction models.

How to model a collision, static, and kinetic friction using a penalty-based method is described in Appendix A. The model can be used in any MBS dynamics simulation tool that allows to introduce forces into a body and measure the position and velocity of a body.

3.6 Full State Space Model of the Robot

After the introduction and complete description of the single components of the robot model interacting with the ground—rigid joint-link structure, actuator models as well as contact model—the dynamics of the bipedal system can be rewritten in state space by defining the state $\boldsymbol{x} \in \mathbf{R}^{\mathbf{n}}$, input $\boldsymbol{u} \in \mathbf{R}^{\mathbf{p}}$, and output $\boldsymbol{y} \in \mathbf{R}^{\mathbf{q}}$. Here we must distinguish 2-D running or alternate hopping from 1-D synchronous in-place hopping.

The motion of each DoF can be described by four state variables: motor position θ and velocity $\dot{\theta}$, joint position q and velocity $\dot{q}$. The number of DoFs for each leg amount to three, in total for both legs to six. Thus, the motions of the hip, knee, and ankle joint of both legs are fully represented by 24 state variables.

In addition, in order to exactly predict future motions based on the current robot state, we need the state of the feet and of the torso. The feet have two contact points at the heel and the toe at which the friction, stiction, and normal forces are computed. In order to determine the next foot state, it is important to capture from the current foot state the stiction position, p_{T}, with respect to the world reference frame and the stiction state, χ_{T}, i. e., whether the foot is in stiction. The stiction state $\chi_{\mathrm{T}} = 1$ implies the existence of ground contact. In total, four additional states are needed for each foot: $p_{\mathrm{T\,Toe\_r}}$, $p_{\mathrm{T\,Toe\_l}}$, $p_{\mathrm{T\,Heel\_r}}$, $p_{\mathrm{T\,Heel\_l}}$, $\chi_{\mathrm{T\,Toe\_r}}$, $\chi_{\mathrm{T\,Toe\_l}}$, $\chi_{\mathrm{T\,Heel\_r}}$, $\chi_{\mathrm{T\,Heel\_l}}$.

The torso can be fully described by its position and velocity in the sagittal plane, respectively along the z-axis for 1-D motions. Depending on the dimension of the target motions, the torso

has consequently either two or four state variables: x_{Torso}, $\dot{x}_{\text{Torso}}$, z_{Torso}, $\dot{z}_{\text{Torso}}$. In total, this adds up to either 34 or 36 independent state variables for 1-D hopping, respectively 2-D running motions. The collection of all variables that completely characterize the motion of the robot system for the purpose of predicting future motions can be gathered in $\boldsymbol{x}$:

$$\boldsymbol{x} = \begin{pmatrix} \boldsymbol{\theta} \\ \dot{\boldsymbol{\theta}} \\ \boldsymbol{q} \\ \dot{\boldsymbol{q}} \\ \boldsymbol{p}_{\mathbf{T}} \\ \boldsymbol{\chi}_{\mathbf{T}} \\ \boldsymbol{p}_{\mathbf{Torso}} \\ \dot{\boldsymbol{p}}_{\mathbf{Torso}} \end{pmatrix} \tag{3.143}$$

$$\begin{aligned}
\text{with} \quad \boldsymbol{\theta} &= \begin{pmatrix} \theta_{\text{Hip_r}} & \theta_{\text{Kne_r}} & \theta_{\text{Ank_r}} & \theta_{\text{Hip_l}} & \theta_{\text{Kne_l}} & \theta_{\text{Ank_l}} \end{pmatrix}^T \\
\dot{\boldsymbol{\theta}} &= \begin{pmatrix} \dot{\theta}_{\text{Hip_r}} & \dot{\theta}_{\text{Kne_r}} & \dot{\theta}_{\text{Ank_r}} & \dot{\theta}_{\text{Hip_l}} & \dot{\theta}_{\text{Kne_l}} & \dot{\theta}_{\text{Ank_l}} \end{pmatrix}^T \\
\boldsymbol{q} &= \begin{pmatrix} q_{\text{Hip_r}} & q_{\text{Hip_l}} & q_{\text{Kne_r}} & q_{\text{Kne_l}} & q_{\text{Ank_r}} & q_{\text{Ank_l}} \end{pmatrix}^T \\
\dot{\boldsymbol{q}} &= \begin{pmatrix} \dot{q}_{\text{Hip_r}} & \dot{q}_{\text{Kne_r}} & \dot{q}_{\text{Ank_r}} & \dot{q}_{\text{Hip_l}} & \dot{q}_{\text{Kne_l}} & \dot{q}_{\text{Ank_l}} \end{pmatrix}^T \\
\boldsymbol{p}_{\mathbf{T}} &= \begin{pmatrix} p_{\text{T Toe_r}} & p_{\text{T Toe_l}} & p_{\text{T Heel_r}} & p_{\text{T Heel_l}} \end{pmatrix}^T \\
\boldsymbol{\chi}_{\mathbf{T}} &= \begin{pmatrix} \chi_{\text{T Toe_r}} & \chi_{\text{T Toe_l}} & \chi_{\text{T Heel_r}} & \chi_{\text{T Heel_l}} \end{pmatrix}^T \\
\boldsymbol{p}_{\mathbf{Torso}} &= \begin{pmatrix} x_{\text{Torso}} & z_{\text{Torso}} \end{pmatrix}^T \\
\dot{\boldsymbol{p}}_{\mathbf{Torso}} &= \begin{pmatrix} \dot{x}_{\text{Torso}} & \dot{z}_{\text{Torso}} \end{pmatrix}^T
\end{aligned}$$

The control variables can be manifold depending on the motion generation, as will be further explained in Section 4. The input vector $\boldsymbol{u}$ can gather either the input voltages to each motor:

$$\boldsymbol{u} = \begin{pmatrix} u_{\text{Hip\_r}} & u_{\text{Kne\_r}} & u_{\text{Ank\_r}} & u_{\text{Hip\_l}} & u_{\text{Kne\_l}} & u_{\text{Ank\_l}} \end{pmatrix}^T \tag{3.144}$$

or the motor position, velocities, and torques:

$$\boldsymbol{u} = \begin{pmatrix} \boldsymbol{\theta} \\ \dot{\boldsymbol{\theta}} \\ \boldsymbol{\tau}_{\mathbf{m}} \end{pmatrix} \tag{3.145}$$

$$\text{with} \quad \boldsymbol{\tau}_{\mathbf{m}} = \begin{pmatrix} \tau_{\text{m Hip\_r}} & \tau_{\text{m Kne\_r}} & \tau_{\text{m Ank\_r}} & \tau_{\text{m Hip\_l}} & \tau_{\text{m Kne\_l}} & \tau_{\text{m Ank\_l}} \end{pmatrix}^T$$

or only a subset of these variables.

As the output vector differs for the simulation and real robot model, it is not explicitly listed here. In the real robot platform, position sensors are available for the motor and joint side. For the joint side, these sensors are absolute and, thus, well usable in contrast to the incremental

encoders at the gearboxes. The robot torso is equipped with a gyroscope and accelerometer which measure the rotational and linear 3-D velocities. In addition, each foot has three hall sensors measuring the normal forces at the heel and toe and the parallel forces. These sensors provide the measured signals that can be gathered in $\boldsymbol{y}$. In addition, the simulation model provides the velocities and accelerations of the joints and many more signals, if desired.

Note that a linear state space model for this nonlinearly coupled dynamic system is neither the purpose of this section nor does it provide any advantages for the studies performed in this thesis.

3.7 Experimental Validation

In order to ensure that the insights gained in simulation are also valid for the real robot platforms and to elaborate in an easier and a more time-efficient manner on motion generation methods and concepts, the simulation model must be validated. To benefit from the accurate modeling and simulation efforts, it is, therefore, necessary to perform a model calibration. Traditionally, a model calibration can be carried out in many different ways and enables an accurate use of the validated simulation model of the robot in off-line manner, in order to allow different investigations and controller designs to be tested prior to implementation on the real robot hardware.

Whereas learning methods may allow to approximate the dynamics of even very complex systems quite well for specific, repetitive motion trajectories [128] and to use this model for the learned configurations, a sufficiently detailed mathematical model with identified parameters enables a far wider range of investigations. Classical methods for dynamic model identification, however, lack approaches for the identification of complex models that involve a number of actuated and passive elastic tendons and a quite dynamic ground contact. In [14], an overview of parameter identification methods for conventionally built humanoid robots without elasticties is given. To the best of our knowledge, there is no available method that can be applied to successfully identify all parameters of a complex musculoskeletal robot, like BioBiped1, in an all-at-once approach. A framework for parameter identification of more complex, bio-inspired robots had been proposed in [80]. The framework uses two different methodologies for the actuation dynamics of the series elastically actuated BioRob arm [86] and for the rigid robot dynamics [129]. An extension of this framework to the BioBiped robot platforms requires enormous efforts, since the BioBiped robots differ, with respect to the actuation, substantially in complexity from the BioRob arm. Developing a calibration method dedicated to highly nonlinear, dynamic musculoskeletal systems is beyond the scope of this thesis. As mentioned in Section 3.1, the model of the BioBiped1 platform can be divided into two parts: (1) actuation dynamics and (2) rigid body dynamics. Additionally, when interacting with the environment, the ground contact model comes into play. As for the actuation dynamics, we already learned in Section 3.4 that the knee and ankle joints are characterized by highly nonlinear dynamics. Only in the hip joint, the compliant actuation can be described by a linear relationship. Yet, even in the case of linear elastic actuation, generating a regressor matrix involves many challenges and assumptions. According to [80], by reformulating (3.6),

$$\tau_{\mathrm{m}} = (I_{\mathrm{r}} + I_{\mathrm{g}})\,\ddot{\theta} + d_{\mathrm{vg}}\,\dot{\theta} + \tau_{\mathrm{e,M}}\,, \tag{3.146}$$

to

$$\tau_{\mathrm{m}} - (I_{\mathrm{r}} + I_{\mathrm{g}})\,\ddot{\theta} = d_{\mathrm{vg}}\,\dot{\theta} + \tau_{\mathrm{e,M}}\,, \tag{3.147}$$

it is possible to develop a regressor matrix, $\boldsymbol{\phi}$, with a vector of unknown linear parameters, $\boldsymbol{p}$, to be estimated:

$$\boldsymbol{\tau} = \boldsymbol{\phi}\, \boldsymbol{p}\,. \tag{3.148}$$

This, however, requires accurate current measurements to retrieve the motor torques:

$$\tau_{\mathrm{m}} = k_{\mathrm{t}}\, i\,. \tag{3.149}$$

Additionally, the motor rotor and gearbox inertia given by the manufacturer need to be sufficiently accurate. This approach also presumes a linear friction model—load-dependent torque models would add enormously to the complexity of this procedure. By means of all these assumptions, it is possible to retrieve step-by-step the unknown parameters of the actuation dynamics. Identifying the rigid body dynamics, although a rigid dynamic structure without elasticities is considered, can be also quite challenging. Each rigid link can be described by 10 inertial parameters—mass, CoM position, three inertia moments and products—thus, in the case of BioBiped1 leading to 70 parameters. Furthermore, using the Newton-Euler formalism, first, a robot model must be generated that is linear in terms of these inertial parameters and, possibly, a parameter reduction to a base set must be performed. Then, the process of determining exciting trajectories and estimating the link parameters using, e. g., a standard least-squares procedure can start [129]. Therefore, due to these challenges, the focus lies on the identification of the most essential parameters that are expected to cause the largest deviations of the simulation model from the real robot. Furthermore, due to their design and parameter settings, the current sensors of the robot platform do not provide useful data. This means that it is not possible to determine accurate motor torques, which, however, are needed, as described above, to retrieve the unknown parameters. Despite these problems, various measurements and parameter identifications for sub-models were performed on the real robot to achieve a good agreement of the real robot and the simulation model. These sub-models, their identification, and corresponding experimental setup are described in the following.

3.7.1 Rigid Body Dynamics

Since the goal is a representation of the relevant dynamical effects of the physical robot with the simulation model to enable valuable and valid insights through simulations and predictions based on the simulation model, most of the parameters provided by the CAD data were assumed as correct and not further identified. These data include, in particular, the segment masses and dimensions. Additionally, the inertia and CoM of the segments were extracted from the CAD data. These data were only subject of further improvements in case it was necessary. In a set of experiments, we collected data from the rigid body dynamics of the robot to identify the joint friction d. Strictly speaking, since the behavior of each joint within a leg is different due to varied construction of the mechanical parts and use of low-quality bearings by the manufacturer, the following experiments need to be carried out for all joints, which is quite tedious work. Therefore, only one leg was investigated in experiment; the identified models are used for both legs.

In the experimental setup, the ankle and knee joints were first decoupled from the actuators. Subsequently, the shank and foot were held by hand at the mechanical joint limits, which

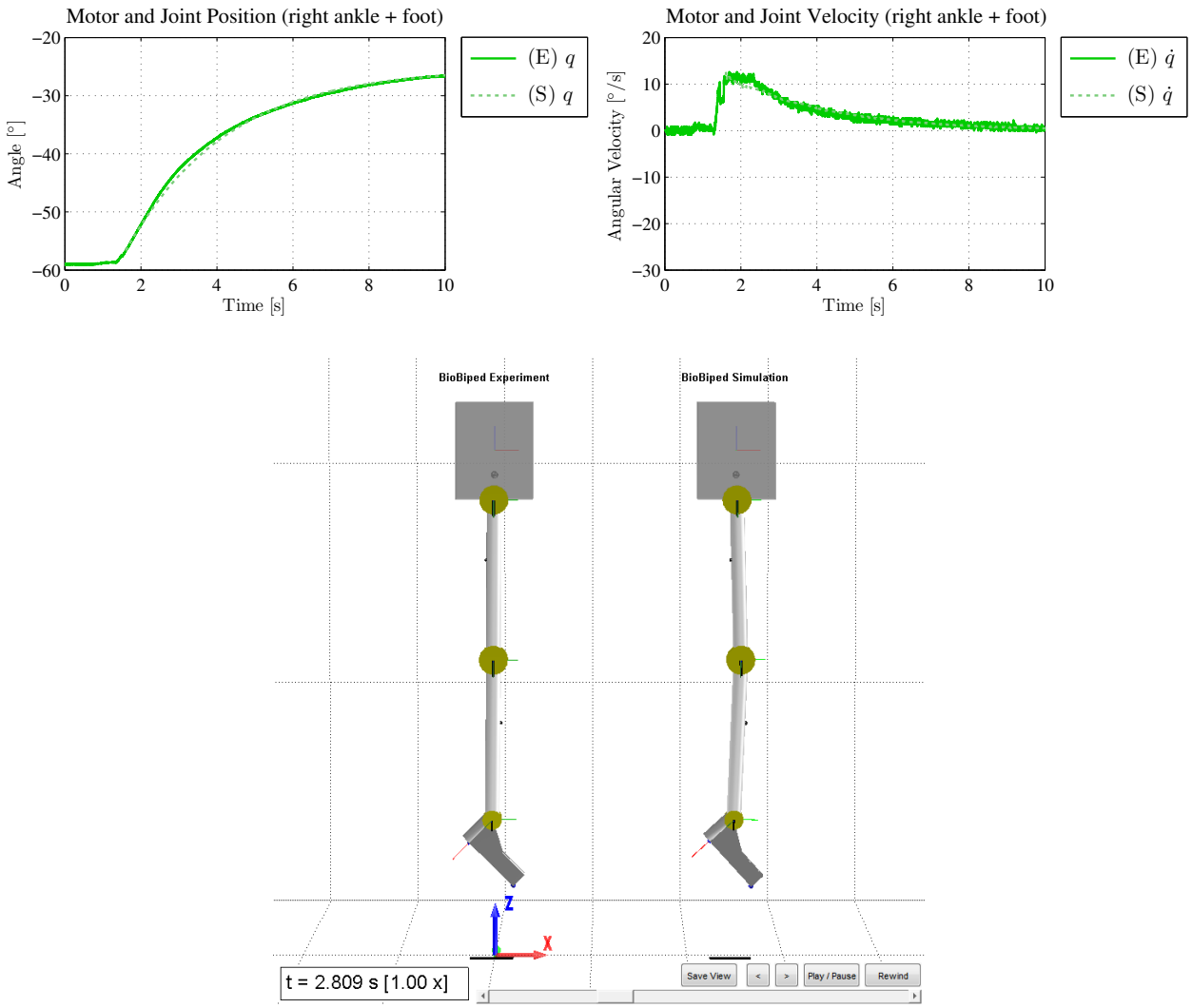

Figure 3.15.: Identification of the rigid body dynamics parameters for the ankle joint with the joint position signals in experiment (E) and simulation (S).

also correspond to the motor zero position, and then released to move. These experiments were performed separately. The starting positions of the mechanical joint limits are shown in Fig. 3.15 and 3.16. The figures also contain diagrams illustrating the course of the joint position trajectories. Both in Fig. 3.15 and 3.16 a good agreement of the simulation model with the real robot platform can be detected. As, initially, the deviations were not large, it was possible to manually tune the joint friction which resulted in $d_{\text{Ank}} = 0.29\,\text{Nms/rad}$ for the ankle joint and $d_{\text{Kne}} = 0.07\,\text{Nms/rad}$ for the knee joint. To confirm this result, the same experiment for the knee joint was repeated in presence of a counteracting torque through the passive antagonist PL. With $0.552\,\text{N/mm}$, the spring of PL was quite soft to enable rigid knee movement. The trajectories of the real and simulated robot are illustrated in Fig. 3.17 and confirm the correctness of the identified friction value.

As decoupling the thigh from the actuator without disassembling the hip actuation is not possible, we dropped this experiment for the hip actuation. Normally, due to the linear transmission dynamics, it is also possible to perform PD motor control and record the motor and joint trajectories in order to determine the hip friction by least-squares calculations. But this

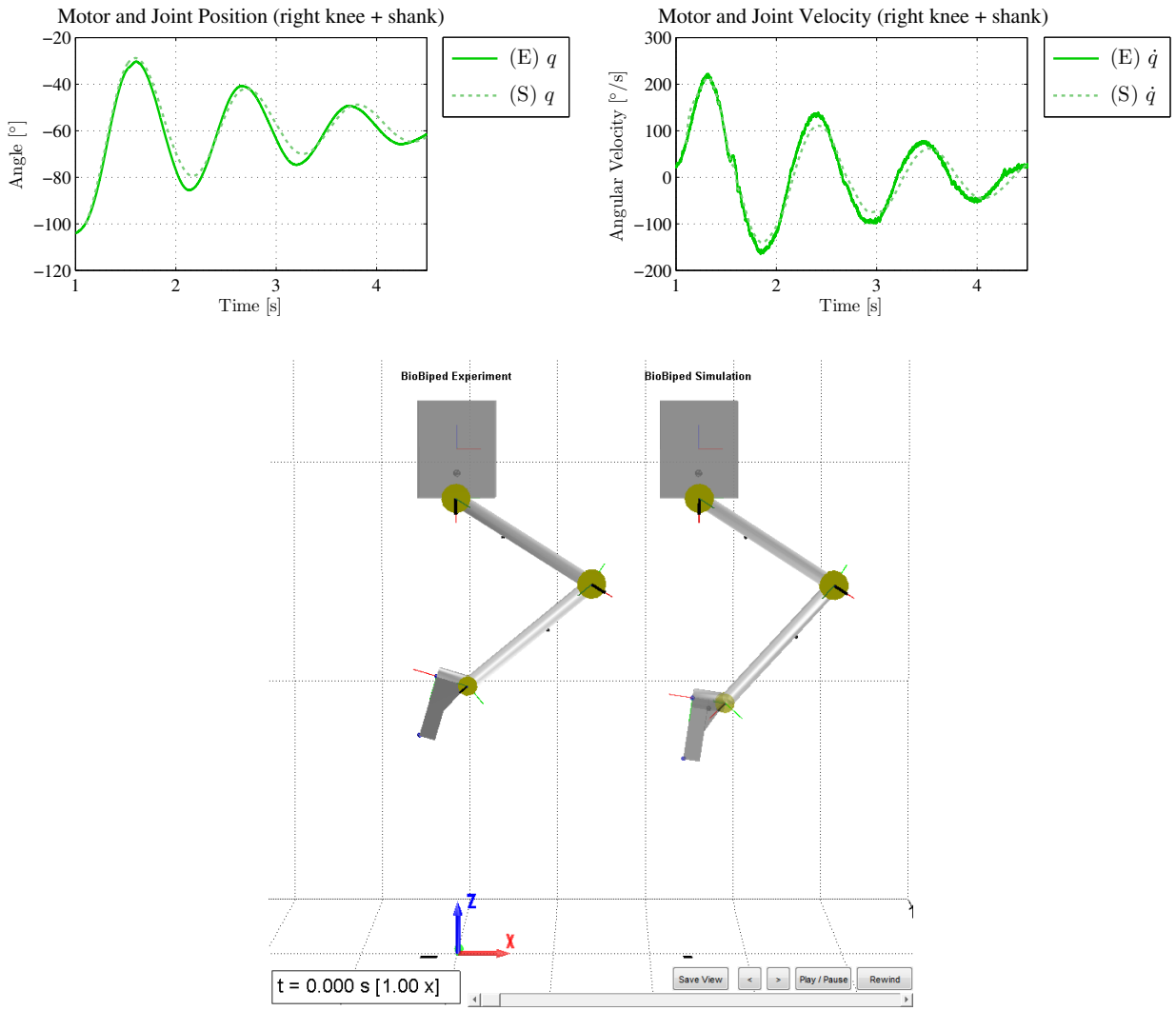

Figure 3.16.: Identification of the rigid body dynamics parameters for the knee joint.

experiment could not be performed due to the insufficient quality of the current measurements of the respective robot hardware components. Furthermore, due to the technical construction of the transmission, the hip actuation of the investigated robot hardware is characterized by substantial play which also needs to be improved for the next hardware version of the robot.

3.7.2 Actuation Dynamics

The actuation dynamics consists of the motor dynamics and the transmission dynamics. With the exception of the motor viscous friction, d_{vg}, all motor parameters were retrieved from the motor data sheet and are given in Table 4.1. The value for the motor viscous friction was previously estimated for a motor with similar specification in [86].

The transmission dynamics of the different actuators represent, therefore, the more interesting and challenging part of the identification of the actuation dynamics. The hip actuation is characterized by the linear transmission ratio $n_{\text{p,Hip}}$, spring stiffness $k_{\text{e,Hip}}$, and viscous damping $d_{\text{e,Hip}}$. With the exception of the friction, these parameters were provided by the manufacturer

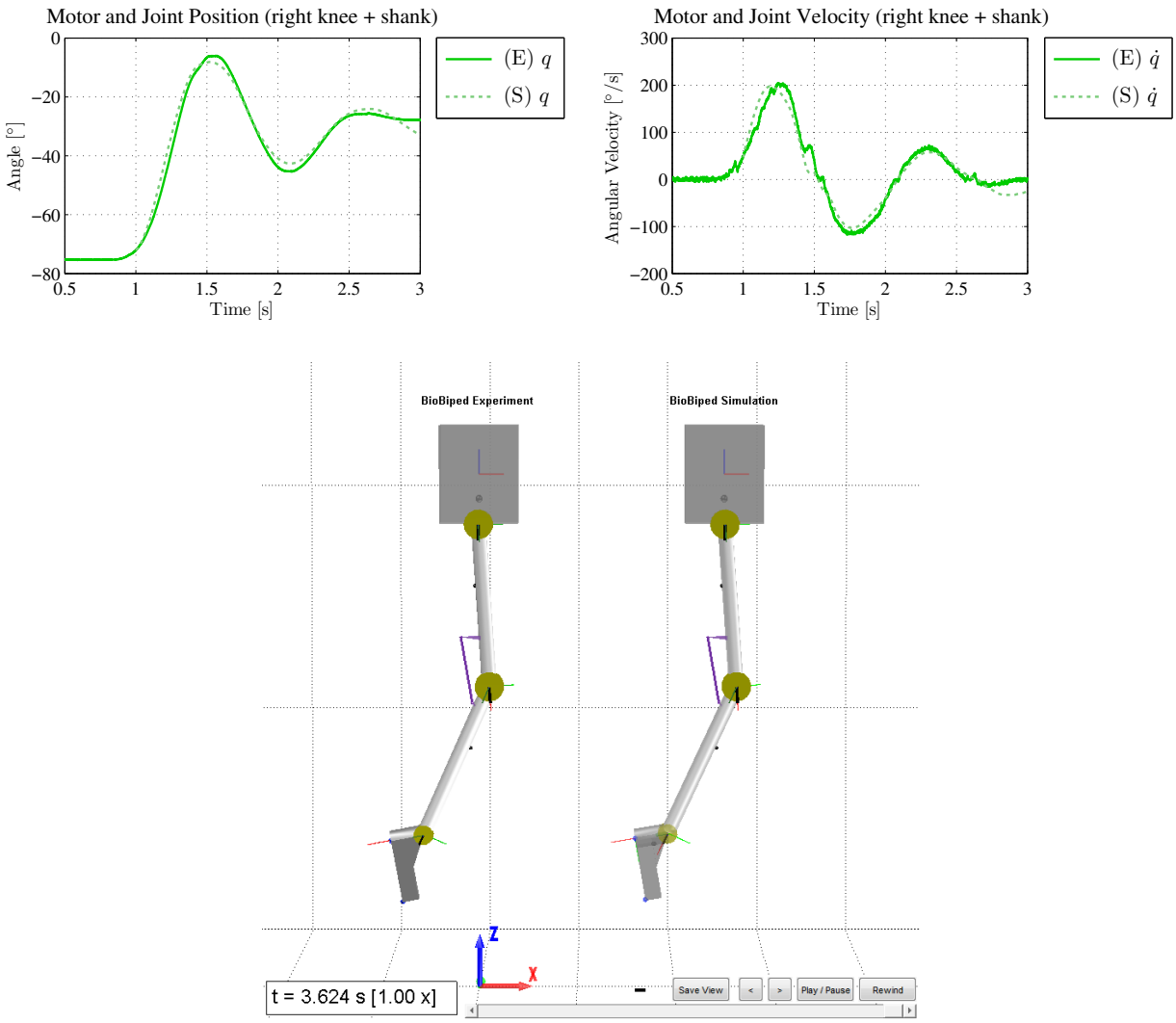

Figure 3.17.: Identification of the rigid body dynamics parameters for the knee joint in the presence of the passive antagonist PL.

and the measurements of the transmission, respectively. The viscous damping was estimated to take the value $d_{\mathrm{e,Hip}} = 0.05\,\mathrm{Nms/rad}$.

As for the knee and ankle actuation, the kinematics of the actuators, i. e., the location of the spring-tendon fixations and of the pulleys on the segments, were measured and readjusted during the studies, as the spring-tendon fixations tend to move slightly from their original position during experiments. Additionally, the corresponding motor offsets for the zero position had to be determined. The spring stiffness data were extracted from the manufacturer's data sheet. As mentioned in Section 3.4, transmission friction is neglected for the nonlinear actuators. The transmission ratio changes nonlinearly based on the implemented model equations. Therefore, the purpose of the following experiment was to collect data from the real robot and repeat the experimental setup in simulation, rather than identifying a parameter. We considered the knee actuator with integrated VAS and PL tendons. The stiffness of VAS and PL were $7.9\,\mathrm{N/mm}$ and $3.2591\,\mathrm{N/mm}$, respectively. The motor started to pull the tendon at the rest angle $q_0 = 58.9°$. Snapshots of this experiment and the corresponding simulation are illustrated in Fig. 3.18. The knee motor was controlled to follow the same motor trajectory as in the experiment. As can be

seen from Fig. 3.19, the joint position signals of the real and simulation model, as well as the velocities, match both qualitatively and quantitatively well, without the necessity of any further parameter tuning.

3.7.3 Full Robot Model including Ground Contact Dynamics

Finally, after validating these sub-models, a direct comparison of the real to the simulated hopping robot was carried out. Note that the ground contact model is a further component of the full robot model that was separately validated in a different work [87]. For the details of the validation of the contact model see the Appendix A.

The motors of the robot platform were controlled to perform two-legged hopping motions. In addition to the motor and joint position and velocity signals, the total GRF of both legs were measured by a force plate. Subsequently, in order to compare the real and simulated robot model, the motors of the simulation model were controlled to track the actual motor position signals of the robot experiment. Snapshots of the animation are given in Fig. 3.24.

As can be recognized, the GRF of the robot experiment overlap quite well with the GRF of the simulation model (cf. Fig. 3.20). The several peaks at the beginning of each pattern are assumed to be due to the oscillation of the force plate, which can be avoided by additional padding in future experiments. Due to the experimental setup in simulation, the motor trajectories match quite well (cf. Fig. 3.21, 3.22, 3.23). But, more interestingly, the position signals agree qualitatively for almost each joint. For the knee joint the signals overlap even quantitatively. These good agreements can be also observed from the diagrams illustrating the voltage trajectories. The grey colored areas in the motor torque diagrams in each figure indicate the poor current measurements in one direction, respectively, for the hip motor in both directions. Despite these problems, we were able to achieve a good agreement of the simulation with the real robot model.

3.8 Summary and Further Perspectives

In this chapter, we presented the METArob simulator, which is specifically designed for the requirements of musculoskeletally actuated robotic systems. The design problem for a vast number of possible passive and active actuator combinations requires a simulation environment with a database of musculoskeletal actuators that easily enables the creation and comparison of robot models actuated by different types of actuators. This simulation tool, which is based on a high-level scripting and technical computing language, uses object-oriented design to enable easy comparison of different actuation designs in simulations and experiments. With the advent of musculoskeletal systems and the questions related to them, such simulators are important for tackling the design and motion control issues. The publication of the simulator code is in preparation, so that other research groups can also benefit from this environment.

A further emphasis of this chapter was directed at the development of mathematical models that enable a systematic analysis of the interactions of actuators and joints by MBS dynamics simulations at a high level of detail. The BioBiped1 robot is characterized by a highly nonlinear complex actuation system consisting of electrically driven and passive tendons spanning one or two joints with various setting possibilities for the spring stiffness, attachment point, and rest angle of each muscle-tendon unit. The characteristic curves of motor and joint torques, as well as moment arms, are highly nonlinear, depending on the coupled joint angle. For biarticular

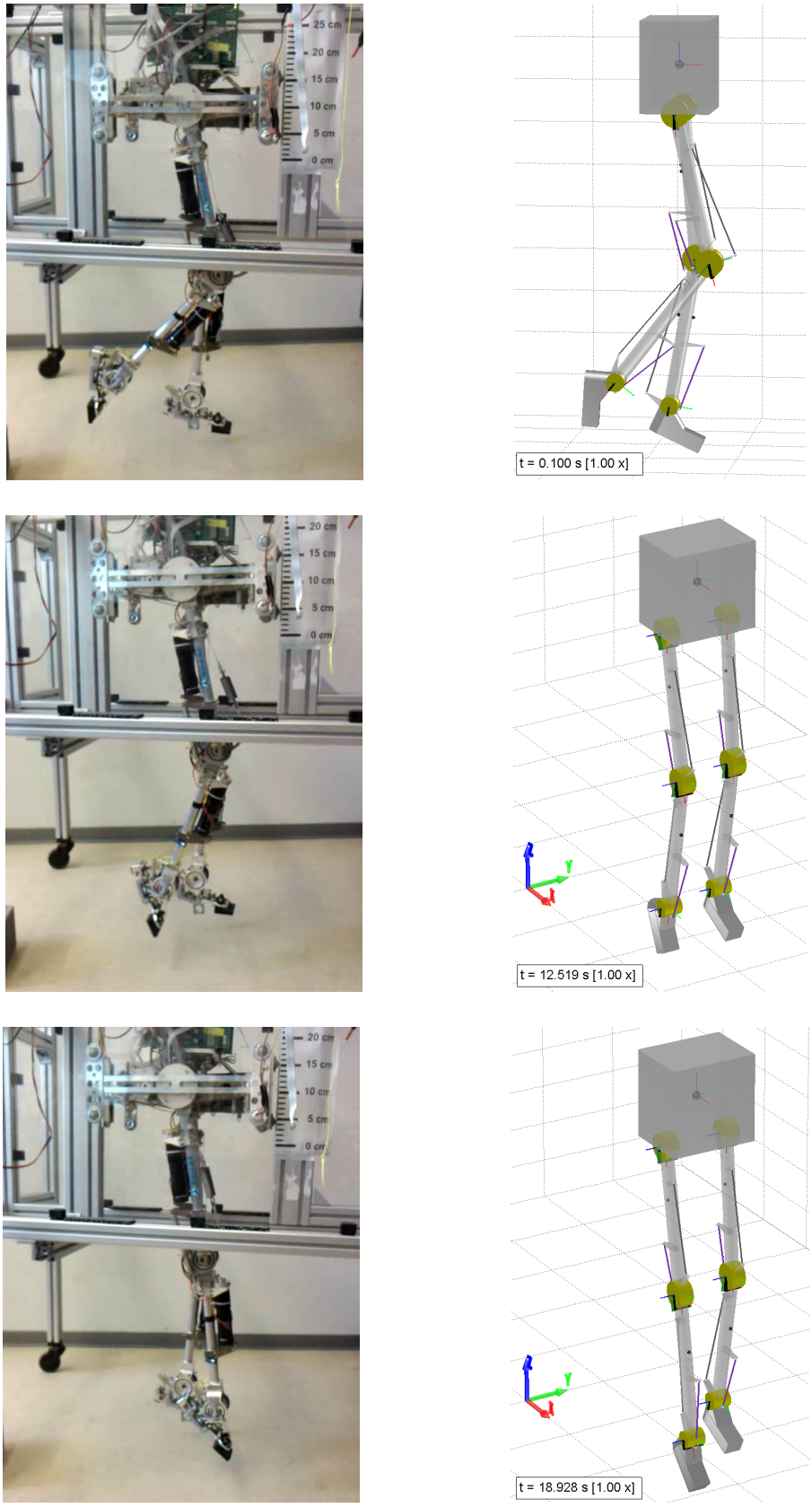

Figure 3.18.: Experimental setup for the identification of the knee transmission dynamics: snapshots of the experiment (left) and of the corresponding simulation (right). From top to bottom, the beginning, an intermediate position, and the final position of the movement are displayed.

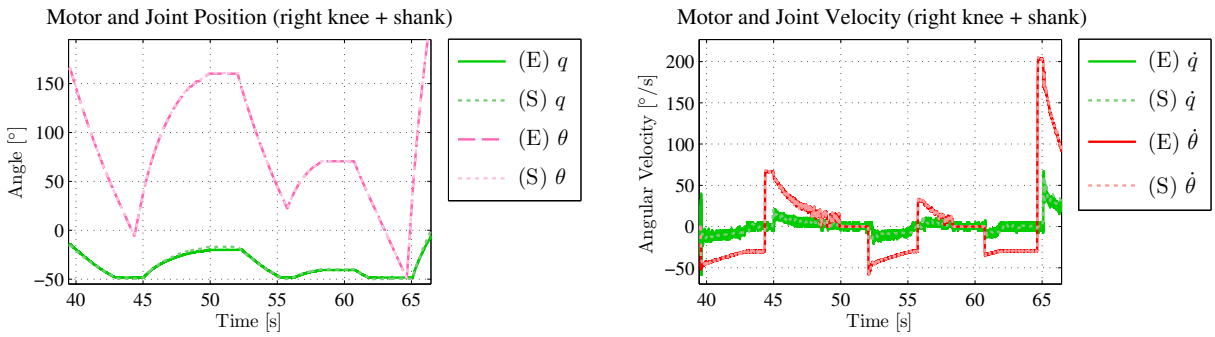

Figure 3.19.: Identification of the knee transmission dynamics with the motor and joint position signals in experiment (E) and simulation (S).

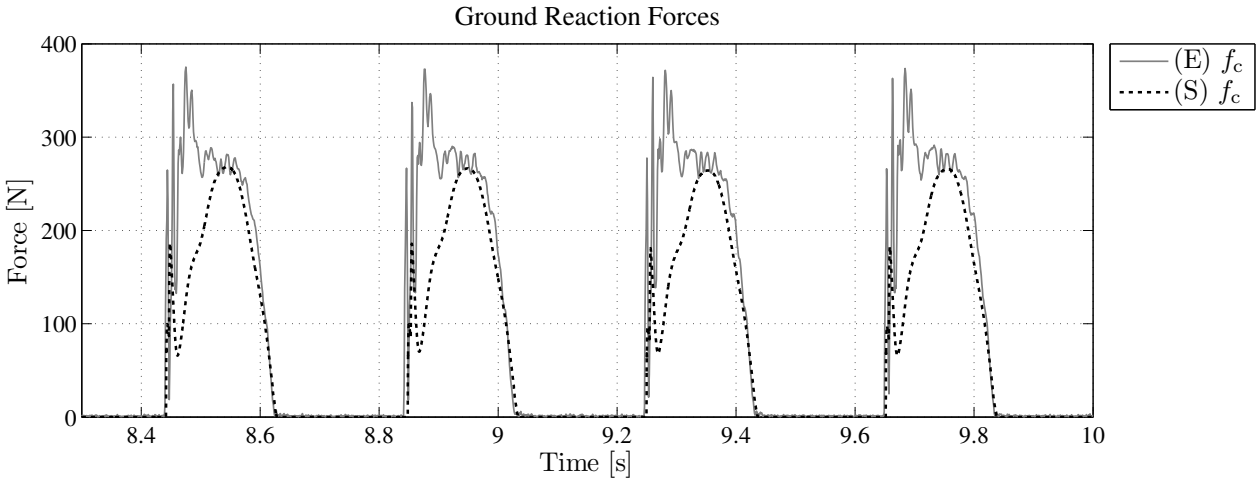

Figure 3.20.: Identification of the full robot model: GRF of the real and simulated robot.

tendons, these curves vary, based on two joint angles. To recognize cause-effect relationships in such a complex robot motion dynamics, we also presented the detailed MBS dynamics model of the BioBiped1 robot model. The working principles and detailed mathematical models for the active and passive, mono- and biarticular elastic tendons of the electrically actuated BioBiped1 robot were derived from the classical mechanical principle of virtual displacement and work. To validate the proposed models, we investigated the output torque functions and the characteristic curves extensively, to check the plausibility of the results. The mathematical approach presented here is not limited to the specific construction of BioBiped robots. The models can be used in MBS dynamics simulations to study the specific roles of muscles mentioned in biomechanical literature and their optimal layout and parameters.

Furthermore, due to the underlying ground contact modeling, forces can be measured in two dimensions, i. e., the normal and friction. Additionally, the possibility of stick-slip effects, which occur particularly during bipedal locomotion, is considered by the modeling approach. The model was also experimentally validated. The penalty-based approach makes it possible to extend the model easily to 3-D and surface contacts, which becomes interesting as soon as the lateral constraining mechanisms for the external stabilization of BioBiped1 are no longer needed.

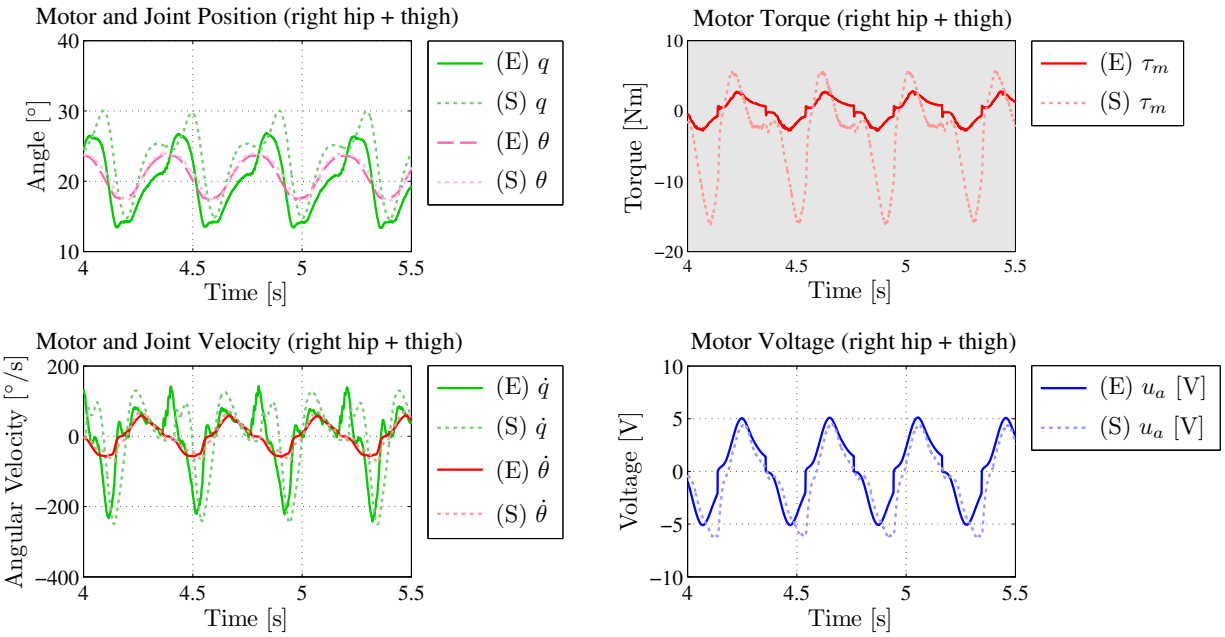

Figure 3.21.: Identification of the full robot model: hip trajectories of the real (E) and simulated (S) robot.

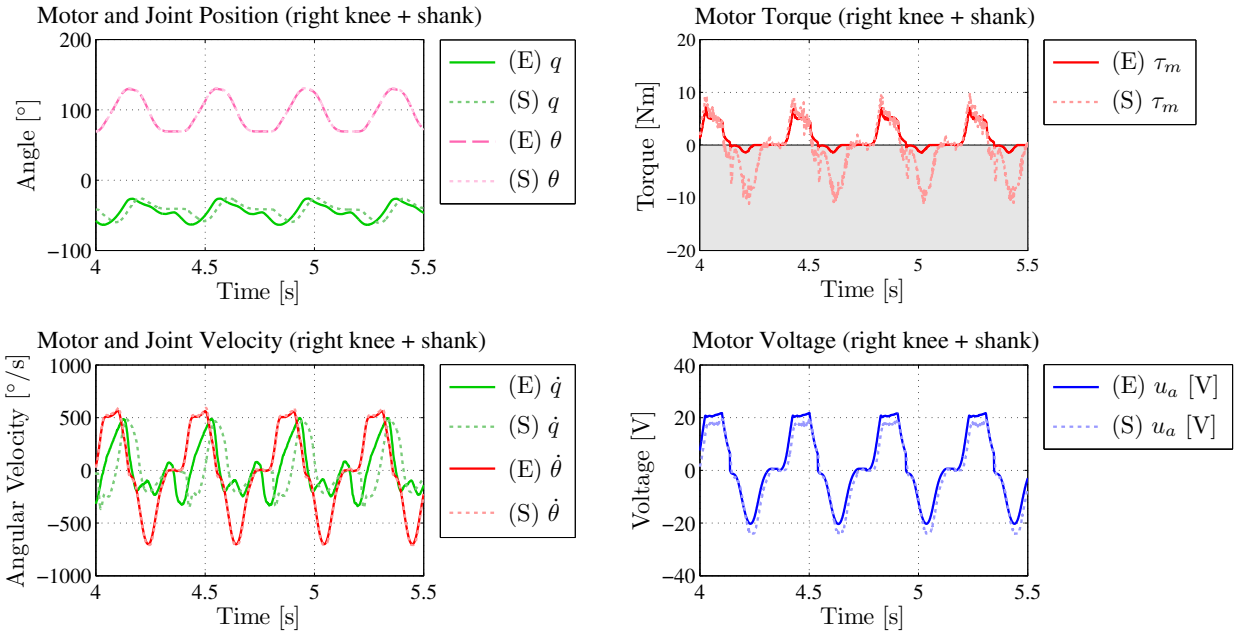

Figure 3.22.: Identification of the full robot model: knee trajectories of the real (E) and simulated (S) robot.

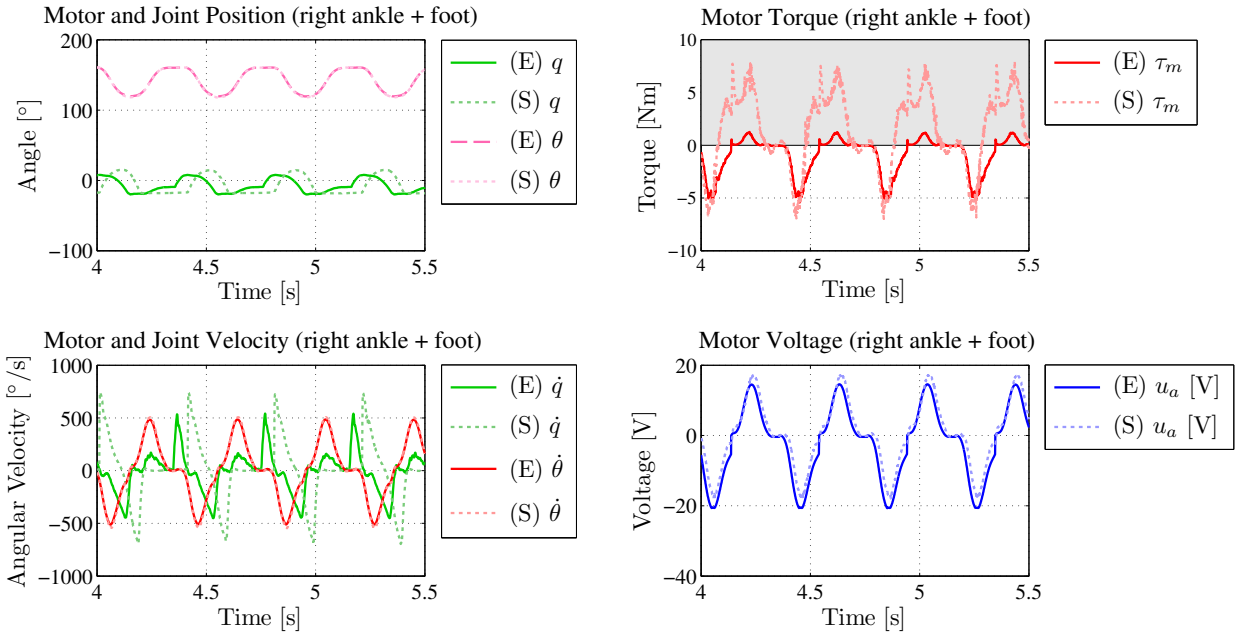

Figure 3.23.: Identification of the full robot model: ankle trajectories of the real (E) and simulated (S) robot.

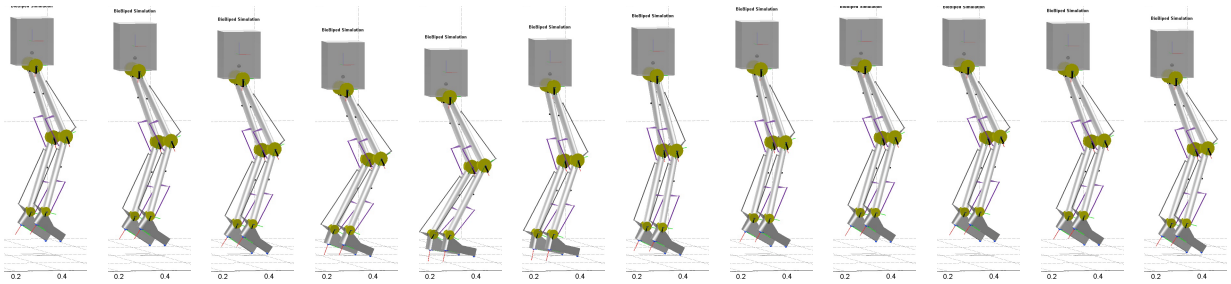

Figure 3.24.: Snapshots of the animated robot experiment for the identification of the full robot model.

Finally, using extensive experimental data, we validated the full robot model. The simulator and model can be further enhanced by an interface to the real hardware to carry out hardware-in-the-loop optimizations and to investigate controller development.

3.9 Reference to Own Publications

A preliminary version of Sections 3.1, 3.3, and 3.5 was published in: Proceedings of the International Conference on Advanced Robotics 2011 [87]. The work presented in Section 3.5 was carried out in collaboration with Thomas Lens and published in [87].

A condensed version of Section 3.4 was published in: Proceedings of the IEEE/RSJ International Conference on Intelligent Robots and Systems 2012 [131].

4 Motion Generation and Control for Musculoskeletal Bipedal Robots

4.1 Literature Review and Strategy in this Thesis

This chapter addresses the challenging question of motion generation and control for a musculoskeletal biped with three-segmented legs driven by a number of active and passive, mono- and biarticular elastic tendons. Despite a recent increase in their popularity, such designs are, to date, quite rare, resulting in a research gap regarding suitable methods for trajectory planning and execution for these platforms, particularly with regard to the goal of an efficient controller that exploits the intrinsic system dynamics.

Conventional approaches for bipedal robot locomotion achieve impressively stable and versatile locomotion by using combined posture and motion controllers. Kinematic leg trajectories are generated from the body and the feet trajectories by applying inverse kinematics [59, 112, 74, 88, 155, 179]. With this approach, both walking and running motion capabilities have been demonstrated [161]. However, the gaits of these robots appear very stiff and even sophisticated impedance controllers cannot react quickly enough to changes in and unevenness of the ground. To improve the behavior of such stiff robots, Khatib *et al.* developed a torque to position transformer that produces torques instead of positions [78]. This mapping was successfully implemented on the ASIMO robot and combined with the balance control [182].

A large number of researchers, both in the robotics and graphics community, have also focused on applying human motion capture data to humanoid robots [30, 180, 156, 144]. Most of these approaches are restricted to the kinematic level.

Several authors have developed bipedal locomotion controllers using oscillator models, with and without coupling to the robot dynamics, to modulate sinusoidal patterns [165, 141, 110, 111]. However, designing robust controllers with coupled oscillators and manually tuning all open parameters to achieve a desired behavior can be a tedious task. In [114], a method for learning bipedal locomotion from human demonstration has been proposed. The frequency of the learned trajectories is adjusted, based on phase resetting using the dynamical movement primitives. With regard to machine learning techniques, reinforcement learning methods have been applied to optimize bipedal walking controllers [109]. In this context, optimal control is another technique that has been studied extensively for the purpose of motion generation and control in several robot systems [58]. Often, optimal control schemes are only concerned with trajectory planning and an open-loop optimization of the control commands. During execution, errors are corrected by simple proportional-integral-derivative (PID) controllers. Variations, such as adding the learned forward dynamics of the system under investigation, have been proposed, in order to improve the optimal feedback control commands and to resolve redundancies of the actuation system [104].

To realize dynamically hopping machines, Raibert developed a three-part state machine that controls the forward velocity, body attitude, and hopping height. The one-, two- and four-legged machines consisted of telescopic legs. By projecting the behavior of a two-segmented leg onto the dynamics of the SLIP model, it was possible to use the Raibert controller in the flight phase, in combination with virtual model control in the stance phase, to generate running motions on an articulated leg [69].

As mentioned earlier, the topic of motion generation and control for robots with musculoskeletally arranged compliant actuators has not yet been discussed extensively. The common aim of most studies involving a musculoskeletal robot design, to date, was a beneficial contribution of the implemented elasticities to the overall locomotion performance; in legged systems, particularly for jumping motions [62, 118]. For pneumatically actuated systems, basic feedforward controllers for the operation of the valves have been employed, based on ground contact sensing to realize walking, running, and jumping motions [63]. The timely operation of the valves, based on experimental tuning, was reported as being particularly important because, otherwise, the actuators interfered with each other. Slow walking motions have been realized in the pneumatically driven Lucy robot by using joint trajectory tracking control.

Iida *et al.* showed, in simulation and experiment, that a bipedal locomotion model, JenaWalker I, consisting of three-segmented legs with four tension springs referring to the GAS, BF, RF, and TA muscle, can generate both walking and running behavior [71] by simple sinusoidal control of the hip motors. Based on these insights, a large-scale succeeding version, JenaWalker II, was developed and shown to also be capable of nearnatural walking and jogging behavior [152]. In the recently launched project centered around the FastRunner robot, the only SEAs in the hip, one for each leg, are commanded to also track a sinusoidal trajectory by means of a high gain proportional controller. Running motions were achieved so far in simulation.

The strategy regarding motion generation and control in this thesis is as follows. As stated previously,

- *the hopping and running gait are considered to be the main locomotory behaviors that a bipedal robot claiming to move in a more human-like way should be capable of. Therefore, the mechanical robot design under investigation here first needs to demonstrate the capability of dynamic hopping and jogging motions (see Section 1.2).*

Further, at this stage

- *postural stability control is neglected in favor of particularly thorough analyses of compliant leg behavior (see Section 1.2).*

Biomechanics research showed that it is possible to neglect the postural stability issue when focusing solely on the mechanical robot design and integration of compliance. It should be noted that the approach of the original passive dynamic walkers was based on the simple principle of inclined walking and did not consider the incorporation of mechanical elasticities into the design of the walkers, at first. Only further research pointed out that self-stability can be an important outcome if the system dynamics is well designed [47].

Additionally, the emphasis lies on a systematic analysis of the interactions of the implemented active and passive elastic tendons by MBS dynamics simulations at a high level of detail, using the mathematical models derived in Section 3.4. Determining the roles of the tendons requires a dedicated method. In order to compare different leg actuation designs for identical motions in the joint space, we will therefore derive a method for model-based motion generation combining feedforward and feedback control. Consequently, comparisons with other types of elastic actuation or even stiff actuation also become viable. Furthermore, such an approach is particularly required for realizing running motions, because it is difficult to identify the necessary actions of the motors and to design the motor controller appropriately for running motions.

In the following, we first formulate the required equations and review the necessary tools to generate and control periodic sinusoidal signals. Related issues are also discussed. In Section 3,

we present a novel method, based on the mathematical MBS dynamics model of BioBiped1, to realize complex motions such as running. In order to measure the locomotion performance, various criteria and their computations are introduced in Section 4. Subsequently, the model-based and motor excitation method are compared for the realization of in-place hopping motions in Section 5. Additionally, the model-based method is applied to generate and control human running motions in the BioBiped1 MBS dynamics model. Details, variation options, and advantages of the proposed scheme are discussed in Section 6. An important application of the model-based tracking method, namely the dimensioning of the actuators prior to a robot's construction, is suggested in Section 7. The chapter concludes with a summary of the contributions and a discussion of future research directions.

4.2 Open-Loop Oscillatory Excitation of the Actuators and General Techniques

Generating bipedal locomotion by linear or nonlinear oscillatory models is a well-studied concept [165, 111, 110]. Previous research on the JenaWalker I and II showed that, solely by basic sinusoidal oscillations of the hip motors and an appropriate coupling of the distal joints, i. e., knee and ankle joint, partially human-similar walking and jogging motions could be achieved [71]. A very basic sinusoidal oscillation of the hip actuation yielded patterns in the GRF, CoM position, and knee and ankle joint courses that were partially comparable to those of humans. Although the similarities could be greater, this is an important result indicating that the motion generation and controller for a bipedal robot can be greatly simplified, provided an appropriate embodiment of the robot. In fact, biological systems seem to have both a simpler and more robust locomotion strategy than existing bipedal robots [110]. Thus, it may be argued that the elasticity and compliance of a robot system support a simpler and more robust locomotion algorithm. As simple excitatory reference signals in conjunction with basic controllers are in line with the idea behind BioBiped1's complex compliant actuation system, we review in the following general techniques and issues related to sinusoidal excitation of complex systems.

4.2.1 Sinusoidal Function and Application

The function for a sinusoidal pattern can be of the form:

$$y(t) = A\sin(\omega t + \phi) + B \tag{4.1}$$

with amplitude A, angular frequency ω, phase ϕ, and offset angle B. An output signal by such function was used in [71] to excite in asynchronous order the hip joints. The application of these signals to the JenaWalker I system was straightforward due to the direct and linear coupling of servo motors to the hip joints. The signals desired for the joint motion were directly fed to the servo motors without any adaptation. In case of BioBiped1, however, a direct application is not feasible, in general, and depends among others on the target motions.

Nonlinear coupling of joint to an apparatus of different active and passive tendons
Each leg joint has its own actuation concept comprising one active motor and a number of passive tendons. These actuation concepts differ tremendously with regard to the resulting joint dynamics. Except for the b-SEA, the elastic transmission function of the u-SEA is highly nonlinear.

Additionally, with all the regulating screws highlighted in Section 3.4.7 and the ideas in mind to define design guidelines for future prototypes, it is advisable to apply motor or at least combined motor and joint control instead of pure joint control. Therefore, it is necessary to identify the corresponding motor actions.

Choosing the step frequency

The second problem is to choose the frequency of the trajectory appropriately such that the eigenfrequency of the system is not exceeded. Otherwise the system is not capable of tracking the desired motions and might become unstable. In general, the computation of eigenfrequencies is only carried out for linear or linearized systems. Even for the JenaWalker I with its underactuated legs, where only one actuator directly and indirectly drives three DoFs, this computation is not so straightforward and was, to our knowledge, not performed. But in the case of BioBiped1, the computation is particularly complicated, as the system is comprised of several subsystems, each with a different eigenfrequency. Each subsystem comprises a different, highly nonlinear actuation concept driving one or even two joints. Only the b-SEA in the hip joints can be considered as a linear system. For these reasons, it is very difficult to determine a unique operating frequency. Nevertheless, it would be beneficial to select the range of suitable operating frequencies. Therefore, to avoid linearizing this complex system about an operating point, which entails the further difficulty of finding such an operating point, we will approximate the overall actuation in each joint by a b-SEA. As an example, an overall actuation by a u-SEA, a passive monoarticular and biarticular tendon for the knee joint is approximated by a b-SEA. This requires, first, computing the output stiffness and, then, linearizing it such that a b-SEA with a fixed k_e represents the output characteristics sufficiently well.

Using this simplification, we can start now with our considerations for computing the eigenfrequency of an undamped, elastically actuated single rotational joint. The differential equation for the drive side of an undamped, elastically actuated joint can be written as follows:

$$I_\mathrm{eff}\,\ddot{q} = k_\mathrm{e}\,(\theta - q) \tag{4.2}$$

with I_eff denoting the effective inertia:

$$I_\mathrm{eff} = (l - x_\mathrm{CoM})^2\; m + I_{zz}\;. \tag{4.3}$$

l stands for the length and x_CoM for the x-component of the CoM of the corresponding link. The mass is represented by m and I_{zz} is the mass moment of inertia about the z-axis. Applying the Laplace transform to (4.2), we obtain

$$I_\mathrm{eff}\,s^2\,q(s) = k_\mathrm{e}\,(\theta(s) - q(s))\;. \tag{4.4}$$

By transforming the equation step-by-step, we can formulate now the transfer function for output $q(s)$ and input $\theta(S)$ as follows:

$$G(s) = \frac{q(s)}{\theta(s)} = \frac{1}{\frac{I_\mathrm{eff}}{k_\mathrm{e}}\,s^2 + 1}\,. \tag{4.5}$$

Comparing (4.5) to the equation of a second-order underdamped system,

$$G(s) = \frac{K}{\frac{1}{\omega_0^2}\,s^2 + 1} \tag{4.6}$$

we recognize the undamped natural angular frequency as:

$$\omega_0 = \sqrt{\frac{k_{\mathrm{e}}}{I_{\mathrm{eff}}}} \tag{4.7}$$

which equals, in the case of an undamped system, the eigenfrequency: $\omega_e = \omega_0$. Computing the minimal and maximal stiffnesses as well as effective inertias occurring in each leg by the above mentioned simplifications for each actuator system, lets us find by means of (4.7) four different eigenfrequencies: $\omega_{e1}, \omega_{e2}, \omega_{e3}, \omega_{e4}$. The operating frequency ω_e for the overall system then needs to ensure: $\omega_e \leq \omega_{ei}$ for $i = 1, \ldots, 4$.

The natural resonant frequency plays an important role for an optimal behavior of the robot. Another important factor influencing the optimal dynamic locomotion behavior is the chosen leg stiffness or joint stiffness. In particular, it should be noted that the computed resonant frequencies are only valid for the applied joint stiffnesses. The resonant frequencies differ based on the used joint stiffnesses.

Sine waves as representation of a running gait?

Neglecting the above two problems, there is still a third problem. In contrast to running, hopping appears as a comparably simple gait. One sine wave oscillating periodically between the flexed and extended joint configuration, as generated in (4.1), may represent sufficiently well the alternating flexion and extension of a joint which is necessary to generate synchronous hopping motions (cf. Section 2.3.1).[1] Using such a sine wave with different parameters for each leg joint to simultaneously flex and extend all leg joints can lead to stable dynamic hopping motions (cf. Section 5.3) provided that the mapping from joint to actuator space can be easily performed or, respectively, computed by inverse models (cf. Section 4.3). However, the human running motions presented in Section 2.3, are not expressible by a single sine wave, but rather by a superposition of sinusoids. Fourier analysis is an important analytical tool to decompose a periodic function into harmonics determining the fundamental frequency and the overtones. In order to better understand the running gait, which is considered as the main locomotion capability of BioBiped1, we will review this important technique in the following.

4.2.2 Fourier Analysis and Synthesis

Each signal has a characteristic frequency content, also referred to as the signal spectrum. It is a plot of all the harmonics in the signal from the lowest to the highest [31]. The lowest frequency is called the fundamental frequency; all other frequencies are integer multiples of the fundamental frequency, called overtones. Using the Fourier transform, it is possible to express any signal with alternating-current (AC) and direct-current (DC) component as the sum of a number of these harmonics, i. e., sine and cosine waves. Such an expression is called a Fourier series and has the following form:

$$V(t) = V_{\mathrm{DC}} + V_1 \sin(\omega_0 t + \theta_1) + V_2 \sin(2\omega_0 t + \theta_2) + \cdots + V_n \sin(n\omega_0 t + \theta_n) \tag{4.8}$$

where $\omega_0 = 2\,\pi\, f_0$ with f_0 denoting the fundamental frequency. θ_n is the phase angle of the nth harmonic, V_n represents the amplitude of the sine wave, and V_{DC} stands for the DC component.

[1] Although it should be noted that flexion and extension of all leg joints occur in humans with a slight time lag.

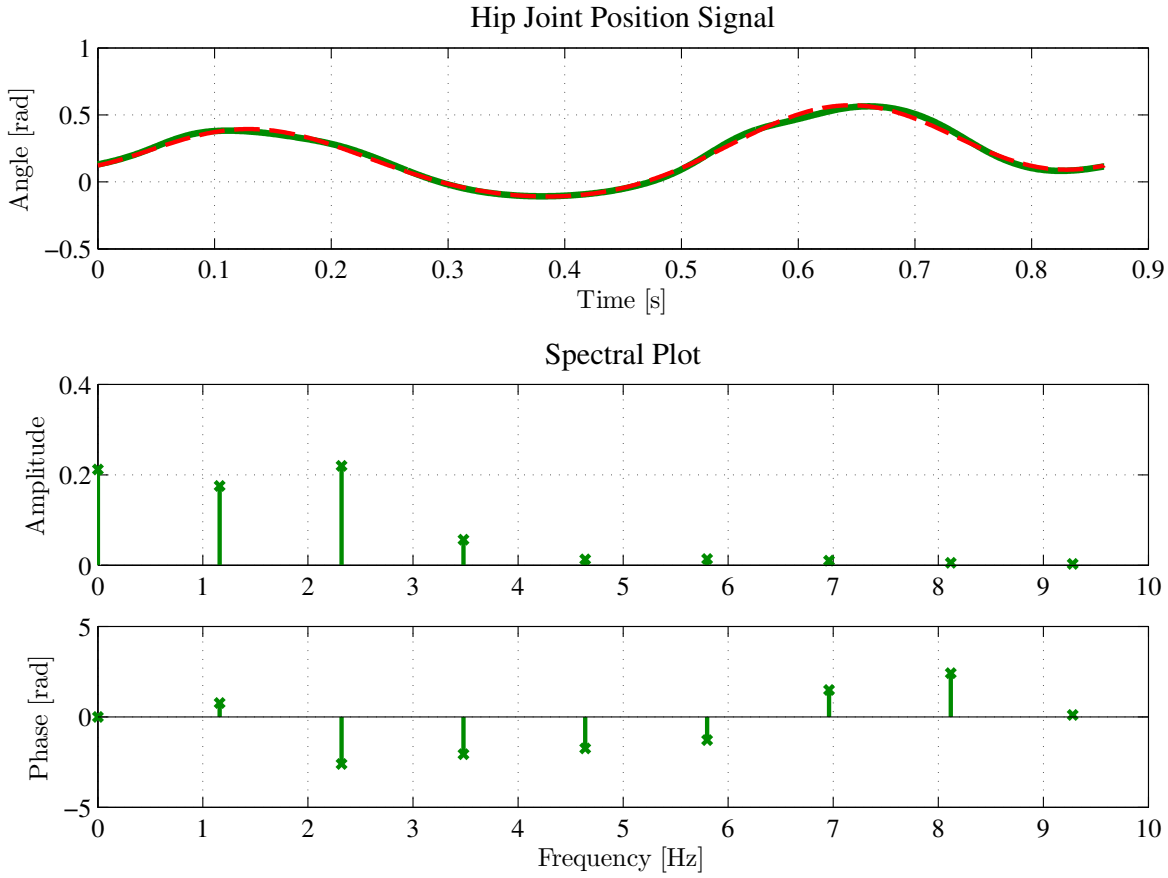

Figure 4.1.: Spectral plots illustrating the results of Fourier transformation of the human hip joint position signal: The topmost diagram depicts the original signal in green color. The red dashed line represents the signal gained by Fourier synthesis (cf. (4.9)). The diagrams below illustrate the results of the spectral analysis.

To understand better the human running gait, we apply this algorithm to the running motion of a human subject. The selected running gait is similar to that shown in Section 2.3.1. The chosen subject runs at step frequency 2.3209 Hz with step length 0.9052 m. The cycle time amounts to 0.8621 s and the duty factor is about 36 %. The subject has a particularly smooth GRF pattern, i. e., it has only a very small bump in contrast to the pattern in Fig. 2.3.

The spectral analysis of the sagittal joint position signals yields a broad spectrum of different frequencies and amplitudes for the underlying sinusoidal curves. In Fig. 4.1, 4.2, and 4.3 we have plotted separately the results of the frequency analysis for the joints of one leg. The topmost diagrams display the original joint position signal in green color and the reconstituted signal as red dashed line. Subsequently, the spectral plots are shown: Here the amplitudes and phases of each frequency component are plotted against the frequencies of all harmonics.

Analyzing the spectral density functions, the original position signal of each joint can be reconstituted as a combination of sine or cosine waves of the form given in (4.8). The harmonic plots in Fig. 4.1, 4.2, and 4.3 display all harmonics. For the signal reconstruction, however, we tried to reduce the necessary number of harmonics for a sufficiently well matching signal, in order not to complicate the reconstituted signal. Furthermore, keep in mind that exact position tracking is not the goal, particularly as the motions of human subjects differ tremendously even for the same gait and step frequency. Thus, we started testing with two harmonics which did

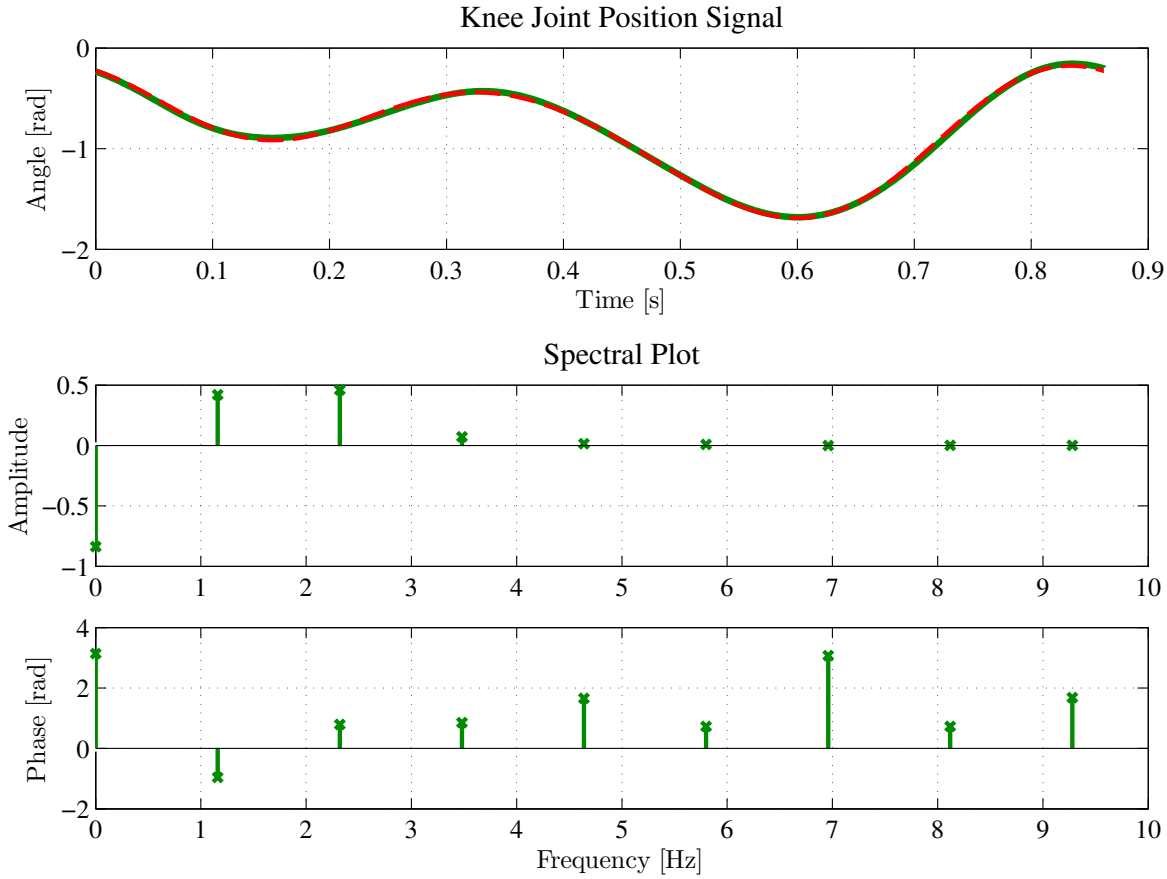

Figure 4.2.: Harmonic plots with the results of Fourier transformation of the human knee joint position signal: In the topmost diagram the original and reconstituted signal are illustrated by the green colored and the red colored, dashed line, respectively. The function equation of the reconstituted signal is given by (cf. (4.10)).

not yield a good result. A total of three harmonics seemed to be sufficient to represent the original signal; the addition of higher harmonics did not improve the curve of the original data. Therefore, we skipped the fourth frequency component. The good resemblance of the reconstituted signal and original signal can be observed in the first diagram of Fig. 4.1, 4.2, and 4.3. Using (4.8), the functions of the reconstituted position signal for the hip, knee, and ankle joint are:

$$\begin{aligned} V_{\text{Hip}}(t) =& 0.2118 + 0.175\,\cos(7.29\,t + 0.76) + 0.22\,\cos(14.6\,t - 2.61) \\ &+ 0.0567\,\cos(21.9\,t - 2.07) \end{aligned} \tag{4.9}$$

$$\begin{aligned} V_{\text{Kne}}(t) =& -0.8378 + 0.42\,\cos(7.29\,t - 0.962) + 0.461\,\cos(14.6\,t + 0.795) \\ &+ 0.0723\,\cos(21.9\,t + 0.852) \end{aligned} \tag{4.10}$$

$$\begin{aligned} V_{\text{Ank}}(t) =& 0.0257 + 0.281\,\cos(7.29\,t - 0.406) + 0.168\,\cos(14.6\,t - 2.64) \\ &+ 0.0688\,\cos(21.9\,t + 1.83) \end{aligned} \tag{4.11}$$

These signals belong to only one leg. The Fourier transformation now also enables us to analyze to which degree both leg motions are symmetrical. Therefore, we reconstituted the original signal for the other leg joints using again three harmonics:

$$V_{\text{Hip2}}(t) = 0.2125 + 0.166\,\cos(7.29\,t - 2.35) + 0.226\,\cos(14.6\,t - 2.59)$$

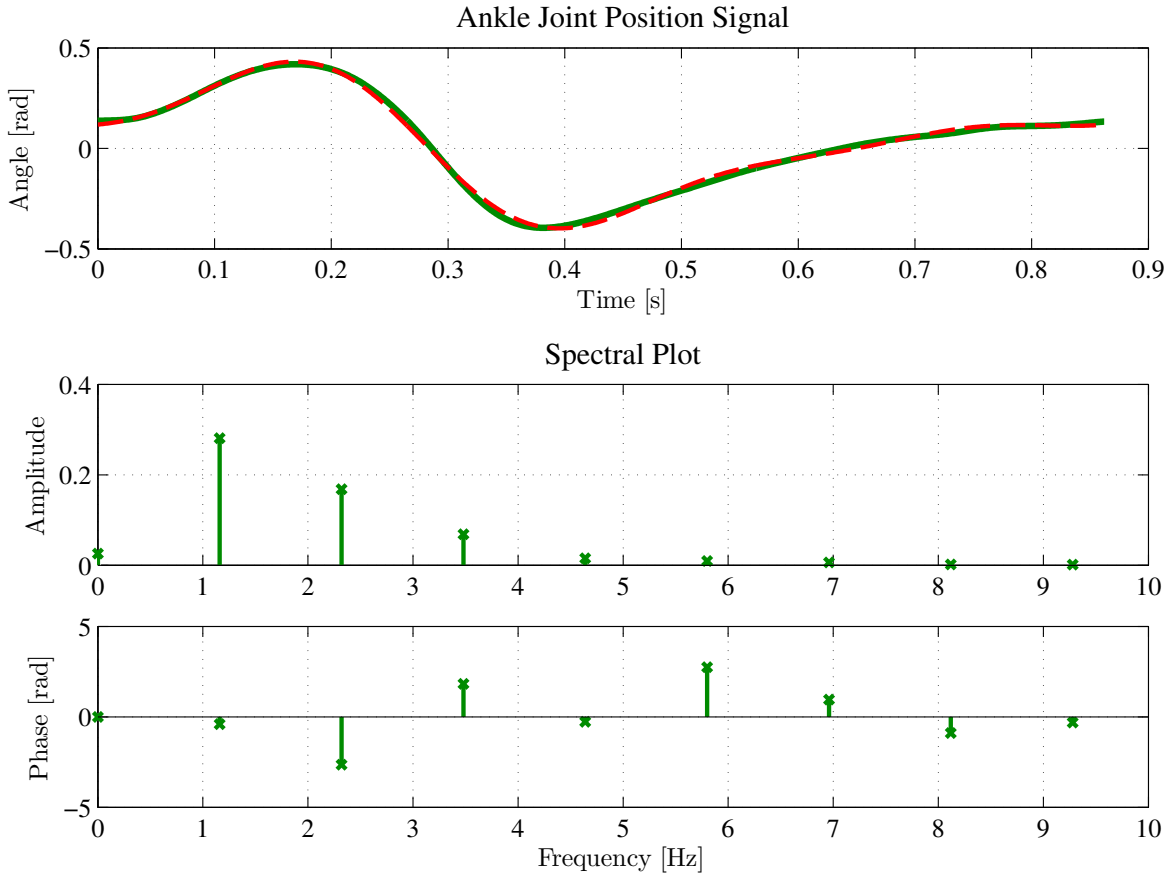

Figure 4.3.: Spectral density functions showing the results of the harmonic analysis of the human ankle joint position signal: The topmost diagram depicts the original signal in green color. The red dashed line represents the signal gained by Fourier synthesis (cf. (4.11)).

$$+ 0.05 \cos(21.9\,t + 1.14) \tag{4.12}$$

$$V_{\text{Kne2}}(t) = -0.8332 + 0.422 \cos(7.29\,t + 2.22) + 0.47 \cos(14.6\,t + 0.812)$$
$$+ 0.0553 \cos(21.9\,t - 2.3) \tag{4.13}$$

$$V_{\text{Ank2}}(t) = 0.0292 + 0.275 \cos(7.29\,t + 2.72) + 0.169 \cos(14.6\,t - 2.68)$$
$$+ 0.0701 \cos(21.9\,t - 1.4) \tag{4.14}$$

Comparing now (4.12)–(4.14) to (4.9)–(4.11), we recognize that neither the DC components nor the amplitudes of the cosine waves amount to the exact same values. There are smaller and larger deviations between the leg motions. Besides, the signals are not shifted by exactly 180°, but by 178.19° between the right and left hip joints, 182.32° between the knee joints, and 179.11° between the ankle joints. Thus, it is also clear that the leg motions are not completely symmetrical confirming the complexity of human motion characteristics analyses, as highlighted in Section 2.3. For the purpose of human motion data processing, it is therefore recommended to apply Fourier analysis and synthesis.

Finally, applying this technique enables us not only to better understand given reference data independently of any system dynamics influences but also to process a smooth differentiable function instead of the original reference signal. For further processing, such function should be clearly given preference, as it has infinitely many derivatives.

4.2.3 Proportional-Derivative Tracking Control of Designated Trajectories

As control algorithm, we apply the PD algorithm due to its simplicity and adequate performance. A PD controller does not require any information neither on the model structure nor on its parameters beforehand. However, if desired, model knowledge can be incorporated as feedforward input, which can be used either as gravity compensation term, to compensate for the amount of forces that create overshooting and an asymmetric transient behavior [22] or for inverse dynamics control purposes. The latter enhancement will be discussed in Section 4.3. Knowledge of the system's dynamics model can be also exploited to tune the controller gains. Additionally, the PD feedback control method was proven to be capable of globally stabilizing elastic joint robots about a reference position by using an adaptation for the gravity term [164].

For our studies, controllers for both stiff and elastic actuation are required. In order to determine the required motor voltages, we take into consideration the inverse dynamics of the corresponding actuator, i. e., in the case of BioBiped1 the geared DC motor. To recall the specific dynamics equations of a DC motor, we refer to Fig. 3.5 and 3.6 in Chapter 3. Note that, in the case of bidirectional hip joint actuation, the variable n_p also incorporates the additional elastic transmission ratio. In the case of unidirectional knee and ankle joint actuation, the elastic transmission ratio changes nonlinearly depending on the motor and joint position. The change in ratio is contained indirectly in the torques exerted on the motor and joint.

The PD tracking controller can of course also be applied to other designated trajectories than sinusoidal curves, such as constant signal trajectories (cf. Section 5.2).

Stiff Actuation Unit

In the case of a raw DC motor without further elastic transmission and, thus, directly coupled rigid joint-link structure of the robot, a model reduction takes place because the motor angle θ corresponds to the joint angle q. The number of state variables is reduced from four to two for each DoF. Using θ representatively for q, the formal form of the PD controller is:

$$\tau_\mathrm{m} = (\theta - \theta_\mathrm{d})\, k_\mathrm{p} + (\dot{\theta} - \dot{\theta}_\mathrm{d})\, k_\mathrm{d} + \tau_\mathrm{m,d} \tag{4.15}$$

with θ and $\dot{\theta}$ denoting the actual motor position and velocity, and θ_d and $\dot{\theta}_\mathrm{d}$ denoting the desired motor position and velocity. τ_m stands for the actual motor torque that needs to be applied to the actuation unit. It is possible to enhance the PD controller by a feedforward input for the desired motor torque, represented in (4.15) by $\tau_\mathrm{m,d}$. A scheme of the controller is depicted in Fig. 4.4.

Elastic Actuation Unit

In the case of elastic actuation, independent of the elastic transmission type, the number of control variables is doubled; for a complete description of the dynamics behavior of a joint, four state variables are required. The choice of the following variables for the motor and joint side, θ, $\dot{\theta}$, q, and $\dot{q}$, leads to the following form for the PD controller:

$$\tau_\mathrm{m} = (\theta - \theta_\mathrm{d})\, k_\mathrm{p} + (\dot{\theta} - \dot{\theta}_\mathrm{d})\, k_\mathrm{d} + (q - q_\mathrm{d})\, k_\mathrm{p} + (\dot{q} - \dot{q}_\mathrm{d})\, k_\mathrm{d} + \tau_\mathrm{m,d}\,. \tag{4.16}$$

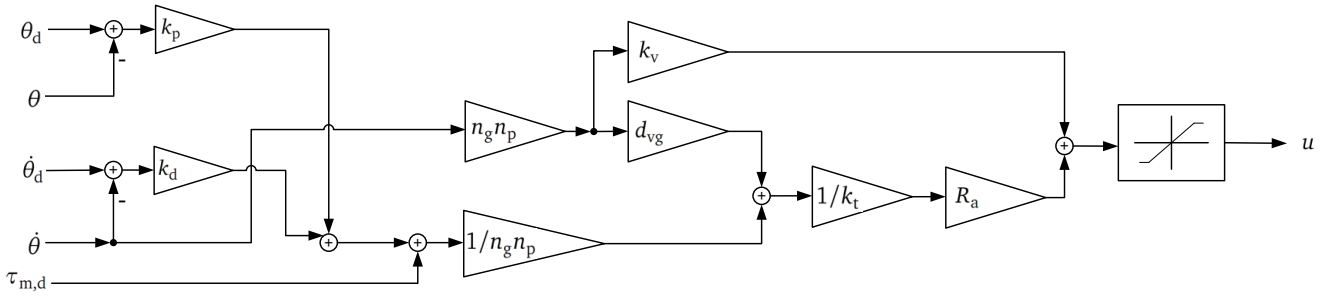

Figure 4.4.: Basic PD position tracking controller scheme for a stiff actuator including the inverse electrical dynamics model of a DC motor.

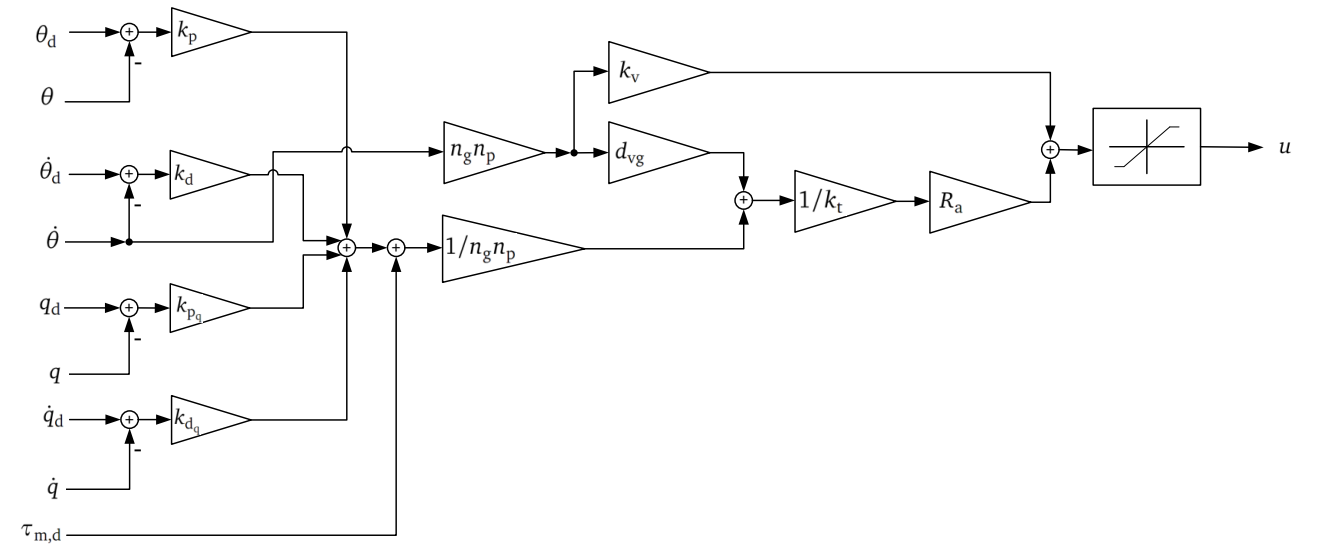

Figure 4.5.: Basic PD position tracking controller scheme for an elastic actuator including the inverse electrical dynamics model of a DC motor.

The controller scheme is illustrated in Fig. 4.5. The conversion of the controller output to motor voltages considers only the inverse model of the electrical dynamics of a DC motor. It does not include its mechanical components. Such components can be incorporated in the feedforward compensation term $\tau_{m,d}$, if desired (cf. Section 4.6). In such case, depending on the reference trajectories, in particular, the accelerations can be very noisy such that good filtering is strongly recommended beforehand. A Fourier analysis and subsequent synthesis yielding a differentiable function avoid such problems.

Concluding this section, we presented some techniques that are useful for a basic oscillatory excitation of a bipedal system. Studies based on this concept using BioBiped1's detailed MBS dynamics model will be presented in Chapter 5. In general, sinusoidal functions are a good choice for the generation of oscillatory signals as they have infinitely many derivatives. Frequency analysis techniques should be applied in any case to process raw signals, clean, and average given measurements from human subjects and, in this way, to find more simple representations of raw experimental data by means of a smooth function obtained by Fourier synthesis. As position controller, the classical PD algorithm can be utilized to track the reference signals.

Mapping of the reference signals from joint space to BioBiped1's actuator space, however, may turn out to be quite challenging for complex motions such as running. Therefore, the realization of complex, dynamic, and energy-efficient motions requires model knowledge which can also improve the trajectory tracking performance. In the following we will elaborate on a novel model-based motion generation and control method for musculoskeletal robots.

4.3 Methodical Approach to Model-based Motion Generation and Control

Since dynamic motions vary in complexity, knowledge of the joint activities during a cycle does not necessarily help to identify directly the required actuator actions, in particular, not for complex musculoskeletal dynamics systems [136]. An intuitive mapping from the joint angles to the corresponding motor action may yield fruitful results in the case of hopping motions, where it is clear that the joints perform almost simultaneous flexion and extension. But for the running gait, the transfer from the kinematic domain of joint actions to the dynamics domain of actuator actions is not straightforward and requires a more sophisticated approach. In particular, it requires first a Fourier analysis, as performed in the previous section, to better understand the human running gait in order to derive proper actuator signals. This issue can certainly be extrapolated to the walking gait and also matters for other motions that humans perform in their daily activities.

Thus, it is often desirable, also with respect to an in-depth comparability, to use human motion capture data. Indeed, a large number of researchers both in the robotics and graphics community have focused on applying human motion capture data to humanoid robots [30, 180, 156, 144]. However, the motions achieved did not include a floating base. Further, the approaches are all restricted to the kinematic level. In the context of the conventional concept of direct motor drive, this is a feasible method. But for robots with elastic transmission actuation dynamics, it is indispensable to take this idea further, i. e., to compute and transform the actuated joint torques to the torques required to act on the actuation side.

Another important motivation for the choice of model-based trajectory planning and execution lies in the fact that various configurations of the leg actuation may lead to the same joint functionalities. As elucidated in Section 2.7, one feature of BioBiped1's musculoskeletal actuation system is the high number of integrated redundant functionalities. For instance, the knee joint flexion is not only due to the passive action of PL, but might also result from the action of GAS or BF. Such redundant functionalities can be found for all joints both for flexion and extension, except for the ankle flexion. This feature makes motion control significantly more complex and unpredictable, if left to chance. Therefore, in order to ensure an efficient use of all tendons, it is advisable to determine beforehand their contributions. This way, minimized motor control efforts can be guaranteed. In order to gain extensive insights on the role of the tendons in different situations and to compare different leg actuation designs, it is necessary to define identical joint motions. We consider joint angle data as eligible reference data for identical joint motions.

Finally, in a long-term perspective, using human gait data yields also a better basis to compare to general biomechanical properties of human gait, as listed in Section 2.3 and 2.4. It allows to compare the activities of the active and passive tendons and to validate the observed dynamic effects in the lower limb system of human subjects using musculoskeletal bipedal systems. However, it should be noted that, at the current state of biomechanics research, inverse dynamics computations of human gait data are not yet very reliable [7]. Human gait data can be used to

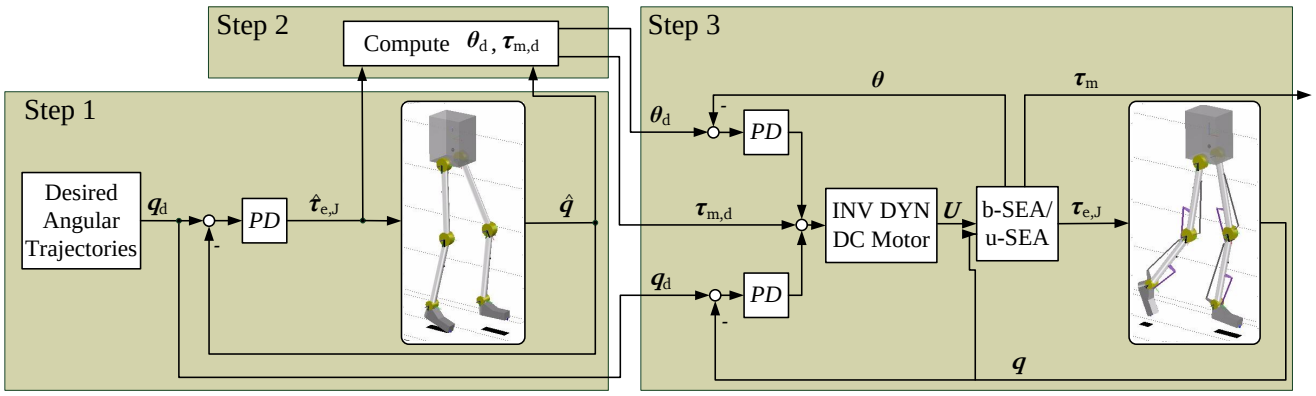

Figure 4.6.: Centralized model-based controller scheme to derive the required motor control signals for given joint reference trajectories.

determine the net joint moments required to generate a measured position, but it cannot deliver any information on the forces applied by a single muscle.

Additionally, it needs to be clarified beforehand how specific gait properties need to be scaled with respect to kinematics or dynamics parameters, such as weight or length of segments. A bipedal robot system, like BioBiped1, obviously lacks dynamics properties of the human leg merely due to nonexistent wobbling masses, not to mention other important components of the human neuromechanical lower limb system. Thus, only in a long-term perspective, provided the above issues have been solved, joint trajectories can provide useful reference data as a basis for comparisons among different human subjects and robot systems. Until then, joint trajectories provide a useful reference basis for comparisons of different leg actuation designs of the same system.

4.3.1 Problem Overview

The main question is: Given desired joint angular data $\boldsymbol{q}_d(t)$ for the hip, knee, and ankle joints of each leg, what are the corresponding motor control signals $\boldsymbol{\theta}(t)$ and $\boldsymbol{\tau}_m(t)$, respectively [133]? This problem can be solved by computing the inverse dynamics of the elastically actuated biped:

$$\boldsymbol{q}_d, \dot{\boldsymbol{q}}_d, \ddot{\boldsymbol{q}}_d \in \mathbb{R}^n \rightarrow \boxed{\text{INV DYN BioBiped1}} \rightarrow \boldsymbol{\theta}, \boldsymbol{\tau}_m \in \mathbb{R}^n \tag{4.17}$$

The computation of the inverse dynamics of a bipedal robot with a realistic nonstiff ground contact is a difficult problem, however. Deriving the motor torques solely from the joint angles includes the computation of the actuated joint torques first. But floating base inverse dynamics control is an ill-posed problem, since the constraint forces, that are required for solving for the actuated joint torques, depend on the applied actuation torques [103]. To address the originally posed question, we split up the computation of the inverse dynamics into several smaller steps without the need for actually computing directly the inverse dynamics of the elastic system. An overview of the designed controller scheme is given in Fig. 4.6 and the steps are described in the following.

4.3.2 Method

Step 1
Independent of the specific actuation, we first compute the forward dynamics of the rigid skeleton based on the time-varying joint reference trajectories $\boldsymbol{q}_{\mathrm{d}}$. The rigid robot can be considered as the decoupled link motion dynamics of the elastic robot whose dynamics will be computed in *Step 3*.

A low-gain PD controller determines the required joint torques, denoted as $\hat{\boldsymbol{\tau}}_{\mathrm{e,J}}$, to move the rigid robot model along the desired motion trajectories. The reference trajectories are specified in joint coordinates, starting from measurements of the current joint states $\hat{\boldsymbol{q}}$ during the forward dynamics computation (cf. Fig. 4.6). The tracking controller is designed so that the joint states $\hat{\boldsymbol{q}}$ track the desired motion $\boldsymbol{q}_{\mathrm{d}}$ as closely as possible. In general, the hat on the variables indicates variables that are computed during the forward dynamics simulation of the rigid skeleton.

The control inputs of each joint only depend on the measurement of the corresponding joint displacement and velocity. Coupling effects among joints, due to varied configuration during motion, are not considered. The forward dynamics is computed in MATLAB/Simulink using the ode23 (Bogacki-Shampine) solver with variable step size, relative tolerance 10^{-3}, and adaptive zero-crossing options. The outcomes of this step, $\hat{\boldsymbol{\tau}}_{\mathrm{e,J}}$ and $\hat{\boldsymbol{q}}$, are used in the next step.

Instead of a PD controller, it is also possible to apply suggested methods such as orthogonal decomposition to project the robot dynamics onto a reduced dimensional space [103] or model-based operational space control (see [113] for a review). The emphasis here, however, lies on a holistic approach to infer the required motor signals. In this respect, let us draw the attention to the next steps.

Step 2
Using the numerical results obtained from the forward dynamics computation of the rigid joint-link structure, $\hat{\boldsymbol{\tau}}_{\mathrm{e,J}}$ and $\hat{\boldsymbol{q}}$, the motor angles and torques required for the elastic robot, $\boldsymbol{\theta}$ and $\boldsymbol{\tau}_{\mathrm{m}}$, are computed analytically based on the corresponding models of the b-SEA, u-SEA, and the passive mono- and biarticular tendons, as presented in Section 3.4.

Computing the motor torques is rather straightforward. The mechanical motor dynamics is composed of a frictional term, an inertial term, and the torques induced by the elastic transmission on the motor, denoted as $\tau_{\mathrm{e,M}}$. The subscript $_d$ is introduced to indicate the variables desired and computed by this means:

$$\begin{aligned} \boldsymbol{\tau}_{\mathrm{m,d}} &= \boldsymbol{I}_{\mathrm{m}}\,\ddot{\boldsymbol{\theta}}_{\mathrm{d}} + \boldsymbol{D}_{\mathrm{vg}}\,\dot{\boldsymbol{\theta}}_{\mathrm{d}} + \boldsymbol{\tau}_{\mathrm{e,M}} \\ \text{with} \quad \boldsymbol{I}_{\mathrm{m}} &= \boldsymbol{E}\,(\boldsymbol{I}_{\mathrm{r}} + \boldsymbol{I}_{\mathrm{g}}) \\ \text{and} \quad \boldsymbol{D}_{\mathrm{vg}} &= \boldsymbol{E}\,(\boldsymbol{d}_{\mathrm{r}} + \boldsymbol{d}_{\mathrm{g}}) \end{aligned} \tag{4.18}$$

with $\boldsymbol{E}$ denoting the identity matrix. $\boldsymbol{I}_{\mathrm{r}}$ and $\boldsymbol{I}_{\mathrm{g}}$ refer to the rotor and gearbox inertia, respectively. $\boldsymbol{d}_{\mathrm{r}}$ and $\boldsymbol{d}_{\mathrm{g}}$ stand for the rotor and gearbox damping vectors, respectively. All motor variables and parameters are written with respect to the joint side as reflected variables. Both $\boldsymbol{\tau}_{\mathrm{e,M}}$ and $\boldsymbol{\theta}_{\mathrm{d}}$ will be computed below. It should be noted that a related concept had been previously introduced by De Luca to describe the equations of motion of flexible manipulators [91]. In this thesis, these equations are used in a novel context for musculoskeletal bipedal robots.

Determining the motor position trajectories, however, is not straightforward and depends on the specific actuator concept. Let us consider a leg configuration with all proposed active and

passive tendons, as depicted in Fig. 2.10c. For the sake of simplicity, the joint output functions derived in Section 3.4.7 are listed in the following:

$$\tau_{\mathrm{e,Hip}}(q_{\mathrm{Hip}}, \theta_{\mathrm{Hip}}, q_{\mathrm{Kne}}) = \tau_{\mathrm{GLILIO}}(q_{\mathrm{Hip}}, \theta_{\mathrm{Hip}}) + \tau_{\mathrm{RF,Hip}}(q_{\mathrm{Hip}}, q_{\mathrm{Kne}}) + \tau_{\mathrm{BF,Hip}}(q_{\mathrm{Hip}}, q_{\mathrm{Kne}}) \tag{4.19}$$

$$\begin{aligned}\tau_{\mathrm{e,Kne}}(q_{\mathrm{Kne}}, \theta_{\mathrm{Kne}}, q_{\mathrm{Ank}}) = {} & \tau_{\mathrm{VAS}}(q_{\mathrm{Kne}}, \theta_{\mathrm{Kne}}) + \tau_{\mathrm{PL}}(q_{\mathrm{Kne}}) + \tau_{\mathrm{GAS,Kne}}(q_{\mathrm{Kne}}, q_{\mathrm{Ank}}) \\ & + \tau_{\mathrm{RF,Kne}}(q_{\mathrm{Kne}}, q_{\mathrm{Hip}}) + \tau_{\mathrm{BF,Kne}}(q_{\mathrm{Kne}}, q_{\mathrm{Hip}})\end{aligned} \tag{4.20}$$

$$\tau_{\mathrm{e,Ank}}(q_{\mathrm{Ank}}, \theta_{\mathrm{Ank}}, q_{\mathrm{Kne}}) = \tau_{\mathrm{SOL}}(q_{\mathrm{Ank}}, \theta_{\mathrm{Ank}}) + \tau_{\mathrm{TA}}(q_{\mathrm{Ank}}) + \tau_{\mathrm{GAS,Ank}}(q_{\mathrm{Ank}}, q_{\mathrm{Kne}}) \tag{4.21}$$

Using the measured joint angles and torques yielded in *Step 1*, we can solve (4.19)-(4.21) for the required motor positions $\boldsymbol{\theta}_{\mathrm{d}}$. The only terms that depend on the motor position are those caused by a b-SEA or u-SEA. That leaves a number of passive tendons that contribute to the joint dynamics in addition to the actuators. Their contributions can be determined based on the simulated joint angles $\hat{\boldsymbol{q}}$. Rewriting (4.19)-(4.21) with respect to the active terms we obtain:

$$\tau_{\mathrm{GLILIO}}(\hat{q}_{\mathrm{Hip}}, \theta_{\mathrm{Hip}}) = \hat{\tau}_{\mathrm{e,Hip}} - \tau_{\mathrm{RF,Hip}}(\hat{q}_{\mathrm{Hip}}, \hat{q}_{\mathrm{Kne}}) - \tau_{\mathrm{BF,Hip}}(\hat{q}_{\mathrm{Hip}}, \hat{q}_{\mathrm{Kne}}) \tag{4.22}$$

$$\begin{aligned}\tau_{\mathrm{VAS}}(\hat{q}_{\mathrm{Kne}}, \theta_{\mathrm{Kne}}) = {} & \hat{\tau}_{\mathrm{e,Kne}} - \tau_{\mathrm{PL}}(\hat{q}_{Kne}) - \tau_{\mathrm{RF,Kne}}(\hat{q}_{\mathrm{Kne}}, \hat{q}_{\mathrm{Hip}}) - \tau_{\mathrm{BF,Kne}}(\hat{q}_{\mathrm{Kne}}, \hat{q}_{\mathrm{Hip}}) \\ & - \tau_{\mathrm{GAS,Kne}}(\hat{q}_{\mathrm{Kne}}, \hat{q}_{\mathrm{Ank}})\end{aligned} \tag{4.23}$$

$$\tau_{\mathrm{SOL}}(\hat{q}_{\mathrm{Ank}}, \theta_{\mathrm{Ank}}) = \hat{\tau}_{\mathrm{e,Ank}} - \tau_{\mathrm{TA}}(\hat{q}_{\mathrm{Ank}}) - \tau_{\mathrm{GAS,Ank}}(\hat{q}_{\mathrm{Ank}}, \hat{q}_{\mathrm{Kne}}) \tag{4.24}$$

The right-hand sides of (4.22)–(4.24) now contain only the known total joint torques and the torques generated by the passive, mono- and biarticular tendons. These torques can be computed by means of the mathematical models given in Section 3.4. The left-hand sides represent the torques excerted by the active tendons and include the unknown motor positions as linear terms.

Consequently, we will focus in the following on the models of a b-SEA and u-SEA and solve the equations for the motor position. Let us start with the hip actuation. The torque transmitted by the b-SEA, representing the tendons GL-ILIO, is similar to the original SEA in its functionalities [126]:

$$\tau_{\mathrm{GLILIO}} = k_{\mathrm{e}} \left(\theta_{\mathrm{Hip}} - \hat{q}_{\mathrm{Hip}}\right). \tag{4.25}$$

where k_{e} stands for the constant torsional stiffness of the elastic spring. Due to the linearity of the transmission, the solution for θ_{Hip} is rather straightforward. Note that, for simplicity and consistent treatment, we neglect damping terms in the computation of the inverse dynamics. However, damping is incorporated in the motor, transmission, and joint dynamics for the forwards dynamics simulation of the complete model (cf. Section 3.4). Combining the solution of (4.25) for θ_{Hip} and (4.22) leads to the following function for the hip motor signal:

$$\theta_{\mathrm{Hip}} = \hat{q}_{\mathrm{Hip}} + \frac{1}{k_{\mathrm{e}}}\,\hat{\tau}_{\mathrm{e,Hip}} - \frac{1}{k_{\mathrm{e}}}\,\tau_{\mathrm{RF,Hip}}(\hat{q}_{\mathrm{Hip}}, \hat{q}_{\mathrm{Kne}}) - \frac{1}{k_{\mathrm{e}}}\,\tau_{\mathrm{BF,Hip}}(\hat{q}_{\mathrm{Hip}}, \hat{q}_{\mathrm{Kne}}) \tag{4.26}$$

In order to determine the full motor torques using (4.18), the transmission torques induced on the motor side are also needed. For this specific actuator, the transmission torques on motor and joint side are equal, i. e., $\tau_{\mathrm{e,M\,Hip}} \equiv \tau_{\mathrm{GLILIO}}$ holds for reflected variables.

The u-SEA of the knee joint has a more complex output torque function involving a cross product computation:

$$\tau_{\mathrm{VAS}}(\hat{q}_{\mathrm{Kne}}, \theta_{\mathrm{Kne}}) = {}^{K}\boldsymbol{\tau}(\hat{q}_{\mathrm{Kne}}, \theta_{\mathrm{Kne}}) \tag{4.27}$$

$$= \left({}^{K}\boldsymbol{p}_{\mathrm{KAJ}} \times {}^{K}\boldsymbol{F}(\hat{q}_{\mathrm{Kne}}, \theta_{\mathrm{Kne}})\right) \bullet e_Z \tag{4.28}$$

$$= \left({}^{K}\boldsymbol{p}_{\mathrm{KAJ}} \times \left(k_{\mathrm{e}}\, \Delta l(\hat{q}_{\mathrm{Kne}}, \theta_{\mathrm{Kne}}) \frac{{}^{K}\boldsymbol{l}(\hat{q}_{\mathrm{Kne}})}{\|{}^{K}\boldsymbol{l}(\hat{q}_{\mathrm{Kne}})\|}\right)\right) \bullet e_Z \tag{4.29}$$

Introducing two new variable names.

$$\boldsymbol{d} \equiv {}^{K}\boldsymbol{p}_{\mathrm{KAJ}} = \text{const.} \tag{4.30}$$

$$\text{and} \quad \boldsymbol{f} \equiv {}^{K}\boldsymbol{l}(\hat{q}_{\mathrm{Kne}}) \tag{4.31}$$

we can break down (4.29):

$$\begin{aligned}\left({}^{K}\boldsymbol{p}_{\mathrm{KAJ}} \times {}^{K}\boldsymbol{F}(\hat{q}_{\mathrm{Kne}}, \theta_{\mathrm{Kne}})\right) \bullet e_Z &= \underbrace{\underbrace{\frac{k_{\mathrm{e}}}{\|{}^{K}\boldsymbol{l}(\hat{q}_{\mathrm{Kne}})\|}}_{c_1} (d_1 f_2 - d_2 f_1)}_{c_4} \left(\underbrace{\underbrace{\left\|{}^{K}\boldsymbol{l}(\hat{q}_{\mathrm{Kne}})\right\|}_{c_2} - \underbrace{\left\|{}^{K}\boldsymbol{l}(q_{0\,\mathrm{Kne}})\right\|}_{c_3}}_{c_5} + r_{\mathrm{M}}\, \theta_{\mathrm{Kne}} \right) \\ &= c_4 (c_5 + r_{\mathrm{M}}\, \theta_{\mathrm{Kne}}) \\ &= c_4\, c_5 + c_4\, r_{\mathrm{M}}\, \theta_{\mathrm{Kne}} \end{aligned} \tag{4.32}$$

The left-hand side of (4.23) can now be substituted by the above solution (4.32):

$$\begin{aligned} c_4\, c_5 + c_4\, r_{\mathrm{M}}\, \theta_{\mathrm{Kne}} = \hat{\tau}_{\mathrm{e,Kne}} &- \tau_{\mathrm{PL}}(\hat{q}_{\mathrm{Kne}}) - \tau_{\mathrm{GAS,Kne}}(\hat{q}_{\mathrm{Kne}}, \hat{q}_{\mathrm{Ank}}) - \tau_{\mathrm{RF,Kne}}(\hat{q}_{\mathrm{Kne}}, \hat{q}_{\mathrm{Hip}}) \\ &- \tau_{\mathrm{BF,Kne}}(\hat{q}_{\mathrm{Kne}}, \hat{q}_{\mathrm{Hip}}) \end{aligned} \tag{4.33}$$

to solve for θ_{Kne}:

$$\begin{aligned}\theta_{\mathrm{Kne}} = \big(&\hat{\tau}_{\mathrm{e,Kne}} - \tau_{\mathrm{PL}}(\hat{q}_{\mathrm{Kne}}) - \tau_{\mathrm{GAS,Kne}}(\hat{q}_{\mathrm{Kne}}, \hat{q}_{\mathrm{Ank}}) - \tau_{\mathrm{RF,Kne}}(\hat{q}_{\mathrm{Kne}}, \hat{q}_{\mathrm{Hip}}) \\ &- \tau_{\mathrm{BF,Kne}}(\hat{q}_{\mathrm{Kne}}, \hat{q}_{\mathrm{Hip}}) - \underbrace{c_4\, c_5}_{W}\big) \underbrace{\frac{1}{c_4\, r_{\mathrm{M}}}}_{Z}\end{aligned} \tag{4.34}$$

Finally, to determine the full motor torques using (4.18), the transmission torques on the motor side need to be computed. In contrast to the b-SEA, the transmission system of the u-SEA exerts different torques on motor and joint side. For the motor side, the following formula is valid:

$$\tau_{\mathrm{e,M\,Kne}}(\hat{q}_{\mathrm{Kne}}, \theta_{\mathrm{Kne}}) = \begin{cases} -r_{\mathrm{M}} \left\|{}^{H}\boldsymbol{F}(\hat{q}_{\mathrm{Kne}}, \theta_{\mathrm{Kne}})\right\| & \text{for } \Delta l(\hat{q}_{\mathrm{Kne}}, \theta_{\mathrm{Kne}}) > 0 \\ 0 & \text{for } \Delta l(\hat{q}_{\mathrm{Kne}}, \theta_{\mathrm{Kne}}) \leq 0 \end{cases} \tag{4.35}$$

where ${}^{H}\boldsymbol{F}$ denotes the tendon forces in the S_H frame.

Due to the similar actuation concept the ankle motor signal can be derived in the same way. Therefore, (4.24) can be rewritten as:

$$\theta_{\text{Ank}} = \left(\hat{\tau}_{\text{e,Ank}} - \tau_{\text{TA}}(\hat{q}_{\text{Ank}}) - \tau_{\text{GAS,Ank}}(\hat{q}_{\text{Ank}}, \hat{q}_{\text{Kne}}) - W\right) \frac{1}{Z} \tag{4.36}$$

with the auxiliary variables

$$W \equiv c_4\, c_5 = \underbrace{\frac{k_{\text{e}}}{\left\|{}^{N}\boldsymbol{l}(\hat{q}_{\text{Ank}})\right\|}\left(d_1\, f_2 - d_2\, f_1\right)}_{c_4} \left(\underbrace{\left\|{}^{N}\boldsymbol{l}(\hat{q}_{\text{Ank}})\right\| - \left\|{}^{N}\boldsymbol{l}(q_{0\,\text{Ank}})\right\|}_{c_5} \right) \tag{4.37}$$

$$Z \equiv -\,c_4\, r_{\text{M}} \tag{4.38}$$

where $\boldsymbol{d}$ is represented by ${}^{N}\boldsymbol{p}_{\text{AAJ}}$ and $\boldsymbol{f}$ stands for ${}^{N}\boldsymbol{l}$. Note the negative sign in (4.38) which is due to the negative winding direction of the tendon in the ankle u-SEA. In the knee u-SEA the winding direction of the tendon is positive.

For the motor torques it follows:

$$\tau_{\text{e,M Ank}}(\hat{q}_{\text{Ank}}, \theta_{\text{Ank}}) = \begin{cases} r_{\text{M}} \left\|{}^{L}\boldsymbol{F}(\hat{q}_{\text{Ank}}, \theta_{\text{Ank}})\right\| & \text{for } \Delta l(\hat{q}_{\text{Ank}}, \theta_{\text{Ank}}) > 0 \\ 0 & \text{for } \Delta l(\hat{q}_{\text{Ank}}, \theta_{\text{Ank}}) \leq 0\,. \end{cases} \tag{4.39}$$

With these precomputed motor position and torque signals we can now proceed with the next step.

Step 3

In this last step, the forward dynamics of the complete MBS dynamics model including its complex actuation is simulated. The forward dynamics simulation uses the same solver settings as in *Step 1*. Each actuator is PD-controlled to track the motor positions $\boldsymbol{\theta}_{\text{d}}$. The motor velocities $\dot{\boldsymbol{\theta}}_{\text{d}}$ are obtained by numerical differentiation and filtering. The PD controller can be enhanced to also track the desired joint positions $\boldsymbol{q}_{\text{d}}$ resulting in a multi-variable control. This, however, requires a very careful setting of the controller gains which is an extra effort, particularly since the desired joint positions are indirectly captured in the transmission dynamics equations derived in *Step 2* for the motor positions and torques. Note also that including $\boldsymbol{q}$ and $\dot{\boldsymbol{q}}$ still does not lead to a full-state feedback controller, as the torso position, $\boldsymbol{p}_{\textbf{Torso}}$, the torso velocity, $\dot{\boldsymbol{p}}_{\textbf{Torso}}$, and the feet conditions, represented by $\boldsymbol{p}_{\text{T}}$ and $\boldsymbol{\chi}_{\text{T}}$, are not taken into account by this scheme (cf. Section 3.6). But it is also not the objective to apply a full-state feedback controller. Rather, the goal is to demonstrate the general applicability of the controller scheme to musculoskeletal robots in order to realize a desired motion.

The feedforward compensation term, represented by the computed torques $\boldsymbol{\tau}_{\text{m,d}}$, constitutes the most important component of this controller (cf. Fig. 4.6). Under the assumption of the correctness of the joint torques and positions obtained in *Step 1* for the rigid joint-link structure and the validity of the actuator models, the addition of this feedforward term substantially reduces the control effort. It unburdens the control loop because most of the necessary power converter

excitation can be generated in the feedforward path. The PD control law is required to provide only corrections and to respond to disturbances [35]. Note that it basically is also possible to choose between the two modes, either complete feedback control with high gain parameters tuned to track the reference signals very precisely or sole feedforward control exploiting the eigen dynamics. It should be also mentioned that the choice to control the motor positions instead of the torques is rooted in the possibility of instabilities at ground contact in the case of torque control. This is also a reason for the popularity of impedance over force control. In this context, position control does not automatically stand for energy inefficiency or stiff behavior. It depends on the way it contributes to the generated motion and also on the controller gains. This will be subject of further detailed discussion in the simulation and discussion section below (cf. Sections 4.5 and 4.6).

It should be also highlighted that, in the case of BioBiped1, voltage limitation is a quite critical parameter due to the pulse-width modulation which might be different for other robot platforms. For BioBiped1 this means that only the maximum voltages of ±24 V can be applied. Therefore, as shown in Fig. 4.6 and introduced in Section 3.4, the actuators, both b-SEA and u-SEA, are designed to take voltages as input variables. Beforehand, the necessary voltages are computed by the PD controller using the equations of the inverse motor dynamics, as described in Section 4.2.

4.4 Criteria for Locomotion Performance Evaluation

In Sections 2.3 and 2.4 we reviewed the key characteristics of human hopping, running, and walking gaits and highlighted the most important properties for the locomotion performance analyses carried out in this thesis. Aside from the joint angle curves of the sagittal hip, knee, and ankle joints during a cycle, as most important criteria, the energy consumption and the specific patterns of the resultant GRF will be analyzed. Additionally, to assess the degree of dynamic mobility, the duty factor and hopping height, respectively ground clearance, will be evaluated. It is also possible to get a notion of the global leg and internal joint dynamics based on the force-leg length and torque-angle curves. Note, however, as already scrutinized in Section 2.4, the goal is not to claim that a gait is human-like. These criteria shall mainly serve as benchmark for evaluating the performance of a gait and highlighting the differences among various gaits. In the following, an overview of suitable criteria and their computations is given.

4.4.1 Energy Consumption

From the robotics view point, energy consumption is one of the most important criteria for mobile, autonomously moving robots. From the biomechanics view point, it is even considered as a measure for the degree of “human-likeness” [24]. The classical formula from physics to determine the power is:

$$\begin{aligned} P(t) = u(t)\,i(t) &= \left(\frac{R_\mathrm{a}}{k_\mathrm{t}}\,\tau_\mathrm{m} + k_\mathrm{v}\dot{\theta}\right)\frac{\tau_\mathrm{m}}{k_\mathrm{t}} \\ &= \frac{R_\mathrm{a}}{k_\mathrm{t}^2}\,\tau_\mathrm{m}^2 + \frac{k_\mathrm{v}}{k_\mathrm{t}}\,\dot{\theta}\,\tau_\mathrm{m} \end{aligned} \tag{4.40}$$

The first term stands for the electrical system losses, representing the efficiency level of the motor. The second term computes the amount of power required for the mechanical work,

which, to be more precise, is given by $P_{\text{mech}}(t) = \dot{\theta}\,\tau_{\text{m}}$. Equation (4.40) includes, however, also the conversion of energy to work and gives us the total power consumed over a time period. Integrating this power over the time yields the total energy consumption: $E = \int P(t)\text{dt}$. If only the mechanical work amount, P_{mech}, is taken into account, we use the notation E_{mech}.

The current BioBiped1 hardware platform uses external power supply and does not have any electric energy recovery mechanisms. Therefore, only the positive components of the power trajectories, $P_+(t)$, will be used to compute the total consumed energy $E = \int P_+(t)\text{dt}$. For completeness, each diagram contains both amounts, negative and positive, in order to illustrate also the amount of losses. This measure is justified for comparisons of different gaits and simulation studies for the same robot and the same traveled distance.

Specific Resistance and Cost of Transport

For comparisons to other platforms or the human, it is necessary to incorporate, in addition to the output power, also the mass moved and the velocity attained to receive a fairer measure for the evaluation of the robot energetic performance [54]. Such measure was proposed by Gabrielli and von Kármán in 1950 and named the specific resistance ϵ [46]:

$$\epsilon = \frac{P}{mg\,v_{\max}}\,. \tag{4.41}$$

Instead of the maximum speed, Gegorio *et al.* introduced the more general measure [54]:

$$\epsilon(v) = \frac{P(v)}{mg\,v} \tag{4.42}$$

which allows to determine the energetics of a machine over an entire range of velocities. But often the better known definition, incorporating the energy used, E, for a traveled distance s, can be found:

$$c_{\text{et}} = \frac{E}{mgs} \tag{4.43}$$

It is known as the energetic CoT [85] and led to the formulation of the mechanical CoT which does not include the conversion of energy to work. The mechanical CoT, c_{mt}, does not consider the negative mechanical work either. As stated in [23], it is only of interest how much positive work has to be carried out by the actuators to realize a specific motion. The reason for this interesting, but also questionable definition is based on the achievements with the Cornell biped [24], a development of the same authors. Level-ground walking was shown to be possible with only little positive and zero negative actuator work. Therefore, as it is apparently feasible to completely avoid negative actuator work, only the positive mechanical work is taken into account for the computation of the c_{mt}. Another reason provided is to "isolate the effectiveness of the mechanical design and controller from the actuator efficiency" ([23], p. 1083). As however energy losses also occur during human walking, when, for instance, a foot hits the ground, this extreme definition is a bit ambivalent. In the end, it is also important how efficient the overall system behaves, which can be read off of the discrepancy between the c_{mt} and the c_{et}.

Note that (4.43) is only applicable to running or walking gaits where the robot or object is moving forward, but not for motions in place such as 1-D hopping. However, since comparisons to other machines are not discussed in this thesis, we will use throughout this thesis only the total power consumption as computed in (4.40) to derive the energy consumption for each motor and, in total, for given trajectories.

Kinetic and Potential Energy Fluctuations

Further related criteria in this respect are the kinetic and potential energy fluctuations. Particularly from the biomechanics perspective, these two measures are essential as they help to distinguish, for instance, running from the walking gait [89] (cf. Section 2.3) and, in this way, to determine the *energy restitution* from cycle to cycle.

To compute the potential energy of the robot's CoM due to the vertical velocity we use:

$$E_{\text{pot}} = m\, g\, h \tag{4.44}$$

with m and g denoting the total mass of the robot and the gravitational acceleration constant, respectively, and $h = z_{\text{CoM}}$. Instead, it is also possible to compute the potential energy of each link and determine the total potential energy of the robot's CoM as sum of the partial potential energies. The kinetic energy of the robot's CoM due to forward speed is determined as follows:

$$E_{\text{kin}} = \frac{1}{2}\, m\, v^2 \tag{4.45}$$

where v describes the velocity of the CoM in $\mathbf{R}^3$. Here, a partial computation of the links yields also the same result. The energy restitution ratio is then computed from one cycle to another cycle based on the maximum potential energy in each flight phase considering the potential energy when the robot is at rest.

4.4.2 Ground Contact Dynamics Related Measures

The GRF represent the reaction of the ground to the accelerations of all body segments [142] and provide a wealth of information: from the shape of the patterns to the impact forces. The shape of the patterns can be either "M-shaped" or camel-back for walking or single-humped for running and hopping. The normal impact forces, F_{N}, the sum of the normal forces at each contact point of a foot, let us indirectly compare the leg compliance. During running, the friction forces, F_{T}, the sum of all friction forces at each contact point of a foot, indicate the breaking torques after touch-down which switch to acceleration torques after the first half of stance phase to prepare the take-off (see Fig. 2.3). Finally, measures, such as the duty factor of the motion, can be derived which can indicate the gait type. However, similar to the pattern of the GRF, the computed duty factor must be interpreted with caution (cf. Section 2.3.3).

4.4.3 Hopping Height and Ground Clearance

The degree of dynamic mobility can be evaluated for hopping by the hopping height and for running by the ground clearance. The hopping height is determined by measuring the vertical fluctuations of the robot's CoM within a cycle. The CoM course during a cycle, $\boldsymbol{p}_{\text{CoM}}$, can be derived either by the GRF or updated by the according link CoM, $\boldsymbol{p}_{\text{CoM i}}$, via the following formula:

$$\boldsymbol{p}_{\text{CoM}} = \begin{pmatrix} \boldsymbol{x}_{\text{CoM}} \\ \boldsymbol{y}_{\text{CoM}} \\ \boldsymbol{z}_{\text{CoM}} \end{pmatrix}^T = \frac{\sum m_i\, \boldsymbol{p}_{\text{CoM i}}}{\sum m_i}\,. \tag{4.46}$$

Subsequently, the hopping height can be computed as the deviation of the apex, the maximum CoM position along the z-axis, from the minimum CoM position during leg compression within each cycle.

The ground clearance indicates the maximum distance between foot and ground during a flight phase. It is an indirect indicator of how dynamically the joint moves during a cycle. It can be read off of the z-coordinates of the corresponding foot contact points obtained by the simulations.

4.4.4 Force-Leg Length Curve

The global leg characteristics can be evaluated by means of the force-leg length curves, i. e., the relation of the resultant GRF and corresponding leg length. It is also referred to as the leg's work loop and indicates whether energy losses and supplies during the stance phase are in balance [89]. The leg length is defined as the distance between the CoM and center of pressure (CoP) of the foot. The coordinates of the CoP for each foot is calculated as the sum of all contact point positions scaled by the corresponding normal forces occurring at these points:

$$x_{\mathrm{CoP}} = \frac{\sum F_{\mathrm{N}i} p_{\mathrm{T}i}}{\sum F_{\mathrm{N}i}} \tag{4.47}$$

where $F_{\mathrm{N}i}$ stands for the normal forces at the i^{th} contact point and $p_{\mathrm{T}i}$ denotes the tangential position of the i^{th} contact point with respect to world coordinate system. The resultant GRF are obtained by:

$$F_{\mathrm{R}} = \sum F_{\mathrm{N}i} + \sum F_{\mathrm{T}i}. \tag{4.48}$$

4.4.5 Torque-Angle Curve

The force-leg length curve gives us only a notion of the leg stiffness. To get also an insight of the joint stiffness, the torque-angle curves can be analysed, similar to the ones shown in Section 2.3 for a human running and walking gait. Typically, the joint torques, normalized by body weight and body length, which is defined as the length from CoM to the CoP, are plotted against the joint angles of a complete gait cycle. Even for human running, however, it is hardly possible to find linear slopes. Only by a phasewise approximation, separating the loading and unloading phase during stance, for instance, linear stiffness values can be assigned. It has also been shown in a related study that a linear leg force-length relation does not necessarily entail linear joint stiffnesses [143].

4.5 Simulation of 1-D Hopping and 2-D Running Motions

In this section, the proposed model-based controller scheme is applied to the simulation model of BioBiped1 to realize hopping and running motions [136]. Since postural stability control is not dealt with, the upper body's motions are constrained to 1-D and 2-D for hopping and running motions, respectively. The forward dynamics of both rigid joint-link structure and the fully

Table 4.1.: Technical parameters of the geared DC motor in hip, knee, and ankle.

Motor torque constant	$k_t = 2.6 \cdot 10^{(-2)}\,\mathrm{Nm/A}$
Motor rotor inertia	$I_r = 3.3 \cdot 10^{(-6)}\,\mathrm{kg\,m^2}$
Motor speed constant	$k_v = 2.6 \cdot 10^{(-2)}\,\mathrm{Vs/rad}$
Motor armature resistance	$R_a = 0.611\,\Omega$
Gearbox ratio	$n_g = 66$
Gearbox inertia	$I_g = 7 \cdot 10^{(-8)}\,\mathrm{kg\,m^2}$
Rotor and gearbox viscous damping	$d_{vg} = 1.5 \cdot 10^{(-4)}\,\mathrm{Nms/rad}$

actuated BioBiped1 robot model is computed in MATLAB/Simulink using the ode23 (Bogacki-Shampine) solver with variable step size, relative tolerance 10^{-3}, and adaptive zero-crossing options.

The parameters of the deployed motor (RE30 Maxon motor, 60 W, 24 V) and planetary reduction gearbox (GP32C) are given in Table 4.1. All parameters, except for the gearbox viscous damping (cf. Section 3.7), are extracted from the data sheet. For the simulations in this section, the motor specifications for the maximum applicable voltages and available power are neglected, as the goal of this section is solely demonstrating the suitability of the proposed method for motion generation and control. This means that the controller outputs are not limited to ±24 V and, possibly, power consumptions higher than 60 W will be detected.

The contact model parameters are listed in Table 4.2. The gains for the PD control of the rigid joint-link structure and the fully actuated BioBiped1 robot model are given in Table 4.3. Since accurate position tracking is not the objective here, the gains are kept small in order to avoid high energy consumption.

The leg actuation design chosen for simulation of both hopping and running motion includes all tendons except for the biarticular ones (see Fig. 4.7). The hip is actuated by the deployed b-SEA without any further torque inputs by the biarticular tendons; the knee is actuated by the u-SEA VAS and the passive, monoarticular tendon PL; and the ankle is driven by the u-SEA SOL and the passive, monoarticular tendon TA. This specific actuation setup allows active actuation of all joints in both directions to extend and flex the legs. Redundant actuation cannot occur, as the biarticular tendons are not utilized. Studies involving additionally these important two-joint tendons are presented in Chapter 5. The actuation settings are summarized in the table of Fig. 4.7. The springs of the active tendons are selected based on human experiment data using the joint angular stiffnesses and maximum angular deflections during hopping at preferred height [39] and running at moderate speed (2 m/s) [89], as described in [132]. For the goal of demonstrating the suitability of the proposed motion pattern generation and control approach for hopping and running motions and discussing the practical issues, such spring selection can provide already good initial estimates of the required stiffnesses. A more sophisticated approach for selecting springs is discussed in Section 5.2. The actual springs of the antagonist tendons are computed to achieve proper gravity compensation (cf. Section 3.4.7).

Joint damping in hip, knee, and ankle is set to the constant value $d = 0.2\,\mathrm{Nms/rad}$. Recall that for simplicity the transmission dynamics model of the nonlinear u-SEA and of the passive tendons does not include any viscous damping parameter, in contrast to that of the linear b-SEA (see the table in Fig. 4.7).

Table 4.2.: Contact model parameters used for the simulations.

Vertical collision force constant	$k_c = 8 \cdot 10^3\,\mathrm{N/m}$
Collision damping coefficient	$\lambda_c = 10^4\,\mathrm{Ns/m^2}$
Sliding friction coefficient	$\mu_{fk} = 0.6$
Sliding friction to stiction transition velocity limit	$v_{stic} = 0.001\,\mathrm{m/s}$
Maximum stiction force coefficient	$\mu_{fs} = 0.8$
Horizontal ground interaction stiffness	$k_{fs} = 10^4\,\mathrm{N/m}$
Stiction damper	$d_{fs} = 40\,\mathrm{Ns/m}$

Table 4.3.: Controller gains used for the simulation of computer-generated hopping motions.

Joint controller gains of the rigid joint-link structure	
P-gain hip: $k_{p,Hip} = 100$	D-gain hip: $k_{d,Hip} = 2$
P-gain knee: $k_{p,Kne} = 80$	D-gain knee: $k_{d,Kne} = 2$
P-gain ankle: $k_{p,Ank} = 100$	D-gain ankle: $k_{d,Ank} = 0.5$
Motor controller gains of the BioBiped1 robot model	
P-gain hip b-SEA $k_{p,Hip} = 200$	D-gain hip b-SEA $k_{d,Hip} = 50$
P-gain knee VAS $k_{p,Kne} = 30$	D-gain knee VAS $k_{d,Kne} = 8$
P-gain ankle SOL $k_{p,Ank} = 30$	D-gain ankle SOL $k_{d,Ank} = 4$

4.5.1 Trajectory Planning and Execution for 1-D Hopping

As discussed previously in Section 4.2, a properly actuated system, such as that of BioBiped1, is expected to simplify the motion generation. For example, for realizing synchronous two-legged hopping motions, the application of sine waves to the motors may be sufficient, as the hopping movements can be regarded as periodic oscillations between a flexed and extended leg configuration. Yet, we also pointed out the problems inherent to such an approach and motivated the use of a model-based method that incorporates the actuation dynamics of the robot. Therefore, we will now compare these two methods with respect to the realization of 1-D hopping.

First, the open-loop oscillatory excitation method presented in Section 4.2 is applied to the simulation model of BioBiped1, with the parameter settings given above. The general procedure is as follows:

1. Choose the desired leg configuration for the flexion and extension phase, denoted as $\boldsymbol{q}_{\mathrm{flex}}$ and $\boldsymbol{q}_{\mathrm{ex}}$.
2. Compute the motor positions required to compensate the gravitational forces occurring at these configurations (cf. Section 3.4.7).
3. Where violated, change the spring stiffnesses (of the passive antagonist tendons) to enable gravity compensation.

Fixed settings			
Viscous damping of the transmission in hip: $d_{e,Hip} = 0.05\,^{Nms}/_{rad}$			
Ratio in hip $n_{p,Hip} = 2$ Ratio in knee and ankle nonlinearly changing	Stiffness in hip $k_{e,Hip} = 87\,^{Nm}/_{rad}$ Stiffnesses in knee and ankle see below		
Free settings			
Tendon	**Stiffness** [$^{N}/_{mm}$]	**Attachment** [number]	**Rest angle** [deg]
VAS	15.5	4	-70
PL	6.7	1	-70
SOL	13	4	15
TA	4.1	1	15

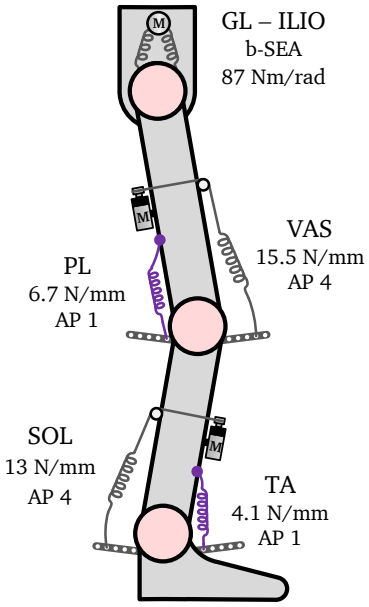

Figure 4.7.: Leg actuation design and parameter settings chosen for the simulation of computer-generated hopping motions.

4. Choose the fundamental frequency f_0.

5. Compute the amplitude A, angular frequency ω, phase ϕ, and offset angle B.

6. Generate the sinusoidal patterns, $y_{\text{Hip}}, y_{\text{Kne}}, y_{\text{Ank}}$, using (4.1), and their derivatives.

For this simulation run, motivated by experiences from experiments, the leg configurations are chosen as follows: $\boldsymbol{q}_{\text{flex}} = \left(q_{\text{Hip}}, q_{\text{Kne}}, q_{\text{Ank}}\right) = (26°, -63°, 13°)$ and $\boldsymbol{q}_{\text{ex}} = \left(q_{\text{Hip}}, q_{\text{Kne}}, q_{\text{Ank}}\right) = (13°, -26°, -13°)$. The fundamental frequency is set to $f_0 = 2\,\text{Hz}$. Using the controller gains in Table 4.3, the forward dynamics of BioBiped1 is simulated for ten cycles in MATLAB/Simulink using the ode23 (Bogacki-Shampine) solver with variable step size, relative tolerance 10^{-3}, and adaptive zero-crossing options. The motor and resulting joint position trajectories for all joints are displayed in Fig. 4.8. Steady state motions are achieved after approximately four cycles.

As proof of concept and validation, we now apply the model-based approach outlined in Section 4.3 utilizing the motions obtained by the open-loop motor excitations. Based on $\hat{\boldsymbol{\tau}}_{\text{e,J}}$ and $\hat{\boldsymbol{q}}$ from the above simulation run, we determine the required motor positions $\boldsymbol{\theta}_{\text{d}}$ and torques $\boldsymbol{\tau}_{\text{m,d}}$ by means of (4.18), (4.25)–(4.26), and (4.34)–(4.39), as described in *Step 2*. In order to ensure that irrelevant peaks are not unnecessarily tracked by the method, it is essential to smooth both the joint torques and positions, i. e., $\hat{\boldsymbol{\tau}}_{\text{e,J}}$ and $\hat{\boldsymbol{q}}$. This is particularly important, since the motor torques to be computed include implicitly the fourfold derivation of $\hat{\boldsymbol{q}}$. Therefore, using the Savitzky-Golay smoothing filter, successive sets of 50 data points (with window size of 0.05 s) are fitted to a first-order polynomial by the method of linear least squares [146]. Note that this filter is also applied to the computed signal $\boldsymbol{\theta}_{\text{d}}$ to avoid the introduction of further peaks into the motor torques $\boldsymbol{\tau}_{\text{m,d}}$. Subsequently, according to *Step 3*, the forward dynamics of the BioBiped1 robot is simulated in MATLAB/Simulink with the same solver settings and controller gains as in the previous simulation run.

In Fig. 4.9 snapshots of the BioBiped1 robot executing the hopping motions are illustrated. The GRF occurring during each cycle are aligned with the corresponding frames of the snapshots.

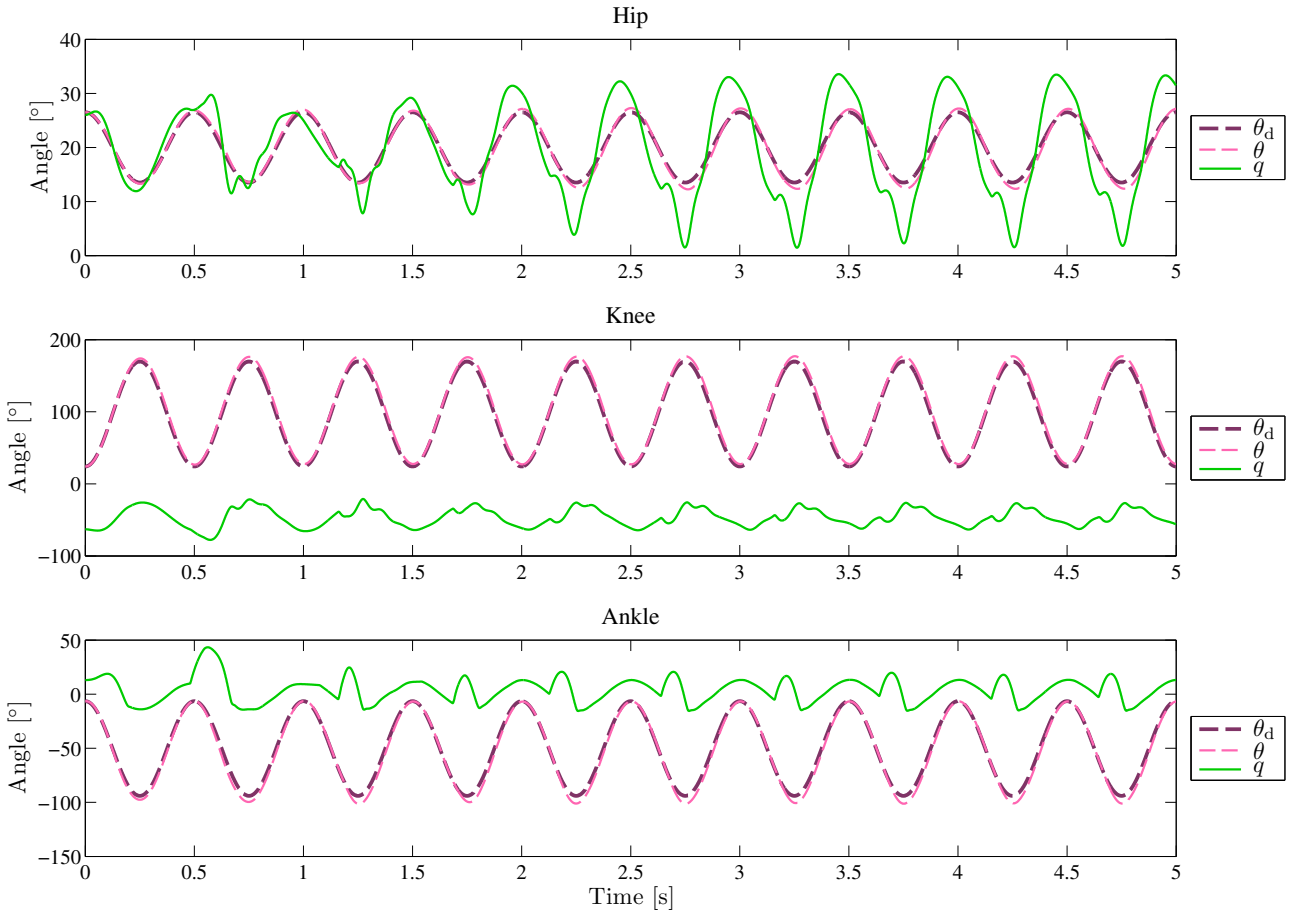

Figure 4.8.: Motor and joint position trajectories for the hip (top diagram), knee (middle diagram), and ankle joint (bottom diagram) generated by the open-loop excitation method in order to realize synchronous in-place hopping motions. θ_d is the desired motor position. θ and q stand for the actual motor and joint position, respectively.

As both legs move symmetrically, the GRF curves of both feet overlap. The robot starts directly in the stance phase from the ground in the flexed position, i. e., it is capable of an active push-off.

The realized motions match very well with the motions obtained by the open-loop feedforward excitation method, with respect to the evaluated dynamic performance criteria as well as the trajectory curves. To assess the quality of the trajectories, we computed the standard deviations of the actual joint and motor positions, the motor voltages, and currents as follows:

$$\sigma_x = \sqrt{\frac{1}{n}\sum (x_{OE} - x_{MB})^2}\,, \tag{4.49}$$

where n is the length of the vectors. The subscripts $_{OE}$ and $_{MB}$ are introduced to indicate variables computed by the open-loop excitation method and the model-based approach, respectively. The values for the standard deviations are listed in Table 4.4. Considering a motion range of about 30 ° in the hip, 40 ° in the knee, and 33 ° in the ankle joint, the obtained values for σ_q can be regarded as insignificant. In Fig. 4.10 we have depicted exemplary the results of the knee joint to give a broader insight into the performance of the model-based approach and the open-loop excitation method. The diagram in the left top corner displays the actual motor and joint positions of both approaches. The signals overlap very well reflecting the slight

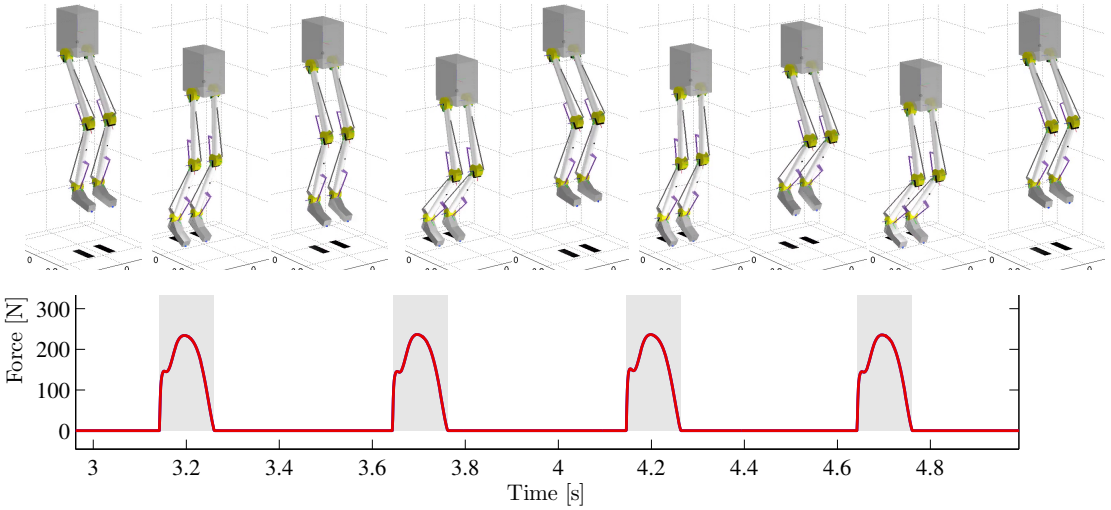

Figure 4.9.: Snapshots of the simulated BioBiped1 robot tracking the in-place hopping motions obtained by the open-loop excitation of the motors applying the model-based approach. Note that the robot's upper body movements are constrained to 1-D. The lower diagram depicts the corresponding patterns of the GRF of both legs, which overlap due to symmetric movements.

deviations of $\sigma_q = 1.7741$ and $\sigma_\theta = 4.2434$. Note also that particularly the motor position trajectory computed for the model-based approach agrees quite well with the open-loop desired motor position trajectory. Further important are the GRF in the left bottom corner which were displayed for the model-based approach already in Fig. 4.9. Here the GRF of both approaches are illustrated. The patterns match quite well with a time shift of about 1 ms. Finally, it is also important to compare the various torque signals, i. e., the total joint torques, $\tau_{e,J}$, the total torques generated by the motor, τ_m, the torques acting by VAS on the motor, $\tau_{e,MVAS}$, the torques acting by VAS on the joint, τ_{VAS}, and the torques induced by the passive tendon PL, τ_{PL}. In the model-based approach we have an additional torque signal, i. e., the computed motor torques $\tau_{m,d}$. These torques are displayed in the diagrams on the right-hand side. It can be noted that, on the one hand, the torque signals of both approaches agree very well. But even more important, in favor of the model-based approach, it should be mentioned that the actually generated motor torques, τ_m, match particularly well with the computed feedforward torques, $\tau_{m,d}$. This is very important, since the feedforward compensation term can highly reduce the efforts of the feedback control and, in this way, turn the motion control more robust in the presence of external disturbances.

In addition to the trajectory curves, we have also evaluated a few selected performance criteria as listed in Table 4.5: the hopping height, ground clearance, duty factor, and flight phase during each cycle and in average. The average duty factor and hopping height of the motions created by the model-based approach amount to 25.574 % and 0.261 m, respectively, which are very close to the average duty factor of 26.125 % and hopping height of 0.260 m generated by the open-loop excitation method. These criteria behave similarly also during each cycle. In addition, the values for the ground clearance and flight phase during each cycle and in average behave similarly.

In general, the slight variations from the expected joint angles are a result of the deviations existent between the actual motor positions of the open-loop excitation and model-based method.

Table 4.4.: Standard deviations of the model-based from the open-loop controlled excitation trajectories regarding the joint angle σ_{q}, motor angle σ_{θ}, motor voltage σ_{u}, and motor current σ_{i} .

Joint	Hip	Knee	Ankle
$\sigma_{\mathrm{q}}[^\circ]$	0.8252	1.7741	3.0559
$\sigma_{\theta}[^\circ]$	0.2789	4.2434	3.2883
$\sigma_{\mathrm{u}}[\mathrm{V}]$	0.22277	3.1192	1.7518
$\sigma_{\mathrm{i}}[\mathrm{A}]$	0.3485	0.8337	0.5538

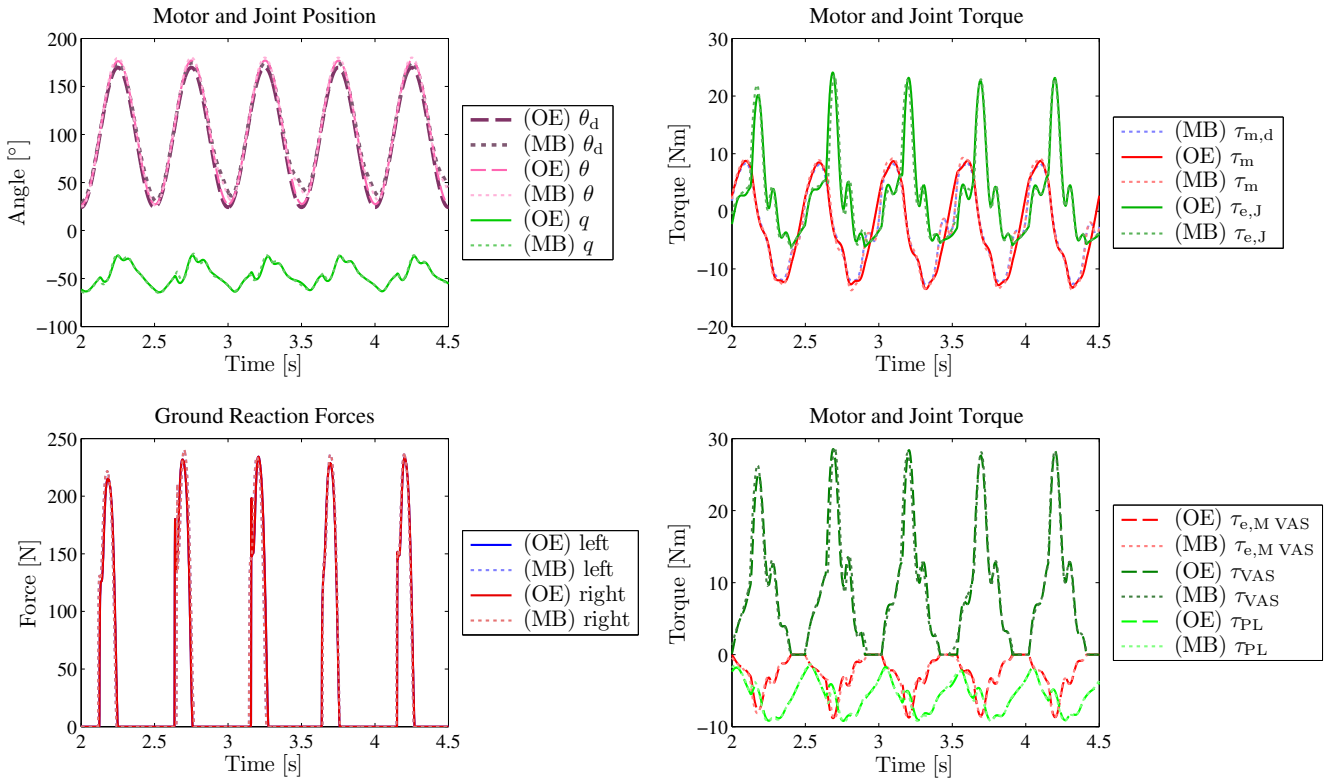

Figure 4.10.: Simulation results of the model-based approach (MB) and the open-loop excitation method (OE) for synchronous in-place hopping for the knee joint.

These variations are due to the filtering leading to slightly different configurations of $\boldsymbol{q}$ and $\boldsymbol{\theta}$ which in turn may cause tendon slackening subsequently. Obviously, the variations from the expected motor positions also cause deviations in the voltages and currents. Besides, the computation of the hip transmission torque does not consider any friction, which also causes slight deviations, as friction is included in the forward model. Hence, it is even more noteworthy that the model-based approach is capable of tracking the original motions incorporating dynamic ground contacts so well, without any ground contact sensing. The most important result is that the motions can be tracked without increasing the power consumption (see the values for σ_{u} and σ_{i}). This result confirms that the open-loop excitation method is not necessarily superior

Table 4.5.: Evaluation of various performance criteria in each cycle, from the first to the ninth cycle, comparing the model-based approach (MB) with the open-loop excitation method (OE).

Cycle	Method	1	2	3	4	5	6	7	8	9	Average
Hopping height [m]	**MB**	0.156	0.475	0.253	0.189	0.288	0.241	0.251	0.252	0.245	0.261
	OE	0.157	0.442	0.295	0.185	0.255	0.274	0.228	0.262	0.240	0.260
Ground clearance [m]	**MB**	0.083	0.364	0.232	0.180	0.260	0.227	0.236	0.237	0.232	0.228
	OE	0.081	0.330	0.268	0.176	0.229	0.248	0.214	0.240	0.223	0.223
Duty factor [%]	**MB**	36.623	26.857	21.971	26.164	23.408	24.138	23.553	23.705	23.743	25.574
	OE	39.112	27.434	21.333	26.471	24.462	23.654	24.689	23.782	24.187	26.125
Flight phase [ms]	**MB**	0.288	0.511	0.379	0.332	0.408	0.373	0.382	0.382	0.378	0.381
	OE	0.287	0.491	0.412	0.324	0.385	0.396	0.362	0.390	0.372	0.380

to the model-based approach with respect to the energy efficiency of a specific motion. Rather, considering the important issues discussed in Section 4.3, the model-based method provides even manifold advantages, in contrast to the open-loop excitation method:

- the transfer from the kinematic domain of joint actions to the dynamics domain of actuator actions,
- the opportunity to study different leg actuation designs for identical joint motions, and
- a basis to compare to general biomechanical properties of human gait and validate the observed dynamic effects in the lower limb system of human subjects.

Furthermore, running gaits, for instance, cannot be realized by means of the open-loop excitation method. The Fourier analysis of human running motions in Section 4.2.2 yielded the result that at least three harmonics are necessary to represent the original position signals of each joint. As a result, identifying the motor actions for more complicated motions requires a sophisticated approach. In the next section, we will, therefore, investigate the suitability of the model-based motion control method for achieving running motions.

4.5.2 Trajectory Planning and Execution for 2-D Running

Human running data were obtained from human gait experiments using an instrumented treadmill with force sensors and a camera system, consisting of eight high speed infrared cameras [89] (cf. Section 2.3). Kinematic data were collected from 21 human subjects [89]. The selected human subject gait is characterized by cycle time 0.7926 s, step frequency 2.5237 Hz, and duty factor 39.01 %. The reference motion consists of mean joint angles in the sagittal plane recorded at discrete time points during a running gait cycle and includes only single support phases, i. e., the running pattern is represented by an alternating sequence of single and nonsupport phases.

Table 4.6.: Controller gains used for the simulation of human running motions.

Joint controller gains of the rigid joint-link structure	
P-gain hip: $k_{\mathrm{p,Hip}} = 300$	D-gain hip: $k_{\mathrm{d,Hip}} = 16$
P-gain knee: $k_{\mathrm{p,Kne}} = 300$	D-gain knee: $k_{\mathrm{d,Kne}} = 16$
P-gain ankle: $k_{\mathrm{p,Ank}} = 300$	D-gain ankle: $k_{\mathrm{d,Ank}} = 16$
Motor controller gains of the BioBiped1 robot model	
P-gain hip b-SEA $k_{\mathrm{p,Hip}} = 400$	D-gain hip b-SEA $k_{\mathrm{d,Hip}} = 56.56$
P-gain knee VAS $k_{\mathrm{p,Kne}} = 200$	D-gain knee VAS $k_{\mathrm{d,Kne}} = 16$
P-gain ankle SOL $k_{\mathrm{p,Ank}} = 200$	D-gain ankle SOL $k_{\mathrm{d,Ank}} = 4$

As suggested in Section 4.2.2, we applied the Fourier analysis and synthesis technique to obtain a smooth function for the raw discrete trajectories. More importantly, this analysis also allowed us to scale the amplitudes of the selected harmonics which is quite essential, since the robot's dynamics and kinematics do not match those of the human subject. In this case, we scaled the amplitude of the first harmonic contained in the ankle joint position signal to enlarge the ankle motion range. In order to assess the proper scaling factor, we first carried out the forward dynamics simulation of the rigid joint-link structure as described in *Step 1*. The robot model was controlled to track the smooth trajectories with the controller gains given in Table 4.6. From the animations, it was recognized that the human subject is running with the feet very close to the ground which may not exactly apply to the real human subject. The measurement data are noisy and do not reveal the complete posture of the human subject on the treadmill, although the orientation of the trunk plays an important role. Yet, as humans we have the amazing capability of gaining quickly stability and sensing whether we need to change our legs' movements to avoid falling. These essential capabilities do not apply neither to the simulation nor the real robot model. Therefore, it is highly important to ensure beforehand that the trajectories created will not cause any unnecessary collisions with and bumps into the ground. By this iterative approach of testing and animating, we finally set the scaling factor of the first harmonics contained in the ankle joint position signal to 1.2. As for the contact model parameters, we had to adapt the vertical collision force constant increasing it by $2 \cdot 10^3\,\mathrm{N/m}$ to $k_{\mathrm{c}} = 10^4\,\mathrm{N/m}$. Furthermore, since the trajectories of the human subject were quite demanding for the robot model, the controller gains had to be modified to achieve a more accurate tracking (cf. Table 4.6).

Using the results of the forward dynamics simulation of the rigid body dynamics, $\hat{\boldsymbol{\tau}}_{\mathrm{e,J}}$ and $\hat{\boldsymbol{q}}$, we subsequently computed the required motor positions and torques. In the third step, the actuators of each leg joint were PD-controlled to follow the desired motor position signal $\boldsymbol{\theta}_{\mathrm{d}}$. Here again an iterative approach was required, since the leg actuation parameter settings chosen for the realization of the hopping motions were not suitable for the running motions. The robot would bump into the ground, as the hip stiffness was too soft; the hip motor was, therefore, not capable of tracking the reference trajectories. The leg actuation design remained the same, but the parameter settings were modified (cf. Table 4.11). Particularly the hip stiffness was increased to $k_{\mathrm{e,Hip}} = 600\,\mathrm{Nm/rad}$, which corresponds well to highly stiff hip joints in human running. Also the controller gains had to be modified to track more precisely the reference motor trajectories. The gear ratios of the ankle and knee motors were decreased to $n_{\mathrm{g}} = 22$, since the motor velocities

Fixed settings			
Viscous damping of the transmission in hip: $d_{e,Hip} = 0.05\,^{Nms}/_{rad}$			
Ratio in hip $n_{p,Hip} = 2$ Ratio in knee and ankle nonlinearly changing	Stiffness in hip $k_{e,Hip} = 600\,^{Nm}/_{rad}$ Stiffnesses in knee and ankle see below		
Free settings			
Tendon	**Stiffness** [N/mm]	**Attachment** [number]	**Rest angle** [deg]
VAS	15.5	4	-75
PL	8	1	-75
SOL	15.5	4	20
TA	6.7	1	20

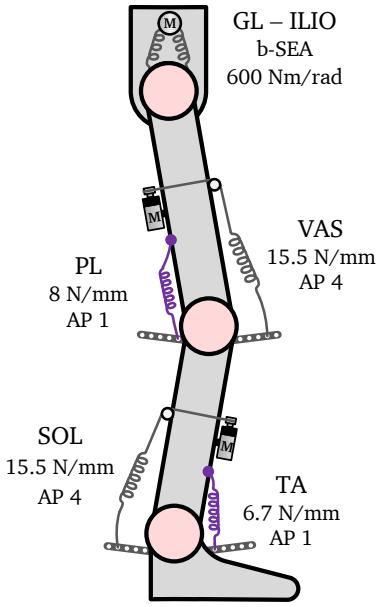

Figure 4.11.: Leg actuation design and parameter settings chosen for the simulation of human running motions.

would otherwise exceed the maximum motor velocities and, thus, the desired motions would not be feasible with BioBiped1's current motor specifications.

The final forward dynamics simulation determined the resulting joint motions depicted in Fig. 4.12 for the ankle and knee joint and Fig. 4.13 for the hip joint. Each foot alternately touches the ground and prepares for take-off. Clear flight phases where both feet are off the ground can be detected. Smaller bumps can be recognized during some stance phases which is due to the not perfectly suited trajectory for the robot model.

The generated motor torques match very well the computed motor torques, demonstrating the suitability of the model-based approach also for more complex motions like human running. The actuation requirements can be decreased by slowing down the commanded reference motions.

4.6 Discussion of the Proposed Model-based Method and Practical Issues

In the previous section, we applied the model-based approach outlined in Section 4.3 to computer-generated hopping-in-place and human running motions. It was shown that the approach is well capable of generating the required motor signals for given reference trajectories. More importantly, the motions can be tracked without increasing the power consumption required for open-loop motor excitations (see the values for σ_u and σ_i in Table 4.4). Furthermore, it could be demonstrated that the centralized model-based control approach is adept at generating and controlling also more complex gaits such as human running motions.

By this method, the complete musculoskeletal system including all active and passive actuators and the corresponding dimension space can be studied. For instance, it is possible to vary the spring stiffness or the attachment point of all integrated tendons for a defined leg actuation design and to recompute the changed actuation requirements demanded of the motors. Being well suited for systems with highly redundant actuation, the method allows to precompute each tendon's contribution to the overall joint dynamics and motor dynamics and to adapt the

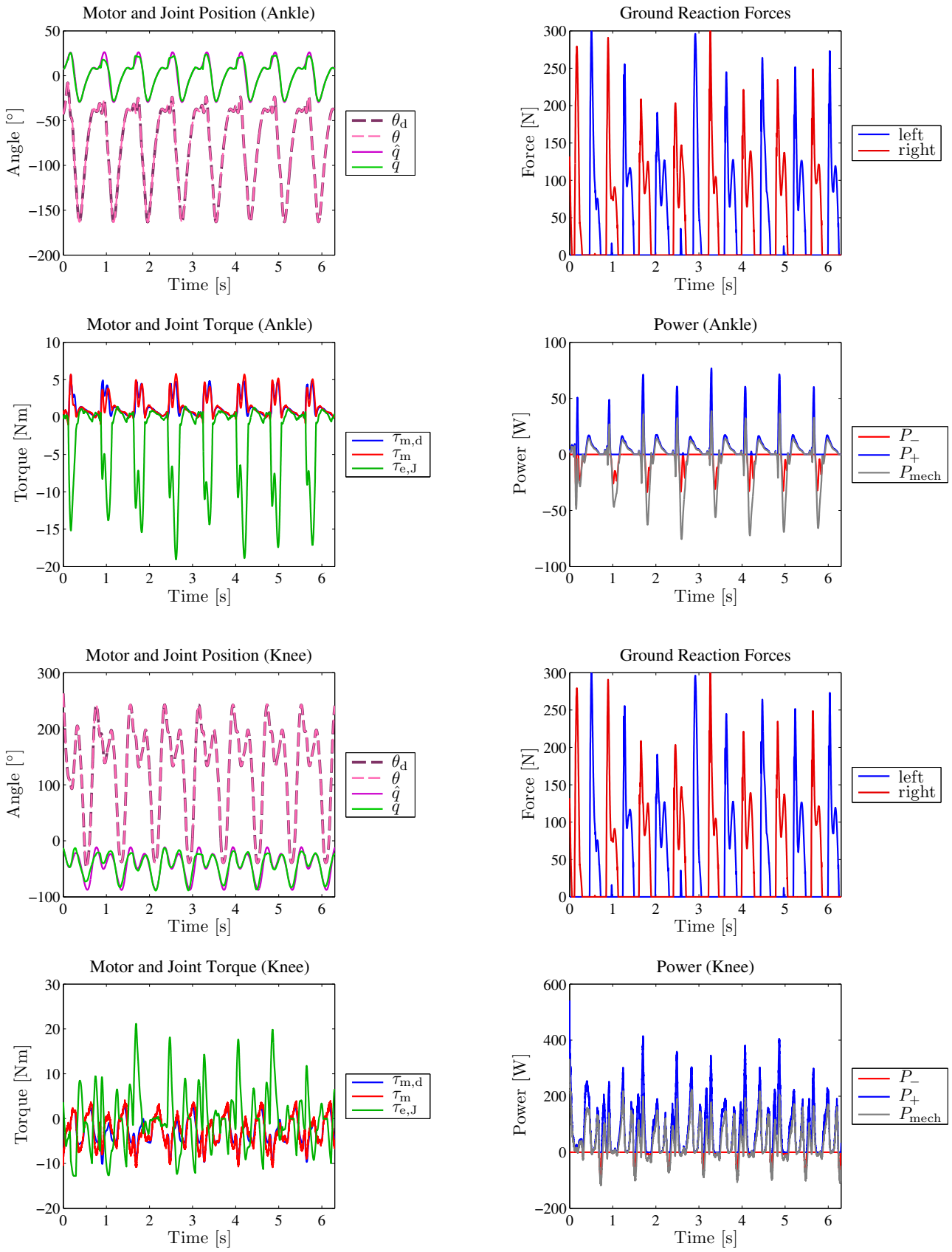

Figure 4.12.: Simulation results for human running with BioBiped1 for the ankle and knee joint.

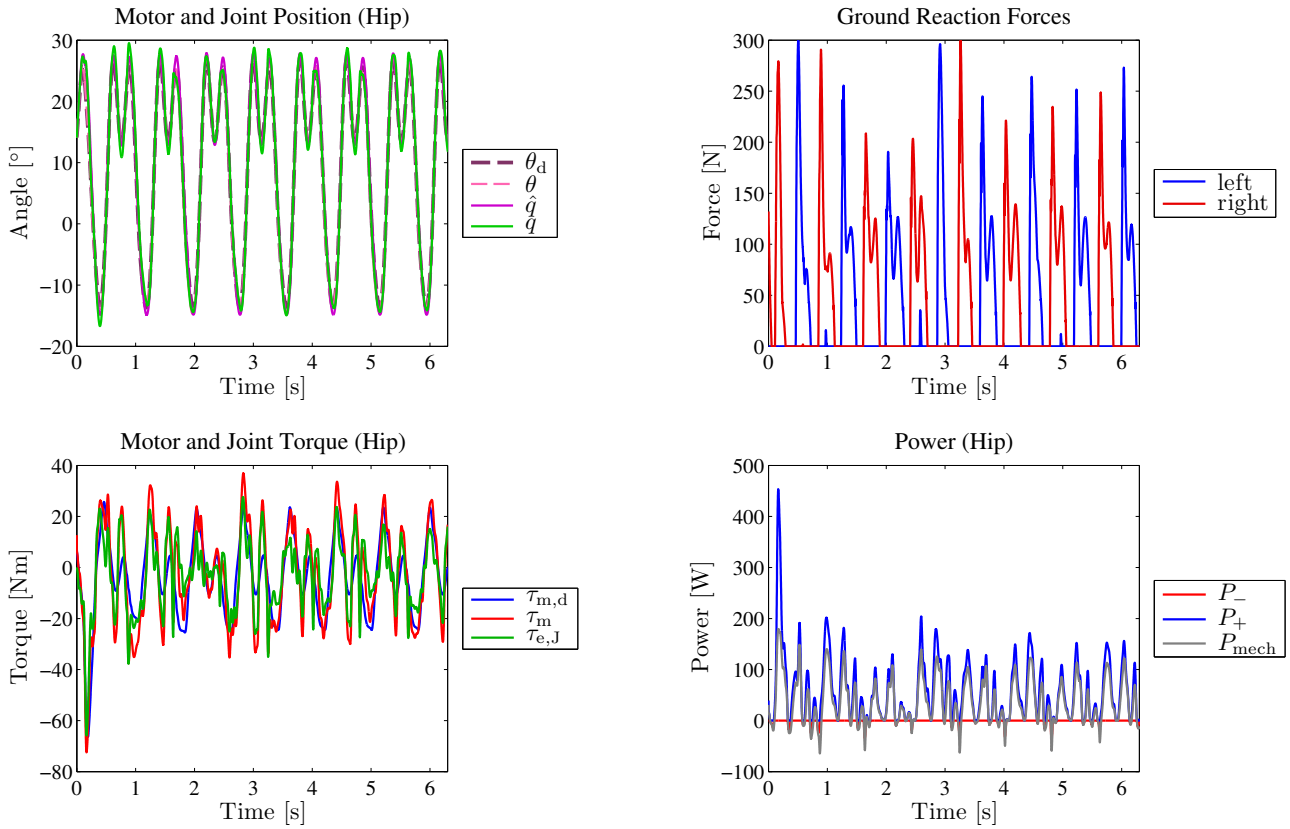

Figure 4.13.: Simulation results for human running with BioBiped1 for the hip joint.

requirements demanded of the motors to achieve, for example, energy-efficient locomotion. Moreover, it can be analyzed how varied actuation requirements for the same reference motions result in different locomotion performance characterized by performance criteria, such as the duty factor, energy consumption, or hopping height. In this context, the method has clear advantages over basic sinusoidal motor excitations. In order to utilize successfully the approach, a few important points must be taken into consideration:

- In order to generate a correct feedforward compensation term, $\boldsymbol{\tau}_{\mathrm{m,d}}$, the actuation dynamics need to be modeled rather precisely. Linear approximations of the strongly nonlinear actuation dynamics may result in false compensation terms that lead to higher demands on the motors.

- Furthermore, each joint must be actuated by one active unit, otherwise the leg will be underactuated. In that case, the motion of the nonactuated joint will depend mostly on the internal passive dynamics induced by the coupled motions of the other joints and the external forces. Note, however, that each joint can have torque inputs from several passive tendons, as their contributions can be considered in the formulas determining the required motor positions and torques.

- Additionally, the reference trajectories for the joints, $\boldsymbol{q}_{\mathrm{d}}$, should be smoothed previously, otherwise peaks will be introduced in the joint torques which will in turn lead to motor peak torques. The goal should be to keep the joint torques, $\hat{\boldsymbol{\tau}}_{\mathrm{e,J}}$, as low as possible. For this purpose, several opportunities exist that we will elaborate in the following.

In general, high joint torques will occur more likely during the stance phase at ground contact. Therefore, it is important to choose spring stiffnesses that keep the joint torques at a low level. On the other hand, it is important to note that soft spring stiffnesses may lead to high joint torques during the swing phase, thus, entailing a compromise. The ground contact and its parameters represent further important regulating screws. Since the contact dynamics of the rigid model, used in the first step for the forward simulation, differs from the dynamics of the full MBS dynamics model, it is possible to eliminate the ground contact, i. e., to exclude the gravity compensation for ground contact. This way, high joint torque peaks will automatically be avoided. On the other hand, this makes it more difficult for the controller to track the desired trajectories, particularly at ground contact. Additionally, it is possible to adapt the vertical collision force constant and the collision damping coefficient to decrease the impact forces. Another possibility is to decrease the joint friction, however, this change may lead to system oscillation and, as a result, may require increasing the D gains. Saturating the joint torques should be avoided, because the commanded trajectories may not be followed as requested due to less available joint torque amount.

In general, however, all the above comments can be neglected, if smooth reference trajectories are selected, such as sinusoidal functions or Fourier series. Additionally, it is essential to smooth the signals after each computation step, i. e., $\hat{\boldsymbol{\tau}}_{\mathrm{e,J}}$ and $\hat{\boldsymbol{q}}$ after the first step, and $\boldsymbol{\theta}_{\mathrm{d}}$ and $\boldsymbol{\tau}_{\mathrm{e,M}}$ after the second step, to avoid the introduction of unnecessary peaks into the motor torques $\boldsymbol{\tau}_{\mathrm{m,d}}$.

The presented concept can be highly beneficial to advance musculoskeletal designs and their use. It paves the way for a number of possible adaptations and extensions, such as optimization of specific performance criteria incorporating the outcomes of the approach as initial trajectories. For instance, the proposed control concept can be also applied to other reference data than joint angle trajectories, such as the patterns of the CoM or the GRF which will be the subject of follow-up investigations. These latter reference signals are interesting to generate a spring-like leg function.

Note, as earlier mentioned, the controller does not consider the full state space of the BioBiped1 robot model. In addition to the motor signals, also the joint position signals can be tracked in the third step. However, the goal is not a precise position tracking. Furthermore, the desired joint angles are included implicitly in the joint torques. Therefore, additional joint position tracking should be only considered, if great improvement of the control performance can be expected.

Finally, ground contact triggering may improve the energy efficiency, as it can be used to either change the spring stiffnesses or to schedule the controller gains appropriately. The former is an alternative in case of online adaptable compliance mechanisms. It is also possible to decouple specific tendons, such as the passive ones for the knee and ankle flexion in the swing phase, to decrease the efforts of the motors for the active knee and ankle extension. These actions will require devices such as a clutch or latch and, consequently, constructional changes to BioBiped1's leg actuation that can be considered for a following prototype. In order to schedule the controller gains, it might be interesting to exploit the benefits of machine learning methods [17].

4.7 Application to Motor-Gear Unit Selection for BioBiped1

An essential issue occurring in the development phase of a bipedal robot is the dimensioning of the actuators. This task can be considered as difficult for conventionally built robots with servo motors intended for slow walking motions [178], but is even more challenging for compliant robots targeted at hopping or running motions, which require both high actuator torques and

velocities. In order to deliver large torques, electrical motors must be either large or connected to a gearbox or further transmission that increases the torques. This overall transmission, however, also reduces the joint velocities entailing the necessity of a trade-off. Additionally, both gearing and the further transmission introduce friction and decrease the level of efficiency. Therefore, the demands on the actuators must be previously carefully analyzed in order not to compromise, for instance, the desired maximum velocity. Such analysis requires beforehand a clear definition of the goals with the platform under investigation.

Motivated by the project goal to realize dynamic locomotion behavior, the general requirements on the overall system behavior are summarized as follows: (1) energy efficiency and low power consumption, (2) lightweight design, and (3) delivering enough torque and speed. Furthermore, it is clear that, with respect to the long-term goal of walking and running with the same kinematic leg design, the running gait imposes tougher conditions on the actuation.

Given useful experimental reference data for the joint side, such as joint angle histories from human subjects, the necessary motor torques and velocities can be computed. For this purpose, the models of the actuators and transmissions must be known. Therefore, the previously described method for motion generation and control is well suited, as it allows to tune the contribution of the passive system eigendynamics and the efforts of the feedback controller independently of the degree of actuation, i. e., underactuation or full actuation. In [133], we applied the presented tracking method to determine the appropriate motor-gear units for BioBiped1 prior to its construction. Beforehand, we made a pre-selection of the required actuators in order to specify the required power of each motor.

It should be mentioned that, as each design phase inherently includes uncertainties with respect to the actual construction outcome, a slightly different actuation system had been used as the basis for the preliminary investigations of the actuation requirements (cf. Fig. 4.14c). Previously, it was assumed that for targeting fast, dynamic movements with BioBiped1 an active energy supply may be required not only for all joints in each leg, but also for both directions, flexion and extension. This decision mainly resulted from biomechanical insights that the monoarticular muscles are strongly responsible for power generation. Consequently, during the design phase of BioBiped1, the original idea was to actuate the monoarticular muscle pairs in each joint, which resulted in the design of the b-SEA earlier described in Section 3.4.3. As depicted in Fig. 4.14c, the role of each of the human muscle pairs GL-ILIO, PL-VAS, and SOL-TA was planned to be mimicked by a b-SEA. This leg configuration provided the basis for the motor-gear unit selection [133]. Additionally, the mechanical design should allow the flexible integration of the biarticular muscles RF, BF, and GAS as passive tendons with built-in springs (marked in purple color in Fig. 4.14b). Thus, in total, each leg would incorporate all nine relevant muscles as in the actual construction outcome, shown in Fig. 4.14a. But only the monoarticular muscle pairs were part of the robot leg configuration considered in the initial phase of the motor-gear unit selection process, as the complete musculoskeletal design had yet to be explored in detail.

4.7.1 Preselection of the Required Actuators

The preselection depends on several factors, including the planned overall weight of the robot, electronics, and battery supply (if autonomous operation is envisaged). Fast dynamic motions demand both high torques and velocities from the actuators. These two requirements help to determine the maximum mechanical power needed: $P = \dot{\theta}\,\tau_{\mathrm{m}}$. By considering the most challenging phase of a jumping or running motion, we can highlight two partial requirements

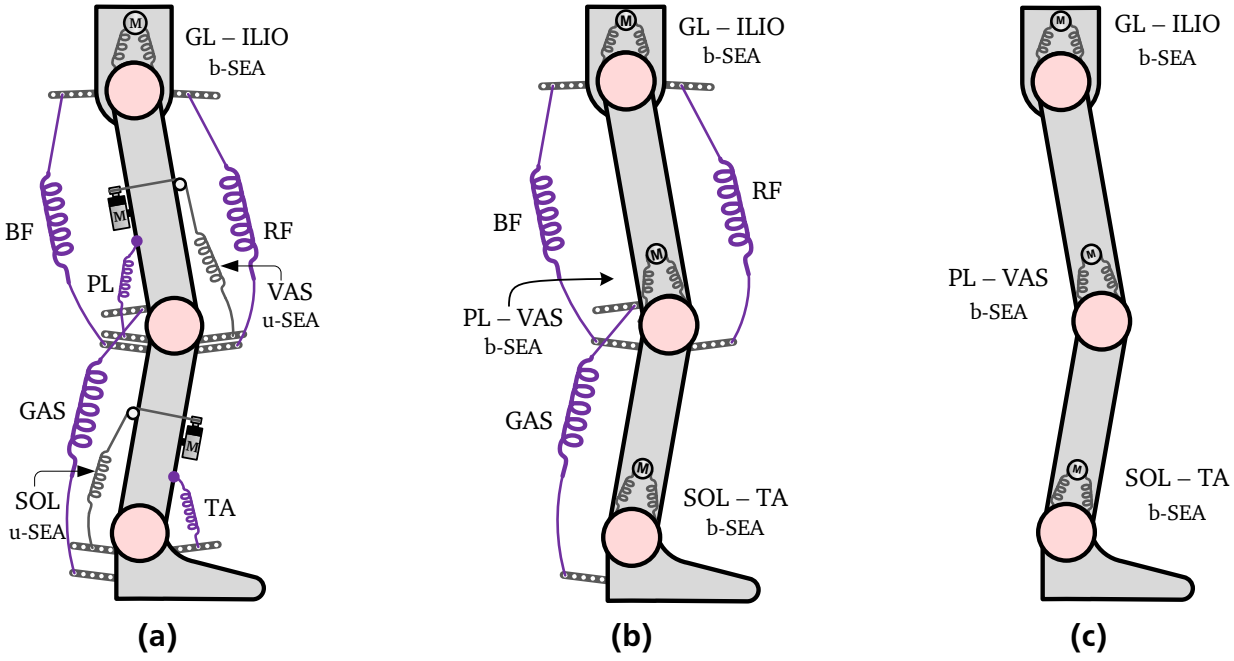

Figure 4.14.: Different leg actuation designs for BioBiped1: (a) actual construction outcome comprising monoarticular b-SEA and u-SEAs and monoarticular and biarticular, passive tendons; (b) envisaged actuation system prior to BioBiped1's construction; (c) actuation system used for the motor-gear unit selection.

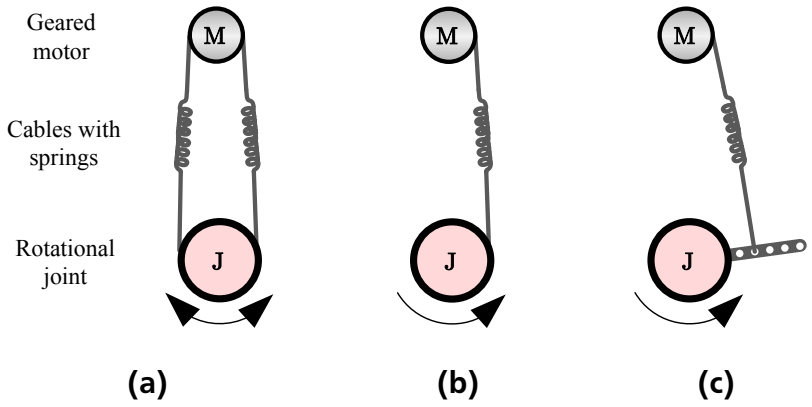

Figure 4.15.: Drawings of different elastic transmission mechanisms: (a) b-SEA with constant transmission ratio function; (b) u-SEA with constant transmission ratio function; (c) u-SEA with nonlinear transmission ratio function.

that need to be fulfilled by the actuators: (1) The robot must be capable of bearing its weight (static requirement) and (2) lifting its weight with a specified velocity (dynamic requirement) in the respective phase of hopping or running. Considering, in addition, the envisaged robot weight, battery supply, and electronics, the findings of the above investigations allowed us decide on the RE30 Maxon motors (60 W, 24 V) with planetary reduction gearbox GP 32C with gear ratio $n_g = 66$. In the calculations, a reduction of 20 % of the level of efficiency was included preventively.

In order to choose also the necessary range for the elastic transmission ratio n_p, a possibility is to set fixed maximum joint velocities/revolutions per minute (rpm) based on the desired motions, for example: 16 rpm in the hip corresponding to about 100 °/s, and 33 rpm in the knee and ankle joints corresponding to about 200 °/s. Reducing 20 % of the efficiency level of the selected motor-gear unit results in the maximum velocity of 7048 rpm. In conjunction with $n_g = 66$, the desired maximum joint velocities would require approximately $n_p = 7$ for the hip and $n_p = 3$ for the knee and ankle joints. These are, however, only rough estimates for the elastic transmission ratios and may need to be further adjusted during the simulations to satisfy the torque or voltage limitations. Furthermore, note that the transmission ratios are either constant being the result of a constant function or highly variable being the result of a nonlinear function depending on the built-in mechanism for the elastic transmission (cf. Fig. 4.15).

4.7.2 Application of the Model-based Method

Due to the pre-selection, *Step 3* of the developed method, as described in Section 4.3.2, could be carried out with approximately correct settings for the DC motor torque constant, rotor inertia, speed constant, terminal resistance and the gearbox inertia, viscous damping, and ratio. Additionally, setting the ratio, mechanical spring stiffness and viscous damping of the elastic transmission is required.

The most realistic and reliable actuator selection for an elastic biped prior to its actual construction presumes appropriate simulation of its dynamics. The rigid joint-link structure corresponded to that depicted in Fig. 3.4, but with different values for the dynamic parameters. Prior to a robot's construction, usually only rough estimates are available. The links were modeled as cylinders of radius r and height h, which equaled the length of the links, aligned along the x-axis. The radii of the cylinders moved in the range of 20 mm and 40 mm. The inertia tensor of each link was represented by a diagonal matrix containing the cylinders' principal moments of inertia given by

$$I_1 = \frac{m_1 r_1^2}{2}, \quad I_2 = \frac{m_1}{4}(r_1^2 + \frac{l_1^2}{3}), \quad I_3 = \frac{m_1}{4}(r_1^2 + \frac{l_1^2}{3}). \tag{4.50}$$

The values for the mass and CoM of the links were roughly estimated. The friction of the transmission was set to $d_e = 0.05\,\mathrm{Nms/rad}$. For the joint damping a quite large value was chosen with $d = 0.5\,\mathrm{Nms/rad}$, compared to the identified maximum friction value (cf. Section 3.7.3).

4.7.3 Results

In this section we present the results obtained by the model-based approach described in Section 4.3.1. The settings of the actuation units are based on the pre-selection described in Section 4.7.1. All simulation parameters used are listed in Table 4.7. The elastic transmission ratios were chosen to fulfill the requirements posed on the actuators for realizing the hopping and human running motions. The torsional stiffness constants were manually tuned, but are estimated to correspond well to the muscle stiffnesses during human hopping and running gaits [39, 89]. The upper body's movements were constrained to 1-D, respectively 2-D.

The results are displayed in Fig. 4.16, which is divided into a left and right column for the hopping and human running motions, respectively. The middle column indicates the key

Table 4.7.: Parameters used for the dimensioning of the motor-gearboxes.

Geared DC motor in hip, knee, ankle	
Motor torque constant: $k_t = 2.6 \cdot 10^{(-2)}\,\mathrm{Nm/A}$	
Motor rotor inertia: $I_r = 3.3 \cdot 10^{(-6)}\,\mathrm{kg\,m^2}$	
Motor speed constant: $k_v = 2.6 \cdot 10^{(-2)}\,\mathrm{Vs/rad}$	
Motor armature resistance: $R_a = 0.611\,\Omega$	
Gearbox ratio: $n_g = 66$	
Gearbox inertia: $I_g = 7 \cdot 10^{(-8)}\,\mathrm{kg\,m^2}$	
Gearbox viscous damping: $d_{vg} = 10^{(-5)}\,\mathrm{Nms/rad}$	
Simulation setup	
Hopping	**Human running**
Elastic transmissions	
Viscous damping in hip, knee, ankle: $d_e = 0.05\,\mathrm{Nms/rad}$	
Ratio in hip, knee, ankle: $n_p = 3$	Ratio in hip, ankle: $n_p = 2$ Ratio in knee: $n_p = 1$
Spring stiffness hip: $k_{e,Hip} = 260\,\mathrm{Nm/rad}$ Spring stiffness knee: $k_{e,Kne} = 100\,\mathrm{Nm/rad}$ Spring stiffness ankle: $k_{e,Ank} = 290\,\mathrm{Nm/rad}$	Spring stiffness hip: $k_{e,Hip} = 280\,\mathrm{Nm/rad}$ Spring stiffness knee: $k_{e,Kne} = 130\,\mathrm{Nm/rad}$ Spring stiffness ankle: $k_{e,Ank} = 250\,\mathrm{Nm/rad}$
Joint controller gains of the rigid joint-link structure	
P-gain hip: $k_{p,Hip} = 200$ P-gain knee: $k_{p,Kne} = 60$ P-gain ankle: $k_{p,Ank} = 200$	P-gain hip: $k_{p,Hip} = 200$ P-gain knee: $k_{p,Kne} = 60$ P-gain ankle: $k_{p,Ank} = 200$
D-gain hip: $k_{d,Hip} = 50$ D-gain knee: $k_{d,Kne} = 13$ D-gain ankle: $k_{d,Ank} = 50$	D-gain hip: $k_{d,Hip} = 50$ D-gain knee: $k_{d,Kne} = 13$ D-gain ankle: $k_{d,Ank} = 50$
Motor controller gains of BioBiped1's approximate model	
P-gain hip, knee, ankle: $k_p = 32$ D-gain hip, knee, ankle: $k_d = 5$	P-gain hip, knee, ankle: $k_p = 16$ D-gain hip, knee, ankle: $k_d = 2$

information for the plotted data, which is the same for both columns. In the topmost left and right plots the GRF of the simulated motions are shown. Subsequently, from top to bottom follow the reference and measured joint angular, respectively motor and joint torque trajectories for each joint in alternate sequence. As the results are almost identical for both legs, we show for each analyzed motion only the results from one leg. Only the GRF in the topmost plot display both feet. For the hopping motions this is, however, not visible, since identical curves are obtained due to the synchronous movement of both legs.

Hopping Motions

The desired trajectories consist of oscillations between the leg configurations $\boldsymbol{q}_{\mathbf{ex}} = (q_{\mathrm{Hip}}, q_{\mathrm{Kne}}, q_{\mathrm{Ank}}) = (0°, -10°, -35°)$ and $\boldsymbol{q}_{\mathbf{flex}} = (20°, -50°, 0°)$ (cf. Diagrams 2a, 4a, 6a of Fig. 4.16). The cycle time amounts to 0.32 s, resulting in the frequency 3.125 Hz, and the maximum joint velocities amount to 21 rpm for the hip, 42 rpm for the knee, and 37 rpm for the ankle joint.

Diagram 1a of Fig. 4.16 displays the GRF. The resulting forces of both the rigid and approximate BioBiped1 robot model have the typical vertical single-humped patterns, known from humans during hopping and running, and therefore match qualitatively well.

As Diagrams 3a, 5a, and 7a of Fig. 4.16 indicate, motor voltage limitations are not violated. In the knee we recognize voltage saturations (Diagram 5a), but the reference motions are still tracked sufficiently well (Diagram 4a). Diagram 5a indicates that faster velocities are not feasible for the knee actuator with the current settings. The voltages $\boldsymbol{U}$ increase with $\dot{\boldsymbol{\theta}}$ (cf. Diagrams 5a and 4a), while the torques $\boldsymbol{\tau}_{\mathrm{m}}$ generated during the voltage peaks are comparably small. With a lower elastic transmission ratio, however, the knee joint could be moved faster, if desired. In the ankle joint, the input voltage almost reaches, but does not touch the limitations. Similar to the knee, maximum voltages $\boldsymbol{U}$ are observed during high velocities $\dot{\boldsymbol{\theta}}$. High torques $\boldsymbol{\tau}_{\mathrm{m}}$ occur immediately before the motor turning direction is about to switch (cf. Diagrams 6a and 7a). In the hip, no saturations are detected (Diagram 2a). Similar patterns can be detected for the motor voltages $\boldsymbol{U}$ and motor torques $\boldsymbol{\tau}_{\mathrm{m}}$, indicating that the hip motor in particular must generate high torques at low velocities.

Further, in Diagram 5a, some consecutive peaks immediately before a ground contact can be observed. This is due to the feedforward compensation term $\boldsymbol{\tau}_{\mathrm{m,d}}$ (not shown here) that prepares the motor for the impact. Such peaks can be decreased or completely avoided by generating smooth trajectories, based on sinusoidal functions. It can be also recognized that the actual joint torques of the rigid and full robot model, $\hat{\boldsymbol{\tau}}_{\mathrm{e,J}}$ and $\boldsymbol{\tau}_{\mathrm{e,J}}$, match well for almost all joints.

Human Running Reference Data

The analyzed running motion data consist of mean joint angles in the sagittal plane, collected from a human subject and recorded at discrete time points during a running gait cycle [89]. The running gait cycle of the human subject is characterized by cycle time 0.8621 s, step frequency 2.3209 Hz, step length 0.9052 m, and flight time 0.1120 s.

During running, the robot's GRF patterns do not exactly resemble the typical single-humped GRF patterns of the human subject, scaled to the body weight of the robot (see Diagram 1b of Fig. 4.16). Particularly in the first two steps illustrated, the patterns are not exactly single humped. The peak forces amount to approximately the same value as during human running. In order to eliminate the smaller hump following the first large hump in the first steps, variable-stiffness actuators may need to be introduced to accommodate for ground stiffness [39].

The analyzed human running motion, as depicted in Diagrams 3b, 5b, and 7b, do not violate, nor even reach the voltage saturation. As also observed during hopping, in the hip, similar patterns for the voltages $\boldsymbol{U}$ and torques $\boldsymbol{\tau}_{\mathrm{m}}$ can be detected, which again indicates that the hip actuator needs to be capable of generating high torques.

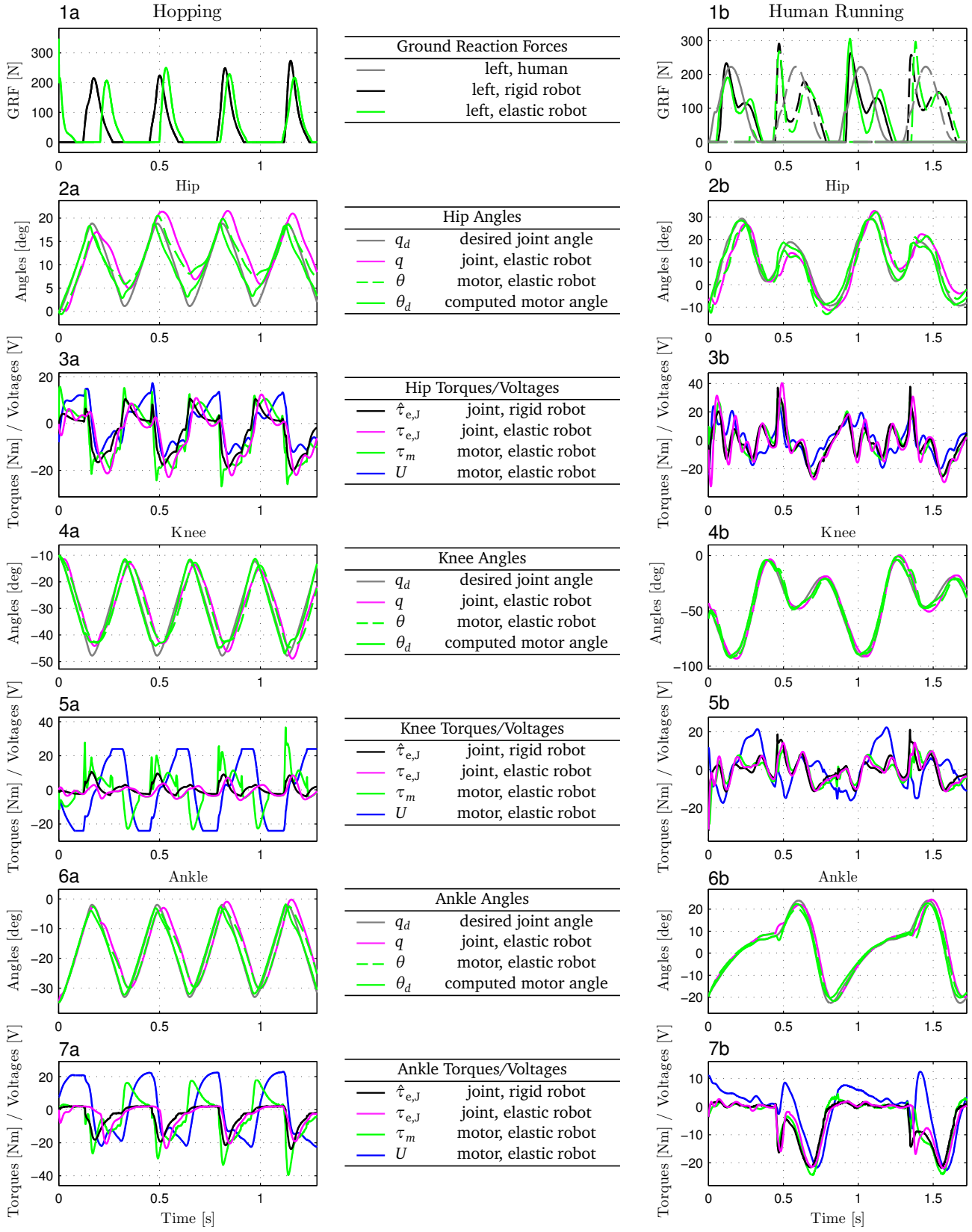

Figure 4.16.: Simulation results of the motor-gear unit selection: The plots in left and right column display the results for the computer-generated hopping and human running trajectories, respectively. In the middle the corresponding key information for the plotted data is listed. The dashed lines in the topmost plot on the right-hand side represent the right foot.

4.7.4 Discussion

From the simulation results obtained we could expect an accordingly constructed robot to perform equally well without violating the maximum voltages. It is worth pointing out that the typical rpm-versus-torque plots, often seen in motor data sheets, were not necessary here. As the input voltages were limited in the motor model, the motor could not generate either torques or velocities that violate the limitations. This allowed a more compact visualization of all data and the direct comparison of torque peaks and voltage saturations with the reference trajectories and GRF.

In experiments, soon after BioBiped1's construction, it could be shown that the robot can perform highly dynamic movements proving that the selected motor-gear units can deliver the required torques and velocities. In the simulation results we used a slightly different actuation setup by using b-SEAs in each joint. This was due to uncertainties inherent to each design phase with respect to the actual construction outcome. Nevertheless, the real robot demonstrated with a different actuation setup that the desired motions can be realized. In the steady state the unidirectional actuation is supposed to be sufficient and powerful enough. The working principle is as follows: The passive tendons are triggered and released by the actuation of the extensors and the ground contact. After the ground impact and touch-down, it is necessary to support actively by electrical motors the extension of the knee and ankle joints to quickly propel the leg forward. In the results shown in Fig. 4.16, the knee motor was identified to turn not quickly enough for the motions desired. The motions tested, however, were chosen to be faster as the ones envisioned for the real platform to ensure that the identified motor-gear units meet the desired requirements. For faster gaits, in general, the knee transmission can be easily adapted, by changing the transmission ratio or the gearbox ratio.

Comparing Fig. 4.10 and Fig. 4.16, it is apparent that the motor torque trajectories generated here for the hopping motions are quite jerky and contain several peaks. In contrast to the guidelines given in Section 4.5, the reference joint trajectories for the hopping motions were composed of partial linear interpolations for the swing and stance phase. To avoid too sudden switching of the motor turning direction, the trajectories were additionally filtered. However, compared to the sinusoidal functions generated in Section 4.5 for the hopping motions, the generated motions were still too demanding in terms of power consumption. As for the human running, it can be said that here as well it is a good idea to smooth first the raw reference signals by applying frequency analysis techniques. This is particularly important since the computation of the motor torques includes an inertia and a damping term including the second and first derivative of the motor position. Due to the nonoptimal trajectories, we omitted these terms in the computation of the actuation requirements.

To our knowledge, there is no method yet for selecting the required motor-gear combinations for a highly biologically inspired robot, that is electrically actuated, prior to its construction. Omitting a thorough investigation related to the required actuation units will possibly lead to the development and selection of actuators by which the intended robot locomotion performance cannot be met. This was the case, for instance, for the electrically actuated humanoid robot Kenshiro [13]. Only after extensive experimental testing on the constructed robot, is was recognized that the chosen motor gearboxes need to be exchanged. This practical approach is quite tedious, in particular, for a robot with complex actuation design involving a high number of electrically driven tendons. We believe that utilizing this approach prior to a robot's construction

is also a very important step towards improved locomotion performance, since the emphasis is put on the issue of energy efficiency already very early in the development process of the robot.

4.8 Summary and Further Perspectives

An important question in the context of musculoskeletal systems is how to design controllers that best utilize the specific mechanical features of the actuation system. Such systems are only as beneficial as enabled and exploited by the control system. The purpose is to make use of the intrinsic dynamics of the robot's mechanical system and actuation so that a dynamic, energy-efficient locomotion performance is achieved.

BioBiped's actuation system is characterized by highly nonlinear, active and passive, mono- and biarticular tendons. In this chapter, we discussed two approaches, one of which is applying open-loop controlled sinusoidal trajectories to the motors. Important issues to be considered during the motion generation process are choosing the step frequency correctly, which is quite difficult for a nonlinear complex musculoskeletal leg design. Further, when using human motion capture data, it is highly recommended to perform a Fourier transformation of the original signals. Considering that the robot's and a human subject's motion dynamics differ tremendously, the Fourier analysis is even more crucial. It allows the derivation of signals for the other leg, based on phase shift. Additionally, it is possible to scale the amplitudes and offsets of the amplitudes, in order to tune the trajectories better to the robot's dynamics.

The second approach represents the main contribution of this chapter: a centralized, nonlinear model-based method for motion generation and control, using the actuator dynamics models. The approach allows investigators to determine each tendon's contribution to the overall joint dynamics and, in this way, to vary the requirements demanded of the motors. The advantage of the method is that it creates a common basis for comparisons of different musculoskeletal and stiff leg actuation designs. Applying this approach, studies comparing the design versus performance are described in Chapter 5. It is shown that the method is particularly well suited for systems with redundant actuation. Furthermore, it can be utilized to dimension the required motor-gearboxes prior to a robot's construction.

Future work includes the implementation of the method in the upcoming BioBiped3 platform. Current platforms lack sufficiently accurate and reliable sensors. In particular, the current sensing and joint position sensing need to be improved prior to a successful implementation of the approach on the robot hardware.

Adding ground contact triggering can enhance the method substantially, through specific extensions such as adapting the leg stiffness during ground contact. Ferris *et al.* have shown that human runners adjust their leg stiffness to accommodate changes in surface stiffness, allowing them to maintain similar running mechanics on different surfaces [42]. Such stiffness adaptations will help to decrease the energy consumption.

It is also possible to implement adaptive controllers using time-varying controller parameters based on some signals in the closed-loop system, such as ground sensing. In this context, it is also interesting to apply machine learning techniques to learn both the optimal elastic transmission parameters and the controller gains [17]. Further considerations include the minimization of ground contact forces, as suggested in [140].

4.9 Reference to Own Publications

A short version of Sections 4.3 and 4.5 was published in: Proceedings of the International Conference on Climbing and Walking Robots and the Support Technologies for Mobile Machines 2013 [136]. A preliminary version of Section 4.3, as well as a condensed version of Section 4.7, was published in: Proceedings of the IEEE/RSJ International Conference on Intelligent Robots and Systems 2011 [133].

5 Investigating Leg Actuation Design versus Locomotion Performance for Dynamic and Energy-Efficient Locomotion

5.1 Introduction

Musculoskeletal leg designs, such as that of BioBiped1, are not yet common and, thus, the benefits of such designs over conventionally built systems with stiff joints may not be completely clarified due to missing environments allowing such studies. Therefore, this chapter deals with the properties of the complex musculoskeletal BioBiped system in terms of both benefits and challenges resulting from the interplay of the active and passive tendons. The goal is to reveal, by thorough investigation of the design versus the locomotion performance, leg actuation designs suited for dynamic and energy-efficient locomotion, according to the definitions introduced in Section 4.4.

The previous chapters laid the foundations for extensive thorough studies with reliable results portable directly to the real robot hardware: In Chapter 3 we derived detailed models of the implemented actuator types and developed the fully validated MBS dynamics model including elastic contact mechanics; motion generation and control concepts for musculoskeletal bipedal systems were presented in Chapter 4. Based on these foundations, in this chapter, we will conduct several studies with the purpose of catching a better glimpse of the important dynamic properties of this complex musculoskeletal system and of highlighting the specific benefits of mechanical elasticities and musculoskeletal system design.

5.2 Passive Rebound and Soft Landing

In this section, we will investigate some preeminent advantages of elastically actuated legs containing mechanical elasticities: (1) shock tolerance, i. e., impacts are absorbed by the springs before they can reach the motors and cause any damage to them, and (2) energy storage and release [138]. These advantages were perceived more and more with the advent of the SEA [126]. Many authors have recognized the previously named benefits as essential properties of a bipedal system for running or jumping motions [139, 20, 68, 117, 62, 70].

The goal of this section is to study the requirements for good passive rebound and soft landing in simulation, evaluate these capabilities and use the insights gained to achieve an overall optimal locomotion behavior of the robot. Inspired by the passive rebound experiments and its results, described in Section 2.7.2, several further questions arise. Assuming that the weakest components of the robot system are the motor-gearboxes, and not the segments, which can break as well depending on the impact forces, we wonder:

- Which falling heights cause the maximum peak torques at the gearbox to be exceeded? What is the maximum possible falling height that will not cause any damage to BioBiped1's actuators? How do the GRF change depending on the falling height and compare among robot systems with different actuator types?
- How do the peak torque, GRF, flight phase, and energy restitution ratio change for robot systems with different actuator types? What is the maximum energy restitution ratio that

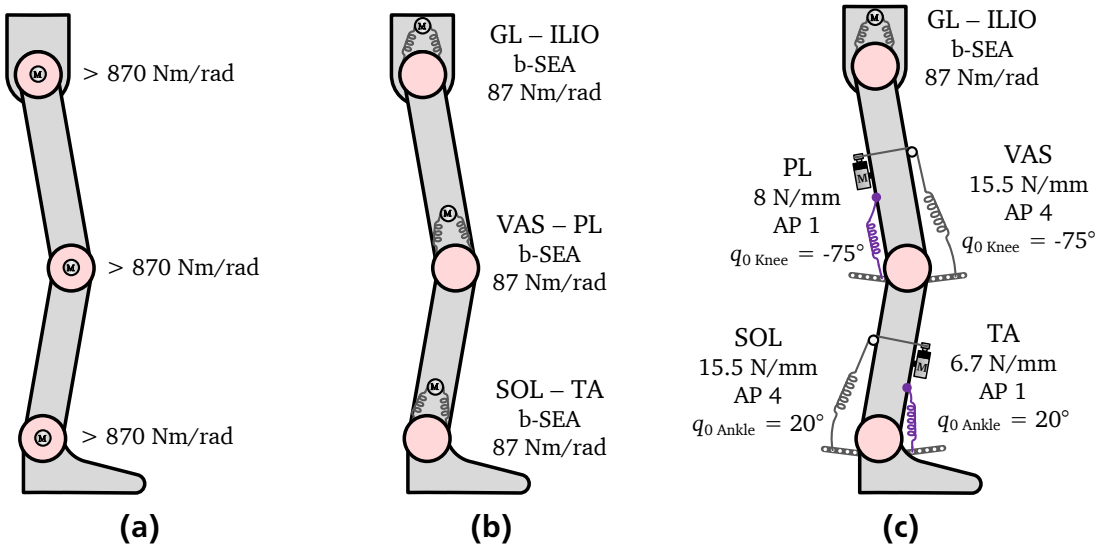

Figure 5.1.: Simulation models used in the passive rebound study: (a) BioBiped1 robot with completely stiff joint actuation (*stiff robot*); (b) BioBiped1 robot with rotational series elastic joint actuation (*b-SEA robot*); (c) validated model of the BioBiped1 robot platform with the given actuation settings (*BioBiped1*).

can be obtained with which actuator type and when is the shock absorption the largest? Is there a trade-off between these two criteria?

- How does a compliant robot with rotational joint stiffness relate to a stiff robot? Which rotational joint stiffnesses of a compliant robot result in the joint behavior of a stiff robot? What are the advantages of series elastic tendons coupling one or more joints over rotational SEA joints?

Answering these questions requires setting up different simulation models while ensuring a valid comparability of the results. Based on the actuators introduced in Section 3.4, three different simulation models providing internal variation possibilities will be used:

1. *stiff robot*: BioBiped1 robot model with completely stiff joints actuated by geared DC motors (cf. Fig. 5.1a),
2. *b-SEA robot*: BioBiped1 robot model with rotational series elastic joint actuation, i. e., b-SEAs in each joint (cf. Fig. 5.1b),
3. *BioBiped1*: BioBiped1 robot model with active and passive elastic tendon actuation as in the real robot platform (cf. Fig. 5.1c).

The segment kinematics and dynamics are identical in all robot models in terms of mass, length, CoM, and inertia of the links. In the stiff robot model the inertia of the links additionally include the reflected rotor and gearbox inertia, as described in Section 3.4.2. A snapshot of the animation is shown in Fig. 5.2. The animation function of the METArob simulator allows to animate simultaneously different models; in this way, the behavior of the models can be directly compared.

In the following we will carry out various studies for the above three robot models analyzing the passive rebound capabilities. The models are all dropped from different heights starting

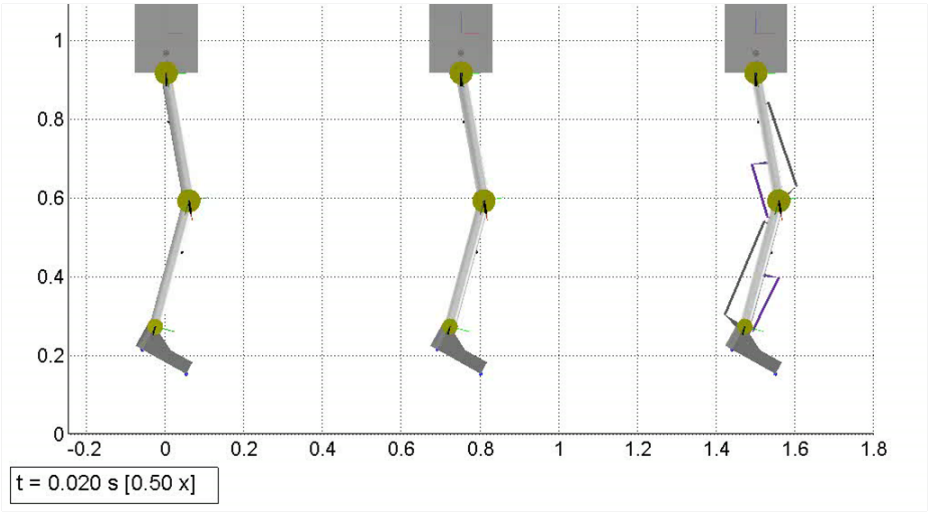

Figure 5.2.: Snapshot of the animation: stiff robot (left), b-SEA robot (middle), and validated BioBiped1 robot model (right).

at 5 cm. In order to gain further insights, we will additionally tune the actuation of the compliant robots, such as the mechanical spring stiffness of a b-SEA or tendon, or alter the controller gains. In contrast to the experiment, presented in Section 2.7.2, we will use springs instead of ropes for the antagonists in the BioBiped1 model. The ground contact model parameters are identical in all studies throughout this thesis (cf. Table 4.2). The initial joint angles for the knee and ankle are the same as in the experiment ($q_{\mathrm{Kne}} = -25°$, $q_{\mathrm{Ank}} = -14°$). Additionally, we choose also a slightly flexed configuration for the hip joint with $q_{\mathrm{Hip}} = 10°$. This leg configuration corresponds approximately to that taken at touch-down during synchronous hopping motions. At touch-down the leg is neither fully extended nor flexed. Full extension occurs only at take-off, while full flexion of the legs can be detected during the stance phase. To keep the desired joint positions, for the elastic robots the corresponding motor positions compensating for the gravity in this leg configuration are determined beforehand, using the formulas given in Section 3.4.7.

For such a study it is important to ensure a valid comparability of the results among the different models. In this context, strictly speaking, the actuation of the stiff robot needs to include also Coulomb friction [8]. But, as it is extremely difficult to develop an appropriate model for the Coulomb friction and as the target motions are rather fast, it is omitted here. Another important role is assigned to the controller gains. Since the controller is defined in joint space, the controller parameters are identical in all models. The conversion to motor space occurs in the controller model considering the transmission ratio z, which consists of the gear ratio and, if existent, an elastic transmission ratio. A controller for motor position $\boldsymbol{\theta}$ with gain k_{p} and controller output torque $\boldsymbol{\tau}_{\mathrm{e,M}}$ on motor level

$$\boldsymbol{\tau}_{\mathrm{e,M}} = (\boldsymbol{\theta}_{\mathrm{d}} - \boldsymbol{\theta})\, k_{\mathrm{p}} \tag{5.1}$$

can be reformulated with respect to the joint side

$$\boldsymbol{\tau}^{*}_{\mathrm{e,J}} = z\ \boldsymbol{\tau}_{\mathrm{e,M}} = z\,(z\,\boldsymbol{\theta}^{*}_{\mathrm{d}} - z\,\boldsymbol{\theta}^{*})\, k_{\mathrm{p}} = (\boldsymbol{\theta}^{*}_{\mathrm{d}} - \boldsymbol{\theta}^{*})\, z^2 k_{\mathrm{p}}\,, \tag{5.2}$$

which yields that the controller parameters are reflected to the joint side, similar to the inertia and friction, with z^2. We confirmed this relation by testing the deviation of q from q_{d} in all

Table 5.1.: Simulation results for passive rebound with the stiff robot dropped from different heights.

Dropping height [m]	Energy restitution [%]	Hopping height [m]	Ground clearance [m]	Duty factor [%]	Flight phase [ms]	$\tau_{e,M\,Ank}$ $\tau_{e,M\,Kne}$ $\tau_{e,M\,Hip}$ [Nm]	GRF [N]
0.05	17.15	0.036	0.004	52.49	85	13.89 3.67 0.95	188.32
0.10	13.12	0.036	0.009	52.49	85	19.16 4.9 1.38	258.4
0.15	11.05	0.036	0.012	52.49	85	23.54 5.91 1.73	316

models without ground contact. We started with rather stiff control parameter gains k_p and k_d for the stiff robot model and, subsequently, tuned the gains for the artificially stiffened, elastic robot models until the deviations in all models were equally small. The artificial stiffening is necessary to couple the actuators to the joints so that a comparison of the deviations between the actual and desired joint positions becomes possible. Through this tuning, identical controller parameters could be obtained for all models. Note that we decided to choose rather stiff P and D gains for the motors. With low gains the motors of the compliant robot models are able to keep constantly their predefined positions after ground contact, in particular, when large impact forces are induced.

For the motor-gear units, as deployed in the BioBiped1 robot and indicated in Table 4.1, the maximum torques at the gearbox may not exceed 6 Nm, according to the manufacturer's specification which is always rather conservative. We assume that, on short term, the peak torques arriving at the gearbox may be up to at least twice as high as the specification, i. e., 12 Nm.

As the movements of the robot models are completely constrained to 1-D, , it is also easier than in experiment to maintain the same circumstances for all simulation runs.

Tables 5.1–5.5 contain the results of the simulation study. The evaluated criteria include the energy restitution, the achieved hopping height and ground clearance after each support phase, the duty factor, and the measured flight phase. The definitions of these performance criteria were previously provided in Section 4.4. In addition to these criteria, we are keen to know how the peak GRF during each bounce change depending on the dropping height and which peak torques arrive at the gearboxes ($\tau_{e,M\,Ank}$, $\tau_{e,M\,Kne}$, $\tau_{e,M\,Hip}$) and the joints ($\tau_{e,Hip}$, $\tau_{e,Kne}$, $\tau_{e,Ank}$). Note that the joint torques are given with respect to the joint, i. e., including the complete transmission ratio, while the torques acting on the motors are given with respect to the gearbox output, i. e., including only the motor gear ratio.

5.2.1 BioBiped1 Robot Model with Stiff Joint Actuation

First, we analyzed the passive rebound and landing behavior of a completely stiff robot. Assuming a maximum possible peak torque of 12 Nm, a dropping height of only 5 cm seem to be already causing some damage to the motors. The maximum torques arriving at the gearbox of the ankle motor amounts to 13.99 Nm, significantly higher than that for the knee or hip motor. The peak torques on the gears caused by the peak GRF at ground contact seem to decrease

drastically for the distal joints respectively motors. At all different dropping heights, the same hopping height[1], duty factor, and flight phase duration are achieved. Note, however, that the achieved hopping heights correlate with different ground clearances. This is due to the increased impact forces at ground contact. As can be seen in Fig. 5.3, due to the greater falling heights, the first contact points after falling are shifted, but the duration of the contact and flight phases are identical. Note also, that the energy restitution decreases for greater falling heights, i. e., more energy is dissipated. Furthermore, based on the peak torques given in Table 5.1, it can be concluded that dropping such a stiff robot from heights greater than 5 cm can cause critical damage to the ankle motor; in addition to the fact that it cannot store any energy.

5.2.2 BioBiped1 Robot Model with Linear Elastic Joint Actuation

This study was repeated with the b-SEA robot with identical torsional stiffness of $87\,^{\mathrm{Nm}}/_{\mathrm{rad}}$ in each joint (cf. Table 5.2). This joint stiffness value was chosen since it corresponds to the fixed stiffness of the hip actuator transmission of the real BioBiped1 system. In contrast to the stiff robot, here the falling heights can be up to 25 cm before the torques acting on the motor gearboxes enter the range of critical values potentially damaging the motors. The falling heights can be even greater for less stiffer joints. In the last row of Table 5.2 we have listed the results of the passive rebound behavior for half of the original joint stiffness: The torsional joint stiffness in all joints was set to $\frac{1}{2}\,\mathrm{x}\,87\,^{\mathrm{Nm}}/_{\mathrm{rad}}$. According to the results, decreasing the stiffness of all joints leads to higher energy restitution ratios, greater hopping heights and ground clearances, and longer lasting flight phases for both bounces, thus, increasing in total the overall dynamics behavior of the robot.

As for the GRF peaks, it can be noted that they increase less quickly than for the stiff robot. At 5 cm they are already significantly smaller and increase slower than for the stiff robot at greater falling heights. It can be also recognized that the torques at the joints agree very well with the torques on the motor of the stiff robot at this falling height, proving the same simulation conditions and setup for each study. This is also true for the other falling heights the stiff robot was tested at.

Note that the energy restitution ratio increases with joint compliance; it decreases with increased falling height. In a further study, the joint stiffness values were increased to detect the effects of joint compliance at the falling height of 15 cm, which falls into the range of desired falling and subsequent hopping heights for BioBiped1's movements, shown in Table 5.3. It can be noticed that the energy restitution ratio diminishes rapidly with higher joint stiffness and with it also the number of bounces from two to one. Further it can be read off of the curves in Fig. 5.4 and of the numbers in Table 5.3 that joint stiffness values of around $20\,\mathrm{x}\,87\,^{\mathrm{Nm}}/_{\mathrm{rad}}$ approximately yield the joint behavior of the stiff robot. The values for each performance criteria are very similar.

[1] These are numerically rounded values. The exact hopping heights slightly differ from the fifth decimal place onwards.

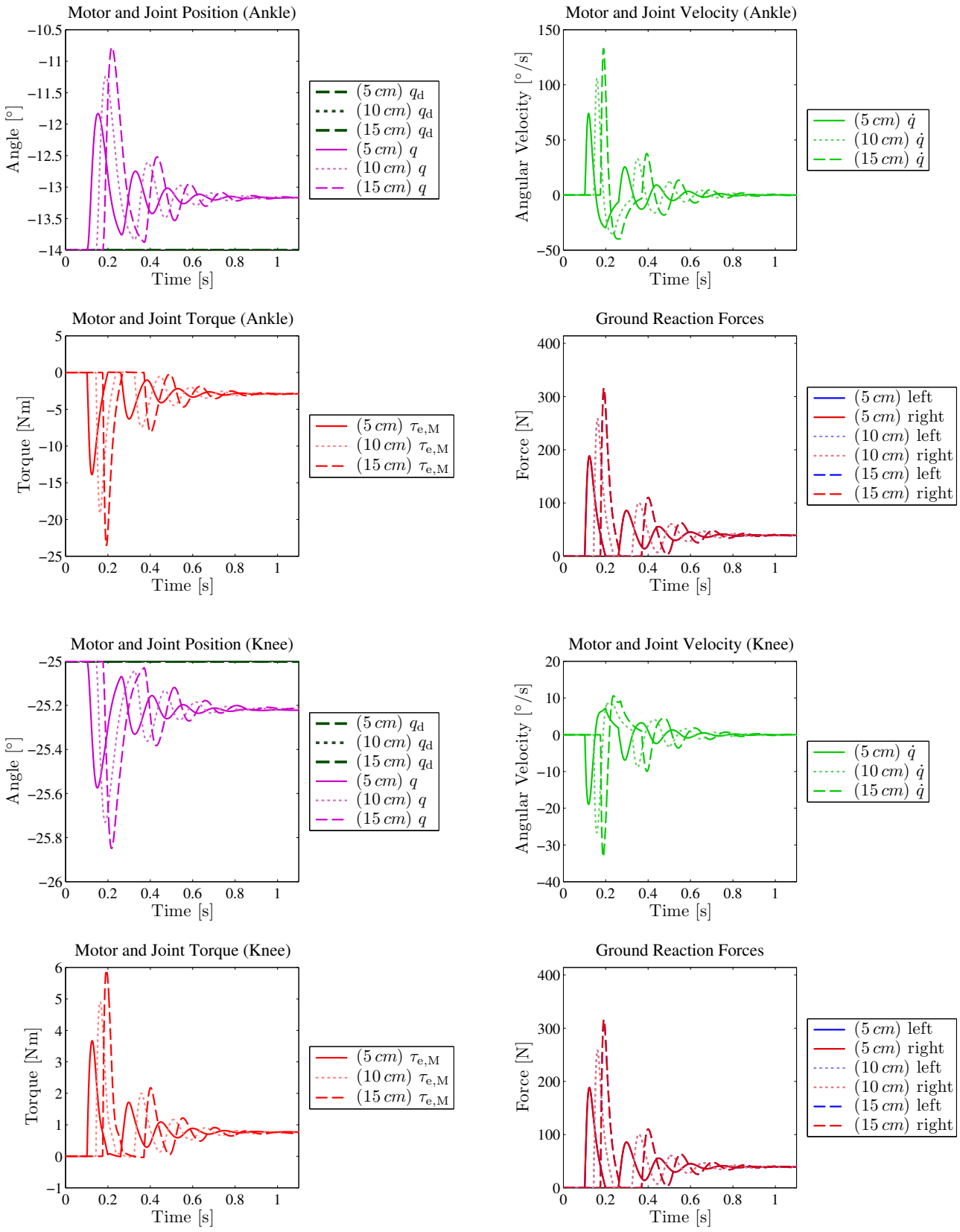

Figure 5.3.: Simulation results for passive rebound with the stiff robot dropped from different heights for the ankle and knee joint.

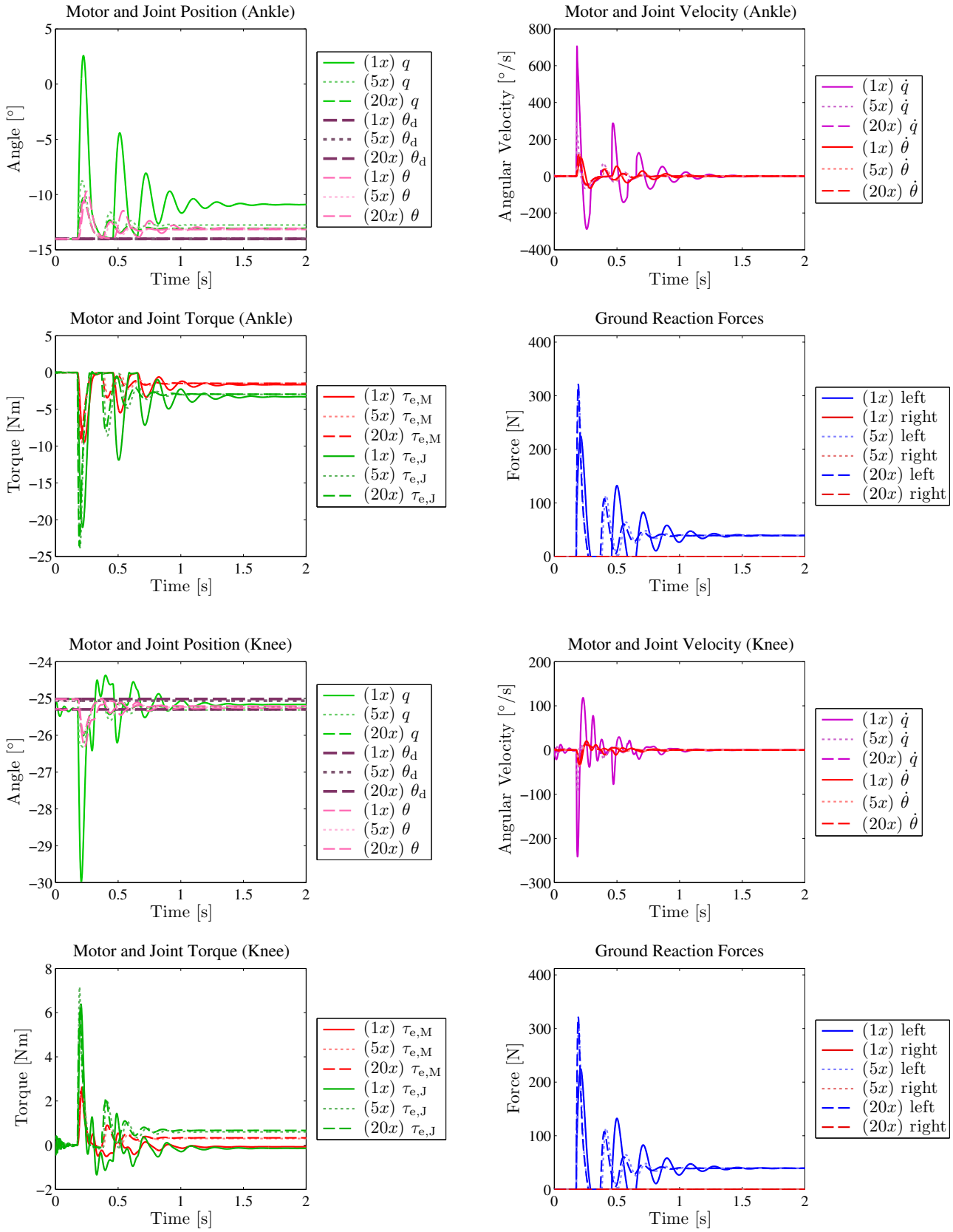

Figure 5.4.: Simulation results for passive rebound with the b-SEA robot with varied joint stiffnesses dropped from 15 cm for the ankle and knee joint.

Table 5.2.: Simulation results for passive rebound with the b-SEA robot with varied joint stiffnesses dropped from different heights.

Dropping height [m]	$k_{e,Ank}$ $k_{e,Kne}$ $k_{e,Hip}$ [$^{Nm}/_{rad}$]	**Bounce**	**Energy restitution** [%]	**Hopping height** [m]	**Ground clearance** [m]	**Duty factor** [%]	**Flight phase** [ms]	$\tau_{e,M\,Ank}$ $\tau_{e,M\,Kne}$ $\tau_{e,M\,Hip}$ $(\tau_{e,Ank}$ $\tau_{e,Kne}$ $\tau_{e,Hip})$ [Nm]	**GRF** [N]
0.05	1 x (87 87 87)	1st	31.24	0.041	0.010	56.13	92	5.92 1.67 0.43 (12.97 3.97 1.03)	150.89
0.10	1 x (87 87 87)	1st	28.61	0.063	0.023	45.28	138	7.9 2.22 0.63 (17.41 5.35 1.52)	193.3
		2nd	33.56	0.027	0.003	74.16	45		116.15
0.15	1 x (87 87 87)	1st	26.9	0.082	0.035	40.14	169	9.51 2.63 0.83 (21.03 6.39 1.98)	224.6
		2nd	31.99	0.034	0.006	64.10	69		132.38
0.20	1 x (87 87 87)	1st	25.66	0.100	0.046	36.69	194	10.92 2.98 0.99 (24.16 7.25 2.38)	250.27
		2nd	31.41	0.040	0.009	58.37	86		144.95
0.25	1 x (87 87 87)	1st	24.79	0.117	0.058	34.35	215	12.18 3.39 1.12 (26.98 8.39 2.67)	271.99
		2nd	31.28	0.046	0.012	54.09	100		155.96
0.25	$\frac{1}{2}$ x (87 87 87)	1st	34.43	0.153	0.076	34.38	251	10.25 3.09 0.45 (22.09 6.45 1.02)	280.48
		2nd	35.09	0.066	0.019	53.96	127		138.09

Table 5.3.: Simulation results for passive rebound with the b-SEA robot with varied joint stiffnesses dropped from 15 cm.

Dropping height [m]	$k_{e,Ank}$ $k_{e,Kne}$ $k_{e,Hip}$ [Nm/rad]	**Bounce**	**Energy restitution** [%]	**Hopping height** [m]	**Ground clearance** [m]	**Duty factor** [%]	**Flight phase** [ms]	$\tau_{e,MAnk}$ $\tau_{e,MKne}$ $\tau_{e,MHip}$ ($\tau_{e,Ank}$ $\tau_{e,Kne}$ $\tau_{e,Hip}$) [Nm]	**GRF** [N]
0.15	1 x (87 87 87)	1st	26.9	0.082	0.035	40.14	169	9.51 2.63 0.83 (21.03 6.39 1.98)	224.6
		2nd	31.99	0.034	0.006	64.10	69		132.38
0.15	5 x (87 87 87)	1st	12.71	0.048	0.014	47.09	108	9.55 2.52 0.42 (23.79 7.17 1.38)	307.78
0.15	10 x (87 87 87)	1st	11.33	0.044	0.012	48.48	101	9.22 2.4 0.39 (23.75 6.23 1.31)	317.71
0.15	20 x (87 87 87)	1st	10.71	0.043	0.011	49.48	97	8.97 2.45 0.53 (23.57 6.23 1.46)	321.11

5.2.3 BioBiped1 Robot Model with Nonlinear Elastic Tendon Actuation

With the previous study we could already demonstrate the intrinsic advantages of compliant actuation. Finally, it is important to clarify how the nonlinear actuation of the knee and ankle joints in BioBiped1 together with the implemented coupled tendon elasticities can improve the above behavior. Therefore, we carried out the same previous simulation runs with the BioBiped1 robot model. In contrast to the experiment, we used here actual spring-tendons for the antagonists instead of solely ropes. The exact actuation setup consists of the b-SEA in the hip (with 87 Nm/rad), the monoarticular pair of VAS (7.9 N/mm, attachment point number 5, $q_0 = -85°$) and PL (4.1 N/mm, $q_0 = -85°$) in the knee, and the monoarticular pair of SOL (6.7 N/mm, attachment point number 3, $q_0 = 10°$) and TA (4.1 N/mm, $q_0 = 10°$) in the ankle. Linearization of the actuation torque vector with respect to the joint side $\boldsymbol{\tau}_{\mathrm{e,J}}$ assuming fixed motor positions $\boldsymbol{\theta} = \bar{\boldsymbol{\theta}}$ yields

$$\boldsymbol{\tau}_{\mathrm{e,J}}(\boldsymbol{q}, \dot{\boldsymbol{q}}, \boldsymbol{\theta}, \dot{\boldsymbol{\theta}}) \approx \boldsymbol{\tau}_{\mathrm{e,J}}(\bar{\boldsymbol{q}}, \bar{\boldsymbol{\theta}}) + \boldsymbol{J}_{\boldsymbol{\tau}_{\mathrm{e,J}}}(\bar{\boldsymbol{q}})(\boldsymbol{q} - \bar{\boldsymbol{q}}) \tag{5.3}$$

with the actuator torque Jacobian

$$\boldsymbol{J}_{\boldsymbol{\tau}_{\mathrm{e,J}}}(\bar{\boldsymbol{q}}) = \frac{\partial\, \boldsymbol{\tau}_{\mathrm{e,J}}(\boldsymbol{q}, \boldsymbol{0}, \bar{\boldsymbol{\theta}}, \boldsymbol{0})}{\partial \boldsymbol{q}}(\bar{\boldsymbol{q}}) \tag{5.4}$$

containing the linearized actuator output stiffnesses on joint level. For the fixed configuration of motor $\bar{\boldsymbol{\theta}}$ and joint positions $\bar{\boldsymbol{q}}$, the chosen actuation setup results in joint stiffness values of 36 Nm/rad for the knee and 19 Nm/rad for the ankle joint. This conversion allows us to compare the results with those of the b-SEA robot and shows how much softer a typical leg actuation configuration of the BioBiped1 robot versus the previously simulated b-SEA robot is.

The results of the simulation runs with BioBiped1 are summarized in Table 5.4 and 5.5. As can be quickly recognized, the falling heights can go up to at least 1.4 m without running the risk of exceeding the maximum possible motor torque values, assuming that the segments and the overall mechanics are robust enough for the impact forces occurring at these heights, which amount to approximately 13 times the body weight of BioBiped1. Furthermore, increasing the falling heights leads only very slowly to increased torques at the gearboxes. The values start already at a much lower level for the BioBiped1 robot compared to the b-SEA robot, which is due to the softer knee and ankle stiffnesses. It should be also noted that the torques on the joints, $\tau_{\mathrm{e,Hip}}$, $\tau_{\mathrm{e,Kne}}$, $\tau_{\mathrm{e,Ank}}$, become extremely large while the torques on the motors remain relatively small. In particular, they do not increase by the same ratio as the joint torques, which is due to the highly nonlinear actuation highlighted in Section 3.4. For instance, at the falling height of 1 m, the torques on the knee joint are almost three times higher than on the coupled motor. Also note that between the falling heights of 20 cm and 40 cm the distribution of the impact forces on the joints seem to change; now the torques on the knee joints are largest followed by those on the hip and then the ankle joints. We assume that as the instantaneous impact forces become greater, the axial deformation of the robot at ground contact changes and, with this, also the distribution of the impact forces to all joints. Fig. 5.5 displays the results of the simulation study where BioBiped1 is dropped from 10 cm, 40 cm, and 140 cm.

In addition, it should be noted that the energy restitution change seems to run counter to the value changes of $\tau_{\mathrm{e,M\,Ank}}$, $\tau_{\mathrm{e,M\,Kne}}$, and $\tau_{\mathrm{e,M\,Hip}}$ (see the results for the falling heights of 5 cm up

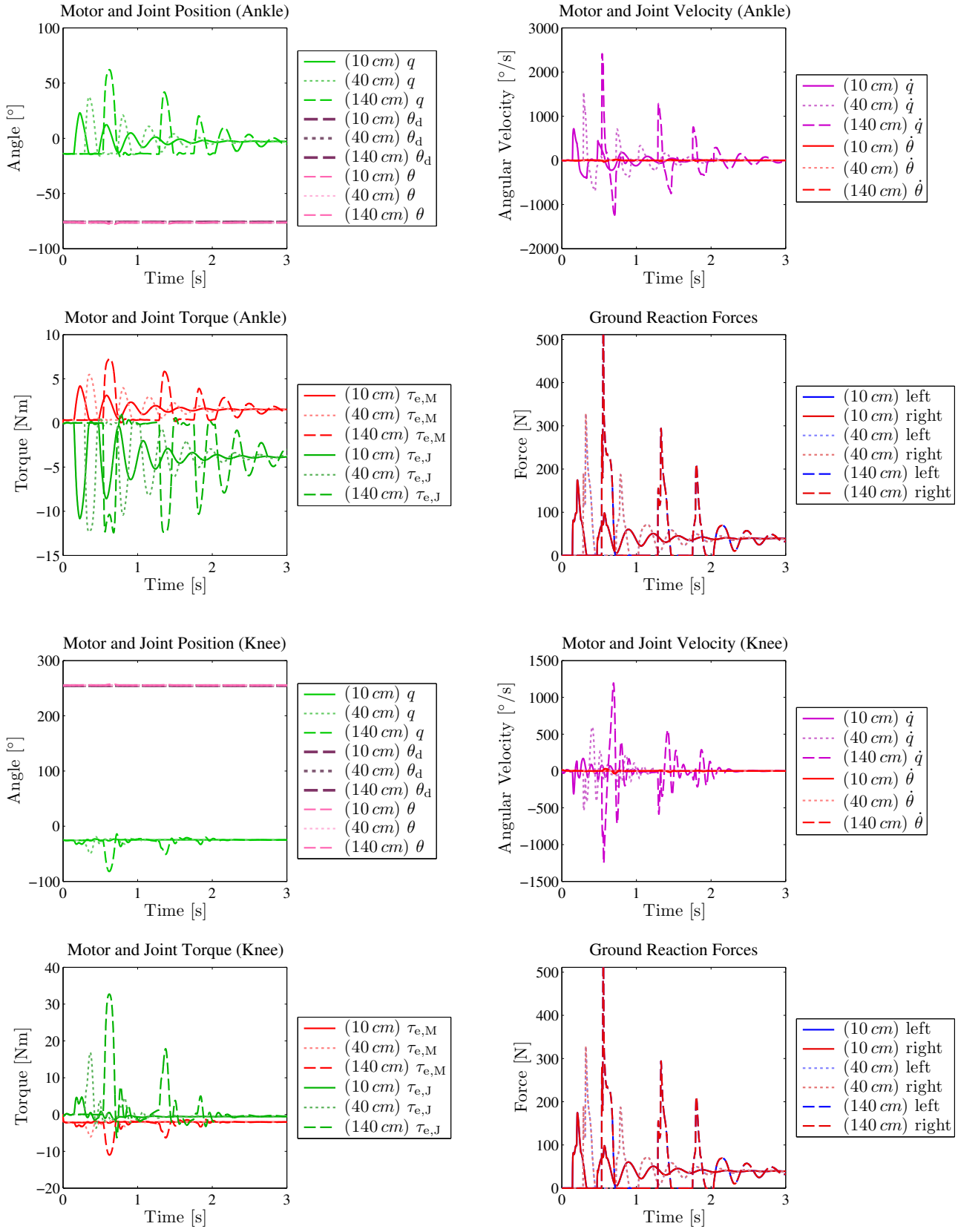

Figure 5.5.: Simulation results for passive rebound with the BioBiped1 robot dropped from 10 cm, 40 cm, and 140 cm for the ankle and knee joint.

to 40 cm). As the energy restitution decreases, the number of bounces increase from one to two; the torques at the gearbox increase continuously.

The influence of the higher compliance in BioBiped1, compared to the b-SEA robot, can be directly read off of the hopping height, for instance. After colliding with the ground when being dropped from 15 cm, BioBiped1 seems to compress much more, by almost 3 cm, than the b-SEA robot does.

Let us also analyze the results obtained for stiffer knee and ankle joint configurations, as depicted in Table 5.5. Here we chose stiffer springs for all knee and ankle tendons: VAS (15.5 N/mm, attachment point number 4, $q_0 = -75°$) and PL (8 N/mm, $q_0 = -75°$) in the knee and the monoarticular pair of SOL (15.5 N/mm, attachment point number 4, $q_0 = 20°$) and TA (6.7 N/mm, $q_0 = 20°$) in the ankle. At first sight, it might not be understandable why the energy restitution ratio rises for increased joint stiffness in knee and ankle joints. Additionally, the number of bounces increase up to four. In fact, the entire passive movement seems to become more dynamic, with greater hopping heights and ground clearances. Only the increase in peak torques on the motors indicates the increased joint stiffness. By analyzing the curves plotted in Fig. 5.6 we recognize that due to the soft ankle joint and the nonlinear actuation dynamics, the GRF slightly decrease before going up to a second even higher peak which causes also a second higher peak on the knee joint torques. So there seems to be a trade-off between the joint stiffness values and consequently the occurring joint and motor torques and desired dynamic behavior. This example tells us that a too soft actuation, particularly of the first joint interacting with the ground, can be negative on the course of energy restitution and all the other dynamic parameters. Additionally, too soft stiffness values will cause problems for the position control in the swing phase and even stance phase. As can be seen in the curves of Fig. 5.6, the original positions are held much better by the stiffer configured robot. These results allow conclusions on the optimal stiffness values that should be used for actuated hopping motions. Instead of using the experimentally tuned and scaled stiffness values based on human data [132], a more sophisticated approach in order to realize an optimal dynamic locomotion behavior is to determine the optimal joint stiffness values by means of such studies.

In the last row of Table 5.5 the results of the simulation with lower controller gains are given. As a result, the peak torques at the gearboxes can be decreased. However, this comes of course at the cost of less precise position control. Depending on the tasks and motions, precise position control may play a more or less important role.

5.2.4 Discussion

Summarizing this vast amount of results and drawing the most important conclusions, there is a clear interdependency between the chosen joint actuation type, controller gains, and resulting dynamics behavior of the leg. Inspired by the experiment with the real robot platform, we analyzed the effects of stiff, linear elastic joint, and nonlinear elastic tendon actuation for passive rebound. There was no doubt that the stiff actuation is very disadvantageous in terms of explosive energy-efficient dynamic behavior. Significant differences in the behavior could be detected between the stiff and b-SEA robot at the same falling heights. Due to the stiff actuation, impact forces are directly transmitted to the motors. Critical damage of the motors can be already expected at falling heights of 5 cm. Further, no energy can be stored from the impact, in contrast to the b-SEA robot.

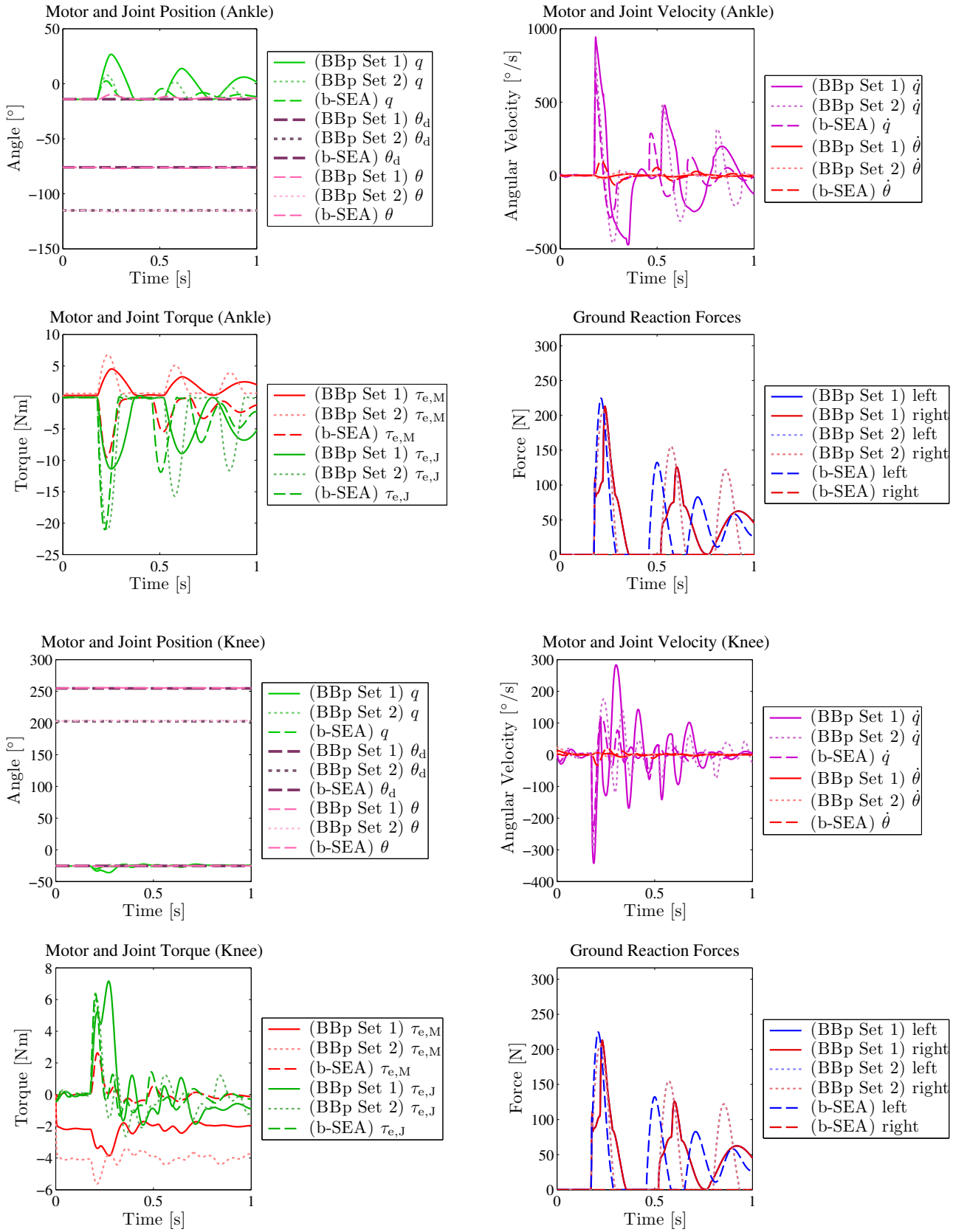

Figure 5.6.: Simulation results for passive rebound with the BioBiped1 robot and b-SEA robot dropped from the same height for the ankle and knee joint. "BBp Set 1" and "BBp Set 2" correspond to the soft, respectively stiffer, leg actuation. The joints of the b-SEA robot have torsional stiffnesses of 87 $^{Nm}/_{rad}$.

Table 5.4.: Simulation results for passive rebound with the BioBiped1 robot dropped from different heights.

Dropping height [m]	$k_{e,Ank}$ $k_{e,Kne}$ $k_{e,Hip}$ [Nm/rad]	**Bounce**	**Energy restitution** [%]	**Hopping height** [m]	**Ground clearance** [m]	**Duty factor** [%]	**Flight phase** [ms]	$\tau_{e,M\,Ank}$ $\tau_{e,M\,Kne}$ $\tau_{e,M\,Hip}$ $(\tau_{e,Ank}$ $\tau_{e,Kne}$ $\tau_{e,Hip})$ [Nm]	**GRF** [N]
0.05	87 36 19	1st	42.33	0.071	0.009	70.85	92	3.63 3.00 1.91 (9.73 3.53 4.28)	106.96
0.10	87 36 19	1st	35.59	0.094	0.022	57.58	139	4.18 3.29 1.34 (10.8 4.68 3.31)	174.58
0.15	87 36 19	1st	31.3	0.11	0.032	51.88	165	4.52 3.85 1.95 (11.36 7.16 4.46)	213.11
0.20	87 36 19	1st	28.53	0.129	0.042	47.79	188	4.79 4.37 2.5 (11.73 9.47 5.8)	245.01
		2nd	37.68	0.060	0.002	80.84	49		143.14
0.40	87 36 19	1st	26.81	0.202	0.091	36.73	278	5.48 6.07 3.75 (12.3 16.86 8.87)	328.33
		2nd	31.84	0.084	0.015	61.13	116		187.14
1.00	87 36 19	1st	28.77	0.438	0.271	26.09	475	6.68 9.38 8.61 (12.42 29.10 18.61)	500.48
		2nd	27.73	0.157	0.060	43.58	223		270.61
		3rd	32.36	0.067	0.004	73.00	70		172.94
1.40	87 36 19	1st	29.21	0.596	0.397	23.94	571	7.24 11.00 11.3 (12.43 32.70 23.95)	609.81
		2nd	28.6	0.217	0.102	38.20	287		294.28
		3rd	27.19	0.081	0.011	62.54	105		212.03

Table 5.5.: Simulation results for passive rebound with the BioBiped1 robot with varied joint stiffnesses and controller parameters dropped from 15 cm.

Dropping height [m]	$k_{e,Ank}$ $k_{e,Kne}$ $k_{e,Hip}$ [Nm/rad]	$k_{p,Ank}$ $k_{p,Kne}$ $k_{p,Hip}$ $k_{d,Ank}$ $k_{d,Kne}$ $k_{d,Hip}$	**Bounce**	**Energy restitution** [%]	**Hopping height** [m]	**Ground clearance** [m]	**Duty factor** [%]	**Flight phase** [ms]	$\tau_{e,M\,Ank}$ $\tau_{e,M\,Kne}$ $\tau_{e,M\,Hip}$ $(\tau_{e,Ank}$ $\tau_{e,Kne}$ $\tau_{e,Hip})$ [Nm]	**GRF** [N]
0.15	87 36 19	200 200 200 8 8 8	1st	31.3	0.11	0.032	51.88	165	4.52 3.85 1.95 (11.36 7.16 4.46)	213.11
0.15	87 56 56	200 200 200 8 8 8	1st	44.61	0.118	0.066	35.73	222	6.77 5.63 1.57 (21.09 6.11 3.62)	205.18
			2nd	53.08	0.070	0.030	45.52	151		155.16
			3rd	54.90	0.043	0.012	57.83	96		122.13
			4th	59.08	0.028	0.003	75.25	48		96.70
0.15	87 56 56	100 100 100 $8\sqrt{0.5}$ $8\sqrt{0.5}$ $8\sqrt{0.5}$	1st	45.59	0.119	0.067	35.43	225	6.65 5.58 1.3 (21.2 6.04 3.65)	205.57
			2nd	52.45	0.071	0.031	45.20	153		156.34
			3rd	55.88	0.044	0.013	57.33	98		123.02
			4th	59.88	0.029	0.004	73.13	53		98.21

The energy restitution ratio increases for compliant systems, depending on the type of actuation. For BioBiped1's nonlinear actuation dynamics a too high joint compliance can cause also high energy losses due to a chain of reactions from the GRF to the actuators absorbing too much energy, whereas a linear actuation type releases directly the stored energy. Therefore, spring selection also depends on the actuation type.

For the specific passive rebound tests studying the landing behavior of the robot, almost identical results could be obtained for both elastic linear joint and nonlinear tendon actuation: Simulating a b-SEA robot with the parameters of "Set 2" (87 $^{\text{Nm}}/_{\text{rad}}$, 56 $^{\text{Nm}}/_{\text{rad}}$, 56 $^{\text{Nm}}/_{\text{rad}}$ for the hip, knee, and ankle joint) yielded almost the same results as for the BioBiped1 actuation. The linearized joint stiffness values are only valid for the initial leg configuration, at ground contact this configuration certainly changes nonlinearly according to BioBiped1's actuation dynamics, which explains the deviations from the b-SEA robot.

Yet, BioBiped1's specific actuation design is advantageous in many respects. To fully exploit the advantages of its actuation system, it is important to concentrate on a few human-like muscle-tendon functionalities. Depending on the gait, not all tendons need to be implemented, as the use of all tendons may introduce timing issues that can be hardly handled. In total, the amount of passive redundant actuation should be kept at a minimum. It should be explored how actuated biarticular tendons can further reduce the complexity of the leg actuation design and improve the energy consumption, while preserving the desired dynamic locomotion behavior. It is also possible to omit the knee motor and the passive monoarticular antagonist and to implement, instead, the passive biarticular tendons spanning the knee joint.

In order to achieve a specific motion performance, it may be necessary, due to the vast amount of "regulating screws", to apply a kind of "cascaded optimization", e. g., to optimize, first, the actuation with respect energy restitution, hopping height, and ground clearance and, subsequently, to optimize the controller gains to keep the torques on the motors as low as possible. On the other hand, the decrease in torques comes at the cost of less precise position control, which is important particularly during swing phase. In general, however, precise position control is rather important for classical controller approaches for conventionally built, stiff robots. Furthermore, this issue could be circumvented in a future prototype by changing the joint stiffnesses depending on the swing and stance phase. Note, however, that too low controller gains lead to shocks being almost completely absorbed.

In the literature we could not find any similar studies except of Niiyama's work in [117]. The pneumatically driven robot was dropped from one meter. It was argued that soft landing was possible, accompanied by snapshots of the falling and landing, because of exploitation of the anti-gravity muscles and compliance. The study did not include any diagrams or tables with more in-depth information about the experimental setup and forces and torques involved.

5.3 Roles and Contributions of the Mono- and Biarticular Tendons during Open-Loop Controlled In-Place Hopping

As previously mentioned, a leg actuation including all tendons is quite complex and, without a prior extensive study, it is impossible to assign observed effects in simulated or real motions to the corresponding responsible active or passive tendon. Determining each tendon's contribution is a challenging task, as it can accelerate joints that it does not span and body segments to which it is not attached [84]. Understanding the impacts of the tendons requires an appropriate

Table 5.6.: Open-loop controlled in-place hopping: parameter settings for the leg actuation in each simulation run.

Simulation run	Joint	Tendon	Stiffness [N/mm]	Attachment [number]	Rest angle [deg]
1	Knee	VAS	15	5	-60
	Ankle	SOL	8	4	3
2 (3)	Knee	VAS	15	5	-60
		PL	8	1 (3)	-60
	Ankle	SOL	8	4	3
		TA	3	3	3
4	Knee	VAS	15	5	-60
		PL	8	3	-60
		GAS	8	1	-45
	Ankle			1	-10
		SOL	8	4	3
		TA	3	3	3

simulation setup including the detailed MBS dynamics model [131]. A study is needed to clarify the roles of the tendons and to rediscover early insights from biomechanics that have not yet been addressed by bipedal robot locomotion studies and have remained in oblivion for the majority of biomechanics researchers. The focus of this section lies on investigating the forward causality of the tendons, i. e., the effect of each tendon by actuating them one by one by means of open-loop controlled trajectories, similar to the experiments with the pneumatically jumping monopod described in [62].

The simulation setup is as follows. Reference motor trajectories are composed of partial linear interpolations designed separately for the swing and stance phase to achieve two-legged hopping motions. Additionally, the trajectories are filtered to avoid sudden switching of the motor turning direction, similar to the trajectories generated for the motor-gear unit selection (cf. Section 4.7.3). The designed PD-controlled motor trajectories for each joint consist of oscillations between two angles corresponding to a bent and stretched leg to simulate the synchronous flexion and subsequent extension in each step with a cycle time of 0.4 s.

The first four studies, presented in the following, were performed prior to the identification of the robot model. Therefore, some parameters such as the spring stiffness of the hip actuator and the geometric attachment points of the tendons do not correspond to those of the real robot. Nevertheless, the results obtained allow us to gain several insights regarding the role and interplay of the tendons.

The motor trajectories and control are not changed such that the reason for any observed effects and changes can be clearly identified, i. e., the P and D controller gains are the same in all simulation runs to avoid variations in the results due to the gains (listed in Table 4.3). The ground contact parameters are given in Table 4.2. The leg actuation setup for each simulation run is displayed in Fig. 5.7. The range of interesting spring stiffnesses are selected based on human experiment data. An overview of the selected rest lengths, attachment points, and spring stiffnesses for all tendons in each run is given in Table 5.6.

5.3.1 On the Role of a u-SEA and its Passive Antagonist

1. Simulation run: In this first run the ground contact is eliminated to avoid any interferences of the results through the contact dynamics. As shown in Fig. 5.7a, the leg is actuated in the hip

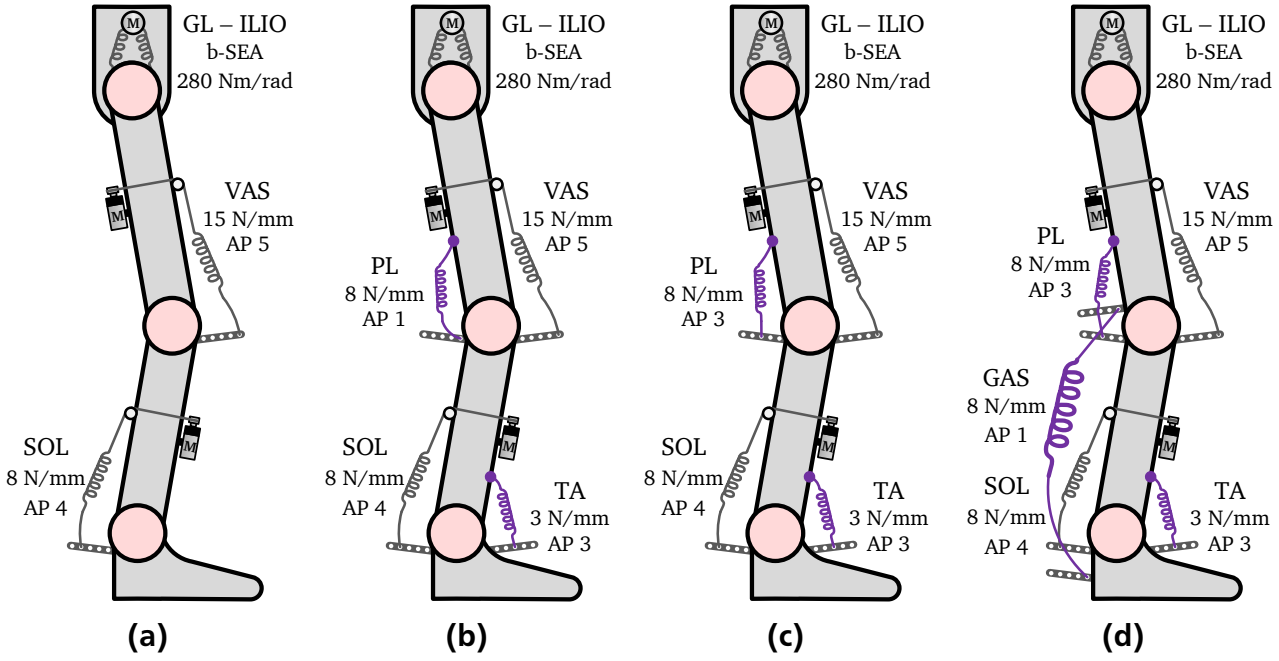

Figure 5.7.: Open-loop controlled in-place hopping: leg actuation setup for each simulation run to study the forward causality of varied leg actuation designs.

Table 5.7.: Open-loop controlled in-place hopping: energy consumption in each simulation run.

Simulation run	Hip E [J]	Knee E [J]	Ankle E [J]	Leg $\sum \mathbf{E}$ [J]
1	39.0458	43.9008	6.3861	89.3327
2	63.5794	58.5832	6.4685	128.6311
3	42.8959	46.5979	10.1847	99.6787
4	54.2539	49.5667	8.4033	112.2286

by a b-SEA, and in knee and ankle joint by the u-SEAs VAS and SOL. As expected, the hip motor activity leads to the desired joint behavior oscillating between the flexed and extended position due to the bidirectional actuation. The knee and ankle motors, however, achieve an actuation in only one direction. Both joints are extended by the motors; however, the movements backwards to the flexing positions do not occur correctly, particularly in the ankle joints. In the knee joints we can recognize a periodic pattern, but with an offset of almost 30° close to quite extended positions. The knee joints are actually overextending. Note that the mechanical joint limits were removed on purpose to detect among others such effects. Apparently, extending and releasing the tendons are not sufficient to retain the desired periodic patterns, particularly in the presence of friction. The most energy is consumed for the actuation of the knee joint which is due to the high motor velocity, followed by the hip joint also due to the high motor velocity. The results are provided in Table 5.8.

2. Simulation run: The antagonistic tendons PL and TA are added to the knee and ankle joint. The desired periodic patterns in knee and ankle joint become now realizable, however, at the price of higher motor torques, due to the opposing torques of the antagonists on the motors. This,

in turn, results in higher overall energy consumption by about 44%, from 89.33 J to 128.63 J. Interestingly, the energy required for the hip motor is increased by 62%, although the introduced tendons do not cross the hip joint. As Kuo noticed, the torques induced do not necessarily only affect directly the joint the tendon is crossing, but can also cause other joints to move [84]. The increased energy is, thus, due to higher external torques acting on the hip.

5.3.2 On the Role of the Ground Contact

3. Simulation run: After the realization of some kind of simultaneous flexion and extension of all leg joints, we introduce the ground contact to see if hopping can be achieved. To accommodate for the ground contact, the attachment point of PL was changed from number 1 to 3. The ground contact supports the flexion of ankle and knee joints. Therefore, the PL tendon can do less than in the previous run. All other settings are not changed to prevent complicating the access to insights. One obvious difference now is the full flexion of the ankle joints due to the ground contact. Although the parameter settings are not tuned to achieve optimal performance, the knee and ankle joints are quite synchronously flexed and extended. We can recognize clear flight phases and substantial hopping heights. The average duty factor amounts to 0.3, i. e., ground contact takes place only during 30% of the total cycle time. The average hopping height is 13 cm. Further, the GRF have the typical vertical single-humped patterns known from humans during hopping and running. The energy required by the hip and knee motors are reduced by 33% and 21%, respectively. Only the ankle motors need more power to track the output joint trajectory due to the external torques induced by the ground contact. In total, the consumed energy is decreased by 23% to 99.68 J confirming the positive supporting impact by the ground.

5.3.3 On the Role of Biarticular Tendons

4. Simulation run: The above run is repeated with a GAS tendon in each leg to analyze its impacts. Several slight changes in a positive direction can be observed. First, the GRF patterns are smoother. Second, the computed average duty factor can be decreased from 0.3 to 0.29, i. e., flight phases are increased. The hopping heights in average amount to 14 cm. Also, it can be noted that the ground contact occurs more regularly and there is less variation in flight phase and hopping height compared to the previous simulation. Besides, the flexion of the ankle joints, intensified by the ground contact already in *3. Simulation*, is now reduced to the necessary degree.

Interestingly, these positive effects are achieved without even having optimized the design parameters for the best possible results. Another effect, that at first sight is not consistent with biomechanical findings, can be detected. While the torques generated by the GAS tendon on the ankle joint are negative and thus “cooperating” with the motor for the ankle extension, the torques on the knee joint by GAS are positive, aside from a small negative curve at the beginning of the hopping motion, i. e., it “cooperates” with the motor for the knee extension. This is not in accordance with the overwhelming consensus in biomechanics literature regarding the joint movements caused by biarticular muscles where the GAS is reported to act only as knee flexor and ankle extensor.

The reason why we observe this during the simulated motion is that the lever lies on the other side of the joint due to the location of the tendon’s attachment on the knee side in the x-y-plane

and the knee joint angle. Apparently, the attachment on the knee side can be adjusted such that the tendon force applied to the thigh and the load experienced by the lever lie on the same side of the joint.

Although positive GAS torques support the knee motor, the energy consumption slightly increases, as the GAS activity also increases the PL torques which, in turn, lead to higher VAS torques. Optimized settings can help to coordinate the various actions optimally. A numerical simulation study for an exoskeleton showed that there is great potential for exploitation of the optimal arrangement of passive tendons [166].

Regarding energy consumption, it is possible to benefit from this observed effect. If the settings are well tuned, the motor for the knee extension must do less work when additionally supported by the GAS tendon. It is even possible to completely omit the knee motor for the extension, as, for instance, also suggested for walking in [36].

5.3.4 On the Importance of the Tendons' Attachment Locations and the Lombard Paradox

In general, biarticular muscles in human legs affect the movements of two joints. In biomechanics literature there is also an overwhelming consensus regarding the joint movements caused by these muscles. While RF acts as combined knee extensor and hip flexor, BF, which is one of three muscles acting within the hamstrings muscle group, behaves exactly the other way. GAS extends the ankle and flexes the knee joint. However, this is a very common description of the above named muscles' actions and does not reveal their actually very complex, gait-dependent functionalities [135].

The previous study showed that the biarticular tendons can be responsible for an additional action during dynamic locomotion and thus appear to have even more sophisticated functionalities than previously assumed. The tendon GAS acted as synergist extending the knee joint at knee angles above a specific position. After extensive search we found a few biomechanics studies confirming this additional action during second half of ground contact in human locomotion [175]. Apparently, it was observed by Lombard already in 1903 and labeled the "paradoxical" function of biarticular muscles. It has not yet been addressed by any bipedal robot locomotion study.

Although there are some more detailed descriptions of this action available, as summarized in Section 2.2, there is only little information about the exact whole-body configuration and lever arms acting. Furthermore, it would be interesting to investigate the nature of this phenomenon, whether it is gait-, phase-, or configuration-dependent. Since detailed studies on human subjects are presumably required to fully understand the reasons for this paradoxical action, we will examine here this behavior by the laws of classical mechanics exemplary for the passive GAS tendon.

Let us draw our attention to Fig. 5.8a and 5.8b. In order to change a flexion into an extension movement of a joint, the torques acting on that joint need to be reversed in their direction. According to the definition of torque as $\boldsymbol{\tau} = \boldsymbol{r} \times \boldsymbol{F}$, where $\boldsymbol{r}$ and $\boldsymbol{F}$ denote the lever arm and force vector, respectively, the torque reversion requires either a reversion of the force or lever arm. In Fig. 5.8a the GAS tendon still acts as both ankle and knee flexor. The tendon force applied to the thigh and the load experienced by the lever lie on the same side of the joint. In Fig. 5.8b we have depicted a possible construction for the attachment of GAS to the thigh such that the lever lies on the other side of the joint and herewith causes reversed torques to extend the knee

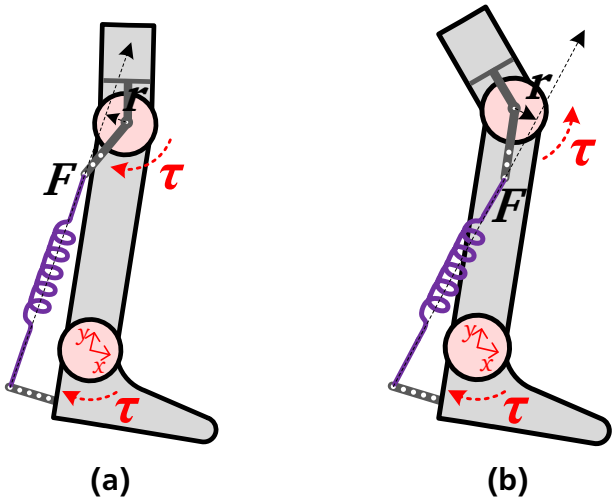

Figure 5.8.: Paradoxical actions of the biarticular GAS tendon can be influenced by the manner the tendon is attached to the thigh: (a) GAS acts as knee flexor and ankle extensor; (b) GAS acts as knee and ankle extensor.

joint. The hinge joint mounted on the thigh passes on the tendon forces to torques acting on the knee joint. Such construction can cause permanently an extension movement of the knee joint. Obviously, it is also possible to reverse the direction of the force vector. In general, a such permanent functionality may turn out to be quite beneficial, as shown in the following.

We use a similar simulation model as in the previous simulation run, but now with a validated model to derive guidelines for future prototypes. The only changes concern the leg actuation parameters and the control input. The model is depicted in Fig. 5.9b and includes all monoarticular pairs in hip, knee, and ankle joint, and additionally the GAS tendon. In order to analyze the benefits of GAS as knee extensor, the tendon is attached to the thigh in the manner shown in Fig. 5.8b. The input trajectories consist of sinusoidal functions generated by (4.1) with $f_0 = 2\,\mathrm{Hz}$. The flexed and extended leg configuration are set to $\boldsymbol{q}_{\mathrm{flex}} = \left(q_{\mathrm{Hip}}, q_{\mathrm{Kne}}, q_{\mathrm{Ank}}\right) = (26°, -63°, 13°)$ and $\boldsymbol{q}_{\mathrm{ex}} = \left(q_{\mathrm{Hip}}, q_{\mathrm{Kne}}, q_{\mathrm{Ank}}\right) = (13°, -26°, -13°)$, respectively. The corresponding motor angles are then computed to compensate the gravitational forces in these configurations. As low gain parameters for each motor PD controller, we choose $k_{\mathrm{p}} = 30$ and $k_{\mathrm{d}} = 8$. The forward dynamics is computed in MATLAB/Simulink using the ode23 (Bogacki-Shampine) solver with variable step size, relative tolerance 10^{-3}, and adaptive zero-crossing options. The outcome of this simulation are dynamic two-legged hopping motions with an average duty factor of 38.67 % and hopping height of 0.2218 m. The GRF are displayed in the topmost diagram of Fig. 5.10. For these synchronous motions the GRF of both feet overlap. In the middle diagram the desired and actual knee motor signal, i. e., θ_{d} and θ, are displayed together with the actual knee joint angle q. The lower diagram is the most interesting, as it displays the total joint torques, $\tau_{\mathrm{e,Kne}}$, and the single torques induced by all tendons coupling the knee: τ_{VAS} by the active VAS tendon, τ_{PL} by the passive PL tendon, and τ_{GAS} by the passive biarticular GAS tendon. It can be recognized that GAS supports the actions of the knee motor by further extending the knee joint. In this leg actuation, however, this also results in higher PL torques, which leads to higher VAS torques due to the interplay of the tendons. Therefore, with respect to an economical leg actuation design, it

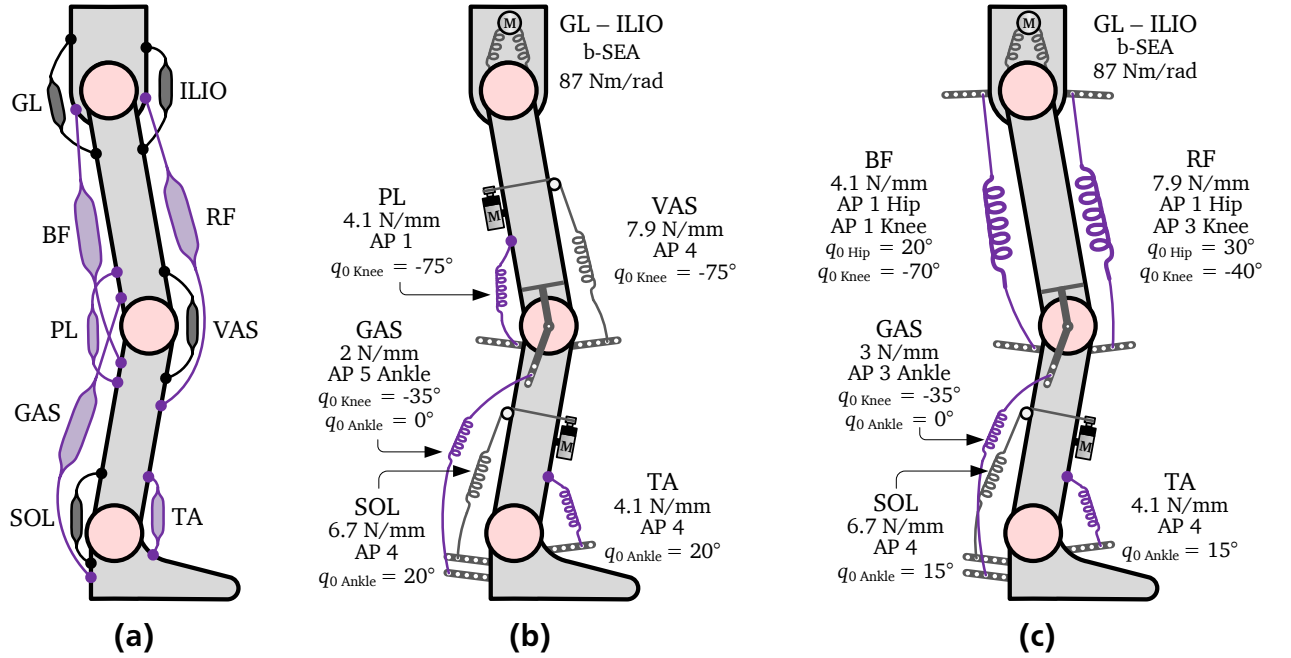

Figure 5.9.: Locomotion models to study the Lombard paradox using BioBiped1's musculoskeletal leg design: (a) essential human muscle groups during locomotion; (b) locomotion model with the parameters used for the implemented tendons (AP stands for attachment point); (c) locomotion model omitting the VAS motor.

is advisable to completely omit the knee motor for the extension, as for instance suggested for level-ground walking in [36].

As one possible example, we suggest to include RF and BF and to remove VAS and PL. The leg actuation design studied here is shown in Fig. 5.9c. The same motor trajectories are applied to this novel underactuated model, with the difference that the knee motions are now only influenced by passive biarticular tendons. As Fig. 5.11 indicates, this novel locomotion model is capable of highly dynamic two-legged hopping motions saving 62.59 % energy compared to the previous leg actuation including the knee motor VAS (see Table 5.8). With an average duty factor of 43.23 % and hopping height of 0.192 m, the motions are not as dynamic as those demonstrated with the previous locomotion model, but rather more regular when comparing the GRF patterns. The results suggest that dynamic hopping motions can be also performed without active knee extension benefiting from the paradoxical behavior of GAS. The only difference between the simulations of the previous and novel locomotion model (cf. Fig. 5.9b and 5.9c) concern the start of the simulation. The previous locomotion model was capable of starting directly from the ground, whereas for the robot model analyzed here we had to simplify the starting conditions by dropping the robot from 10 cm. By systematic optimization of the elastic transmission parameters in the ankle, an active lift-off from the ground is expected to be enabled even with this underactuated leg design.

To our knowledge, this is the first study in which the paradoxical action of biarticular muscles is discussed in the context of robot locomotion and exemplary analyzed for one muscle using the identified MBS dynamics simulation model of the BioBiped1 robot. The simulation results suggest to use the complex functions of these muscles beneficially to reduce the energy consumption. Also, the analyses raise the general question whether implemented human-like

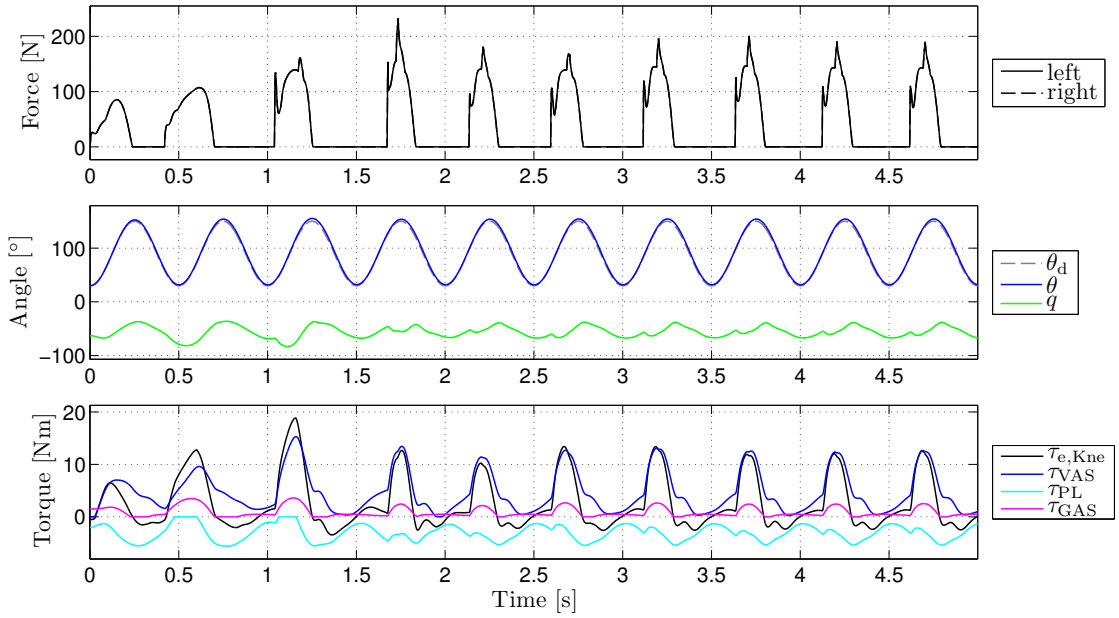

Figure 5.10.: Simulation results for the locomotion model shown in Fig. 5.9b: The top diagram displays the GRF, the middle diagram the desired and actual knee motor signal, i. e., θ_d and θ, and the actual knee joint angle, q, and the lower diagram the total knee joint torques, $\tau_{e,Kne}$, and the single torques induced by all tendons coupling the knee (τ_{VAS} by the active VAS tendon, τ_{PL} by the passive PL tendon, τ_{GAS} by the passive biarticular GAS tendon).

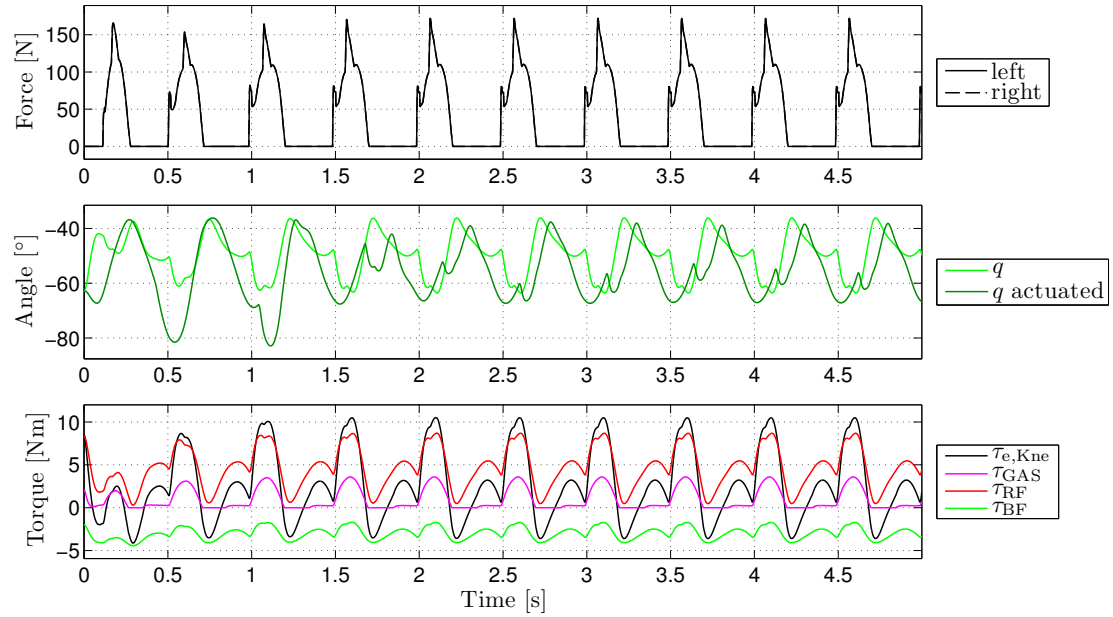

Figure 5.11.: Simulation results for the locomotion model shown in Fig. 5.9c: The top diagram displays the GRF, the middle diagram the actual knee joint angle and, for comparison, that of the locomotion model shown in Fig. 5.9b, and the lower diagram the total knee joint torques and the single torques induced by the passive biarticular tendons (τ_{GAS} by GAS, τ_{RF} by RF, τ_{BF} by BF).

Table 5.8.: Energy consumption of the models shown in Fig. 5.9b and 5.9c.

Locomotion model	Hopping height [m]	Duty factor [%]	Hip E [J]	Knee E [J]	Ankle E [J]	Leg $\sum E$ [J]
With VAS motor (cf. Fig. 5.9b)	0.2218	38.67	7.0526	304.3469	213.6929	525.0925
Without VAS motor (cf. Fig. 5.9c)	0.192	43.23	8.5522	0	187.8801	196.4323

muscle-tendon complexes have to act in conformity with biomechanical observations and suggestions. Rather, reported insights should be seen as valuable hints to enable the derivation of novel design guidelines that support dynamic robot locomotion.

5.3.5 Discussion

By applying the forward causality method, the presented models of all actuator types allowed us to capture their dynamics during vertical hopping motions and to draw several important conclusions. The b-SEA in the hip can be considered as a conventional SEA, because it actuates both directions. More interesting are the u-SEAs and the passive, mono- and biarticular tendons spanning one or two joints. It became clear that, during hopping, the monoarticular tendons cannot fulfill their designated roles without their counteracting tendons. Thus, they should be deployed in pairs, requiring two tendons with built-in extension springs, but only one motor. The flexion then occurs passively at an activation time instant. It depends on the set rest angle triggered by the actively actuated tendon that generates a joint's movement. The passive tendon can only be controlled by the insertion points, the spring stiffnesses, and the moment arms.

The use of the biarticular tendon GAS resulted in smoother ground contact patterns, longer flight phases, and greater hopping heights, even though optimized tendon settings are currently not available. Because GAS is also in charge of the ankle extension, it may be feasible to omit the SOL ankle motor, to enhance energy savings. This omission would also eliminate the timing issue, because the involved tendons may interfere with each other if they are not optimally tuned for their roles beforehand.

With the introduction of the paradoxical action of the GAS tendon, also observed in human locomotion, by using the specific exemplary construction shown in Fig. 5.8b for the attachment to the thigh, we were able to greatly improve the energy consumption. This effect has not yet been addressed in bipedal robot locomotion studies. We demonstrated, by means of a detailed MBS dynamics simulation, how this positive effect subserves energy-efficient dynamic 1-D hopping motions and enables us to establish a novel bipedal locomotion model. We suggest using the complex functions of the biarticular tendons beneficially to reduce the energy consumption, because this also offers an alternative to developing complex variable impedance actuators that cannot be easily dealt with in locomotor systems. Instead, the emphasis should lie on a full exploitation of human-like mono- and biarticular tendons.

In general, the investigations can be extended to analyses of various spring stiffnesses, rest angles, and attachment points for each tendon-based actuator. However, using solely open-loop controlled trajectories complicates access to possible insights. With stepwise addition

of tendons, different joint angle trajectories are generated, due to the changed joint stiffness and the nonadapted motor trajectories. Therefore, it is very difficult to compare different leg actuation designs and to pinpoint the "regulating screws" of the design space, i. e., rest lengths, attachment points, and spring stiffnesses, in addition to the structural placement of the fixed and moving fixation points in general. Furthermore, just adding one tendon does not automatically yield better results for all performance criteria. We observed that the addition of GAS in the fourth simulation run caused better dynamic hopping properties but also increased energy consumption. Realizing the Lombard paradox enabled energy savings of more than 60 %, due to the prior establishment of a novel locomotion model. In general, improvements in locomotion performance defined by the criteria in Section 4.4 can be only achieved if the interplay of all actuators is well coordinated. Ideally, properly designed simulation studies enable the definition of guidelines for the beneficial use of each actuator, in terms of bandwidth, response delay, joint stiffness, and the overall compliance of the entire system. Such opportunities are provided by the model-based motion generation and control method introduced in Section 4.3. In order to create a common basis for different leg actuation designs, and thereby to allow a fairer evaluation of the locomotion performance, it is crucial to use a model-based approach that incorporates detailed models of the actuator dynamics.

5.4 Investigating Leg Actuation Design versus Performance during Model-based Controlled In-Place Hopping

In this section we study identical two-legged hopping motions for robot models with different leg actuation designs applying the model-based centralized motion generation and control approach described in Section 4.3, to create a better basis for comparing the locomotion performance of the different models.

For this purpose, we first design a suitable trajectory to realize in-place hopping on the rigid model of the BioBiped1 robot. Based on previous experiments, the leg configurations are chosen as follows: $\boldsymbol{q}_{\text{flex}} = \left(q_{\text{Hip}}, q_{\text{Kne}}, q_{\text{Ank}}\right) = (26°, -63°, 13°)$ and $\boldsymbol{q}_{\text{ex}} = \left(q_{\text{Hip}}, q_{\text{Kne}}, q_{\text{Ank}}\right) = (13°, -26°, -13°)$, similar to the hopping simulations discussed in Section 4.5.1. As fundamental frequency we choose a sligthly faster frequency with $f_0 = 2.2\,\text{Hz}$. Using the controller gains for the rigid model, given in Table 4.3, the forward dynamics of the rigid BioBiped1 model is simulated for ten cycles in MATLAB/Simulink using the ode23 (Bogacki-Shampine) solver with variable step size, relative tolerance 10^{-3}, and adaptive zero-crossing options. Note that, in order to obtain low joint torques, $\hat{\boldsymbol{\tau}}_{\text{e,J}}$, the rigid model is simulated without ground contact, as suggested in Section 4.6. The outcomes of this step, $\hat{\boldsymbol{\tau}}_{\text{e,J}}$ and $\hat{\boldsymbol{q}}$, are displayed in Fig. 5.12.

5.4.1 BioBiped1 Robot Model with Nonlinear Elastic Tendon Actuation

Applying the centralized, nonlinear, model-based motion generation and control approach, introduced in Section 4.3, we deduce the necessary motor torque and position trajectories for the desired joint angular trajectories obtained by the forward dynamics simulation of the rigid model, $\hat{\boldsymbol{\tau}}_{\text{e,J}}$. Subsequently, the forward dynamics of the BioBiped1 model with a specific leg actuation design is simulated to track the desired joint trajectories, $\hat{\boldsymbol{q}}$. For the PD control of the full BioBiped model we choose $k_{\text{p}} = 30$ and $k_{\text{d}} = 8$.

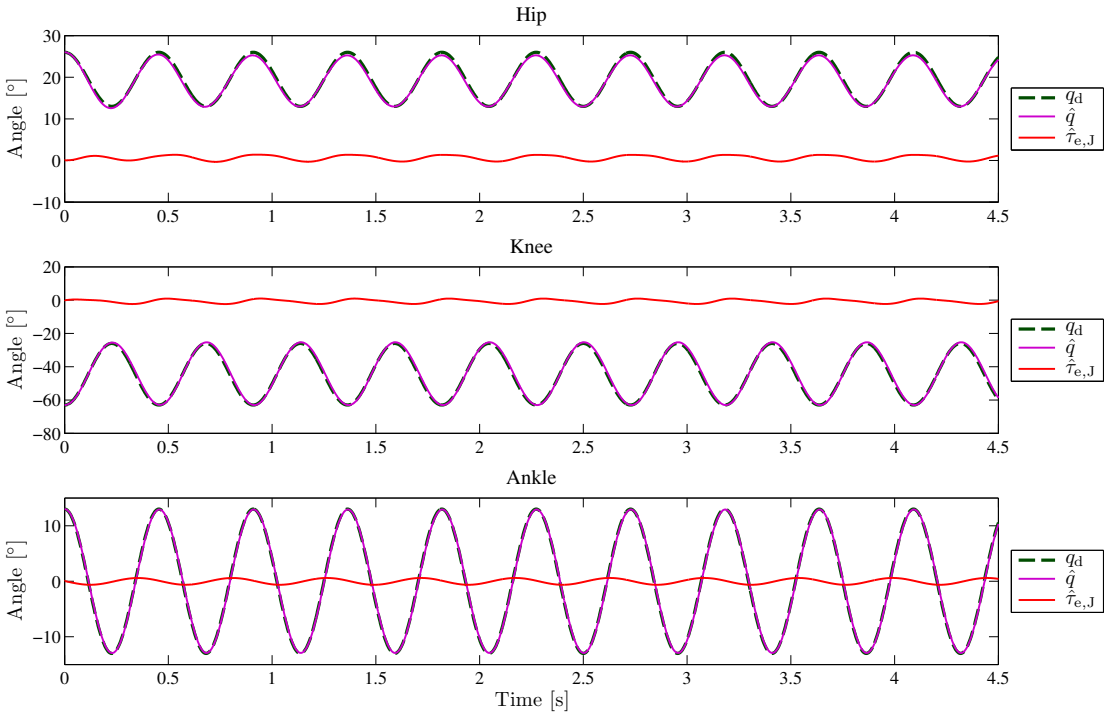

Figure 5.12.: Forward dynamics simulation of the rigid model for desired reference trajectories: The top diagram displays the actual hip joint torques and joint angles, $\hat{\boldsymbol{\tau}}_{\mathrm{e,J}}$ and $\hat{\boldsymbol{q}}$, and the desired joint angles, $\boldsymbol{q}_{\mathrm{d}}$; the middle and bottom diagram display those of the knee and ankle joint, respectively.

Varying the Leg Actuation Design

The different sets for the selected leg actuation designs are given in Table 5.9. We start with the leg actuation design that yielded the best results in terms of energy restitution and dynamic passive rebound behavior (cf. studies in Section 5.2). For set 1, the actuation setup consists of the b-SEA in the hip (with 87 Nm/rad and $n_{\mathrm{p}} = 2$), the monoarticular pair of VAS (15.5 N/mm, attachment point number 4, $q_0 = -75°$) and PL (8 N/mm, $q_0 = -75°$) in the knee, and the monoarticular pair of SOL (15.5 N/mm, attachment point number 4, $q_0 = 20°$) and TA (6.7 N/mm, $q_0 = 20°$) in the ankle. For the fixed configuration of motor and joint positions at ground contact, which is the most critical situation of the locomotion phase, the chosen actuation setup results in joint stiffness values of 66 Nm/rad for the knee and 55 Nm/rad for the ankle joint. This conversion is only valid for this fixed leg configuration and does not allow to compare the results with those of a robot with linear joint elasticities. Due to BioBiped1's nonlinear actuation dynamics, these joint stiffnesses will vary over the locomotion phase and eventually be even softer than at ground contact.

For set 2, we add the biarticular tendon RF with the given spring stiffness, attachment points for the hip and knee side, and the corresponding rest angles. Since the actuation design changes, also the requirements demanded of the motors change, as we will evaluate below. However, at ground contact, the leg actuation design does not change in stiffness. The conversion to linear joint stiffness yields almost exactly the same results as for the previous set: 67 Nm/rad for the knee and 55 Nm/rad for the ankle joint.

To vary now more clearly the overall leg stiffness, for set 3, the stiffnesses of the knee VAS and PL tendon are decreased, whereas the RF stiffness is tripled. The conversion to linear joint

Table 5.9.: Various leg actuation designs for two-legged in-place hopping. The hip actuation remains unchanged in all sets, i. e., the hip is actuated by a b-SEA with torsional stiffness 87 Nm/rad and transmission ratio $n_p = 2$, unless it is additionally actuated by a passive biarticular tendon.

Set	Joint	Tendon	Stiffness [N/mm]	Attachment [number]	Rest angle [deg]	Set	Joint	Tendon	Stiffness [N/mm]	Attachment [number]	Rest angle [deg]
1	Knee	VAS	15.5	4	-75	**4**	Knee	VAS	7.9	4	-75
		PL	8	1	-75			PL	4.1	1	-75
	Ankle	SOL	15.5	4	20		Ankle	SOL	6.7	4	20
		TA	6.7	1	20			TA	4.1	1	20
2	Knee	VAS	15.5	4	-75	**5**	Knee	VAS	7.9	4	-75
		PL	8	1	-75			PL	4.1	1	-75
		RF	2	4	-10			GAS	6.7	1	-30
	Ankle	SOL	15.5	4	20		Ankle	SOL	6.7	4	20
		TA	6.7	1	20			TA	4.1	1	20
	Hip	RF	2	4L	10			GAS	6.7	4	-10
3	Knee	VAS	13	4	-75	**6**	Knee	VAS	7.9	4	-65
		PL	6.7	1	-75			GAS	4.1	1	-35
		RF	6	4	-10			BF	4.1	1	-30
	Ankle	SOL	15.5	4	20		Ankle	SOL	6.7	4	20
		TA	6.7	1	20			TA	4.1	1	20
	Hip	RF	6	4L	10			GAS	4.1	5	-5
							Hip	BF	4.1	4U	-20

stiffness yields now slightly changed values: 56 Nm/rad for the knee and 56 Nm/rad for the ankle joint.

For set 4, we investigate a very soft leg actuation, similar to the one tested in the passive rebound studies for the BioBiped1 model, with VAS (7.9 N/mm, attachment point number 4, $q_0 = -75°$) and PL (4.1 N/mm, $q_0 = -75°$) in the knee and the monoarticular pair of SOL (6.7 N/mm, attachment point number 4, $q_0 = 20°$) and TA (4.1 N/mm, $q_0 = 20°$) in the ankle. Only the prespanning of the tendons and the maximum possible torques applied, due to different rest angles and attachment points, are slightly changed. The knee and ankle joint stiffness at ground contact amount to 34 Nm/rad and 23 Nm/rad, respectively.

For set 5, we add the biarticular tendon GAS. The knee and ankle joint stiffness at ground contact change to 35 Nm/rad and 24 Nm/rad, respectively.

Finally, to avoid too many timing issues with different tendons, we remove PL and include instead the BF tendon (see Table 5.9). The leg actuation design now include in total two biarticular tendons. The knee and ankle joint stiffness at ground contact amount to 27 Nm/rad and 20 Nm/rad, resulting thus in the softest leg of all sets.

Table 5.10.: Evaluation of various leg actuation designs for model-based controlled two-legged in-place hopping with respect to important criteria assessing the energy efficiency and dynamics degree of the performed motions: hopping height, ground clearance, duty factor, flight phase, peak ankle motor torque, $\tau_{\mathrm{e,M\,Ank}}$, peak knee motor torque, $\tau_{\mathrm{e,M\,Kne}}$, peak hip motor torque, $\tau_{\mathrm{e,M\,Hip}}$. These criteria represent the average values for five cycles after each model has reached the steady state. Regarding energy consumption the following values are provided: the total electrical energy, E, the electrical energy consumed by the ankle joint, E_{Ank}, the knee joint, E_{Kne}, and the hip joint, E_{Hip}; the total mechanical energy, E_{mech}, the mechanical energy consumed by the ankle joint, $E_{\mathrm{mech\,Ank}}$, the knee joint, $E_{\mathrm{mech\,Kne}}$, and the hip joint, $E_{\mathrm{mech\,Hip}}$. Further, the standard deviations of the realized from the desired joint angle trajectory are listed for each leg joint: $\sigma_{\mathrm{q\,Ank}}$, $\sigma_{\mathrm{q\,Kne}}$, $\sigma_{\mathrm{q\,Hip}}$.

Criteria		**Set 1**	**Set 2**	**Set 3**	**Set 4**	**Set 5**	**Set 6**
Hopping height	[m]	0.2205	0.2201	0.2139	0.1972	0.20	0.1881
Ground clearance	[m]	0.2051	0.2083	0.1977	0.1567	0.1716	0.1573
Duty factor	[%]	22.54	23.29	23.59	33	33.28	37.20
Flight phase	[ms]	356	354	351	306	308	288
$\tau_{\mathrm{e,M\,Ank}}$	[Nm]	6.86	7.53	7.085	7.52	7.97	8.04
$\tau_{\mathrm{e,M\,Kne}}$	[Nm]	9	10.26	11.897	10.71	15.86	16.4
$\tau_{\mathrm{e,M\,Hip}}$	[Nm]	2.93	2.9	4.78	4.81	4.64	11.73
E	[J]	1521	1636	1994	1442	1591	1274
E_{Ank}	[J]	191	193	194	207	192	184
E_{Kne}	[J]	556	615	792	500	590	429
E_{Hip}	[J]	13	10	11	14	13	25
E_{mech}	[J]	1307	1407	1722	1249	1372	1076
$E_{\mathrm{mech\,Ank}}$	[J]	165	166	167	180	165	157
$E_{\mathrm{mech\,Kne}}$	[J]	477	529	685	433	510	364
$E_{\mathrm{mech\,Hip}}$	[J]	12	9	8	12	11	16
$\sigma_{\mathrm{q\,Ank}}$	[deg]	8.57	8.79	8.71	15.63	15.05	16.89
$\sigma_{\mathrm{q\,Kne}}$	[deg]	3.86	3.84	5.13	8.47	8.5	10.91
$\sigma_{\mathrm{q\,Hip}}$	[deg]	3.5	2.97	2.37	5.22	7	5.69

Evaluation

In order to evaluate these different leg actuation designs, we study the locomotion performance in terms of achieved hopping height, ground clearance, duty factor, and flight phase. Additionally, we compute the peak torques arriving at the gearboxes ($\tau_{\mathrm{e,M\,Ank}}$, $\tau_{\mathrm{e,M\,Kne}}$, $\tau_{\mathrm{e,M\,Hip}}$). We assume, similar to the passive rebound studies, that on short term the peak torques arriving at the gearbox may be up to 12 Nm. For these criteria, only average values are computed, i. e., the first few cycles are excluded until the steady state is reached. For all locomotion models, the last five cycles are taken into consideration for the computation of the criteria. Finally, both the mechanically and electrically consumed energy are considered (E and E_{mech}) and the values for

each leg joint separately. To assess the quality of the tracked trajectories, the standard deviations of the actual from the desired joint angular trajectories are computed. All these criteria and their values are provided in Table 5.10.

The forward simulation of all locomotion models result in dynamic synchronous hopping motions. The motions demonstrate very well that the robot is capable of active pushoff. This capability is indirectly required as the robot starts from the ground in an initial crouched position and needs to generate enough thrust to lift off by itself from the ground. This would be not ensured if the robot was dropped to find its own gait. Therefore for the initiation of hopping a strong push-off movement is induced by these initial starting conditions which results in a quite fast straightening motion of the legs. However, clear differences can be recognized with respect to the evaluated criteria (see Table 5.10).

Let us start with set 1 which represents clearly the stiffest leg design of all simulated sets. This leg design proved to be the most dynamic as well as energy-efficient in terms of the achieved high energy restitution ratio in the passive rebound studies. Therefore, the results are expected to be similar good for dynamic hopping motions. The listed values confirm a high dynamics degree of the performed motions with an average duty factor of 22.54 % and hopping height of 22.05 cm. The energy consumption, however, is quite high for these motions. Particularly the requirements on the knee motor appear to be quite demanding. Note, however, that the energy losses from electrical to mechanical energy consumption are impressively low. The peak torques arriving at the gearboxes are still below our threshold of 12 Nm, causing thus no damage to the motors.

Since the gravity compensation for ground contact was not included in the forward simulation of the rigid model, the controller is expected to do more work at ground contact to track the desired trajectories. The ground contact necessarily leads to modified requirements on the motors and changes both motor and joint torques which in turn result in slightly varied joint motions. In the light of these explanations the listed standard deviations are comparably good and it can be recognized from Fig. 5.13, 5.14, and 5.15 that the desired joint trajectories can be tracked sufficiently well, although the ground contact was excluded in the simulation of the rigid model.

The leg actuation specified by set 2 does not result in a significant leg stiffness change at ground contact. The design is additionally enhanced by the biarticular tendon RF. The results yield a similar locomotion performance in terms of the dynamics degree, but at the price of higher peak torques and energy consumption. With comparable deviations the trajectories are still tracked sufficiently well.

The leg actuation specified by set 3 leads to decreased knee joint stiffness. This change affects both the dynamics degree of the motions and the energy consumption negatively. While the dynamics degree slightly decreases, the energy consumption as well as the peak torques increase significantly. Further, the trajectories are tracked with less precision.

The parameter settings of set 4 lead to greatly decreased knee and ankle joint stiffnesses, entailing greater deviations from the desired joint angle trajectories and a lower dynamics degree of the performed hopping motions. While the peak torques, however, are even higher than for set 1, the energy consumption drops considerably.

Set 5 and 6 (with further decreased knee and ankle joint stiffnesses) cause too high peak torques on the knee motors without offering any advantage compared to the other sets. Set 5 appears to lead to very high ankle compliance resulting in constantly changing patterns from

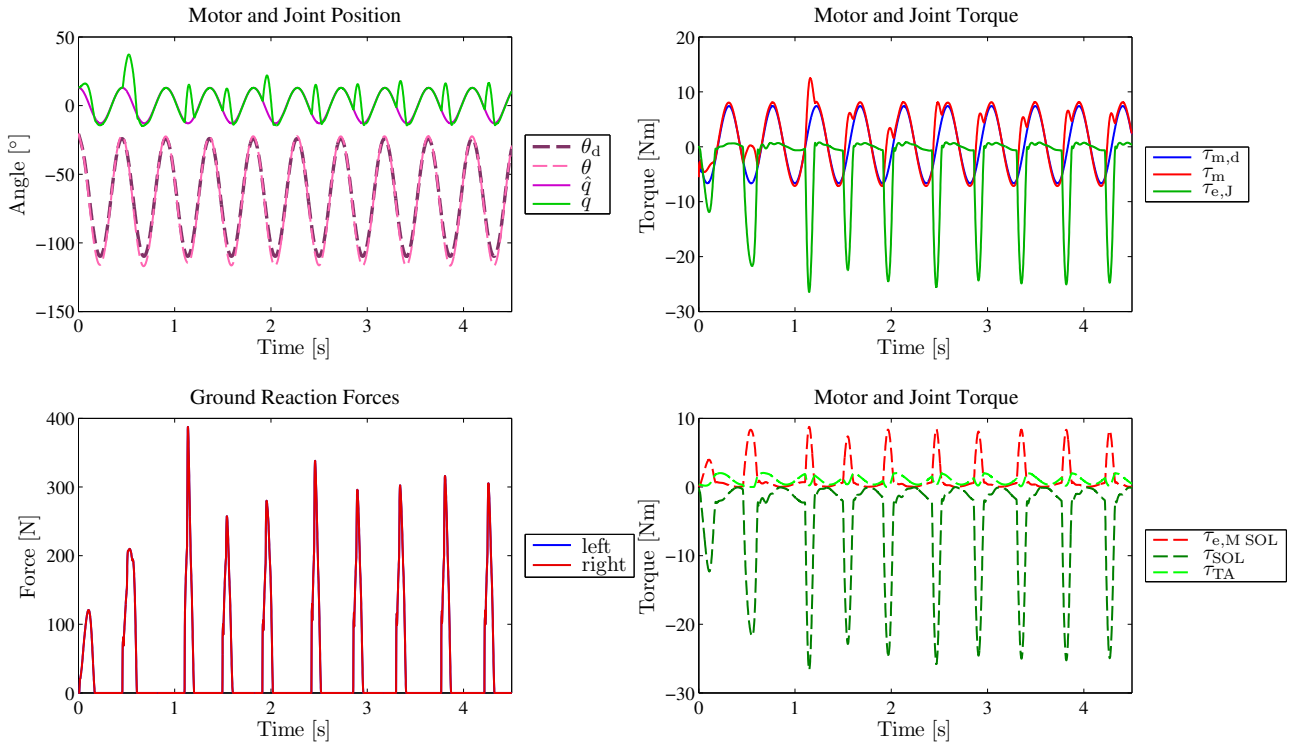

Figure 5.13.: Forward dynamics simulation results for the ankle joint of the BioBiped1 robot with the parameter settings of set 1.

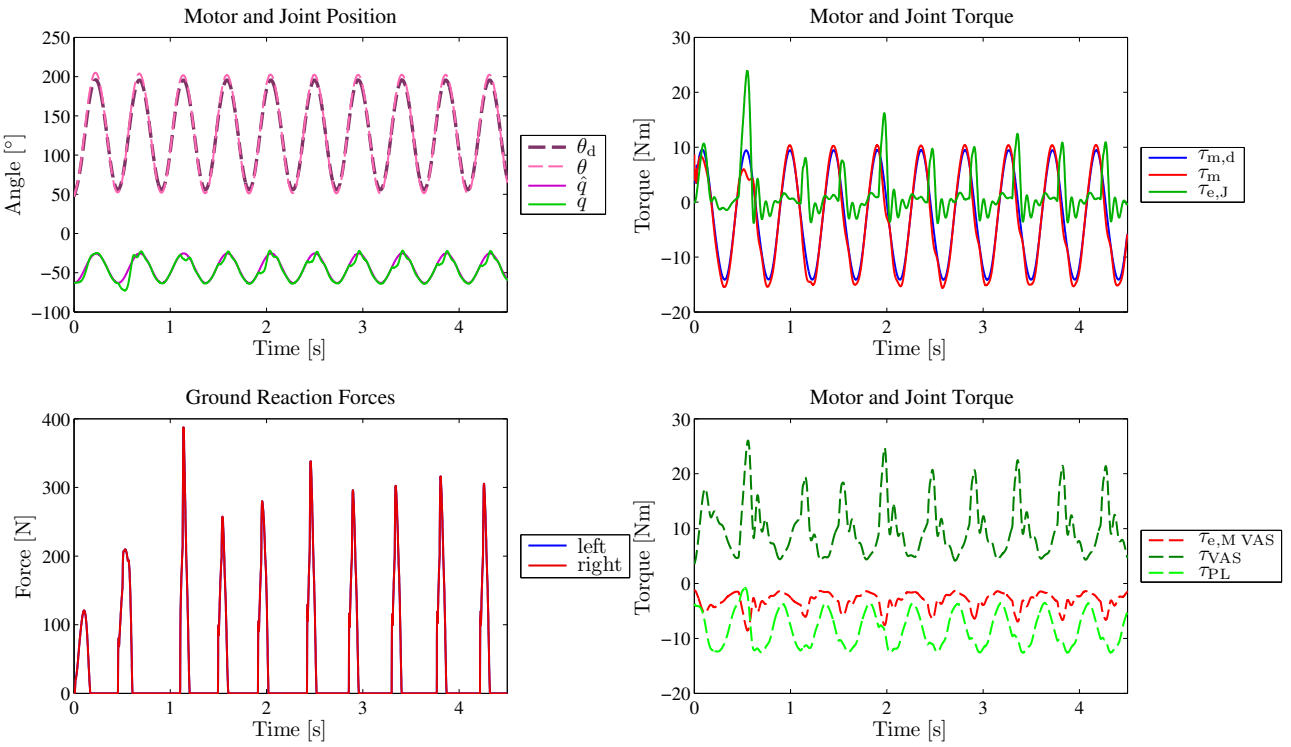

Figure 5.14.: Forward dynamics simulation results for the knee joint of the BioBiped1 robot with the parameter settings of set 1.

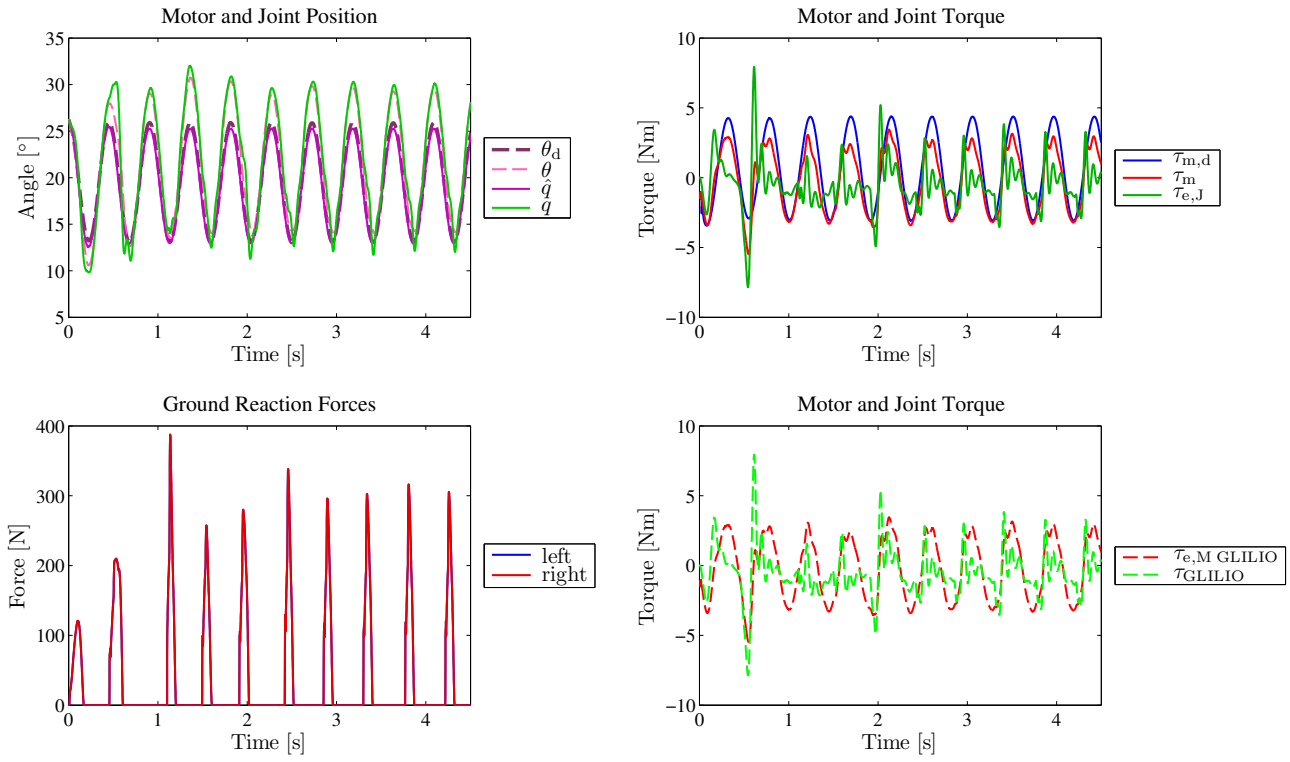

Figure 5.15.: Forward dynamics simulation results for the hip joint of the BioBiped1 robot with the parameter settings of set 1.

cycle to cycle. The parameter settings of set 6 do not offer any advantages with respect to energy efficiency, tracking quality, or dynamics degree.

Finding the Optimal Gear Ratio

Set 1 seems to produce the best results; however, the energy consumption needs to be further investigated. Studying the diagrams in Fig. 5.16 we can recognize that most of the energy is consumed during the swing phase, not even stance phase, which is due to the high motor velocities required. The motion generation method already ensures that the motor stops working when tendon slackening occurs. However, the motor gear ratio with $n_g = 66$ may lead to high friction and inertia moments. In fact, the torques generated by the motor seem to be much greater than the torques exerted by the transmissions on the motors. It can be shown that there is an optimal gear ratio that lets the motor gearbox follow the same trajectories with less energy consumption, both in swing and stance phase, and that this optimal gear ratio, changed in either direction, will increase the energy consumption either due to great electrical system losses or mechanical power requirements.

Therefore, we repeated the simulations for set 1 with different gear ratios (cf. Table 5.11). With $n_g = 44$ neither the dynamics degree nor the deviations change considerably. But there are two positive side-effects: the peak torques on the knee motor can be reduced by more than 30 % and the energy consumption can be drastically reduced by 55.75 %. If we reduce further the gear ratio to $n_g = 22$, we can improve the energy consumption by further 35.66 % and compared to $n_g = 66$ by 71.53 % (cf. diagrams in Fig. 5.16). With $n_g = 5$ the electrical system losses increase significantly leading to a high energy consumption. The simulation results are illustrated in Fig. 5.17, 5.18, and 5.19. It can be clearly recognized that the torques generated by

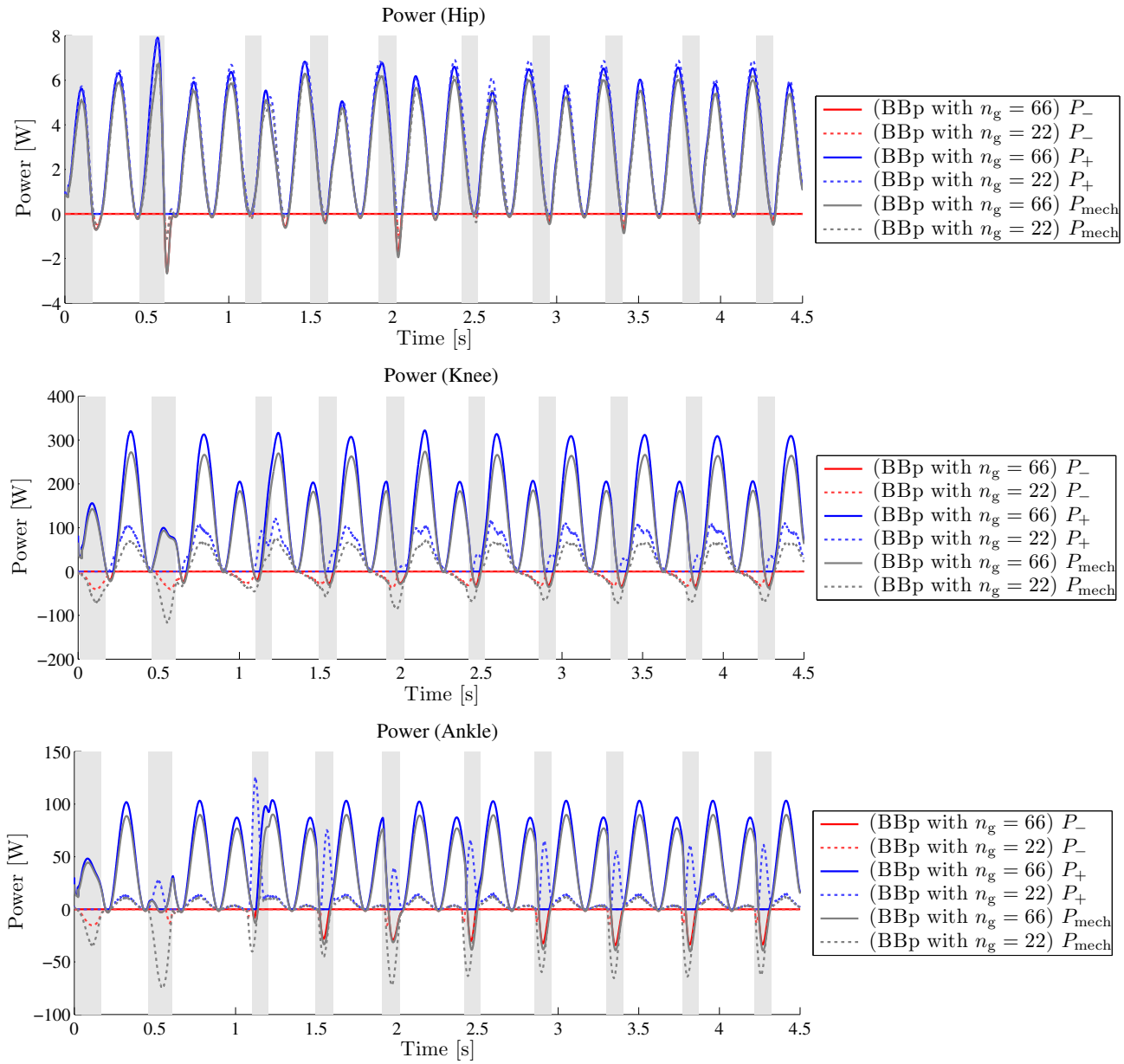

Figure 5.16.: Energy consumption of the BioBiped1 (BBp) robot with the parameter settings of set 1 for $n_g = 66$ and $n_g = 22$. The top, middle, and bottom diagrams display the power trajectories of the hip, knee, and ankle motor, respectively. The dotted lines represent the results for $n_g = 22$. The shaded areas represent the ground contact phases.

the motors for the desired motions are approximately in the same range as the torques exerted by the transmissions on the motors.

5.4.2 BioBiped1 Robot Model with Linear Elastic Joint Actuation

A BioBiped1 robot with linear elastic joint actuation and nonlinear tendon actuation are not directly comparable, since the transmission ratio and leg stiffness change nonlinearly over time. In theory, however, a robot with linear elastic joint actuation and nonlinear tendon actuation

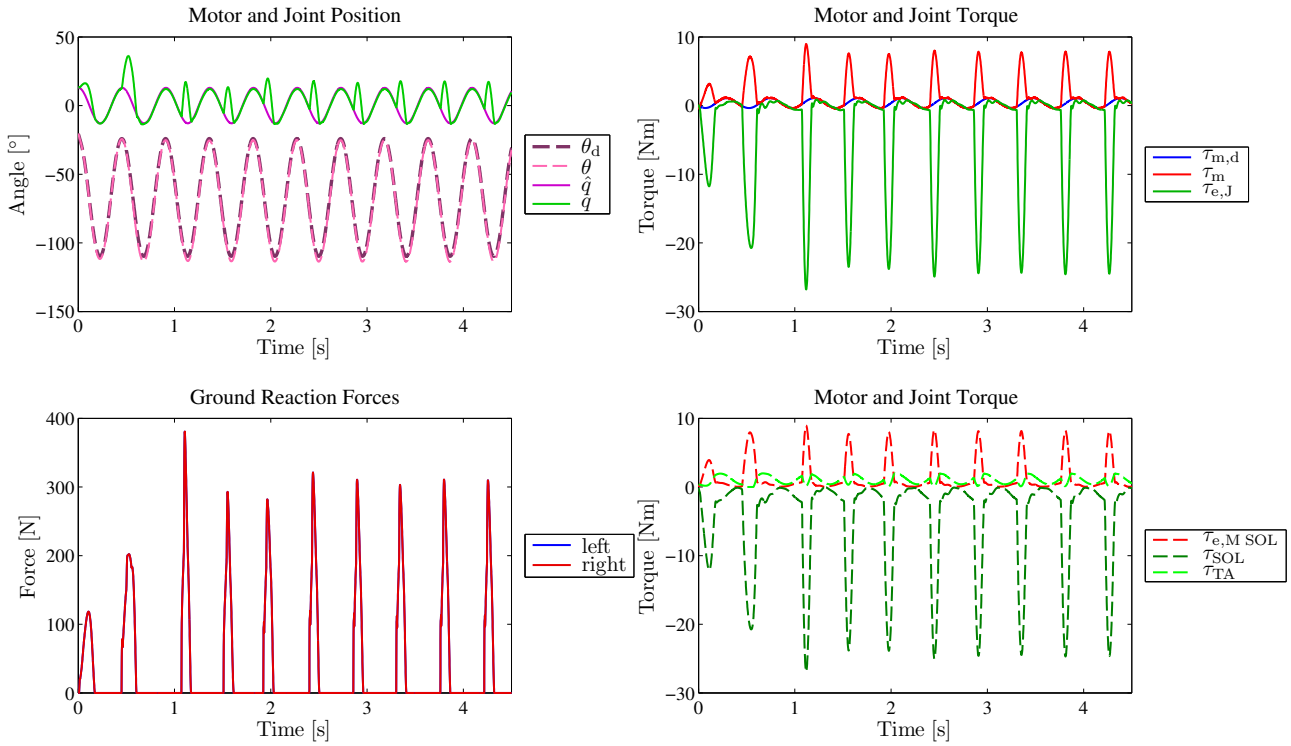

Figure 5.17.: Simulation results of the model-based approach for set 1 with $n_g = 22$ for synchronous in-place hopping for the ankle joint.

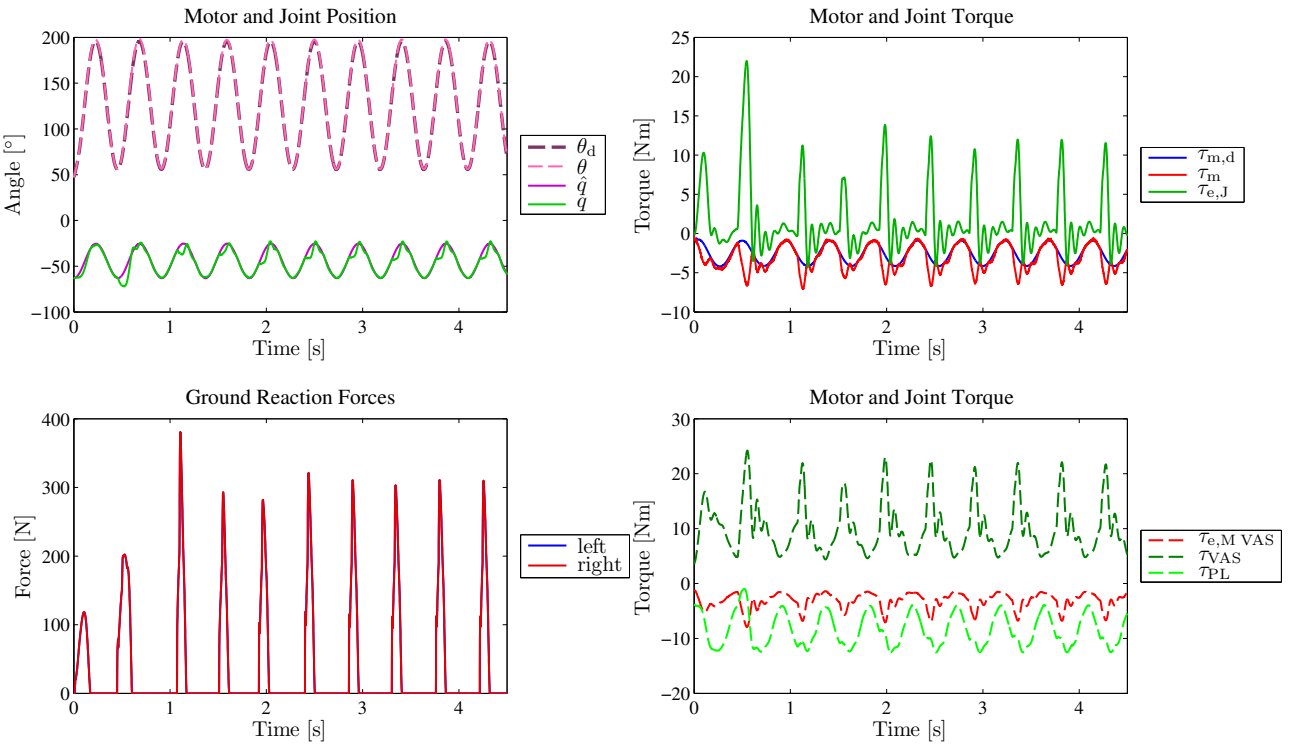

Figure 5.18.: Simulation results of the model-based approach for set 1 with $n_g = 22$ for synchronous in-place hopping for the knee joint.

Table 5.11.: Evaluation of the leg actuation design, specified in Table 5.9, for set 1 with varied gear ratios of the knee and ankle motors for model-based controlled in-place hopping, with respect to the same criteria as in Table 5.10.

Criteria		**Set 1**	**Set 1 with $n_g = 44$**	**Set 1 with $n_g = 22$**
Hopping height	[m]	0.2205	0.2181	0.2169
Ground clearance	[m]	0.2051	0.1992	0.1958
Duty factor	[%]	22.54	22.58	22.71
Flight phase	[ms]	356	355	354
$\tau_{e,M\,Ank}$	[Nm]	6.86	6.84	7.81
$\tau_{e,M\,Kne}$	[Nm]	9	5.85	6.51
$\tau_{e,M\,Hip}$	[Nm]	2.93	3.15	3.27
E	[J]	1521	673	433
E_{Ank}	[J]	191	76	45
E_{Kne}	[J]	556	247	157
E_{Hip}	[J]	13	14	14
E_{mech}	[J]	1307	553	234
$E_{mech\,Ank}$	[J]	165	64	15
$E_{mech\,Kne}$	[J]	477	200	89
$E_{mech\,Hip}$	[J]	12	13	13
$\sigma_{q\,Ank}$	[deg]	8.57	8.66	8.73
$\sigma_{q\,Kne}$	[deg]	3.86	3.98	4.1
$\sigma_{q\,Hip}$	[deg]	3.5	3.55	3.61

with the same stiffness in all leg joints and with same transmission ratio in all actuators should behave similarly. As discussed earlier, the advantages of BioBiped1's nonlinear actuation system comprise the manifold configuration possibilities.

5.4.3 BioBiped1 Robot Model with Stiff Joint Actuation

The passive rebound studies already demonstrated that a stiff actuation is not suited for dynamic and energy-efficient locomotion. We also reported on the difficulty of ensuring a valid comparability of the results among models with different actuation. As mentioned earlier, it is very difficult to determine an appropriate model for the Coulomb friction [8]. Additionally, it is important to consider the resonance frequency of a system.

However, in order to clarify the differences of stiff actuation not only for passive rebound behavior but also for dynamic hopping motions, a BioBiped1 robot model with completely stiff joints actuated by geared DC motors is PD-controlled to track the same reference motions as in the previous studies above. The controller gains of the stiffly actuated BioBiped1 robot model are set to $k_p = 200$ and $k_d = 8$. Note that this possibility, to study different leg actuation designs, is provided by the developed model-based method.

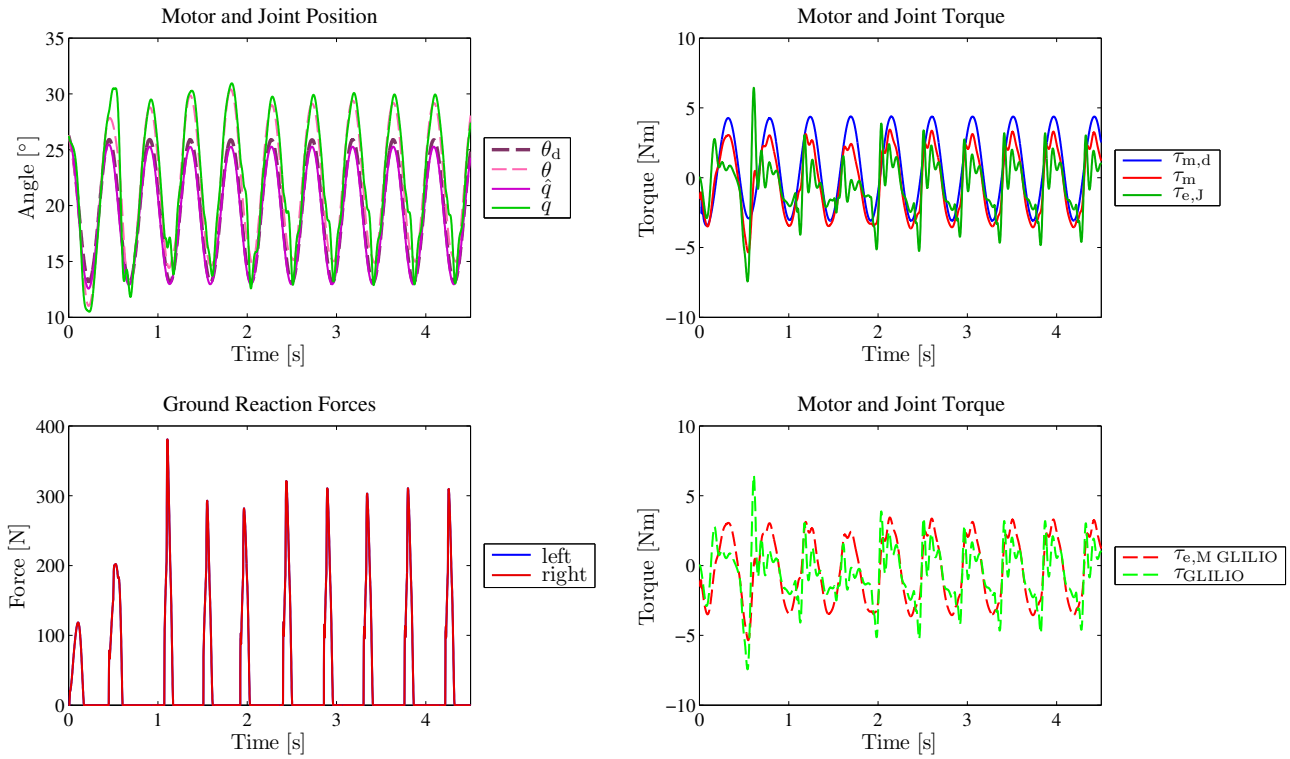

Figure 5.19.: Simulation results of the model-based approach for set 1 with $n_g = 22$ for synchronous in-place hopping for the hip joint.

The forward dynamics simulation of the robot model yields the following results regarding the dynamics degree of the performed hopping motions:

- an average hopping height of 0.2131 m,
- an average ground clearance of 0.1662 m,
- an average duty factor of 20.63 %, and
- an average flight phase of 359 ms.

The standard deviations amount to $\sigma_{q\,Ank} = 5.15°$, $\sigma_{q\,Kne} = 4.27°$, and $\sigma_{q\,Hip} = 1.58°$. Thus, the reference trajectories are tracked with slightly smaller deviations than with the compliant BioBiped1 robot model specified by set 1. However, as expected, the peak torques arriving at the gearboxes of the ankle and knee motor exceed the set threshold enormously, with $\tau_{e,M\,Ank} = 30.03\,\text{Nm}$ and $\tau_{e,M\,Kne} = 19.4\,\text{Nm}$.

5.4.4 Discussion

To conclude, BioBiped1's specific actuation design is advantageous in many respects. To fully exploit the advantages of its actuation system, it is important to concentrate on a few human-like muscle-tendon functionalities, i. e., depending on the gait, not all tendons should be integrated. The integration of all tendons introduces timing issues that can be hardly handled.

Additionally, we could recognize from the studies that a soft leg performs often worse than a stiffer leg. Both the passive rebound studies and the hopping simulations confirmed that a leg

with joint stiffnesses of about 87 $^{\mathrm{Nm}}/_{\mathrm{rad}}$, 66 $^{\mathrm{Nm}}/_{\mathrm{rad}}$, and 55 $^{\mathrm{Nm}}/_{\mathrm{rad}}$ for the hip, knee, and ankle joint is well capable of very dynamic locomotion. With slight tuning, rearrangement, and optimal gear ratio for each motor, such leg design is also capable of energy-efficient behavior.

The amount of work that a motor is forced to do, due to the passive antagonists, should be reduced as much as possible. The passive flexor PL can be omitted; instead, GAS and BF can be integrated. Also, since the requirements on the knee motor are quite demanding, it should be sought out to either use a clutch that engages and disengages the motor during knee flexion or to implement a mechanism that lets the passive flexor engage or disengage depending on the current phase and joint angle.

Furthermore, it is possible to omit the knee motor. Although the above motions were all tested with an active knee extensor, it can be assumed that the desired motions could have been also realized without it. The studies centered around the Lombard paradox demonstrated this possibility.

Additionally, it should be noted that BioBiped's specific actuation design introduces the possibility of parallel elasticities without increasing the motor work. For instance, RF and BF work in parallel to the b-SEA in the hip. But in the knee, too many passively integrated tendons may increase the motor work. Therefore, it is very important to concentrate on a less complex leg design, otherwise a higher energy consumption than in conventional, stiffly actuated robots may be detected [130].

As a guideline for choosing the optimal leg actuation design and parameter setting, passive rebound tests should be carried out, as described in Section 5.2. For nonlinear tendon actuation, the tests only indicate the optimal leg stiffness at ground contact, not during swing phase. Therefore, it needs to be additionally ensured that the optimal gear ratio is determined. Finally, operating at the resonant frequency supports the excitation of the intrinsic dynamics further, without increasing the requirements posed on the actuation.

5.5 Summary and Further Perspectives

In this chapter, we have investigated the beneficial properties of compliant actuation for dynamically locomoting bipedal robots. Shock tolerance as well as energy storage and release are among the most important capabilities of a dynamically moving, but also energy-efficient robot. Not only did we confirm, through extensive simulation studies, the obvious advantages of elastic over stiff actuation, in general, for soft landing, but we also investigated the differences between linear elastic and nonlinear elastic tendon joint actuation. In general, the dynamic locomotion goals envisioned for BioBiped1 are not achievable with stiff actuation. Furthermore, we showed that such passive rebound tests are well suited for determining the optimal leg actuation design.

The second contribution of this chapter is the application of both the open-loop excitation method and the centralized model-based motion generation and control approach presented in Chapter 4. Applying these methods, we could, on the one hand, determine forward causalities, i. e., we rediscovered earlier insights from biomechanics, and, on the other hand, assess the quality of a specific leg actuation design for desired joint motions, thereby studying inverse causalities. In total, we derived several guidelines for choosing appropriate leg stiffnesses and gear ratios. In this context, we could also demonstrate the benefits of a model-based motion generation and control approach for a system with highly redundant actuation, such as that of BioBiped1.

This chapter was also directed towards the key question of how each single muscle-tendon complex contributes to the robot's overall motions. In humans, the muscle PL is very short and does not seem to play an important role. Both the flexion of the knee and ankle are already supported well by the ground contact (cf. Section 5.3.2). This leads to a choice to either use all monoarticular antagonist-agonist pairs in all joints or, which should be clearly the favored version, to integrate all biarticular tendons and omit the PL and even the knee motor. Exploring the Lombard paradox showed that dynamic hopping motions could be achieved without the knee motor. In [36], it was already demonstrated that an active knee is not required for level-ground walking. In total, the amount of passive redundant actuation should be kept to a minimum. Passive actuation dynamics can be indirectly controlled by the proposed model-based motion control method; however, the interplay of BF, GAS, and PL, for instance, negatively affected the overall leg dynamics and the requirements posed on the actuators. Moreover, it should be explored how actuated biarticular tendons can further reduce the complexity of the leg actuation design and improve the energy consumption, while preserving the desired dynamic locomotion behavior.

From the biomechanics analysis of the running gait in Section 2.3.1, it can be assumed that the guidelines derived above are also valid for the running gait. To allow for multi-modal locomotion, the model-based approach should be applied to study different leg actuation designs, including the walking gait, in future work. In addition to these studies, it is also essential to analyze the requirements posed by postural stabilization on the leg actuation design and its parameter settings.

Future work includes the use of optimization and learning techniques to further improve the tendons' attachment locations and the selection of spring stiffnesses and rest lengths, in order to produce the most dynamic and energy-efficient locomotion performance. With the methods developed in this thesis and the results obtained regarding enhanced locomotion, optimal control problems can be formulated and tackled.

5.6 Reference to Own Publications

A condensed version of Section 5.2 was published in: Proceedings of the IEEE International Conference on Robotics and Automation 2014 [138]. A short version of Sections 5.3.1–5.3.3 and 5.3.5 was published in: Proceedings of the IEEE/RSJ International Conference on Intelligent Robots and Systems 2012 [131]. A preliminary version of Sections 5.3.4–5.3.5 was published in: Proceedings of the International Conference on Climbing and Walking Robots and the Support Technologies for Mobile Machines 2013 [135].

6 Conclusion and Outlook

6.1 Summary of the Contributions

The field of bipedal, humanoid robot locomotion requires significant progress towards the goal of realizing agile, versatile, stable, and energy-efficient locomotion for which the human serves as a model.

Multidisciplinary View of the Problem of Advancing Bipedal Locomotion Performance

This thesis has shed light, from many different perspectives, on the problem of achieving bipedal robot locomotion performance that comes close to that of its biological counterpart. In Chapter 2, we described the complex field in which this problem is located and the various disciplines, from neuro- and biomechanics over mechatronics through to humanoid robot locomotion, that need to be involved for successfully approaching the goal of dynamic, energy-efficient robot locomotion performance. In this context, the important characteristics of human hopping, running, and walking gaits have been reviewed in order to discuss the question about which main features of human motion performance should ideally be realized by robots. This relates directly to the issue of the lack of a taxonomy for the term "human-like", which is not rigorously defined but nevertheless used in the literature to assess the presented locomotion performance. However, since robotics research is still far away from claiming that a motion is human-like, emphasis in this thesis was laid on demonstrating improved locomotion performance and presenting novel insights.

Two main requirements were regarded as crucial: (1) the bio-inspired mechanical design of the bipedal robot, and (2) a motion controller exploiting the intrinsic system dynamics. In this respect, we presented a novel musculoskeletal robot design that incorporates two important properties of the human musculoskeletal lower limb system: segmentation and elastic leg behavior [132]. The BioBiped1 robot is a human-inspired musculoskeletal biped with three-segmented legs featuring a highly compliant tendon-driven actuation system. The actuation system builds upon well-established technological components, i. e., geared electrical motors, extension springs, and tendons, but in a novel, bio-inspired setup to mimic key functionalities of the mono- and biarticular muscles that, according to biomechanics research, play an essential role in dynamic, versatile, and energy-efficient locomotion. BioBiped1 features a highly nonlinear complex actuation system consisting of electrically driven and passive tendons spanning one or two joints with various setting possibilities for the spring stiffnesses, attachment points, and rest angles that, however, still needs to be fully investigated, in order to define the strengths and weaknesses of the design.

Early experiments demonstrated that the robot design exhibits a proper fundamental locomotor function that is potentially suited for multi-modal locomotion abilities [132]. This includes the ability to generate sufficient repulsive leg forces during the stance phase, to achieve clear flight phases, and to actively generate enough thrust to induce continuous hopping motions. Combining these two capabilities has led to several variants of dynamic synchronous hopping motions in experiment.

Simulation of Dynamic Locomotion and Flight Phases with Detailed Multibody System Dynamics Models

Using only experimental data to understand and utilize the motion dynamics of BioBiped1 and related musculoskeletal robots has fundamental limitations, because many important variables are generally not measurable in experiments. For example, it is relatively difficult to systematically investigate the role of the deployed tendons during the designed motion trajectories and the impact of their dynamics on the joint, leg, and overall robot behavior, only by physical experiments (which can also be performed only a limited number of times). Consequently, experiments alone are not feasible to fully identify and understand cause-effect relationships in such a complex dynamic system. One of the main questions to be answered, however, is how single tendons contribute to the performed motions, particularly since many of the implemented actuated and passive tendons share similar functionalities.

The key to successful investigations is a mathematical modeling approach that captures the highly complex dynamics of the actuated and passive mono- and biarticular tendons and of the relevant actuated muscoloskeletal robot [131]. Additionally, a simulation environment is required that enables systematic studies related to the necessary degree of design complexity and the development of suitable motion controllers [87]. In Chapter 3, we presented the METArob simulator that is specifically designed for the requirements of musculoskeletally actuated robotic systems [87]. It is based on a high-level scripting and technical computing language and uses object-oriented design to enable easy comparison of various actuation designs in simulation and experiment. Moreover, it includes the detailed dynamics models of the actuators, ground contact, and the full MBS dynamics model of BioBiped1. The detailed motion dynamics model that we present requires a much more complex MBS dynamics model than is needed for conventional robot designs with rigid actuation of joints. For musculoskeletal robots, such as BioBiped1, the characteristic curves of motor and joint torques, as well as moment arms and transmission ratios, are highly nonlinear, depending on the coupled joint angle. For the case of biarticular tendons, these curves vary, based on two joint angles. This thesis provides the working principles and detailed mathematical models for the actuated and passive, mono- and biarticular elastic tendons of the electrically driven BioBiped1 robot, derived from the classical mechanical principle of virtual displacement and work [131]. Mathematical models were derived to determine the motor and joint torque, the nonlinearly changing lever arms, and transmission stiffnesses of the tendons.

To validate the proposed models, the various characteristic curves were extensively investigated to check the plausibility of the results. The presented mathematical approach is not limited to the specific construction of BioBiped1, but can also be applied to general designs of musculoskeletal robots. Additionally, all models, including the full MBS model and the realistic ground contact model incorporating collision, friction, and stiction forces, were experimentally validated and shown to match the behavior of the real robot.

Model-based Motion Generation and Control Method for Musculoskeletal Bipeds

The intelligent combination of actuated and passive mono- and biarticular tendons, that imitate important human muscle groups, offers tremendous potential for improved locomotion performance, but also imposes major challenges for the motion control of the robot. This is caused by the highly nonlinear passive dynamics of the viscoelastic, musculoskeletal actuation. Whereas, recently, musculoskeletal designs for arms and legs have become increasingly popular, the common aim of previous studies has been a beneficial contribution of the implemented actu-

ators to the overall performance, and, in legged systems, particularly for jumping motions. The topic of motion generation and control for robots with musculoskeletally arranged compliant actuators has not yet been investigated extensively. This problem has been thoroughly discussed in Chapter 4 and two different approaches have been proposed and investigated.

Based on the derived detailed dynamics models of the musculoskeletal robot and the implemented actuators, we have presented a centralized, nonlinear model-based approach combining feedforward and feedback control using joint angular trajectories as reference data [133, 136]. The concept was used to realize both computer-generated 1-D hopping and human 2-D running motions. As proof of concept and validation, the model-based approach was applied to joint motions obtained by oscillatory open-loop motor excitation, which represents a popular approach to exploit the intrinsic dynamics. It was shown that the realized motions match very well with the motions obtained by the open-loop feedforward excitation method, with respect to the evaluated dynamic performance criteria and the tracking performance, without increasing the energy consumption [136].

The model-based approach is well suited for systems with redundant actuation and also for more complex motions such as human running gait data, in contrast to the open-loop feedforward excitation method. The proposed approach also allowed us to determine BioBiped1's motor-gear units prior to its construction, which represents an important component of the development process of the BioBiped1 robot [133]. Experiments confirmed that the selected motor-gear units for the BioBiped1 robot are capable of meeting the requirements for dynamic, synchronous, and alternating hopping motions. Additionally, in this chapter we investigated important tools, such as Fourier analysis and synthesis, for further processing of measured human gait data, applied this tool to analyze human running gait data, and provided the definitions of essential locomotion performance criteria evaluated in this thesis.

Deriving Novel Guidelines for the Leg Actuation Design and its Parameter Settings

The developed mathematical models of the various actuator types of musculoskeletal robots and the presented open-loop and model-based motion generation methods enable a systematic analysis of the interactions of actuators and joints by MBS dynamics simulations at a high and realistic level of detail. We have conducted several studies with the goal of achieving a more systematic understanding of the important dynamic properties of this complex musculoskeletal system and of highlighting the specific benefits of mechanical elasticities and musculoskeletal system design, as presented in Chapter 5.

Passive rebound studies demonstrated that shock tolerance and energy storage and release are essential properties of a bipedal system for running or jumping motions that are not provided in a stiffly actuated system. Extensive studies with different dropping heights and leg actuation designs, from stiff over linear elastic joint to nonlinear elastic tendon actuation, were carried out.

In the second part of the chapter, the focus lay on the investigation of forward causalities. We applied the open-loop excitation method to systematically analyze the role of seven active and passive elastic tendons on the performed in-place hopping motions with respect to energy consumption, duty factor, and hopping height [131]. Positive effects of the passive mono- and biarticular tendons could be observed for all of these criteria, this confirming previous demonstrations by biomechanics researchers. However, and most importantly, we rediscovered an earlier insight from biomechanics, known as the Lombard paradox. By thoroughly exploring the paradoxical function of biarticular tendons using the developed detailed MBS dynamics

simulations, we were able to establish a novel bipedal locomotion model for dynamic hopping motions with energy savings of more than 60 % [135].

Finally, the developed model-based motion generation and control method was successfully applied to produce a desired hopping gait with various leg actuation designs and, thus, demonstrated its particular potential for robotic systems with passive redundant actuation. This method also provides a common basis for comparisons between different musculoskeletal and even stiff leg actuation designs. Several performance criteria, including hopping height, ground clearance, duty factor, and flight phase, were systematically evaluated to assess the dynamics degree of the motions. Moreover, peak torques arriving at the gearboxes, the mechanical and electrical energy consumption, and the tracking performance were also analyzed in order to derive essential guidelines for choosing an appropriate leg actuation design and the corresponding parameter settings. The results of these studies are crucial for a highly capable musculoskeletal robot design and would not have been possible without the mathematical approach taken in this thesis.

Finally it should be noted that, although this thesis is centered around the BioBiped1 prototype, all methods and models developed are applicable, in general, not only to any future BioBiped prototypes but also to any other electrically actuated musculoskeletal robot.

6.2 Remaining Problems

This thesis has aimed at advancing musculoskeletal robot design for human-like locomotion and, in this way, to improve our understanding of human locomotion. It has contributed answers to a number of relevant questions posed in Section 2.7.3. Nevertheless, the complexity of BioBiped1's design and the large number of diverse research questions raised by such musculoskeletal robots with tendon-driven SEAs certainly raise several essential questions that can be further investigated, based on the foundations laid in this thesis. We differentiate between practical tasks and scientific questions that are relevant for more significant progress in the field of bipedal robot locomotion.

Simulation Environment and Models

The simulation framework can be further enhanced by a communication interface to the real robot and its real-time software, to ease the development and testing of controllers. Basic software for such an interface has already been developed and is intended to be extended further [93].

For 3-D locomotion, the ground contact model can be easily extended to the third dimension, due to the penalty-based approach that considers elastic deformations. If necessary, it is also possible to extend the point contact to a surface contact [41]. It is also possible to develop 3-D contact models of higher fidelity, based on new volumetric models of 2-D contact between a human foot and the ground [52, 153]. It is expected that, with this biofidelic contact modeling, the understanding of human gait and postural stability, in particular, can be enhanced.

Furthermore, a symbolic representation of the musculoskeletal system's equations of motion will contribute to faster computer simulations and allow extensive optimization studies [101].

Studying Walking Gaits

With regard to the multi-modal locomotion ability of humans, the studies carried out in this thesis regarding a leg design that performs well and is energy-efficient need to be extended

to walking gaits. Based on the hypothesis that the central humanoid motion capability should be jogging, it can be assumed that the conducted studies and results also apply to walking. In particular, omitting knee actuation was also suggested for level-ground walking in a simulation study [36] and is commonly used in prosthetic legs [5].

Exploiting Machine Learning Techniques

In [128], it was shown that the nonlinear musculoskeletal dynamics of a specific leg design of BioBiped1 could be learned, including complex relationships such as the GRF. However, this still requires further investigation, using, e. g., non-parametric Gaussian processes, to determine how various different leg actuation designs can be learned and represented by one model and how the learned nonparametric and the previous, analytically derived models can be merged to yield a higher overall model quality. In this context, it is also interesting to accurately predict the first ground contact after a flight phase, in order to initiate appropriate motor actions to prepare for the contact.

Furthermore, machine learning techniques can be applied to learn the motion controller [32]. Research could be also directed towards learning controllers for postural stability and combining these hierarchically with the model-based motion control method presented here [136].

Human-like Actuation Dynamics

Musculoskeletal robots of varying complexity, like BioBiped1, offer several possibilities for leg actuation, consisting of different types of active and passive tendons spanning either one or two joints.

Besides the various possible settings offered by such designs, it is also very relevant to analyze how much the locomotion performance can be improved by mimicking important properties of human muscles. To this end, the properties of the implemented active and passive muscle-tendon units can be adapted to those of human muscles to achieve, e.g., the same force-length and force-velocity relationships or change in lever arms. These analyses can all be carried out with the detailed MBS dynamics modeling methodology for musculoskeletal robots and the derived mathematical models of the different actuator types. The analyses could be further hastened by a symbolic representation of the musculoskeletal system's equations of motion, applying the modeling approach described in [101].

Moreover, investigations based on the derived mathematical models can also study whether actuated biarticular muscle-tendon units offer any additional benefits with respect to the overall leg locomotor function. Finally, clutches for engaging and disengaging a motor can be modeled to study how well such mechanisms can be integrated into the motion control [85].

Comprehensive Taxonomy and Related Benchmarks for the Assessment of Performance in Human and Humanoid Gaits

As discussed in Section 2.4, the overwhelming majority of authors take a general but not rigorously specified understanding of "human-like" for granted; in fact, the term is associated with very individual interpretations and definitions. Solving this problem requires fruitful biomechanics and robotics collaborations. This also relates directly to the problem of benchmarks for a better comparability of results between the different research groups. Developing such a taxonomy requires, first, a set of systematic criteria for evaluating and comparing gait strategies and mechanisms. This thesis suggested using performance criteria that rate the energy-efficiency and dynamic mobility. For a future comprehensive taxonomy, it is also important to find a

measure for the required control efforts. It is hypothesized that a taxonomy that accounts for the multiple aspects of human locomotion will not only significantly advance the understanding of how to design and control human-like locomoting humanoid robots [43], but also help to advance our understanding of the biomechanical and neurological mechanisms of human gait. Gait data collected and insights gained by biomechanics researchers in experiments with human subjects can substantially support the process of determining a common taxonomy and benchmarks. However, in all relevant approaches that aim at increasing understanding of human locomotion, i. e., (1) conducting experiments to gather useful human motion capture data, (2) modeling human locomotion, and (3) determining the underlying control approaches, several of the central questions have not yet been answered.

Mapping Simple Models of Sufficient Detail onto Complex, Segmented Bodies

Determining the appropriate representation for human locomotion is, thus, another important problem. The biomechanics community mainly uses conceptual models, whereas robotics communities consider complex segmented dynamics models at the actuation level. As discussed in Section 2.5, the SLIP model is often used as a representative model for human walking and running gaits. But this is a great simplification, since neither human walking nor running is exactly linear (cf. Section 2.3). The SLIP model does not adequately predict the effect of impacts and energy losses in the leg during running. Basic models, such as the SLIP, cannot approximate the full complexity of the motion dynamics of musculoskeletal robots like BioBiped1 sufficiently well, because BioBiped1's legs do not behave like a linear spring: the force-leg length curves are strongly nonlinear. In this context, how the global leg behavior of a novel musculoskeletal locomotion model deviates from linear spring behavior must be analyzed, as well as how these deviations affect locomotion performance. This problem involves finding the important relationship between the SLIP and the complex segmented leg actuated by muscles, by applying, for instance, virtual model control [127].

Concluding Remarks

The studies mentioned above have the potential to significantly enhance progress in the field of bipedal robot locomotion for the design and control of more human-like locomoting robots. Moreover, significant benefits for biomechanical human movement analysis that are relevant for gait evaluation and clinical rehabilitation can be expected. In the long term, the understanding of the biomechanical and neurological mechanisms of human gait can be eventually improved and applied to future concepts of physical assistive devices in rehabilitation and prosthetics for humans.

A Ground Contact Model

The following excerpt from [87] describes the model of the ground contact dynamics.

A.1 Point Contact

A point contact is described as a state machine that switches between normal force, kinetic, and static friction and can be attached to any point of a body. Fig. A.1a depicts the considered point contact model. For a realistic modeling of the dynamic properties, a finite surface A has to be assumed. L stands for the measured thickness of the contact layer. Collision forces, that are generated along the surface normal, are denoted as F_N. Tangential forces, that are caused by kinetic and static friction during a collision, are denoted as F_T.

A.2 Collision

Fig. A.1a displays two contacting bodies in a relaxed state and the normal and tangential forces, F_N and F_T, respectively. Fig. A.1b illustrates the collision model. The collision counterforce F_c is computed depending on the penetration p_N along the surface normal vector $\boldsymbol{e}_N$. As mentioned earlier, the contact body 1 is assumed to have a smooth contact surface of size A with an infinite extension (e. g., ground, wall), so that a geometric collision detection can be reduced to:

$$p_\mathrm{N} = \boldsymbol{p}\,\boldsymbol{e}_\mathrm{N}\,, \tag{A.1}$$

where p_N is the relative distance between the colliding objects and negative during collision, $p_\mathrm{N} < 0$.

For small deformations the stiffness of the contact material can be described by a linear stress-strain curve with Young's modulus E of the contact material and the average normal stress σ_N. The normal strain ϵ_N can be approximated by the ratio of penetration p_N and total layer thickness L:

$$\sigma_\mathrm{N} = E\,\epsilon_\mathrm{N} = -E\,\frac{p_\mathrm{N}}{L}\,. \tag{A.2}$$

Using the average stress, the compression force F_c is calculated as a function of compression and material stiffness k_c:

$$F_\mathrm{c} = A\,\sigma_\mathrm{N} = -k_\mathrm{c1}\,p_\mathrm{N} \quad \text{with} \quad k_\mathrm{c1} = \frac{E\,A}{L}\,. \tag{A.3}$$

The stiffness of both colliding bodies, k_c1 and k_c2, are merged into a single collision stiffness k_c:

$$k_\mathrm{c} = \left(\frac{1}{k_\mathrm{c1}} + \frac{1}{k_\mathrm{c2}}\right)^{-1}\,. \tag{A.4}$$

Aside from incorporating the stiffness of the materials and the strain, it is also important to formulate the elasticity of the collision, which is also known as coefficient restitution or

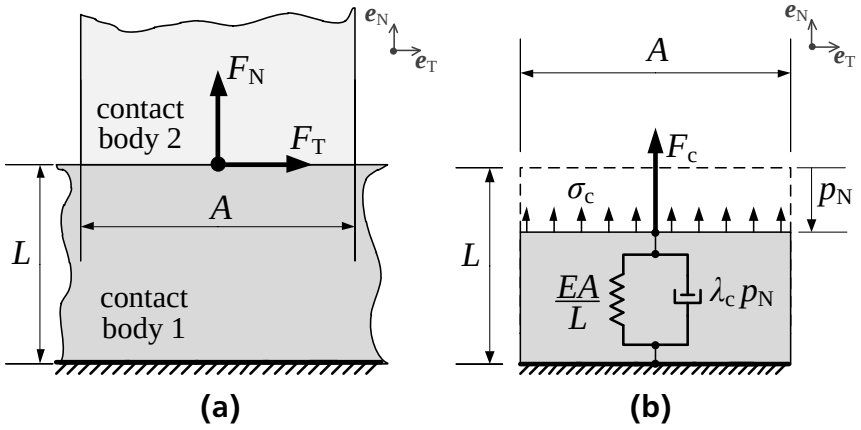

Figure A.1.: (a) Point contact and (b) collision model.

bounciness of the collision [94]. The elasticity of a collision depends on the amount of dissipative energy lost during the impact. The most basic way is to model the contact surface as a visco-elastic Kelvin-Voigt material [50]. But this model has several limitations, such as discontinuity of the contact force at the moment of impact, dependence of the coefficient of restitution on the mass of the impacting bodies and the lack of dependence on the impact velocity [94]. We therefore use the Hunt-Crossley model to extend (A.3) by a nonlinear damping component, which is comprised of the damping constant λ_c and the compression velocity $\dot{p}_N$, scaled by the penetration p_N [66]:

$$F_c = (\lambda_c\, p_N)\, \dot{p}_N - k_c\, p_N\,. \tag{A.5}$$

For the computation of the parameter λ_c, given certain prerequisites, please refer to [94]. An important property of the Hunt-Crossley model is that the contact forces are continuous upon impact, in contrast to the linear viscous damping model. Attracting forces ($F_c < 0$) only occur if the bodies are separated quickly by external forces. This can be interpreted such that the bodies lose contact because the relaxing speed of the compressed material is lower than the relative velocity of the bodies. For negative values of F_c, we therefore saturate $F_c = 0$:

$$\boldsymbol{F}_c = \begin{cases} \mathbf{0} & : \quad \dot{p}_N \geq \frac{k_c}{\lambda_c} \\ ((\lambda_c\, p_N)\, \dot{p}_N - k_c\, p_N)\, \boldsymbol{e}_N & : \quad \dot{p}_N < \frac{k_c}{\lambda_c} \end{cases} \tag{A.6}$$

A.3 Kinetic Friction

The direction of the friction force is the opposite of $\boldsymbol{e}_T$, which represents the direction of the relative contact velocity component perpendicular to the contact surface normal $\boldsymbol{e}_N$

$$\boldsymbol{e}_T = \frac{(\dot{\boldsymbol{p}} - (\dot{\boldsymbol{p}}\, \boldsymbol{e}_N)\, \boldsymbol{e}_N)}{\|(\dot{\boldsymbol{p}} - (\dot{\boldsymbol{p}}\, \boldsymbol{e}_N)\, \boldsymbol{e}_N)\|}\,. \tag{A.7}$$

The friction force in the tangential plane depends on the normal force, e. g., the collision force:

$$\boldsymbol{F}_{fk} = -\mu_{fk}\, F_c\, \boldsymbol{e}_T\,, \tag{A.8}$$

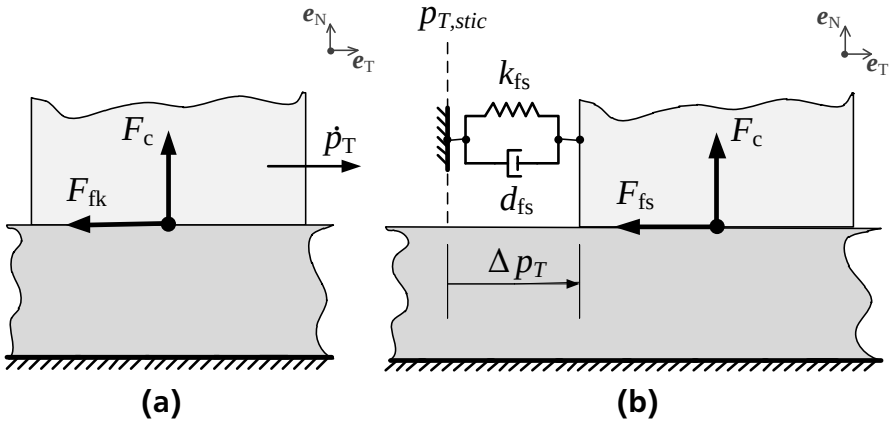

Figure A.2.: (a) Friction and (b) stiction model.

where μ_{fk} denotes the sliding friction coefficient, which depends on the materials of the colliding objects. The friction force is directed opposite to the direction of the tangential velocity $\dot{p}_T$ (cf. Fig. A.2a). If $\dot{p}_T$ decreases below a minimum velocity v_{stic}, the kinematic friction changes to static friction.

A.4 Static Friction

Static friction is depicted in Fig. A.2b. The object sticks to the current position and reacts to external forces as a visco-elastic material. We assume the following Kelvin-Voigt model for the computation of the stiction force:

$$\boldsymbol{F}_{fs} = (-k_{fs}\,\Delta p_T - d_{fs}\,\dot{p}_T)\,\boldsymbol{e}_T \tag{A.9}$$

$$\text{with} \quad \Delta p_T = p_T - p_{T,stic}\,. \tag{A.10}$$

$p_{T,stic}$ denotes the position at which the transition from friction to stiction occurs (cf. Fig. A.2b). The transition to kinetic friction is triggered for static friction forces F_{fs} that exceed a defined maximum static friction F_{stic} which depends on the current normal force and the static friction coefficient μ_{fs} (cf. Fig. A.3):

$$F_{stic} = \mu_{fs}\,F_c, \quad \mu_{fs} \geq \mu_{fk}\,. \tag{A.11}$$

Standard mechanics literature can be referred to for appropriate values of μ_{fs} and μ_{fk}. The values for k_{fs} and d_{fs}, however, are a bit more difficult to determine and require some tuning. Depending on the application and the material properties, usually a high stiffness is chosen for k_{fs} based on which d_{fs} is assigned an appropriate value.

A.5 Collision and Friction State Machine

Fig. A.3 illustrates the state diagram for a point contact including the states and triggering transition conditions.

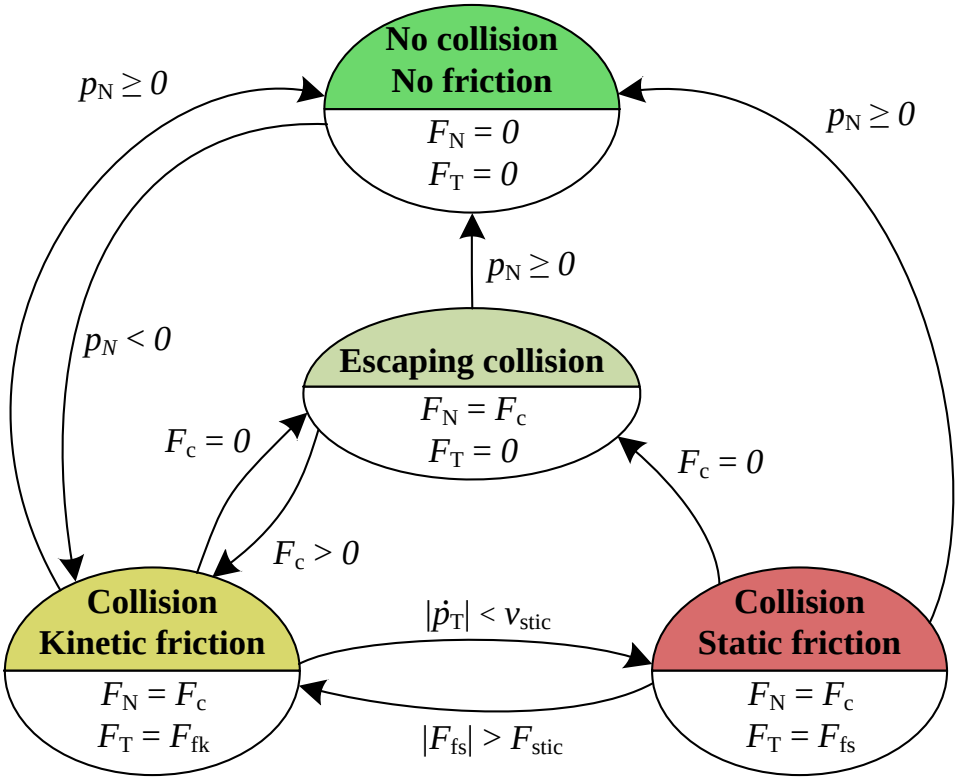

Figure A.3.: State diagram of the contact model.

A.6 Simulation Example

Simulation results of a bouncing contact of a metal object on a soft rubber surface are displayed in Fig. A.4. The parameters used in the simulation example are listed in Table A.1. The elastic modulus $E = 0.01 \cdot 10^9\,\mathrm{N/m^2}$ for soft rubber is given in standard mechanics literature. With a thickness $L = 10\,\mathrm{cm}$ and a contact area of $A = 1\,\mathrm{cm}^2$, the resulting stiffness of the rubber layer is:

$$k_c = \frac{E\,A}{L} = 10^4\,\mathrm{N/m} \tag{A.12}$$

The elastic modulus of the metal object has no significant effect on the combined contact stiffness (cf. (A.4)).

A.7 Validation of the Ground Contact Model

We validated the presented contact model by comparing experimental measurements from a tennis ball dropped on a force plate with the corresponding simulation results. Fig. A.5 describes the experimental setup and results. The simulation results show a very good agreement with the ball motion and the contact forces at the first four bounces; later bounces in the experiment seem to be more damped. This is presumably due to the energy dissipation at low velocities not considered in our model. Both peak values and shape of the highly transient contact situation forces are closely approximated by the simulation, as a close-up of one of the peak forces shows.

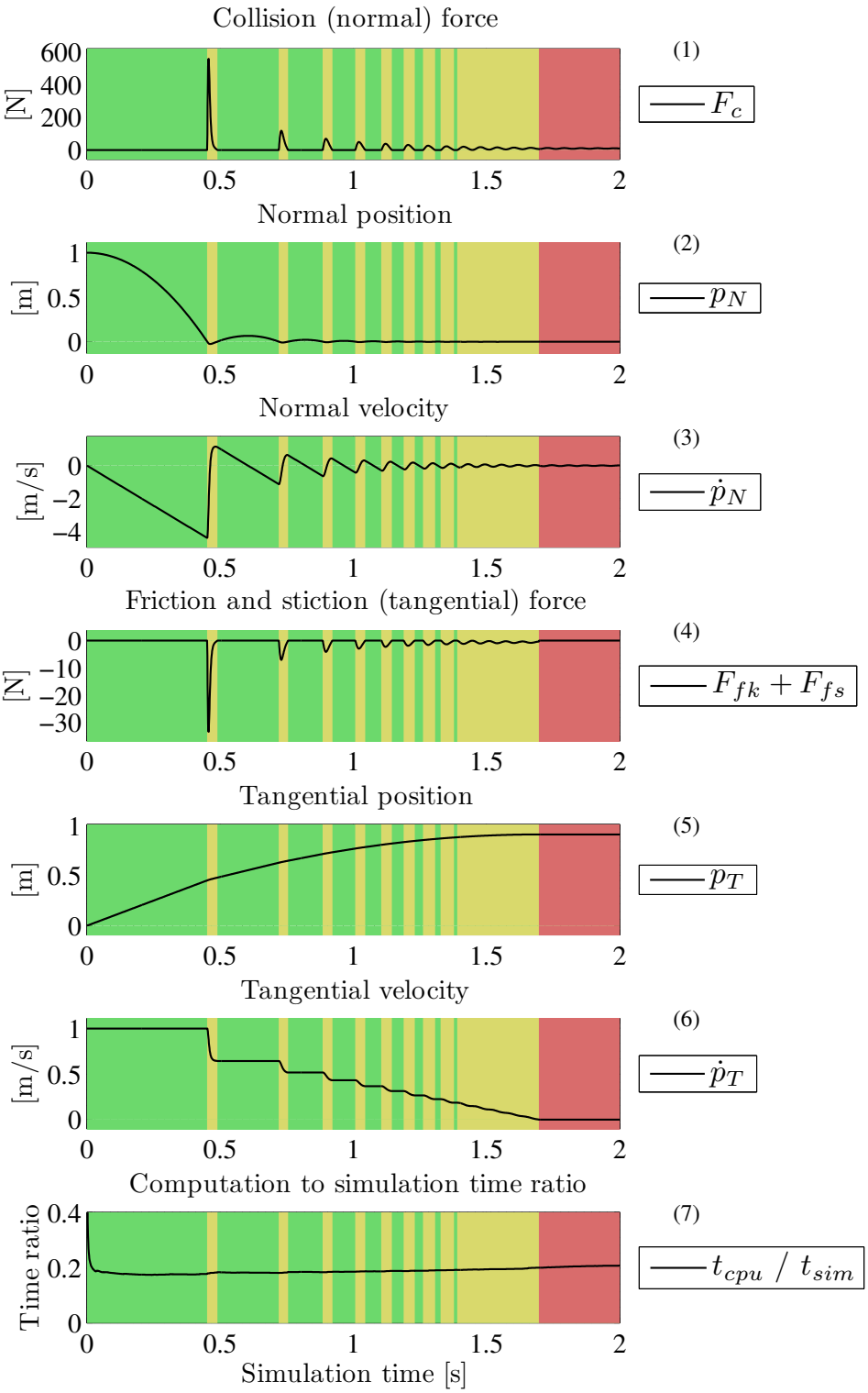

Figure A.4.: Simulation results for a bouncing point mass. Plot 1–3: no collision state (green), collision state (yellow, red), Plot 4–7: no collision state (green), kinetic friction state (yellow), static friction state (red). Solver settings: solver: [ode23 (bogacki-shampine)], relative tolerance: [$10^{(-3)}$], shape preservation: [enable all], number of consecutive minimum steps: [1], maximum simulation step width $\Delta t_{\max} = 1\,\mathrm{ms}$; zero-crossing options: algorithm: [adaptive], number of consecutive zero crossings: [1000]; further available settings: [auto].

Table A.1.: Parameters used in the simulated collision example.

Parameter	Value	Parameter	Value
$p_N(0)$	1 m	μ_{fk}	0.06
$\dot{p}_T(0)$	1 m/s	μ_{fs}	0.1
m	1 kg	v_{stic}	0.001 m/s
k_c	10^4 N/m	k_{fs}	10^4 N/m
λ_c	$7.5 \cdot 10^3$ Ns/m^2	d_{fs}	40 Ns/m

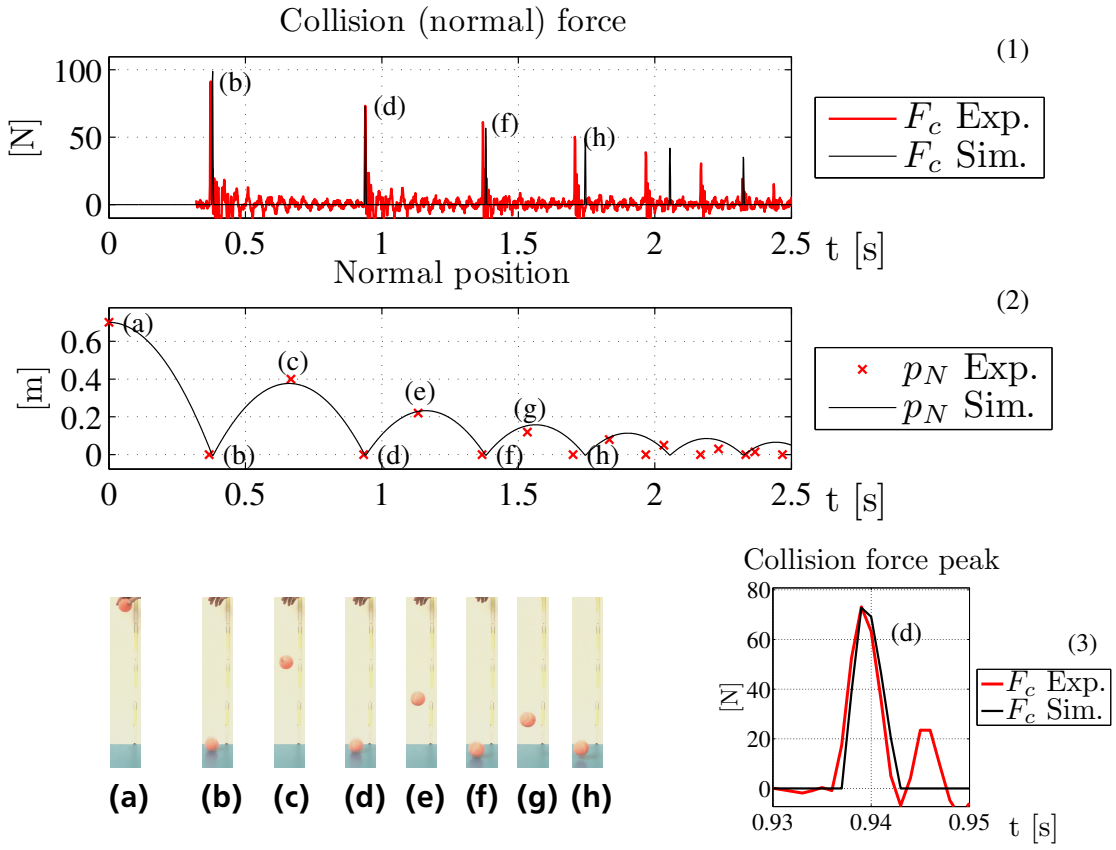

Figure A.5.: Comparison of simulation and experimental data of a bouncing ball. A tennis ball is dropped on a force plate from a height of 70 cm. Plot (1) compares the simulated collision forces (black) with the measurements (red). Plot (3) displays a close-up of the second collision force peak (d). Pictures (a) to (h) come from the video recorded during the experiment and show the peak and collision positions of the ball. Plot (2) compares the ball positions read off of the pictures with the simulation results. Simulation parameters: $m_{Ball} = 0.05\,\text{kg}$, $k_c = 1.7 \cdot 10^4\,\text{N/m}$, $\lambda_c = 2.4 \cdot 10^4\,\text{Ns/m}^2$, $p_N(0) = 0.7\,\text{m}$, $\dot{p}_N(0) = 0\,\text{m/s}$, $\dot{p}_T(0) = 0\,\text{m/s}$. The data of the force plate were measured with a rate of 1 kHz.

Bibliography

[1] "BigDog - The most advanced rough-terrain robot on earth," http://www.bostondynamics.com/robot_bigdog.html, visited on 2014-04-20.

[2] "New Honda robot ASIMO 2012 - all features and behaviors," http://www.youtube.com/watch?v=R8UeT9r4cmg, visited on 2014-04-20.

[3] "Orocos real-time toolkit," http://www.orocos.org/rtt, visited on 2014-04-20.

[4] "Robot operating system (ROS)," http://www.ros.org/, visited on 2014-04-20.

[5] "The New C-Leg - Confidence in the Next Step," http://c-leg.ottobock.com/en/index.php?lang=en, visited on 2014-04-20.

[6] "VIACTORS," http://www.viactors.eu/, visited on 2014-04-20.

[7] M. Ackermann and W. Schiehlen, "Physiological methods to solve the force-sharing problem in biomechanics," in *Multibody Dynamics*, ser. Computational Methods in Applied Sciences, C. L. Bottasso, Ed. Springer Netherlands, 2008, vol. 12, pp. 1–23.

[8] A. Albu-Schäffer, "Regelung von Robotern mit elastischen Gelenken am Beispiel der DLR-Leichtbauarme," Ph.D. dissertation, Technische Universität München, 2002.

[9] R. M. Alexander, "Mechanics of bipedal locomotion," in *Perspectives in experimental biology*. Oxford, UK: Pergamon Press, 1976, pp. 493–504.

[10] ——, "Three uses for springs in legged locomotion," *The International Journal of Robotics Research*, vol. 9, no. 2, pp. 53–61, 1990.

[11] ——, "Simple models of human locomotion," *Journal of Theoretical Medicine*, vol. 2, pp. 129–135, 1995.

[12] J. G. Andrews, "A general method for determining the functional role of a muscle," *Journal of Biomechanical Engineering*, vol. 107, pp. 348 – 353, 1985.

[13] Y. Asano, H. Mizoguchi, T. Kozuki, Y. Motegi, M. Osada, J. Urata, Y. Nakanishi, K. Okada, and M. Inaba, "Lower thigh design of detailed musculoskeletal humanoid "Kenshiro"," in *IEEE/RSJ International Conference on Intelligent Robots and Systems (IROS)*, 2012, pp. 4367–4372.

[14] K. Ayusawa, G. Venture, and Y. Nakamura, "Identification of humanoid robots dynamics using floating-base motion dynamics," in *IEEE/RSJ International Conference on Intelligent Robots and Systems (IROS)*, 2008, pp. 2854–2859.

[15] R. Blickhan, "The spring-mass model for running and hopping," *Journal of Biomechanics*, vol. 22, pp. 1217–1227, 1989.

[16] R. Blickhan, A. Seyfarth, H. Geyer, S. Grimmer, H. Wagner, and M. Günther, "Intelligence by mechanics," *Philosophical Transactions of the Royal Society A*, vol. 365, no. 1850, pp. 199–220, 2007.

[17] J. Buchli, F. Stulp, E. Theodorou, and S. Schaal, "Learning variable impedance control," *The International Journal of Robotics Research*, vol. 0, pp. 1–14, 2011.

[18] M. A. Cairns, R. G. Burdett, J. C. Pisciotta, and S. R. Simon, "A biomechanical analysis of racewalking gait," *Medicine and Sience in Sports and Exercise*, vol. 18, no. 4, pp. 446–453, 1986.

[19] G. Cavagna, N. Heglund, and C. Taylor, "Mechanical work in terrestrial locomotion: two basic mechanisms for minimising energy expenditure," *American Journal of Physiology*, vol. 233, pp. 243–261, 1977.

[20] C.-M. Chew, J. Pratt, and G. Pratt, "Blind walking of a planar bipedal robot on sloped terrain," in *IEEE International Conference on Robotics and Automation (ICRA)*, 1999, pp. 381 – 386.

[21] C.-P. Chou and B. Hannaford, "Measurement and modeling of McKibben pneumatic artificial muscles," *IEEE Transactions on Robotics and Automation*, vol. 12, no. 1, pp. 90–102, 1996.

[22] W. Chung, L.-C. Fu, and S.-H. Hsu, *Handbook of Robotics*. Springer, 2008, ch. Motion Control, pp. 133 – 159.

[23] S. Collins, A. Ruina, R. Tedrake, and M. Wisse, "Efficient bipedal robots based on passive-dynamic walkers," *Science*, vol. 307, no. 5712, pp. 1082–1085, 2005.

[24] S. H. Collins and A. Ruina, "A bipedal walking robot with efficient and human-like gait," in *IEEE International Conference on Robotics and Automation (ICRA)*, 2005, pp. 1983–1988.

[25] P. Corke, "A robotics toolbox for matlab," *IEEE Robotics and Automation Magazine*, pp. 24–32, 1996.

[26] ——, "Matlab toolboxes: Robotics and vision for students and teachers," *IEEE Robotics and Automation Magazine*, vol. 14 (4), pp. 16–17, 2007.

[27] S. Cotton, I. M. C. Olaru, M. Bellman, T. van der Ven, J. Godowski, and J. Pratt, "FastRunner: A fast, efficient and robust bipedal robot. concept and planar simulation." in *IEEE International Conference on Robotics and Automation (ICRA)*, 2012, pp. 2358–2364.

[28] J. Craig, *Introduction to Robotics Mechanics and Control*. Addison-Wesley Pub. Co., 1989.

[29] M. Damsgaard, J. Rasmussen, S. T. Christensen, E. Surma, and M. de Zee, "Analysis of musculoskeletal systems in the AnyBody modeling system," *Simulation Modelling Practice and Theory*, vol. 14, pp. 1100–1111, 2006.

[30] A. DasGupta and Y. Nakamura, "Making feasible walking motion of humanoid robots from human motion captured data," in *IEEE International Conference on Robotics and Automation (ICRA)*, 1999, pp. 1044–1049.

[31] D.A.Winter, *Biomechanics and motor control of human movement*. John Wiley & Sons, 2009.

[32] M. Deisenroth, R. Calandra, A. Seyfarth, and J. Peters, "Toward fast policy search for learning legged locomotion," in *IEEE/RSJ International Conference on Intelligent Robots and Systems (IROS)*, 2012.

[33] S. L. Delp, F. C. Anderson, A. S. Arnold, P. Loan, A. Habib, C. T. John, E. Guendelman, and D. G. Thelen, "Opensim: Open-Source software to create and analyze dynamic simulations of movement," *IEEE Transactions on Biomedical Engineering*, vol. 54, no. 11, pp. 1940–1950, 2007.

[34] J. Denavit and R. S. Hartenberg, "A kinematic notation for a lower-pair mechanisms based on matrices," *ASME Journal o Applied Mechanics*, vol. 22, pp. 215–221, 1955.

[35] G. Ellis, *Control System Design Guide*. Elsevier Academic Press, 2004.

[36] K. Endo and H. Herr, "A model of muscle-tendon function in human walking," in *IEEE International Conference on Robotics and Automation (ICRA)*, 2009, pp. 1909–1915.

[37] C. T. Farley, R. Blickhan, J. Saito, and C. R. Taylor, "Hopping frequency in humans: a test of how springs set stride frequency in bouncing gaits," *Journal of Applied Physiology*, vol. 71, no. 6, pp. 2127 – 2132, 1991.

[38] C. T. Farley, H. H. P. Houdijk, C. V. Strien, and M. Louie, "Mechanism of leg stiffness adjustment for hopping on surfaces of different stiffnesses," *Journal of Applied Physiology*, vol. 85, pp. 1044–1055, 1998.

[39] C. Farley and D. Morgenroth, "Leg stiffness primarily depends on ankle stiffness during human hopping," *Journal of Biomechanics*, vol. 32, pp. 267–273, 1999.

[40] R. Featherstone, *Robot Dynamics Algorithms*. Kluwer, 1987.

[41] ——, *Rigid Body Dynamics Algorithms*. Spinger, 2008.

[42] D. P. Ferries, K. Liang, and C. T. Farley, "Runners adjust leg stiffness for their first step on a new running surface," *Journal of Biomechanics*, vol. 32, pp. 787–794, 1999.

[43] R. Feynman, "What I cannot create, I do not understand."

[44] K. Fischer, "Zur geführten Wirkung mehrgelenkiger Muskeln," *Zeitschrift für Anatomie und Entwicklungsgeschichte*, vol. 83, pp. 752–770, 1927.

[45] R. Full and D. Koditschek, "Templates and anchors: neuromechanical hypotheses of legged locomotion on land," *Journal of Experimental Biology*, vol. 202, pp. 3325–3332, 1999.

[46] G. Gabrielli and T. von Kármán, "What price speed?: Specific power required for propulsion of vehicles," *Mechanical Engineering*, vol. 72, no. 10, pp. 775–781, 1950.

[47] H. Geyer, A. Seyfarth, and R. Blickhan, "Natural dynamics of spring-like running: Emergence of self-stability," in *International Conference on Climbing and Walking Robots and the Support Technologies for Mobile Machines (CLAWAR)*, 2002.

[48] ——, "Compliant leg behaviour explains basic dynamics of walking and running." *Royal Society B: Biological Sciences*, vol. 273, pp. 2861–2867, 2006.

[49] M. Gienger, K. Löffler, and F. Pfeiffer, "Towards the design of biped jogging robot," in *IEEE International Conference on Robotics and Automation (ICRA)*, vol. 4, 2001, pp. 4140–4145.

[50] W. Goldsmith, *Impact: The theory and physical behaviour of colliding solids*. Dover Publications, 2001.

[51] H. Goldstein, *Classical Mechanics*. Addison-Wesley Pub. Co., 1980.

[52] Y. Gonthier, J. McPhee, and C. Lange, "On the implementation of Coulomb friction in a volumetric-based model for contact dynamics," in *Proc. ASME IDETC*, 2007.

[53] A. Goswami, "Postural stability of biped robots and the foot-rotation indicator (FRI) point," *The International Journal of Robotics Research*, vol. 18, no. 6, pp. 523–533, 1999.

[54] P. Gregorio, M. Ahmadi, and M. Buehler, "Design, control, and energetics of an electrically actuated legged robot," *IEEE Transactions on Systems, Man, and Cybernetics—Part B: Cybernetics*, vol. 27, no. 4, pp. 626–634, 1997.

[55] L. Grègoire, H. E. Veeger, P. A. Huijing, and G. J. van Ingen Schenau, "Role of mono- and biarticular muscles in explosive movements," *International Journal of Sports Medicine*, vol. 5, pp. 301–305, 1984.

[56] R. V. Ham, T. Sugar, B. Vanderborght, K. Hollander, and D. Lefeber, "Compliant actuator designs," *IEEE Robotics and Automation Magazine*, vol. 16, no. 3, pp. 81–94, 2009.

[57] R. V. Ham, B. Vanderborght, M. V. Damme, B. Verrelst, and D. Lefeber, "MACCEPA: the mechanically adjustable compliance and controllable equilibrium position actuator for 'controlled passive walking'," in *IEEE International Conference on Robotics and Automation (ICRA)*, 2006, pp. 2195–2200.

[58] M. Hardt and O. von Stryk, "Dynamic modeling in the simulation, optimization, and control of bipedal and quadrupedal robots," *Zeitschrift für Angewandte Mathematik und Mechanik*, vol. 83, no. 10, pp. 1–16, 2003.

[59] K. Hirai, M. Hirose, Y. Haikawa, and T. Takenaka, "The development of Honda humanoid robot," in *IEEE International Conference on Robotics and Automation (ICRA)*, 1998, pp. 1321–1326.

[60] D. Hobbelen, T. de Boer, and M. Wisse, "System overview of bipedal robots Flame and TUlip: tailor-made for Limit Cycle Walking," in *IEEE/RSJ International Conference on Intelligent Robots and Systems (IROS)*, 2008, pp. 2486–2491.

[61] K. W. Hollander and T. G. Sugar, "Powered human gait assistance," *InTech*, 2007. [Online]. Available: http://www.intechopen.com/articles/show/title/powered_human_gait_assistance

[62] K. Hosoda, Y. Sakaguchi, H. Takayama, and T. Takumai, "Pneumatic-driven jumping robot with anthropomorphic muscular skeleton structure," *Autonomous Robots*, vol. 28, no. 3, pp. 307–316, 2010.

[63] K. Hosoda, T. Takuma, A. Nakamato, and S. Hayashi, "Biped robot design powered by antagonistic pneumatic actuators for multi-modal locomotion," *Robotics and Autonomous Systems*, vol. 56, pp. 46–53, 2007.

[64] M. G. Hoy, F. E. Zajac, and M. E. Gordon, "A musculoskeletal model of the human lower extremity: the effect of muscle, tendon, and moment arm on the moment-angle relationship of musculotendon actuators at the hip, knee, and ankle," *Journal of Biomechanics*, vol. 23, no. 2, pp. 157–169, 1990.

[65] Q. Huang, Z. Yu, W. Zhang, X. Duan, Y. H., and K. Li, "Generation of humanoid walking pattern based on human walking measurement," in *IEEE-RAS International Conference on Humanoid Robots (HUMANOIDS)*, 2008, pp. 99–104.

[66] K. H. Hunt and F. R. E. Crossley, "Coefficient of restitution interpreted as damping in vibroimpact," *Journal of Applied Mechanics*, vol. 42, no. 2, pp. 440–445, 1975.

[67] J. W. Hurst, J. Chestnutt, and A. Rizzi, "An actuator with physically variable stiffness for highly dynamic legged locomotion," in *IEEE International Conference on Robotics and Automation (ICRA)*, 2004, pp. 4662–4667.

[68] J. W. Hurst and A. A. Rizzi, "Series compliance for an efficient running gait," *IEEE Robotics and Automation Magazine*, vol. 15, no. 3, pp. 42–51, 2008.

[69] M. Hutter, C. Remy, M. Hoepflinger, and R. Siegwart, "SLIP running with an articulated robotic leg," in *IEEE/RSJ International Conference on Intelligent Robots and Systems (IROS)*, 2010.

[70] ——, "High compliant series elastic actuation for the robotic leg ScarlETH," in *International Conference on Climbing and Walking Robots and the Support Technologies for Mobile Machines (CLAWAR)*, 2011.

[71] F. Iida, J. Rummel, and A. Seyfarth, "Bipedal walking and running with compliant legs," in *IEEE International Conference on Robotics and Automation (ICRA)*, 2007, pp. 3970–3975.

[72] R. Jacobs, M. F. Bobbert, and G. J. van Ingen Schenau, "Mechanical output from individual muscles during explosive leg extensions: The role of biarticular muscles," *Journal of Biomechanics*, vol. 29, no. 4, pp. 513–523, April 1996.

[73] S. Kajita and B. Espiau, *Springer Handbook of Robotics*. Springer, 2008, ch. Legged Robots, pp. 361 – 389.

[74] S. Kajita, F. Kanehiro, K. Kaneko, K. Fujiwara, K. Harada, K. Yokoi, and H. Hirukawa, "Biped walking pattern generation by using preview control of zero-moment point," in *IEEE International Conference on Robotics and Automation (ICRA)*, 2003, pp. 1620–1626.

[75] T. Kane, *Dynamics: Theory and Applications*. McGraw-Hill, 1985.

[76] K. Kaneko, S. Kajita, F. Kanehiro, K. Yokoi, K. Fujiwara, H. Hirukawa, T. Kawasaki, M. Hirata, and T. Isozumi, "Design of advanced leg module for humanoid robotics project of METI," in *IEEE International Conference on Robotics and Automation (ICRA)*, 2002, pp. 38–45.

[77] I. Kao, K. Lynch, and J. W. Burdick, *Springer Handbook of Robotics*. Springer, 2008, ch. Contact Modeling and Manipulation, pp. 647 – 669.

[78] O. Khatib, P. Thaulad, T. Yoshikawa, and J. Park, "Torque-position transformer for task control of position controlled robots," in *IEEE International Conference on Robotics and Automation (ICRA)*, may 2008, pp. 1729 – 1734.

[79] S. Kim and S. Park, "Leg stiffness increases with speed to modulate gait frequency and propulsion energy," *Journal of Biomechanics*, vol. 44, pp. 1253–1258, 2011.

[80] J. Kirchhoff, "Parameter identification for a non-modular elastic joint robot arm for observer-based collision detection," Master's thesis, Technische Universität Darmstadt, 2011.

[81] T. J. Klein and M. A. Lewis, "A robot leg based on mammalian muscle architecture," in *IEEE International Conference on Robotics and Biomimetics (ROBIO)*, 2009, pp. 2521–2526.

[82] T. J. Klein, T. Phuam, and M. A. Lewis, "On the design of walking machines using biarticular actuators," in *International Conference on Climbing and Walking Robots and the Support Technologies for Mobile Machines (CLAWAR)*, 2008.

[83] D. E. Koditschek, R. J. Full, and M. Buehler, "Mechanical aspects of legged locomotion control," *Arthropod Structure & Development*, vol. 33, pp. 251–272, 2004.

[84] A. D. Kuo, "The action of two-joint muscles: The legacy of W. P. Lombard." in *Classics in Movement Science*, Human Kinetics ed., M. L. Latash and V. M. Zatsiorsky, Eds. Champaign, 2001, pp. 289–316.

[85] ——, "Choosing your steps carefully: Trade-offs between economy and versatility in dynamic walking bipedal robots." *IEEE Robotics and Automation Magazine*, vol. 14, pp. 18–29, 2007.

[86] T. Lens, "Physical human-robot interaction with a lightweight, elastic tendon driven robotic arm," Ph.D. dissertation, Department of Computer Science, Technische Universität Darmstadt, Darmstadt, Germany, 2013.

[87] T. Lens, K. Radkhah, and O. von Stryk, "Simulation of dynamics and realistic contact forces for manipulators and legged robots with high joint elasticity," in *International Conference on Advanced Robotics (ICAR)*, June 20-23 2011, pp. 34–41.

[88] K. Löffler, M. Gienger, and F. Pfeiffer, "Sensor and control design of a dynamically stable biped robot," in *IEEE International Conference on Robotics and Automation (ICRA)*, 2003, pp. 484–490.

[89] S. Lipfert, "Kinematic and dynamic similarities between walking and running," Ph.D. dissertation, Friedrich-Schiller-Universität, Jena, Germany, 2009.

[90] G. E. Loeb, "Control implications of musculoskeletal mechanics," in *Proceedings of 17th International Conference of the Engineering in Medicine and Biology Society 2*, 1995, pp. 1393–1394.

[91] A. D. Luca, "Feedforward/feedback laws for the control of flexible robots," in *IEEE International Conference on Robotics and Automation (ICRA)*, 2000, pp. 233 –239.

[92] J. D. Madden, "Mobile robots: Motor challenges and materials solutions," *Science*, vol. 318, no. 5853, pp. 1094–1097, 2007.

[93] S. Manschitz, "Implementierung einer Code-Brücke zwischen C++ und Matlab zur Optimierung von Simulation-In-The-Loop," Department of Computer Science, Technische Universität Darmstadt, Darmstadt, Germany, Studienarbeit, 2013.

[94] D. W. Marhefka and D. E. Orin, "Simulation of contact using a nonlinear damping model," in *IEEE International Conference on Robotics and Automation (ICRA)*, 1996, pp. 1662–1668.

[95] H. G. Marques, M. Jäntsch, S. Wittmeier, O. Holland, C. Alessandro, A. Diamond, M. Lungarella, and R. Knight, "Ecce1: The first of a series of anthropomimetic musculoskeletal upper torsos," in *IEEE-RAS International Conference on Humanoid Robots (HUMANOIDS)*, 2010, pp. 391–396.

[96] T. McGeer, "Passive dynamic walking," *The International Journal of Robotics Research*, vol. 9, no. 2, pp. 62–82, 1990.

[97] ——, "Passive walking with knees," in *IEEE International Conference on Robotics and Automation (ICRA)*, vol. 2, 1994, pp. 1640–1645.

[98] P. J. McKerrow, *Introduction to Robotics*. Addison Wesley, 1991.

[99] T. A. McMahon, *Muscles, Reflexes, and Locomotion*. Princeton University Press, 1984.

[100] T. A. McMahon, G. Valiant, and E. C. Frederick, "Groucho running," *Journal of Applied Physiology*, vol. 62, no. 6, pp. 2326 – 2337, 1987.

[101] J. McPhee, C. Schmitke, and S. Redmond, "Dynamic modelling of mechatronic multibody systems with symbolic computing and linear graph theory," *Math. Comp. Mod. Dyn. Sys.*, vol. 10, pp. 1–23, 2004.

[102] G. Medrano-Cerda, H. Dallali, M. Brown, N. G. Tsagarakis, and D. G. Caldwell, "Modelling and simulation of the locomotion of humanoid robots," in *Proc. UK Automatic Control Conf. (UKACC)*, 2010.

[103] M. Mistry, J. Buchli, and S. Schaal, "Inverse dynamics control of floating base systems using orthogonal decomposition," in *IEEE International Conference on Robotics and Automation (ICRA)*, 2010, pp. 3406–3410.

[104] D. Mitrovic, S. Klanke, and S. Vijayakumar, "Adaptive optimal feedback control with learned internal dynamics models," in *From Motor Learning to Interaction Learning in Robots*, ser. SCI, O. Sigaud and J. Peters, Eds. Springer, Heidelberg, 2010, vol. 264, pp. 65–84.

[105] I. Mizuuchi, Y. Nakanishi, Y. Sodeyama, Y. Namiki, T. Nishino, N. Muramatsu, J. Urata, K. Hongo, T. Yoshikai, and M. Inaba, "An advanced musculoskeletal humanoid Kojiro," in *IEEE-RAS International Conference on Humanoid Robots (HUMANOIDS)*, 2007, pp. 294–299.

[106] I. Mizuuchi, T. Yoshikai, Y. Sodeyama, Y. Nakanishi, A. Miyadera, T. Yamamoto, T. Niemela, M. Hayashi, J. Urata, Y. Namiki, T. Nishino, and M. Inaba, "Development of musculoskeletal humanoid Kotaro," in *IEEE International Conference on Robotics and Automation (ICRA)*, 2006, pp. 82–87.

[107] S. Molbech, "On the paradoxical effect of some two-joint muscles," *Acta Morphologica Neerlando-Scandinavica*, vol. 6, pp. 171 – 178, 1965.

[108] K. Mombaur, M. Scheint, and M. Sobotka, "Optimal control and design of bipedal robots with compliance," *at - Automatisierungstechnik*, vol. 57, no. 7, pp. 349–359, 2009.

[109] J. Morimoto and C. G. Atkeson, "Learning biped locomotion," *IEEE Robotics and Automation Magazine*, vol. 14, no. 2, pp. 41–51, 2007.

[110] J. Morimoto, G. Endo, J. Nakanishi, and G. Cheng, "A biologically inspired biped locomotion strategy for humanoid robots: Modulation of sinusoidal patterns by a coupled oscillator model," *IEEE Transactions on Robotics*, vol. 24, no. 1, pp. 185–191, 2008.

[111] J. Morimoto, G. Endo, J. Nakanishi, S. Hyon, G. Cheng, D. Bentivegna, and C. Atkeson, "Modulation of simple sinusoidal patterns by a coupled oscillator model for biped walking," in *IEEE International Conference on Robotics and Automation (ICRA)*, 2006, pp. 1579–1584.

[112] K. Nagasaka, I. Masayuki, and H. Inoue, "Walking pattern generation for a humanoid robot based on a optimal gradient method," in *IEEE International Conference on Systems, Man and Cybernetics (SMC)*, 1999, pp. 908–913.

[113] J. Nakanishi, R. Cory, M. Mistry, J. Peters, and S. Schaal, "Operational space control: A theoretical and empirical comparison," *The International Journal of Robotics Research*, vol. 27, no. 6, pp. 737–757, 2008.

[114] J. Nakanishi, J. Morimoto, G. Endo, G. Cheng, S. Schaal, and M. Kawato, "Learning from demonstration and adaptation of biped locomotion," *Robotics and Autonomous Systems*, vol. 47, no. 2-3, pp. 79–91, 2004.

[115] Y. Nakanishi, T. Izawa, M. Osada, N. Ito, S. Ohta, J. Urata, and M. Inaba, "Development of musculoskeletal humanoid Kenzoh with mechanical compliance changeable tendons by nonlinear spring unit," in *IEEE International Conference on Robotics and Biomimetics (ROBIO)*, 2011, pp. 2384–2389.

[116] R. Neptune, S. Kautz, and F. Zajac, "Contribution of the individual ankle plantar flexors to support forward progression and swing initiation during walking," *Journal of Biomechanics*, vol. 34, pp. 1387 – 1398, 2001.

[117] R. Niiyama, "Design of a musculoskeletal Athlete robot: A biomechanical approach," in *International Conference on Climbing and Walking Robots and the Support Technologies for Mobile Machines (CLAWAR)*, 2009, pp. 173–180.

[118] R. Niiyama, A. Nagakubo, and Y. Kuniyoshi, "Mowgli: A bipedal jumping and landing robot with an artificial musculoskeletal system," in *IEEE International Conference on Robotics and Automation (ICRA)*, 2007, pp. 2546–2551.

[119] Y. Ogura, K. Shimomura, A. Kondo, A. Morishima, T. Okubo, S. Momoki, H. ok Lim, and A. Takanishi, "Human-like walking with knee stretched, heel-contact and toe-off motion by a humanoid robot," in *IEEE/RSJ International Conference on Intelligent Robots and Systems (IROS)*, 2006, pp. 3976 –3981.

[120] D. K. Pai, U. M. Ascher, and P. G. Kry, "Forward dynamic algorithms for multibody chains and contact," in *IEEE International Conference on Robotics and Automation (ICRA)*, 2000.

[121] G. Palli, G. Borghesan, and C. Melchiorri, "Tendon-based transmission systems for robotic devices: Models and control algorithms," in *IEEE International Conference on Robotics and Automation (ICRA)*, 2009, pp. 4063–4068.

[122] M. Pandy and N. Berme, "Synthesis of human walking: a planar model for single support," *Journal of Biomechanics*, vol. 21, pp. 1053 – 1060, 1988.

[123] I.-W. Park and J.-Y. Kim, "Fourier series-based walking pattern generation for a biped humanoid robot," in *IEEE-RAS International Conference on Humanoid Robots (HUMANOIDS)*, 2010, pp. 461–467.

[124] G. A. Parker and J. M. Smith, "Optimality theory in evolutionary biology," *Nature*, vol. 348, pp. 27–33, 1990.

[125] R. Pfeifer, M. Lungarella, and F. Iida, "Self-organization, embodiment, and biologically inspired sobotics," *Science*, vol. 318, no. 5853, pp. 1088–1093, 2007.

[126] G. A. Pratt and M. M. Williamson, "Series elastic actuators," in *IEEE International Workshop on Intelligent Robots and Systems*, 1995, pp. 399–406.

[127] J. Pratt, C.-M. Chew, A. Torres, P. Dilworth, and G. Pratt, "Virtual model control: An intuitive approach for bipedal locomotion," *The International Journal of Robotics Research*, vol. 20, pp. 129–143, 2001.

[128] K. Radkhah, R. Calandra, and M. Deisenroth, "Learning musculoskeletal dynamics with non-parametric models," in *Workshop on "Novel Methods for Learning and Optimization of Control Policies and Trajectories for Robotics", IEEE International Conference on Robotics and Automation (ICRA)*, Karlsruhe, Germany, May 10 2013.

[129] K. Radkhah, D. Kulic, and E. Croft, "Dynamic parameter identification for the CRS A460 robot," in *IEEE/RSJ International Conference on Intelligent Robots and Systems (IROS)*, October 29 - November 2 2007, pp. 3842 – 3847.

[130] K. Radkhah, T. Lens, A. Seyfarth, and O. von Stryk, "On the influence of elastic actuation and monoarticular structures in biologically inspired bipedal robots," in *IEEE International Conference on Biomedical Robotics and Biomechatronics (BIOROB)*, September 26 - 29 2010, pp. 389–394.

[131] K. Radkhah, T. Lens, and O. von Stryk, "Detailed dynamics modeling of BioBiped's monoarticular and biarticular tendon-driven actuation system," in *IEEE/RSJ International Conference on Intelligent Robots and Systems (IROS)*, October 7 - 12 2012, pp. 4243 – 4250.

[132] K. Radkhah, C. Maufroy, M. Maus, D. Scholz, A. Seyfarth, and O. von Stryk, "Concept and design of the BioBiped1 robot for human-like walking and running," *International Journal of Humanoid Robotics*, vol. 8, no. 3, pp. 439–458, 2011. [Online]. Available: http://www.worldscinet.com/ijhr/08/0803/S0219843611002587.html

[133] K. Radkhah and O. von Stryk, "Actuation requirements for hopping and running of the musculoskeletal robot BioBiped1," in *IEEE/RSJ International Conference on Intelligent Robots and Systems (IROS)*, September 25 - 30 2011, pp. 4811–4818.

[134] ——, "Human-like model-based motion generation combining feedforward and feedback control for musculoskeletal robots," in *Proc. 7th Annual Dynamic Walking Conference*, Pensacola, Florida, USA, May 21 - 24 2012.

[135] ——, "Exploring the Lombard paradox in a bipedal musculoskeletal robot," in *International Conference on Climbing and Walking Robots and the Support Technologies for Mobile Machines (CLAWAR)*, July 14 - 17 2013, pp. 537–546.

[136] ——, "Model-based elastic tendon control for electrically actuated musculoskeletal bipeds," in *International Conference on Climbing and Walking Robots and the Support Technologies for Mobile Machines (CLAWAR)*, July 14 - 17 2013, pp. 719–728.

[137] ——, "The need for a common taxonomy and benchmarks to achieve "human-like" performance in bipedal robot locomotion," in *Workshop on "Benchmarking of Human-like Robotic Locomotion", IEEE International Conference on Humanoid Robots (Humanoids)*, Atlanta, USA, October 15 2013.

[138] ——, "A study of the passive rebound behavior of bipedal robots with stiff and different types of elastic actuation," in *IEEE International Conference on Robotics and Automation (ICRA)*, May 31 - June 7 2014, pp. 5095–5102.

[139] M. H. Raibert, *Legged robots that balance*. MIT Press, 1986.

[140] L. Righetti, J. Buchli, M. Mistry, M. Kalakrishnan, and S. Schaal, "Optimal distribution of contact forces with inverse dynamics control," *The International Journal of Robotics Research*, vol. 0, no. 0, pp. 1–19, 2013.

[141] L. Righetti and A. J. Ijspeert, "Programmable central pattern generators: an application to biped locomotion control," in *IEEE International Conference on Robotics and Automation (ICRA)*, 2006, pp. 1585– 1590.

[142] R.M.Enoka, *Neuromechanics of human movement*. Human Kinetics, 2008.

[143] J. Rummel and A. Seyfarth, "Stable running with segmented legs," *The International Journal of Robotics Research*, vol. 27, no. 8, pp. 919–934, 2008.

[144] A. Safonova, J. Hodgins, and N. Pollard, "Synthesizing physically realistic human motion in low-dimensional, behavior-specific spaces," *ACM Transactions on Graphics*, vol. 23, no. 3, pp. 514–521, 2004.

[145] M. Sartori, D. G. Lloyd, M. Reggiani, and E. Pagello, "An EMG-driven musculoskeletal model of the human lower limb for the estimation of muscle forces and moments at the

hip, knee and ankle joints in vivo," in *Workshop on "Biomechanical Simulation of Humans and Bio-Inspired Humanoids", Simulation, Modeling, and Programming for Autonomous Robots (SIMPAR)*, Darmstadt, Germany, 2010.

[146] A. Savitzky and M. Golay, "Smoothing and differentiation of data by simplified least squares procedures," *Analytical Chemistry*, vol. 36, no. 8, pp. 1627–1639, 1964.

[147] M. Scheint, M. Sobotka, and M. Buss, "Optimized parallel joint springs in dynamic motion: Comparison of simulation and experiment," in *IEEE International Conference on Biomedical Robotics and Biomechatronics (BIOROB)*, 2010.

[148] G. Schultz and K. Mombaur, "Modeling and optimal control of human-like running," *IEEE/ASME Transactions on Mechatronics*, vol. 15, no. 5, pp. 783 – 792, 2010.

[149] S. Seok, A. Wang, D. Otten, and S. Kim, "Actuator design for high force proprioceptive control in fast legged locomotion," in *IEEE/RSJ International Conference on Intelligent Robots and Systems (IROS)*, 2012, pp. 1970–1975.

[150] A. Seyfarth, H. Geyer, M. Günther, and R. Blickhan, "A movement criterion for running," *Journal of Biomechanics*, vol. 35, pp. 649–655, 2002.

[151] A. Seyfarth, H. Geyer, S. Lipfert, J. Rummel, Y. Minekawa, and F. Iida, "Running and walking with compliant legs," in *Fast Motions in Biomechanics and Robotics - Optimization and Feedback Control*. Berlin Heidelberg: Springer, 2006, pp. 383–402.

[152] A. Seyfarth, R. Tausch, M. Stelzer, F. Iida, A. Karguth, and O. von Stryk, "Towards bipedal jogging as a natural result for optimizing walking speed for passively compliant three-segmented legs," *The International Journal of Robotics Research*, vol. 28, no. 2, pp. 257–265, 2009.

[153] M. S. Shourijeh and J. McPhee, "Efficient hyper-volumetric contact dynamic modelling of the foot within human gait simulations," in *Proc. ASME IDETC*, 2013.

[154] E. B. Simonsen, L. Thomsen, and K. Klausen, "Activity of mono- and biarticular leg muscles during sprint running," *European Journal of Applied Physiology and Occupational Physiology*, vol. 54, no. 5, pp. 524–532, 1985.

[155] T. Sugihara, "Simulated regulator to synthesize zmp manipulation and foot location for autonomous control of biped robots," in *IEEE International Conference on Robotics and Automation (ICRA)*, 2008, pp. 1264–1269.

[156] S. Tak, O. Song, and H. Ko, "Motion balance filtering," *Eurographics, Computer Graphics Forum*, vol. 19, no. 3, pp. 437–446, 2000.

[157] A. Takanishi, M. Ishida, Y. Yamazaki, and I. Kato, "The realization of dynamic walking by the biped walking robot wl-10rd," in *International Conference on Advanced Robotics (ICAR)*, 1985, pp. 459–466.

[158] T. Takenaka, T. Matsumoto, and T. Yoshiike, "Real time motion generation and control for biped robot - 1st report: Walking gait pattern generation," in *IEEE/RSJ International Conference on Intelligent Robots and Systems (IROS)*, 2009, pp. 1084–1091.

[159] ——, "Real time motion generation and control for biped robot - 3rd report: Dynamics error compensation," in *IEEE/RSJ International Conference on Intelligent Robots and Systems (IROS)*, 2009, pp. 1594 – 1600.

[160] T. Takenaka, T. Matsumoto, T. Yoshiike, T. Hasegawa, S. Shirokura, H. Kaneko, and A. Orita, "Real time motion generation and control for biped robot - 4th report: Integrated balance control," in *IEEE/RSJ International Conference on Intelligent Robots and Systems (IROS)*, 2009, pp. 1601–1608.

[161] T. Takenaka, T. Matsumoto, T. Yoshiike, and S. Shirokura, "Real time motion generation and control for biped robot - 2nd report: Running gait pattern generation," in *IEEE/RSJ International Conference on Intelligent Robots and Systems (IROS)*, 2009, pp. 1092–1099.

[162] T. Takuma, S. Hayashi, and K. Hosoda, "3D bipedal robot with tunable leg compliance mechanism for multi-modal locomotion," in *IEEE/RSJ International Conference on Intelligent Robots and Systems (IROS)*, 2008, pp. 1097–1102.

[163] D. Tlalolini, C. Chevallereau, and Y. Aoustin, "Human-like walking: Optimal motion of a bipedal robot with toe-rotation motion," *IEEE/ASME Transactions on Mechatronics*, vol. 16, no. 2, pp. 310 – 320, 2011.

[164] P. Tomei, "A simple PD controller for robots with elastic joints," *IEEE Transactions on Automatic Control*, vol. 36, no. 10, pp. 1208–1213, oct 1991.

[165] K. Tsuchiya, S. Aoi, and K. Tsujita, "Locomotion control of a biped locomotion robot using nonlinear oscillators," in *IEEE/RSJ International Conference on Intelligent Robots and Systems (IROS)*, vol. 2, 2003, pp. 1745 – 1750 vol.2.

[166] A. J. van den Bogert, "Exotendons for assistance of human locomotion," *BioMedical Engineering OnLine*, vol. 2, no. 17, 2003. [Online]. Available: http://www.biomedical-engineering-online.com/content/2/1/17

[167] G. J. van Ingen Schenau, M. F. Bobbert, and R. H. Rozendal, "The unique action of bi-articular muscles in complex movements," *Journal of Anatomy*, vol. 155, pp. 1–5, 1987.

[168] J. F. Veneman, R. Ekkelenkamp, R. Kruidhof, F. C. van der Helm, and H. van der Kooij, "A series elastic- and bowden-cable-based actuation system for use as torque actuator in exoskeleton-type robots," *The International Journal of Robotics Research*, vol. 25, no. 3, pp. 261–281, 2006.

[169] B. Verrelst, R. V. Ham, B. Vanderborght, F. Daerden, D. Lefeber, and J. Vermeulen, "The pneumatic biped "Lucy" actuated with pleated pneumatic artificial muscles," *Autonomous Robots*, vol. 18, no. 2, pp. 201–213, 2005.

[170] A. V. Voronov, "The roles of monoarticular and biarticular muscles of the lower limbs in terrestrial locomotion," *Human Physiology*, vol. 30, no. 4, pp. 476–484, July 2004.

[171] M. Vukabratovic and B. Borovac, "Zero-Moment Point - thirty five years of its life," *International Journal of Humanoid Robotics*, vol. 1, no. 1, pp. 157–173, 2004.

[172] M. Vukobratovic and J. Stepanenko, "On the stability of anthropomorphic systems," *Math. Biosci.*, vol. 15, pp. 1–37, 1972.

[173] M. W. Walker and D. E. Orin, "Efficient dynamic computer simulation of robotic mechanisms," *Journal of Dynamic Systems, Measurement, and Control*, vol. 104, pp. 205–211, 1982.

[174] Y.-T. Wang, V. Kumar, and J. Abel, "Dynamics of rigid bodies undergoing multiple frictional contacts," in *IEEE International Conference on Robotics and Automation (ICRA)*, 1992, pp. 2764–2769 vol.3.

[175] K. Wiemann and G. Tidow, "Relative activity of hip and knee extensors in sprinting - implications for training," *New studies in Athletics 1*, vol. 10, pp. 29–49, 1995.

[176] D. A. Winter, "Energy generation and absorption at the ankle and knee during fast, natural and slow cadences," *Clinical orthopaedics and related research*, vol. 197, pp. 147–154, 1983.

[177] ——, "Moments of force and mechanical power in jogging," *Journal of Biomechanics*, vol. 16, pp. 91–97, 1983.

[178] D. Wollherr, M. Hardt, M. Buss, and O. von Stryk, "Actuator selection and hardware realization of a small and fast-moving autonomous humanoid robot," in *IEEE/RSJ International Conference on Intelligent Robots and Systems (IROS)*, 2002, pp. 2491–2496.

[179] J. Yamaguchi, A. Takanishi, and I. Kato, "Development of a biped walking robot compensating for three-axis moment by trunk motion," in *IEEE/RSJ International Conference on Intelligent Robots and Systems (IROS)*, 1993, pp. 561–566.

[180] K. Yamane and Y. Nakamura, "Dynamics filter – concept and implementation of online motion generator for human figures," *IEEE Journal of Robotics and Automation*, vol. 19, no. 3, pp. 421–432, 2003.

[181] ——, "Dynamics simulation of humanoid robots: Forward dynamics, contact, and experiments," in *17th CISM-IFToMM Symposium on Robot Design, Dynamics, and Control*, 2008.

[182] T. Yoshikawa and O. Khatib, "Compliant humanoid robot control by the torque transformer," in *IEEE/RSJ International Conference on Intelligent Robots and Systems (IROS)*, 2009, pp. 3011 – 3018.

[183] F. Zajac, R. Neptune, and S. Kautz, "Biomechanics and muscle coordination of human walking part ii: lessons from dynamical simulations and clinical implications," *Gait Posture*, vol. 17, pp. 1 – 17, 2003.

List of Publications (Selection)

Journal Papers

K. Radkhah, C. Maufroy, M. Maus, D. Scholz, A. Seyfarth, and O. von Stryk, "Concept and design of the BioBiped1 robot for human-like walking and running," *International Journal of Humanoid Robotics*, vol. 8, no. 3, pp. 439–458, 2011. [Online]. Available: http://www.worldscinet.com/ijhr/08/0803/S0219843611002587.html

K. Radkhah, T. Hemker, and O. von Stryk, "Self-calibration for industrial robots with rotational joints," *International Journal of Mechatronics and Manufacturing Systems*, vol. 3, no. 3/4, pp. 187–209, 2010.

Conference Papers

K. Radkhah and O. von Stryk, "A study of the passive rebound behavior of bipedal robots with stiff and different types of elastic actuation," in *IEEE International Conference on Robotics and Automation (ICRA)*, May 31 - June 7 2014, pp. 5095–5102.

——, "Exploring the Lombard paradox in a bipedal musculoskeletal robot," in *International Conference on Climbing and Walking Robots and the Support Technologies for Mobile Machines (CLAWAR)*, July 14 - 17 2013, pp. 537–546.

——, "Model-based elastic tendon control for electrically actuated musculoskeletal bipeds," in *International Conference on Climbing and Walking Robots and the Support Technologies for Mobile Machines (CLAWAR)*, July 14 - 17 2013, pp. 719–728.

K. Radkhah, T. Lens, and O. von Stryk, "Detailed dynamics modeling of BioBiped's monoarticular and biarticular tendon-driven actuation system," in *IEEE/RSJ International Conference on Intelligent Robots and Systems (IROS)*, October 7 - 12 2012, pp. 4243 – 4250.

K. Radkhah and O. von Stryk, "Actuation requirements for hopping and running of the musculoskeletal robot BioBiped1," in *IEEE/RSJ International Conference on Intelligent Robots and Systems (IROS)*, September 25 - 30 2011, pp. 4811–4818.

T. Lens, K. Radkhah, and O. von Stryk, "Simulation of dynamics and realistic contact forces for manipulators and legged robots with high joint elasticity," in *International Conference on Advanced Robotics (ICAR)*, June 20-23 2011, pp. 34–41.

K. Radkhah, S. Kurowski, T. Lens, and O. von Stryk, "Compliant robot actuation by feedforward controlled emulated spring stiffness," in *Simulation, Modeling, and Programming for Autonomous Robots (SIMPAR)*, November 15 - 18 2010, pp. 497–508.

K. Radkhah, T. Lens, A. Seyfarth, and O. von Stryk, "On the influence of elastic actuation and monoarticular structures in biologically inspired bipedal robots," in *IEEE International Conference on Biomedical Robotics and Biomechatronics (BIOROB)*, September 26 - 29 2010, pp. 389–394.

K. Radkhah, D. Scholz, A. Anjorin, M. Rath, and O. von Stryk, "Simple yet effective technique for robust real-time instability detection for humanoid robots using minimal sensor input," in *International Conference on Climbing and Walking Robots and the Support Technologies for Mobile Machines (CLAWAR)*, August 31 - September 3 2010, pp. 680–689.

K. Radkhah, S. Kurowski, and O. von Stryk, "Design considerations for a biologically inspired compliant four-legged robot," in *IEEE International Conference on Robotics and Biomimetics (ROBIO)*, December 19-23 2009, pp. 598–603.

K. Radkhah, T. Hemker, M. Friedmann, and O. von Stryk, "Towards the deployment of industrial robots as measurement instruments - an extended forward kinematic model incorporating geometric and nongeometric effects," in *IEEE/ASME Conference on Advanced Intelligent Mechatronics (AIM)*, July 14 - 17 2009, pp. 124–129.

K. Radkhah, T. Hemker, and O. von Stryk, "A novel self-calibration method for industrial robots incorporating geometric and nongeometric effects," in *IEEE International Conference on Mechatronics and Automation (ICMA)*, August 5 - 8 2008, pp. 864–869.

K. Radkhah, D. Kulic, and E. Croft, "Dynamic parameter identification for the CRS A460 robot," in *IEEE/RSJ International Conference on Intelligent Robots and Systems (IROS)*, October 29 - November 2 2007, pp. 3842 – 3847.

Workshop Papers

K. Radkhah and O. von Stryk, "The need for a common taxonomy and benchmarks to achieve "human-like" performance in bipedal robot locomotion," in *Workshop on "Benchmarking of Human-like Robotic Locomotion", IEEE International Conference on Humanoid Robots (Humanoids)*, Atlanta, USA, October 15 2013.

K. Radkhah, R. Calandra, and M. Deisenroth, "Learning musculoskeletal dynamics with non-parametric models," in *Workshop on "Novel Methods for Learning and Optimization of Control Policies and Trajectories for Robotics", IEEE International Conference on Robotics and Automation (ICRA)*, Karlsruhe, Germany, May 10 2013.

K. Radkhah and O. von Stryk, "Human-like model-based motion generation combining feedforward and feedback control for musculoskeletal robots," in *Proc. 7th Annual Dynamic Walking Conference*, Pensacola, Florida, USA, May 21 - 24 2012.

K. Radkhah, S. Kurowski, T. Lens, and O. v. Stryk, "An extended antagonistic series elastic actuator for a biologically inspired four-legged robot," in *Workshop on "New Variable Impedance Actuators for the Next Generation of Robots", IEEE International Conference on Robotics and Automation (ICRA)*, Anchorage, Alaska, USA, May 3 2010.

Talks

International Conference on Climbing and Walking Robots and the Support Technologies for Mobile Machines (CLAWAR), Sydney, Australia, July 16 2013, "Model-based elastic tendon control for electrically actuated musculoskeletal bipeds."

International Conference on Climbing and Walking Robots and the Support Technologies for Mobile Machines (CLAWAR), Sydney, Australia, July 15 2013, "Exploring the Lombard paradox in a bipedal musculoskeletal robot."

Workshop on "Developments of Simulation Tools for Robotics and Biomechanics", IEEE International Conference on Robotics and Automation (ICRA), Karlsruhe, Germany, May 10 2013, "Dynamic modeling for simulation, optimization and control of bio-inspired elastic robots," invited, presentation held with Oskar von Stryk.

IEEE/RSJ International Conference on Intelligent Robots and Systems (IROS), Vilamoura, Portugal, October 10 2012, "Detailed dynamics modeling of BioBiped's monoarticular and biarticular tendon-driven actuation system."

Workshop on "Dynamic Modeling and Optimal Control of Humanoid Robots", IEEE-RAS International Conference on Humanoid Robots (HUMANOIDS), Bled, Slovenia, October 26 2011, "Dynamics modeling and simulation of hopping and running gaits for the musculoskeletal robot BioBiped1," invited.

IEEE/RSJ International Conference on Intelligent Robots and Systems (IROS), San Francisco, California, USA, September 29 2011, "Actuation requirements for hopping and running of the musculoskeletal robot BioBiped1."

International Conference on Advanced Robotics (ICAR), Tallinn, Estonia, June 21 2011, "Simulation of dynamics and realistic contact forces for manipulators and legged robots with high joint elasticity."

Workshop on "Biomechanical Simulation of Humans and Bio-Inspired Humanoids", Simulation, Modeling, and Programming for Autonomous Robots (SIMPAR), Darmstadt, Germany, November 15 2010, "First results for the BioBiped1 robot designed towards human-like walking and running," invited, presentation held with Andre Seyfarth.

IEEE International Conference on Biomedical Robotics and Biomechatronics (BIOROB), Tokyo, Japan, September 28 2010, "On the influence of elastic actuation and monoarticular structures in biologically inspired bipedal robots."

IEEE International Conference on Mechatronics and Automation (ICMA), Takamatsu, Japan, August 6 2008, "A novel self-calibration method for industrial robots incorporating geometric and nongeometric effects."

Dynamic Walking Conference, Delft, The Netherlands, May 26 2008, "Underactuated 3-segmented elastic legs."

IEEE/RSJ International Conference on Intelligent Robots and Systems (IROS), San Diego, California, USA, November 2 2007, "Dynamic parameter identification for the CRS A460 robot."

Wissenschaftlicher Werdegang[1]

Der Lebenslauf ist in der Online-Verison aus Gründen des Datenschutzes nicht enthalten.

Erklärung[2]

Hiermit erkläre ich, dass ich die vorliegende Arbeit, mit Ausnahme der ausdrücklich genannten Hilfsmittel, selbständig verfasst habe.

[1] gemäß § 20 Abs. 3 der Promotionsordnung der TU Darmstadt
[2] gemäß § 9 Abs. 1 der Promotionsordnung der TU Darmstadt